Electrically-induced degradation of polyester films for photovoltaic devices

A thesis presented in fulfilment of the requirement for the degree of

Doctor of Philosophy

Rong Tang, Msc

2016

Department of Pure and Applied Chemistry

University of Strathclyde

Glasgow, UK

Declaration of Authenticity and Author's Rights

This thesis is the result of the author's original research. It has been composed by the author and has not been previously submitted for examination which has led to the award of a degree.

Signed:

Date: 30-09-2016

Acknowledgements

I would like to express my appreciation and thanks to my supervisors Dr John Liggat and Dr W H Siew for their supervision, encouragement throughout the project. Their experience, in-depth knowledge and constructive comments in both chemistry and high voltage engineering have been of great value for me. Without their patient guidance and supports, this PhD would never have been achievable.

I gratefully acknowledge the University of Strathclyde for providing the PhD studentship and research funding.

I would like to thank all my colleagues from the polymer degradation research group and high voltage technology research group in the university. I greatly appreciate the helpful advice and supports that I received from these people. I would also like to thank all the people from the workshop in the high voltage technology group for manufacturing high-quality test cells, which could allow me to obtain highly reproducible results in dielectric tests.

Special thanks go to Dr Pik Leung Tang and Dr Simson McCreath. Their helpful input in my experiments especially the FTIR and DSC analysis and the weatherometer runs have been invaluable to this project. I would also like to say a big thank you to Dr Jose Portoles from the National EPSRC XPS Users' Service (NEXUS) in Newcastle University, thank you for all your supports on my XPS experiments.

I would like to thank my parents for their supports, encouragement and love during my PhD research. Finally I would like to express my special appreciation to my beloved wife Jieyu Zhang for her understanding, encouragement and love. Thank you.

Abstract

Poly(ethylene terephthalate) (PET) is one of the most common thermoplastics that has been widely used in nearly every field all over the world. Particularly, PET is utilized as a core layer in the backsheets of photovoltaic panels to provide electrical insulation and mechanical stability.

Partial discharge (PD) is localized dielectric breakdown that usually occurs in voids or air gaps within solid or liquid insulation systems. Long-term PD exposure can significantly deteriorate the system and cause final breakdown. PD is believed to be able to occur in PV backsheets under certain circumstances and this is obviously a potential risk of safe operation for the PV modules. PET, as usually being the thickest layer of the backsheet with excellent insulation properties, greatly determines the PD behaviour of the PV backsheet. Therefore a comprehensive understanding of PD-induced degradation and dielectric breakdown of PET films will be vital.

In this project, various types of PET films were studied to understand how physical and chemical properties influence the PD-induced degradation and breakdown of the PET films. Efforts have endeavoured to focus on three primary aspects: morphology effect, performance additive effect and weathering effect.

The main contributions of this work are: the morphology effect has been quantitatively analysed and a straightforward method was introduced to significantly improve the sample performance; great enhancement in voltage endurance has been found once the PET sample equipped with a phosphorus-based flame retardant; the weathering effect (UV and hydrolysis) on the PD-induced degradation and breakdown of PET was investigated for the first time ever.

Contents

Chapter One

1. Introduction

1.1 Poly(ethylene terephthalate)

Poly(ethylene terephthalate) (PET) is a long chain thermoplastic polymer belonging to the polyester family [171]. It was originally synthesized by Dupont in the search for new synthetic fibres in the mid-1940s [172]. Today, PET has become one of the most widely used polymers in the world, the global annual production capacity of PET amounted to 30 million tonnes in 2000 [100].

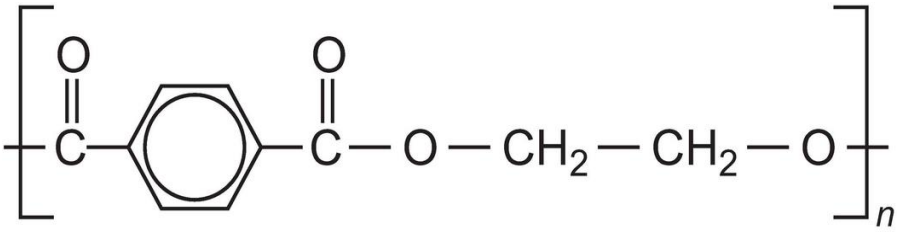

Figure 1.1 Chemical structure of PET

The chemical structure of PET is shown in figure 1.1. PET can be synthesized from ethylene glycol (EG) and dimethyl terephthalate (DMT) or terephthalic acid (TPA). The polymerization of PET is a two-step process, the first reaction is the production of bis(2-hydroxyethyl) terephthalate (BHET), the so-called prepolymer of PET and the second step is polycondensation [100]. In the early years, BHET was

derived by transesterification of DMT with EG (figure 1.2). After the 1960s when high-purity TPA was successfully obtained, TPA has become the main feedstock of PET production and BHET can be produced by direct esterification of TPA with EG, as demonstrated in figure 1.3 [100]. The final polycondensation process is common for the two different BHET producing methods where the transesterification of BHET will be carried out in the melt phase to produce the polymers of ethylene terephthalate and the by-product EG, will be removed using high vacuum [100], as shown in figure 1.4. The molecular weight of PET can be further increased by a second polymerization process called solid-state polymerization after the polymerization in the melt phase.

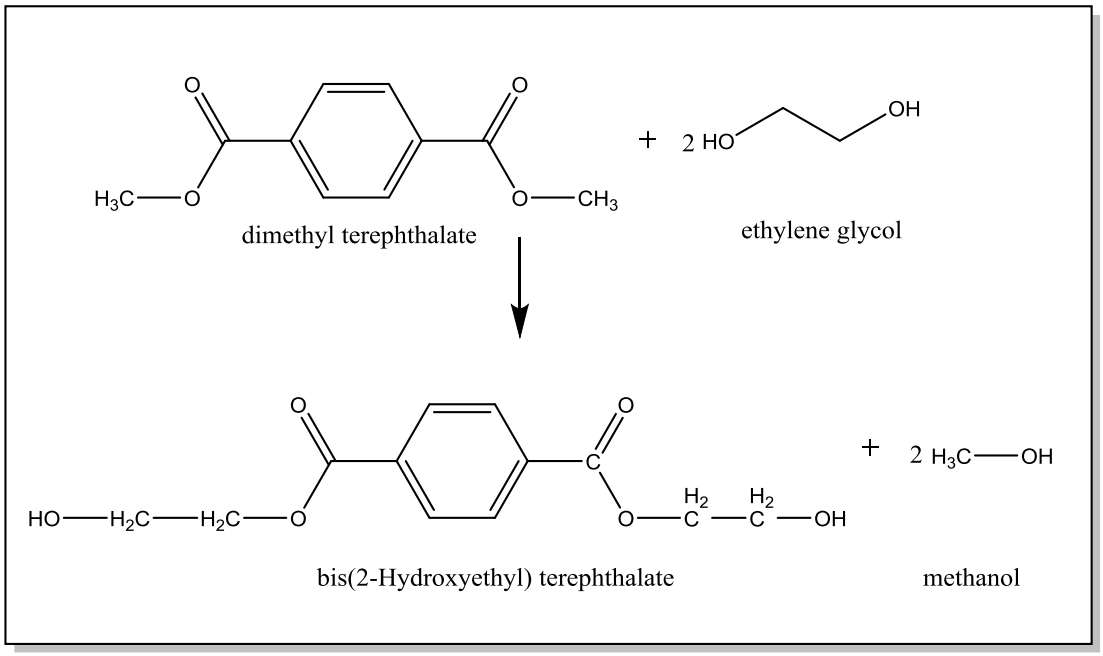

Figure 1.2 Transesterification of dimethyl terephthalate (DMT) with ethylene glycol (EG)

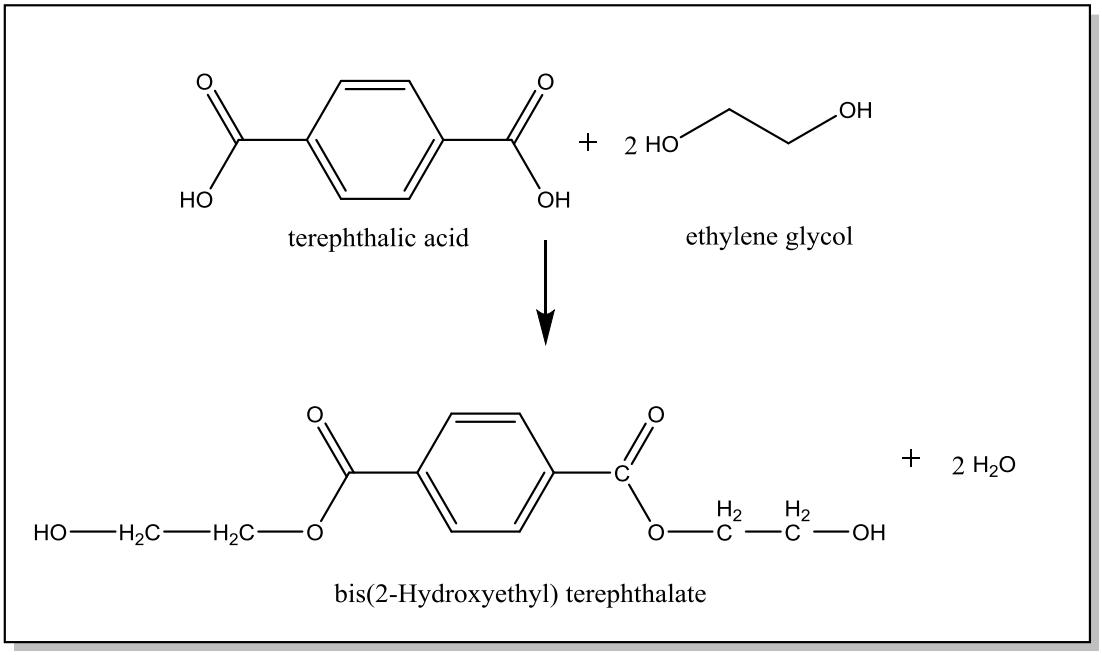

Figure 1.3 Direct esterification of terephthalic acid (TPA) with ethylene glycol (EG)

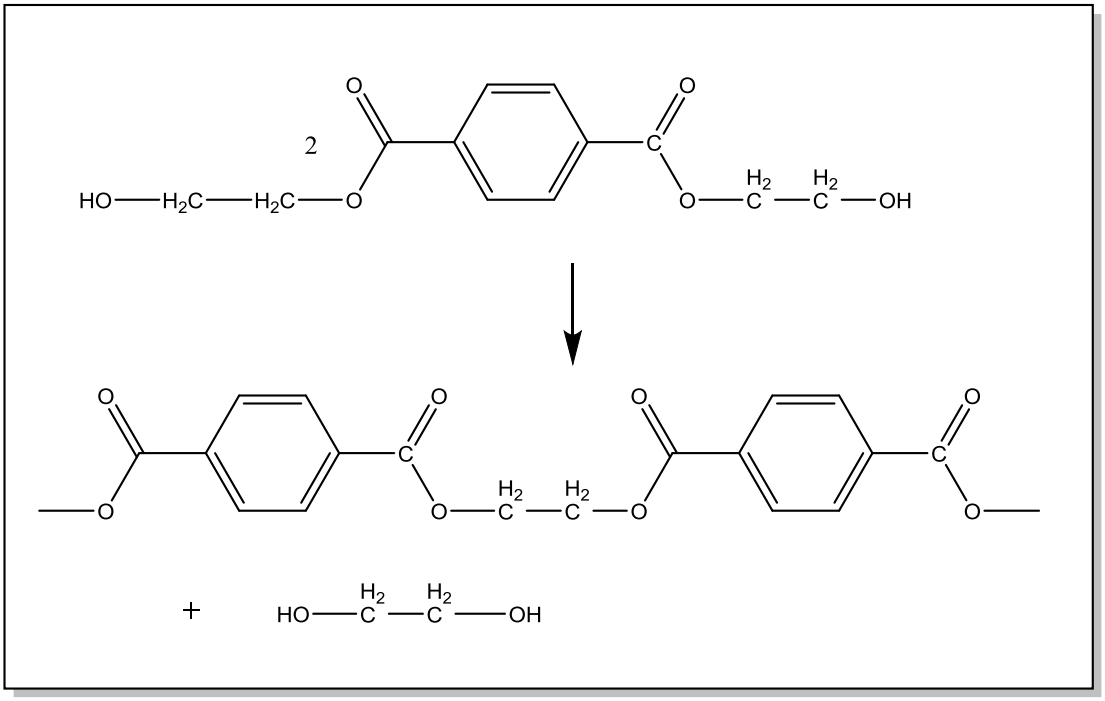

Figure 1.4 Polymerization of ethylene terephthalate

1.1.1 Applications of PET

PET, as being the largest-volume polyester in production today, dominates the global market by fibre-grade PET and bottle-grade PET [100]. Nowadays more than 50% of the world synthetic fibre is made from PET and the PET bottle production accounts for about 30% of global demand [172]. PET is also widely used for food packaging and bottles because of lightweight and low permeability of oxygen and carbon dioxide.

In fact, amorphous and unmodified PET is of little commercial interest due to its low tendency to crystallize, low glass transition temperature and poor mechanical properties [94]. However fortunately plenty of strategies have been developed to overcome the primary limitations of PET by using various additives and thus make PET an engineering-grade polyester with excellent physical and mechanical properties. For example, the rate of crystallization of PET can be increased using nucleating agents and plasticizers; glass fibres are usually used to increase the glass transition temperature and tensile strength of PET; the weatherability of PET can be greatly improved by anti-hydrolysis additives and UV stabilizers [100]. Today, the properties of PET have been enhanced to an extent that it can be used in almost every field such as construction, furniture, medical equipment, electrical and electronic devices and particularly important to this thesis, photovoltaic devices.

1.2 Photovoltaics

Photovoltaics (PV) is the technology that converts sunlight directly into electricity using semiconducting materials via the photovoltaic effect [169]. The first practical PV cell with 4% efficiency was born at Bell Labs in 1954 and after that the PV industry has been rapidly developing. Today, PV has been regarded as one of the most indispensable renewable energy sources along with wind power, hydropower and bio energy. According to a recent report from the International Energy Agency (IEA) [168], the PV market was still growing at a high rate as 50 GW of PV systems were installed in the year of 2015 globally. The evolution of PV installations since 2000 is shown in figure 1.5, rapid increase of total installed capacity can be found after 2006 and at the end of 2015 the global PV installations reached 227 GW, which is 1.3% of global electricity demand [168].

PV systems have some distinct advantages over other traditional electricity sources. First and most importantly, since the energy is directly supplied by the sun it is free and abundant. Secondly, it is one of the most reliable energy systems in terms of steady performance as PV panels usually have no moving parts, as a result the frequency of mechanical breakdown and maintenance will be minimum for PV systems. What's more, unlike some electricity sources that could produce greenhouse gases such as CO_2, PV is much more environmentally friendly.

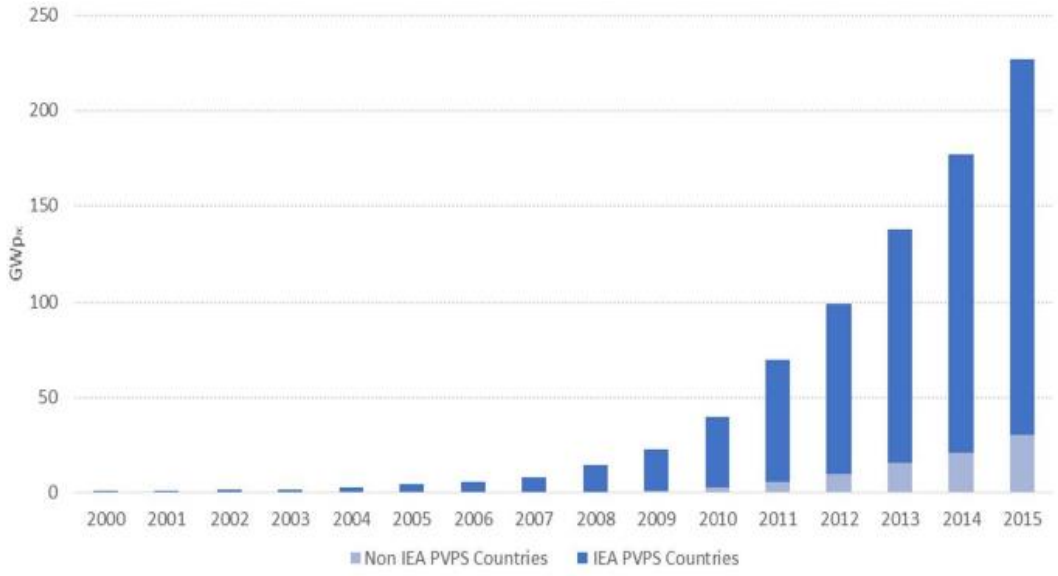

Figure 1.5 Evolution of PV installations since 2000 [168]

1.2.1 PV backsheet

The typical structure of a traditional crystalline silicon PV module is demonstrated in figure 1.6. PV cell, the most important component of the module where the photovoltaic effect takes place, is encapsulated by ethylene-vinyl acetate (EVA). On the front side, a glass layer is used to not only to protect the PV cell from external stresses but also allow the sunlight to pass through and reach the PV cell. On the back side, the PV backsheet – a laminate of different polymers, is used to the protect the module from UV rays, moisture, temperature and chemicals, most importantly the backsheet will provide the insulation property to the module to ensure safety of people who work with the module.

PV modules are designed to maintain at least 80% of their rated power output after 20 or 25 years. PV backsheet, as being the most important protecting component of the PV module, can directly influence the performance of the module. Backsheet made of inappropriate polymeric materials will degrade rapidly under harsh environments. Water ingress, yellowing and cracks formation will be initiated when the backsheet materials are excessively degraded which will significantly accelerate the power declining rate of the module.

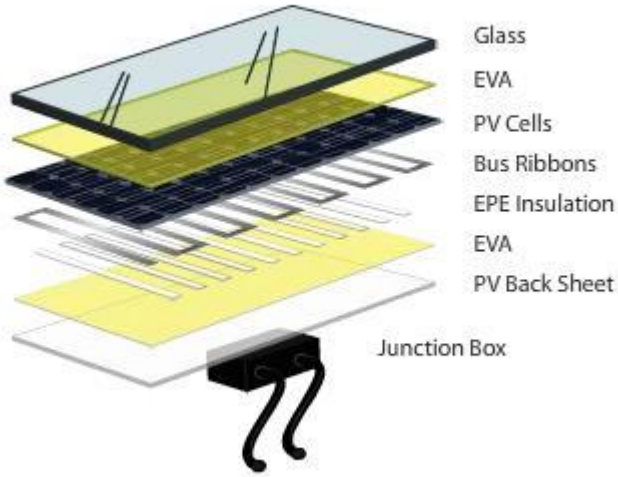

Figure 1.6 Anatomy of a traditional crystalline silicon PV module

The first generation of backsheet structure is known as TPT, where a poly(ethylene terephthalate) (PET) film is sandwiched between two polyvinyl fluoride (PVF) films, as shown in the left image of figure 1.7. The PVF film on the air side is very effective in resisting UV and hydrolytic degradation since the C-F bond in the PVF molecule is extremely strong. The PET film in the core layer insulates the module and provides mechanical stability due to its outstanding insulation and mechanical properties.

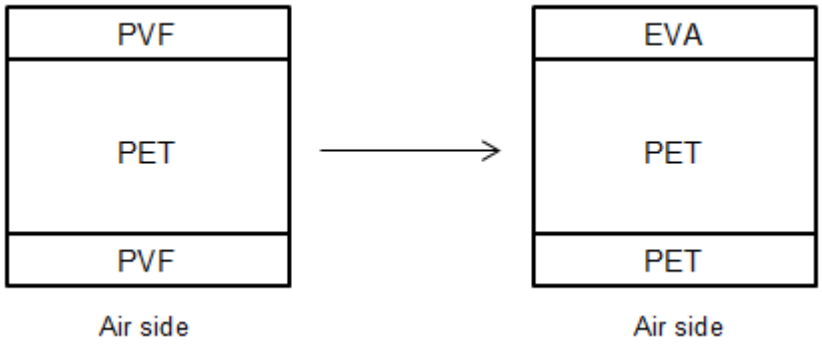

Figure 1.7 Development of PV backsheet structure

Although the TPT backsheet has over 25 years field-proven lifetime due to excellent weatherability of PVF, the global PV market has shown more interest in PET-based backsheet structure in recent years under the pressure of price competition between different backsheet manufacturers and limited supply of the PVF materials. In the PET-based structure (the right image of figure 1.7), the core layer of the backsheet remains a PET film and EVA is usually used on the cell side to provide better adhesion between the encapsulant and the backsheet. On the air side, the PVF film will be replaced by an engineering-graded PET film with good weatherability to protect the module from weathering. A recent study discovered that after 2000 hours of damp heat exposure, the PET-based module exhibited less power output degradation than the TPT one [170]. Therefore, it would be no exaggeration to expect that PET will become more vital in the PV industry in the future.

1.2.2 Laboratory tests for PV backsheet

In order to determine and predict the long-term durability of PV backsheets, there are a number of laboratory standard tests defined in IEC 61215, IEC 61646 and IEC 61730 which PV backsheets need to pass including climate tests (e.g. UV, damp heat and thermal cycling), fire tests (e.g. hot-spot test and bypass diode thermal test), mechanical tests (e.g. module breakage test and mechanical load test) and insulation tests (e.g. dielectric withstand test and partial discharge test) [174-176]. Among these tests, the partial discharge test is of great importance since it not only

determines the safe electrical operation during the expected lifetimes of PV modules, but also puts constraints on material selection particularly the sample thickness [16].

1.3 Partial discharge

Partial discharge (PD) is a localized dielectric breakdown phenomenon that can occur in solid or liquid insulation system under high non-uniform electric field, normally it will not cause an immediate breakdown to the insulation since electrical discharge only partially bridges the insulation between conductors [177]. PD usually occurs in defects such as gas voids and air gaps within insulations under high electrical stress, these gas filled voids will have a permittivity lower than that of the surrounding material therefore the electric field within the void will be intensified and local air breakdown can thus occur. It is well known that microvoids, which can be formed due to the decomposition and migration of impurities and additives during manufacturing process, are practically inevitable in polymeric materials. For example, an epoxy resin which is produced under extremely strict conditions may still have 10^{12}-10^{13} microvoids per cubic meter with diameters up to $5x10^{-7}$ m. Larger voids (~4 μm) can be found in the case of steam-cured polyethylene cables [99].

The equivalent circuit of partial discharge in polymeric materials can be illustrated in figure 1.8. The void, the insulation in series with the void and the remainder of the insulation can be represented as three capacitors, C_c, C_b and C_a, respectively with $C_b << C_c << C_a$ [99]. When a voltage V_a is applied to the insulation the voltage across the void will be:

$$V_v = V_a \frac{C_b}{C_c + C_b}$$

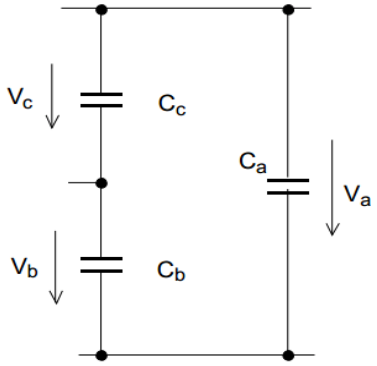

Figure 1.8 Equivalent circuit of partial discharge in polymers

The voltage waveform of the air void and the dielectric is shown in figure 1.9. The voltages across the whole dielectric and the void are represented by the solid sine wave V_a and the dashed sine wave V_v, respectively. $V_c(-V_c)$ denotes the breakdown voltage of the void which is determined by the void size and the gas pressure within the void, according to Paschen's Law. As can be seen in the figure, when the voltage across the void V_v reaches its breakdown threshold V_c, an electrical discharge appears in the void. Then because of the temporary short circuit by the discharge bridging the void, V_v will drop to 0 and the discharge extinguishes. Afterwards V_v will start to increase again according to the shape of the applied voltage V_a and another new discharge will appear within the void when V_v reaches the breakdown voltage V_c again. This phenomenon occurs regularly in each period of the sine wave. As a result of this, some recurrent discharges in the void could be found.

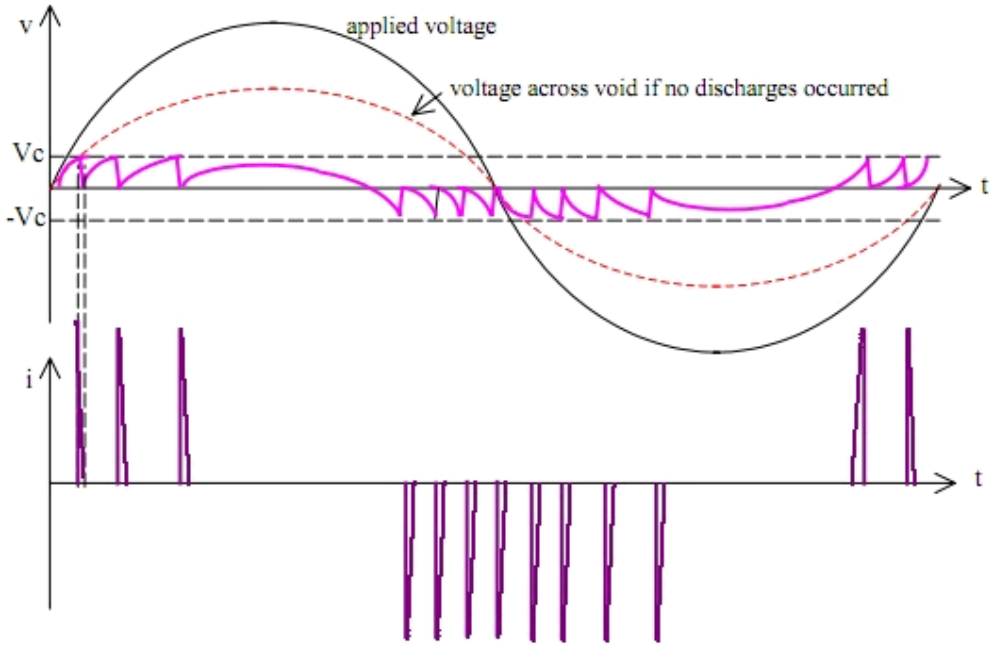

Figure 1.9 Voltage waveform of partial discharge

1.3.1 PD degradation on polymeric materials

When PD is present within polymers, it will deteriorate the material slowly and eventually leads to total dielectric breakdown if no remedial measures are taken. Some details of PD degradation on polymeric materials will be reviewed in this section.

There are four types of partial discharge in insulation systems, i.e. internal discharge, surface discharge, corona discharge and treeing [179]. Due to the fact that the polymer degradation mechanisms caused by these four types of PD are essentially the same, the condition of polymer degradation by surface discharge will be used as an example here. A typical, well established theory of PD-induced degradation and breakdown for polymers was demonstrated in figure 1.10 [178]. In the early stage, excited oxygen species such as ozone and O_2^- are produced due to the high energy of the electrical discharge and thus react with the polymer surface. The subsequent oxidation of the polymers will produce various by-products such as carbon monoxide/dioxide, nitrogen oxides, hydrogen and carboxylic acids, leading to the decline of the molecular weight and the increase of the surface conductivity for the polymers; high energy ions and electrons produced during the discharge

activities will impact the sample surface and break the chemical bonds of the sample, the surface roughness of the sample will be increased as well due to long-term ion bombardment; local melting and thermal decomposition of the material can occur due to local temperature rise which could increase up to several hundreds of kelvin [99]. As a result the sample surface will erode and decompose gradually under the combination effect of chemical attack, high energy ion bombardment and local melting. Long-term erosion by PD can lead to the formation of pits on the sample surface at which the electric field will be greatly enhanced and eventually initiate electrical trees. Once the electrical trees are present they will propagate within the dielectric and lead to total breakdown after the trees bridge the two conductors [99] [178].

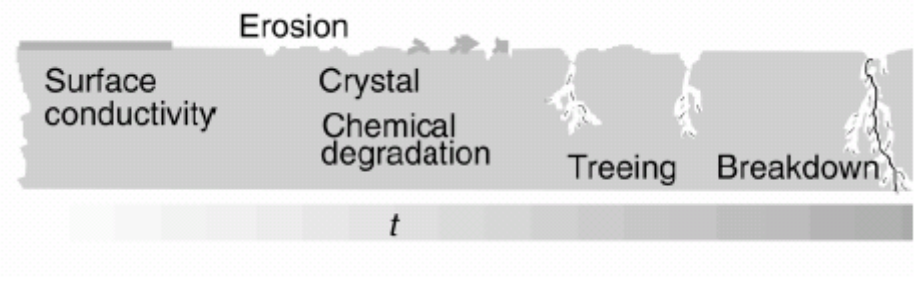

Figure 1.10 Development of PD-induced degradation for polymers [178]

1.3.2 Common experimental designs for PD degradation of polymers

Several common experimental designs for analysis of PD-induced degradation and breakdown of polymers will be briefly reviewed in this section.

1.3.2.1 IEC (b) electrode system

The IEC (b) electrode is one of the most common systems used to analyse polymer degradation and breakdown caused by surface discharge [1-3, 9, 16, 18, 19, 21, 24]. The system is made of a stainless-steel rod electrode (6 mm in diameter) with an end curvature of 1 mm radius and a larger plane electrode. The sample will be sandwiched between the two electrodes during PD tests, as shown in figure 1.11

[180]. Surface discharge is produced in the junction of the rod electrode and the sample when the applied voltage is sufficiently high. The system is usually embedded in a sealed PMMA container with silica gel inside to keep the relative humidity constant during the experiment [180].

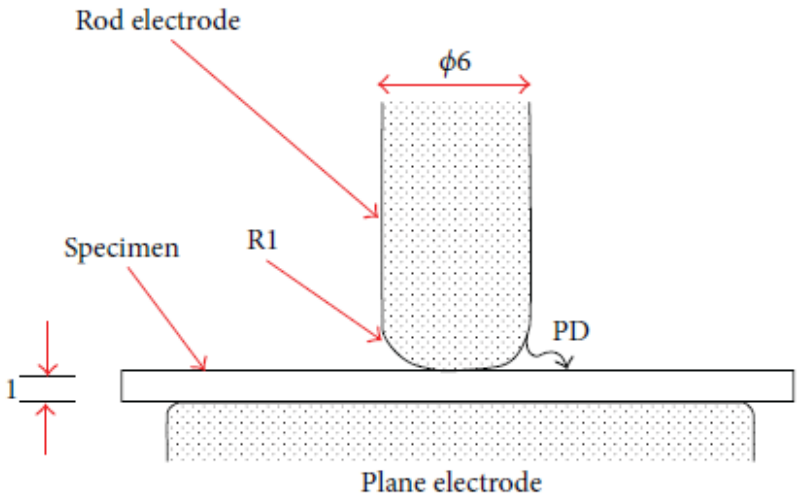

Figure 1.11 IEC (b) electrode system [180]

1.3.2.2 Rod-to-plane system

The rod-to-plane (also called sphere-plane) system is another very common electrode system that is similar to the IEC (b) one with the exception of an adjustable air gap between the upper electrode and the sample, as shown in figure 1.12 [5-6, 10, 11, 13, 180]. The bottom of the upper electrode is usually hemisphere-shaped. The thickness of the air gap can be finely controlled by a precision screw system [5].

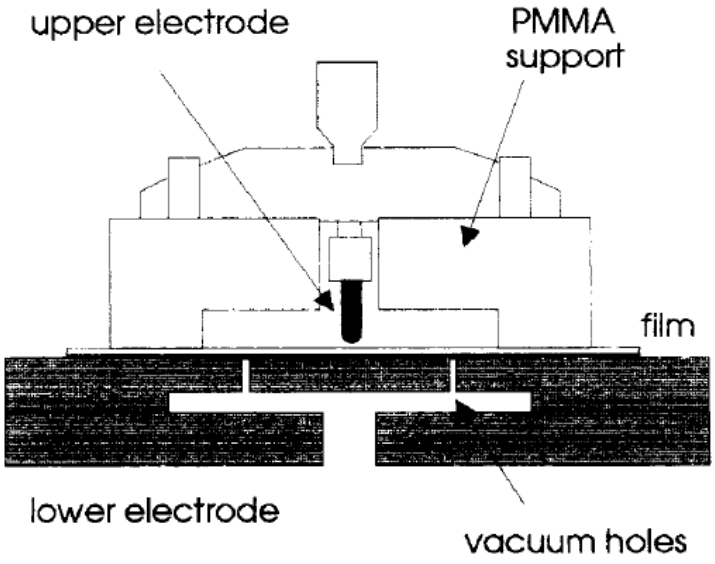

Figure 1.12 Rod-to-plane system [5]

1.3.2.3 CIGRE Method Ⅱ system

This electrode system is not frequently used compared to the previous two. In this configuration a sphere upper electrode is embedded in epoxy resin to ensure no PD will be produced between the upper electrode and the sample. A cylindrical, flat cavity is formed by placing a spacer between the sample and the ground electrode where the PD is supposed to occur during the test. The schematic of the system is shown in figure 1.13 [23].

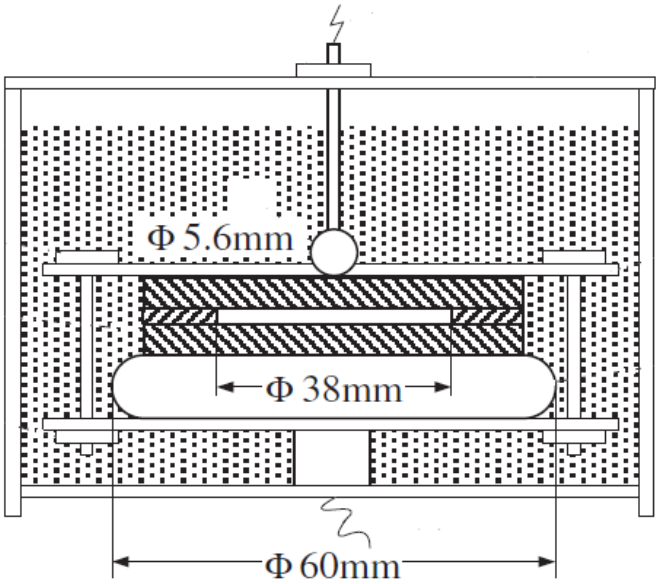

Figure 1.13 CIGRE Method Ⅱ system [23]

1.3.2.4 Plane-to-plane systems

Internal PD within polymers is often investigated by using plane-to-plane electrode systems [4] [21]. More commonly, the system whose schematic diagram is shown in figure 1.14 [21], is used. Several sample sheets are placed between two plane electrodes with an artificial cavity made by removing a circular section from the centre layer. The plane electrodes are either embedded in epoxy resin or immersed in insulating oil to ensure no PD would be produced except from the artificial cavity.

The configuration in figure 1.15 is the standard electrode system for the dielectric strength test of insulation materials with the whole system immersed in insulating oil. The dielectric is placed between the two plane electrodes and voltage is increased at a constant rate until the sample breakdown. However, this electrode system can be also used to detect and investigate the PD within the intrinsic microvoids of polymers [4].

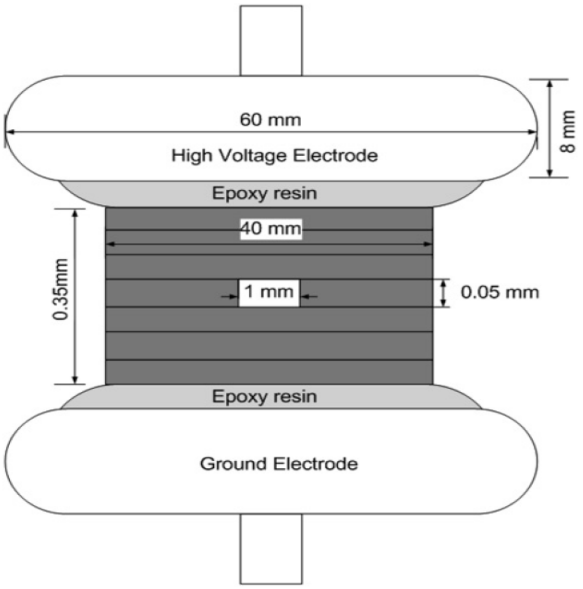

Figure 1.14 Plane-to-plane system with artificial void within the polymer [21]

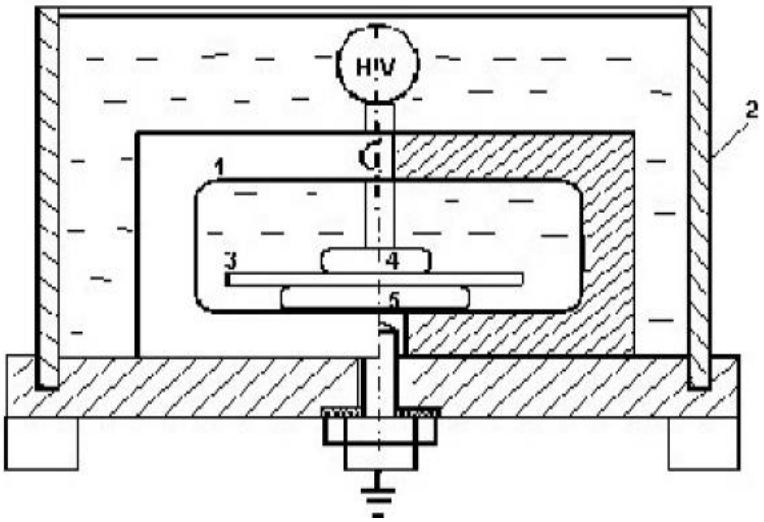

Figure 1.15 Plane-to-plane system immersed in oil without artificial void (1) Inner test cell (2) Oil can (3) Specimen (4) HV electrode (5) Ground electrode [4]

1.4 Motivation of the project

The traditional PD test for PV backsheets in industry is a qualification test carried out in air with the backsheet sandwiched between two conducting electrodes. The PD extinction voltage of the backsheet, which significantly depends on the

backsheet thickness, is measured and then compared to the maximum system voltage (usually 1000 V for Europe) to determine the insulation property of the backsheet. Therefore the test will place a strict criterion on the minimum thickness of the backsheet. As a result, the backsheet has to be much thicker than would be required to pass any other test defined in those IEC standards [173]. N. H. Phillips and B. Givot [181] have shown that experimental comparators such as the number of sampler layers, morphology and molecular weight of the sample, presence of artificial void etc. have very little effect on the traditional PD results and highly similar results can only be obtained when the sample thickness is constant.

During their service lives, PV backsheets are subjected to various environmental stresses such as UV radiation, temperature cycling and moisture etc. In rainy and heavily polluted districts, some parts of the backsheet surface may be covered by thin water film and dirt, leading to the formation of a potential difference across the backsheet and thus the PD, as demonstrated in figure 1.16 [16]. What's more, trends are moving to thinner and lighter PV modules including the backsheet today, which will be particularly challenging for the safe electrical operation of the module since the backsheet will be subjected to a higher electric field under the wet condition hence the possibility of PD occurrence within the backsheet is increased. As a result, the backsheet materials are potentially subjected to long-term PD-induced degradation and even dielectric breakdown since PV modules are expected to perform at least 25 years.

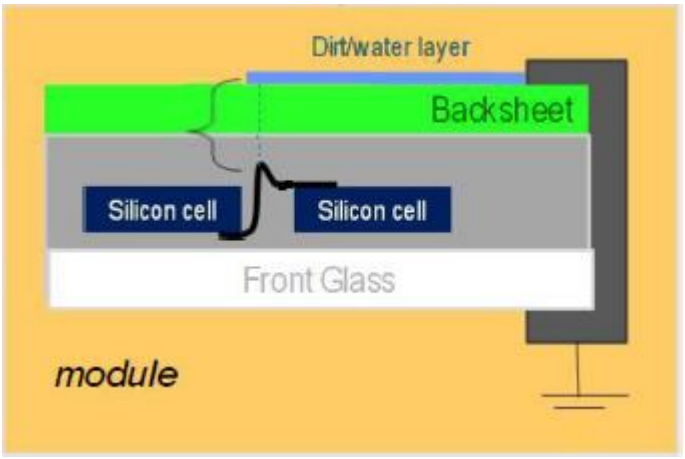

Figure 1.16 Potential PV backsheet degradation caused by PD [16]

Due to the fact that the insulation properties of the PV backsheet are primarily determined by its core layer of PET film plus PET is becoming more and more popular in the PV industry, a comprehensive understanding of PD-induced degradation and dielectric breakdown of PET films will be vital. How physical and chemical properties of PET (thickness, performance additive, morphology and chemical composition etc.) in addition to weathering treatments (mainly UV and hydrolysis) influence the degradation and breakdown caused by PD is of great interest. Quantifying this would enable a bench mark to be established and provides a basis for future work to improve materials for PV backsheets.

1.5 Brief overviews of the thesis

In this chapter, background information of the study is reviewed and a brief summary of the rest of the thesis content is as follows.

In chapter 2, materials and sample preparation methods used in the project were firstly introduced. Then the experimental designs of dielectric (partial discharge and breakdown) and weathering (UV and hydrolysis) tests were described. Thirdly, analytical methods for characterization of the degraded samples were introduced. For each type of method, the principle of the instrument was firstly reviewed, experimental procedures and data processing of the method were then described.

In chapter 3, PD treated samples were analysed by using surface characterization techniques such as ATR-FTIR, XPS, SEM and profilometers to investigate the mechanism of PD degradation on PET films chemically and physically. Morphology effect on PD degradation rate of PET films was explored using same type of samples with different morphology due to various draw ratios in manufacturing process. Lastly, thickness effect on PD-induced dielectric breakdown of PET was discussed.

In chapter 4, performance additive effect on PD degradation of PET was discussed. PET with various additives such as $BaSO_4$, TiO_2, UV stabilizer and phosphorus-based flame retardant were subjected to identical electrical stresses to

quantify the degradation rates of the samples. Relationships between the PD resistances and PD lifetimes of the samples were also discussed in this chapter.

In chapter 5, a straightforward technique was applied to improve the PD resistance and PD lifetime of PET by isothermally crystallizing the samples. Crystalline morphology changes of the samples were observed via DSC and FTIR. The effectiveness of the annealing treatment on PD erosion and breakdown was confirmed by using samples with different additives. The effect of the annealing temperature was also discussed.

In chapter 6, the PET samples were divided into two sets and then subjected to photodegradation and hydrolysis, respectively, prior to dielectric tests to investigate the weathering effect on PD-induced breakdown behaviour of PET films. The degradation extents of the samples due to weathering were analysed by FTIR, DSC and SEM. Very different results of PD lifetimes were observed for the two sets of samples. Mechanism for each case was discussed and the relationship between the crystal structure and PD lifetime of PET was further explored.

In chapter 7, PD degradation and breakdown behaviours of two polyester films i.e. PET and PEN were investigated and compared by applying identical electrical stresses to the both sample. Effects of chemical composition and mechanical properties on PD-induced erosion and breakdown of polyester films were discussed.

Chapter 8 summarizes the main contributions of this project and possible future work is given.

Chapter Two

2.Materials, experimental techniques and procedures

2.1 Materials

2.1.1 Poly(ethylene terephthalate) (PET)

Biaxially oriented, semicrystalline poly(ethylene terephthalate) (PET) films with a thickness range from 36µm to 480µm used in this project were supplied by Dupont Teijin Films and Mitsubishi Polyester Film GmbH.

2.1.2 Poly(ethylene naphthalate) (PEN)

Biaxially oriented, semicrystalline poly(ethylene naphthalate) (PEN) films, thickness 125µm, from Dupont Teijin Films were used to compare the partial discharge behaviours with the PET films.

2.1.3 Sample preparations

All samples were cut into a square-shape with dimensions of 40 mm x 40 mm. Samples were stored in a desiccator with silica gel inside at least for a week before any partial discharge or dielectric breakdown tests.

2.2 Experimental techniques and procedures

2.2.1 Partial discharge experimental set-up

2.2.1.1 Electrode systems for partial discharge degradation and breakdown

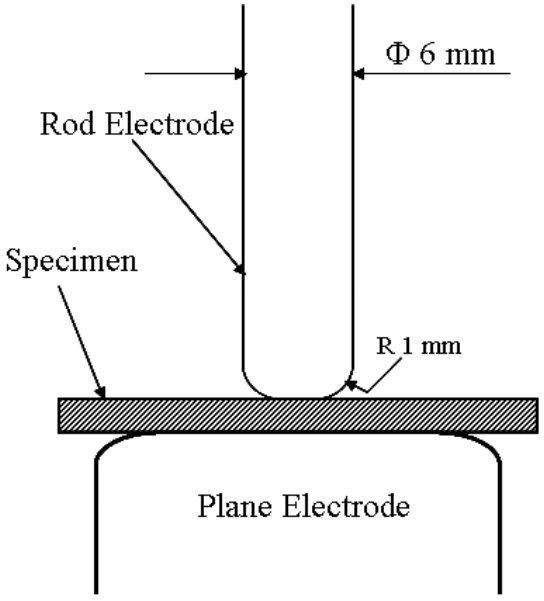

Figure 2.1 Schematic diagram of IEC (b) electrode system

Partial discharge degradation and breakdown experiments in this project were conducted using the IEC (b) electrode system according to IEC 60343. As the schematic diagram shown above, the electrode system consists of a rod and a plane stainless-steel electrodes where the rod electrode has an end curvature of 1mm radius.

The whole system was enclosed in a PMMA tube in which silica gel was used to keep the relative humidity as low as possible. Temperature, 20±2°C, was not specifically controlled during experiments. The voltage frequency is 50 Hz for all tests.

For multiple-samples PD test, a set of high voltage rod electrodes (as many as seven) were used, to enable PD experiments to be run with up to seven samples in parallel. The picture of the sample holder is shown in figure 2.2.

Figure 2.2 Sample holder for multiple-samples PD test

For PD-caused dielectric breakdown test, single high-voltage rod electrode was used. The picture of the set-up is shown in figure 2.3.

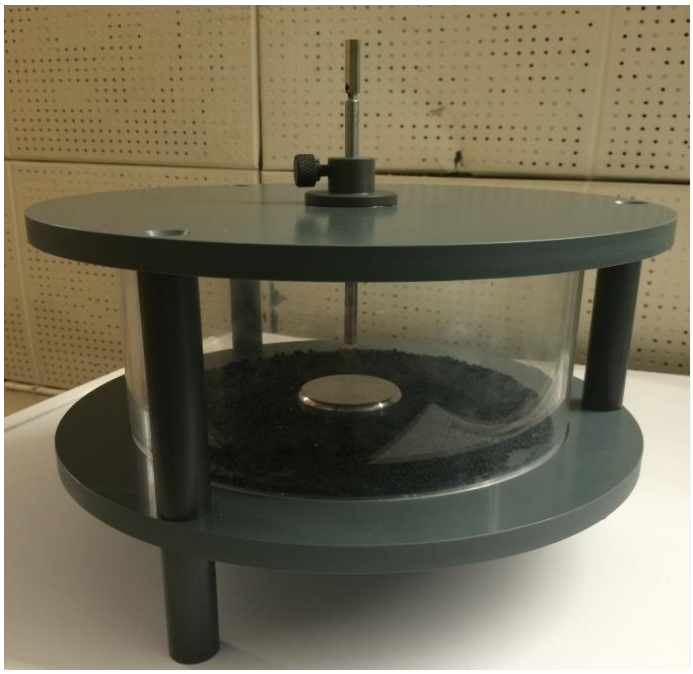

Figure 2.3 Sample holder for PD-caused breakdown test

2.2.1.2 High voltage circuit and equipments

The schematic diagram of high voltage circuit for PD and breakdown test is shown in figure 2.4. A KV30-40 mk2 series instrument is used as a high voltage power generator. The instrument will trip for overload protection when a large current due to sample breakdown is detected.

During an experiment, a DMS portable UHF monitor is used to keep recording PD signals generated by partial discharges. When a breakdown occurs, the tripping of the power generator will break the circuit and subsequently the data recording will

be stopped, hence by checking the starting and ending time of data, the lifetime of a sample under partial discharge can be known.

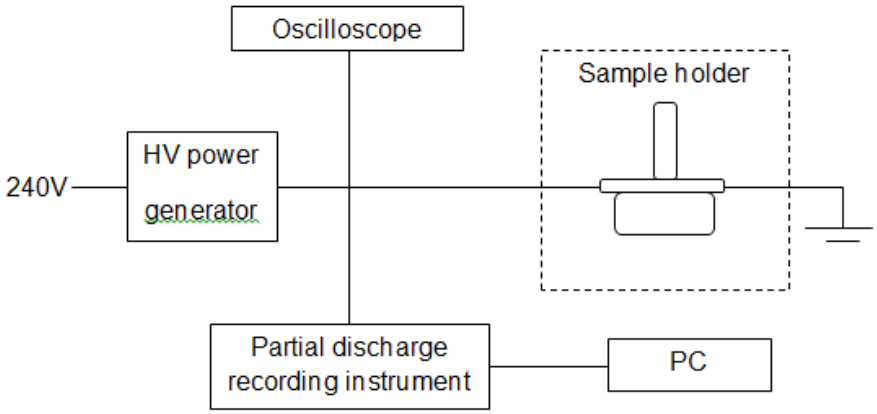

Figure 2.4 Schematic diagram of high voltage circuit

2.2.2 Weathering and hydrolysis experimental

2.2.2.1 Weathering experimental

Weathering experiments were carried out using an Atlas Suntest XLS+ weatherometer (figure 2.5). The instrument is equipped with a xenon arc lamp. The combination of filters was appropriately selected (filter A of the weatherometer) so that the xenon lamp can simulate the spectral distribution of outdoor sunlight. Irradiance E, in the wavelength range of 300 – 800 nm and the black standard temperature (BST) can be measured and controlled between 250 – 765 W/m^2 and 45 – 100°C, respectively. The calibration of the weatherometer was carried out at a condition of E = 700 W/m^2 and BST = 50°C before and after each experiment.

For weathering experiments, the irradiance intensity and black standard temperature were set as E = 700 W/m^2 and BST = 65°C, respectively. There was no light/dark weathering cycle in the running programme, therefore, the xenon lamp was set to constantly irradiate during the whole experiment.

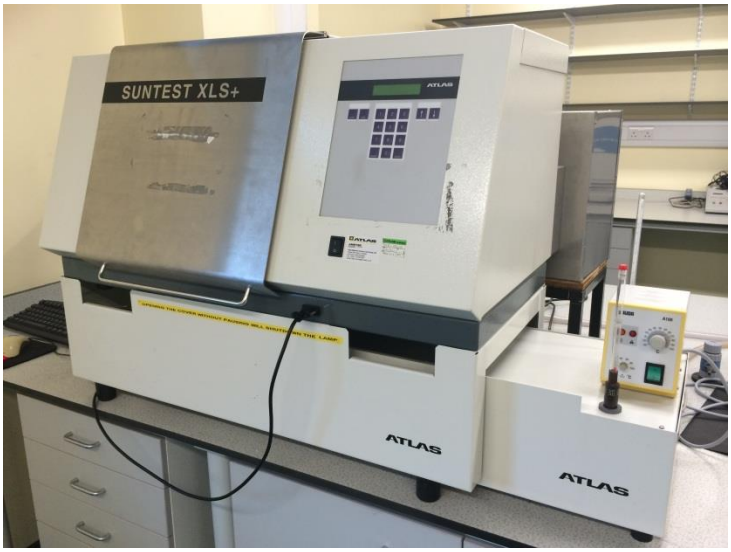

Figure 2.5 Suntest XLS+ weatherometer

2.2.2.2 Hydrolysis experimental

Samples were treated in deionised water up to 50 days (1200 hours). The temperature of the water was set to 90°C, which is well above the glass transition temperatures of the samples (about 80°C). The samples were completely immersed in the hot water and 5 sheets for each kind of samples were taken out every week for further tests. The deionised water in sample containers was refreshed every week as well to avoid autocatalysis by soluble degradation products.

2.2.3 Fourier-transform infrared spectroscopy

2.2.3.1 Introduction of FTIR

Infrared spectroscopy, a material analytical technique that has been used over seventy years, is still one of the most important techniques in today's polymer science. The technique is based on the vibrations of molecules in polymers. When infrared radiation passes through a sample, some of the infrared radiation will be absorbed by the sample while the other radiation will penetrate the sample. Therefore, the infrared spectrum of a sample can be obtained by looking at the infrared radiation absorption or transmittance against the frequencies of infrared photons.

In 1940s, the original infrared instruments used prisms for dispersive methods. After that, thanks to the introduction of Fourier-transform infrared spectrometers, the infrared measurements became more precise, moreover, both the speed and the sensitivity of measurements have been greatly improved.

The components of the most common interferometer, namely Michelson interferometer used in FTIR spectrometry is shown in figure 2.6. If an IR beam strikes to a beam splitter, ideally, 50% of the IR beam will be reflected to the stationary mirror and the other 50% of the beam will pass through the beam splitter to reach the moving mirror. Both beams will be reflected back from the two mirrors to the beam splitter where 50% of the two beams will interfere and pass to the sample compartment and 50% of the two beams will pass through the beam splitter and back to direction of the IR beam source. The interfered IR beam will be absorbed selectively by the sample and refocus on the detector. The FTIR spectrum

of the sample will be obtained by converting the interferograms with and without the sample to a spectrum by Fourier transformation.

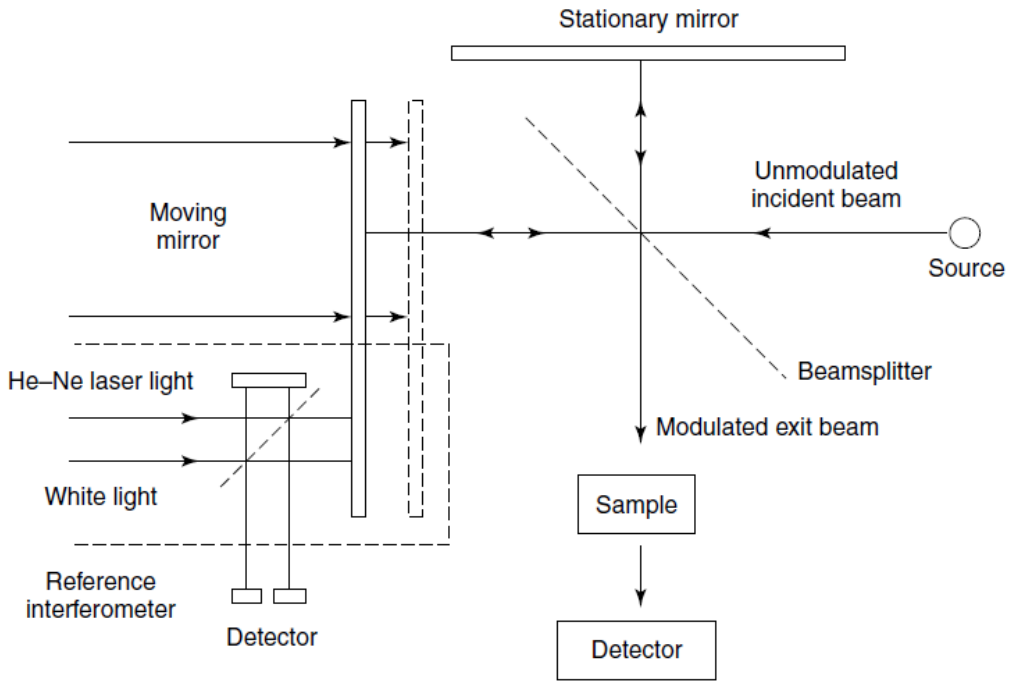

Figure 2.6 Schematic diagram of the Michelson interferometer

2.2.3.2 Attenuated total reflectance (ATR)

For traditional transmission IR spectroscopy, the intensity of a sample spectrum greatly depends on the sample thickness which normally will be required to be no more than a few tens of micrometres. Hence it can be problematic when the transmission method is applied to test some thick samples (thickness>100 μm) as some of the IR bands are totally absorbed, making the IR spectrum saturated.

To overcome this limitation, attenuated total reflectance (ATR) spectroscopy has been introduced and become the most popular sampling technique in FTIR. Figure 2.7 represents a typical schematic diagram of a single reflection ATR. An IR beam

enters an ATR crystal with a high refractive index. A total internal reflectance will occur if the incident angle θ is greater than the critical angle θ_c, which is defined as:

$$\theta_c = \sin^{-1}\frac{n_2}{n_1}$$

where n_1 and n_2 are the refractive index of the crystal and the sample, respectively. This internal reflection generates a evanescent wave which will go across the ATR crystal surface and extend into the sample. Some of the radiation of the evanescent wave will be absorbed by the sample and the attenuated IR beam will return to the detector. The penetration depth of the evanescent wave, which is normally less than 5 μm, can be defined as:

$$d_p = \frac{\lambda}{2\pi\left(n_1^2 \sin^2\theta - n_2^2\right)^{1/2}}$$

where λ is the wavelength of the IR radiation, θ is the incident angle of the IR beam, n_1 and n_2 are the refractive index of the crystal and the sample, respectively.

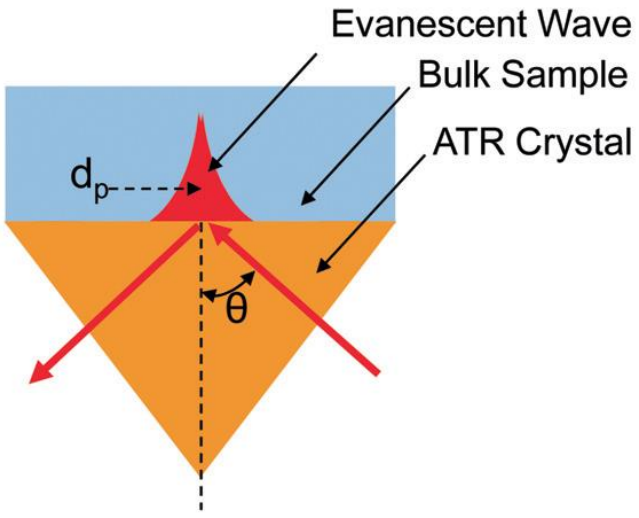

Figure 2.7 A single reflection ATR

One the main advantages of ATR is that little or no sample preparation is usually required for sampling, hence almost any forms of liquids or solids can be easily analysed. Because of the limited penetration depth of the evanescent wave (usually less than 5 microns), another important feature of ATR is it only detects the surface properties of a sample. Therefore, ATR will be a perfect sampling tool for this project since all the degradation areas of PD-treated samples using the IEC (b) electrode as well as weathering-treated samples were on the sample surfaces.

2.2.3.3 Experimental procedures and data processing

2.2.3.3.1 Experimental procedures

FTIR spectra of samples in this project were collected using a Agilent 5500 Series FTIR instrument equipped with a single reflection diamond ATR (Figure 2.8). The spectral range of the instrument is 650-4700 cm^{-1}, with a resolution of 8 cm^{-1}. 128 sample and background scans were accumulated for each spectrum. For each sample, five spectra were collected and then averaged using Panorama from LabCognition.

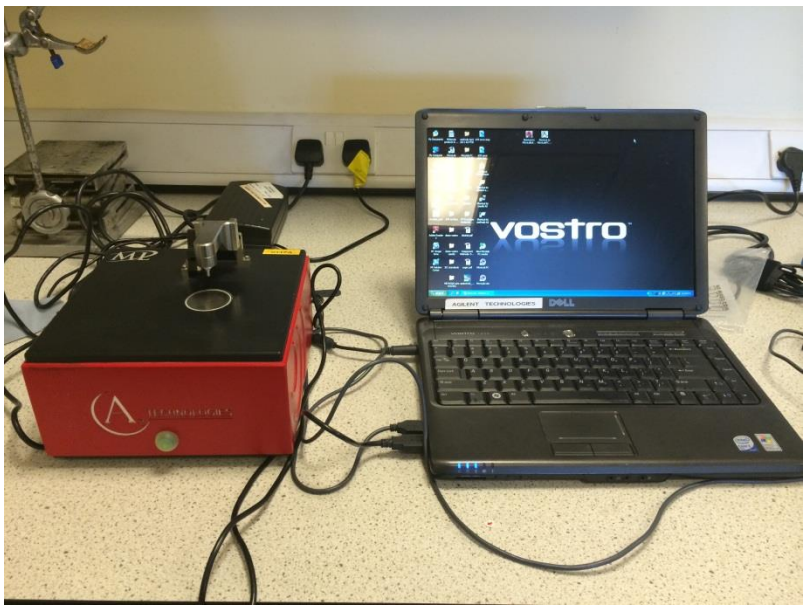

Figure 2.8 Agilent 5500 Series FTIR instrument with a single reflection diamond ATR

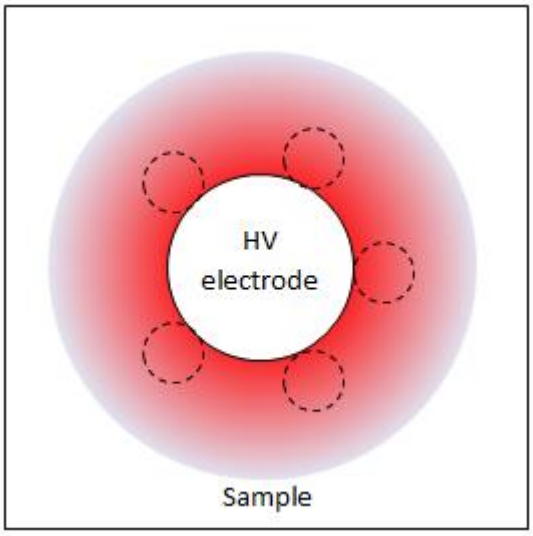

Figure 2.9 ATR-FTIR collecting points on PD-treated samples

For PD-treated samples, ATR-FTIR collecting points are demonstrated in figure 2.9. The part in red represents the PD-degraded area of the sample induced by the IEC (b) electrode system while in the centre of the figure is the location of the high-

voltage rod electrode, where the sample is undamaged since PD would not be present in this area due to lack of air. Five data collecting points (small dash line circles) were chosen to be adjacent to the big white circle as shown in figure 2.9.

For the weathering, hydrolysis degraded samples as well as the pre-treated samples, five random data collecting points were chosen on the sample surfaces as the surface conditions were consistent.

2.2.3.3.2 Data processing

In order to analyse the FTIR data quantitatively such as calculate the carbonyl and carboxyl index, crystallinity degrees etc., separations of overlapping peaks in the raw FTIR data are usually required. OriginPro 8.6 software was utilised in this project for deconvolution of the raw FTIR data. For example, select the two main bands at 1471 cm^{-1} and 1456 cm^{-1} in FTIR spectra of PET, which are attributed to the bending of the glycol CH_2 in amorphous and crystalline phases, respectively. It is essential to calculate the ratio of the intensities of these two bands if one needs to calculate the crystallinity of the sample. To achieve this, use the function of 'Find peaks' to find out the two peaks as shown in figure 2.10. The peak type was then selected as 'Gaussian' and the result of the deconvolution could be obtained when the function of 'Fit' was clicked, as shown in figure 2.11.

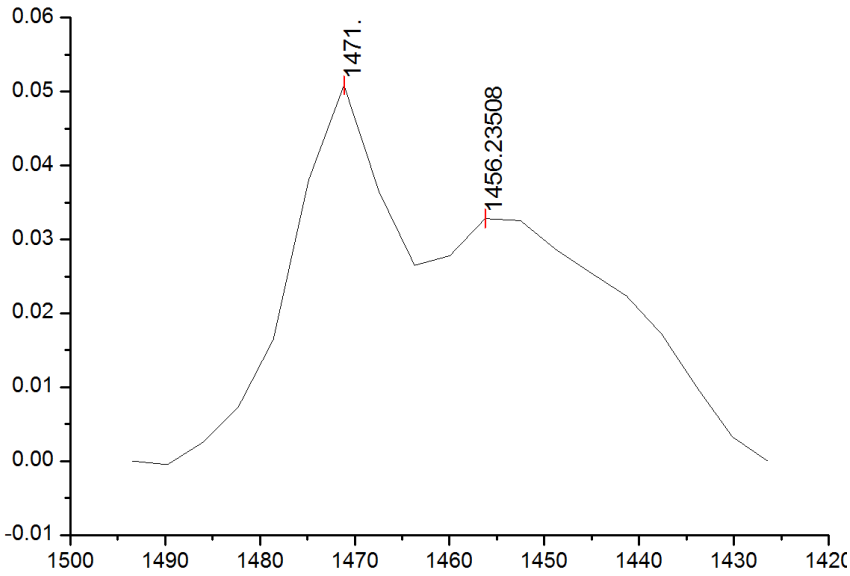

Figure 2.10 ‘Find peaks’ function in OriginPro 8.6

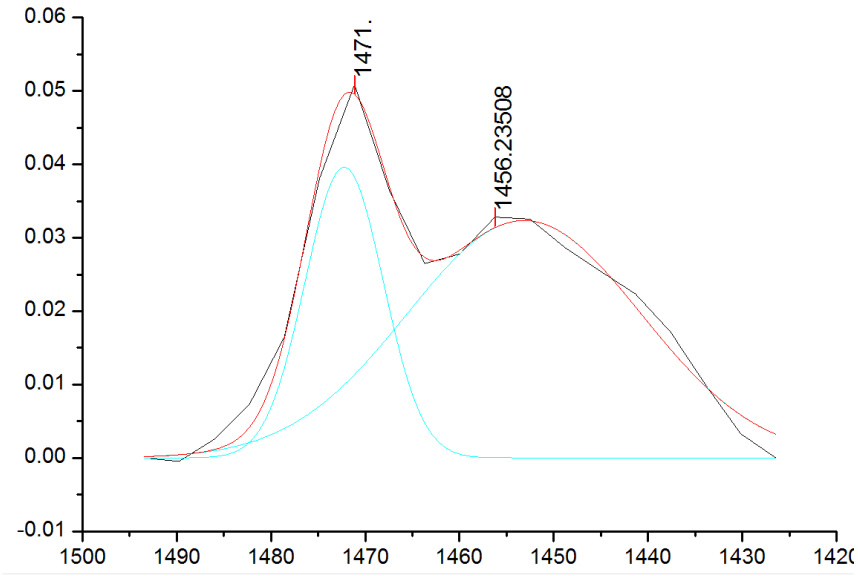

Figure 2.11 ‘Peak fit’ in OriginPro 8.6

2.2.4 X-ray photoelectron spectroscopy

2.2.4.1 Introduction

X-ray Photoelectron Spectroscopy (XPS), also known as Electron Spectroscopy for Chemical Analysis (ESCA), was developed in 1960s by Kai Siegbahn and his research group. XPS is a powerful technique for surface chemistry analysis such as identification and quantification of elements on the sample surface, identification of empirical formula of materials and measurement of chemical or electronic state of each element on the surface. The technique is based on the photoelectric effect discovered by Einstein in 1905.

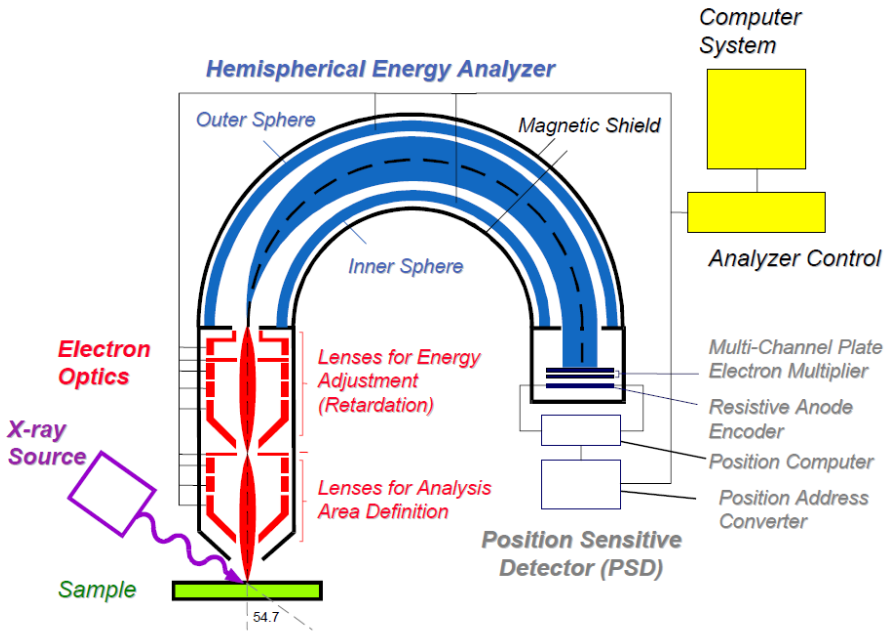

Figure 2.12 Schematic diagram of an X-ray photoelectron spectrometer

The schematic of an X-ray photoelectron spectrometer is illustrated in figure 2.12. A beam of X-rays is applied to irradiate a sample to emit the electrons from the surface of the sample (normally analysing depth<10 nm). Emitted electrons will be energy filtered by a hemispherical energy analyser and the kinetic energy and amount of electrons are measured by the detector. The electron binding energy can be obtained as the following equation:

$$BE = hv - KE - \Phi$$

where hv is the energy of the X-ray beam, KE is the electron kinetic energy and Φ is the spectrometer work function. An XPS spectrum can be obtained by plotting the electrons intensity (usually the amount of electrons per second) versus the electron binding energy. A typical XPS survey spectrum of PET is illustrated in figure 2.13. Since hydrogen cannot be detected in XPS, only carbon and oxygen are present for PET.

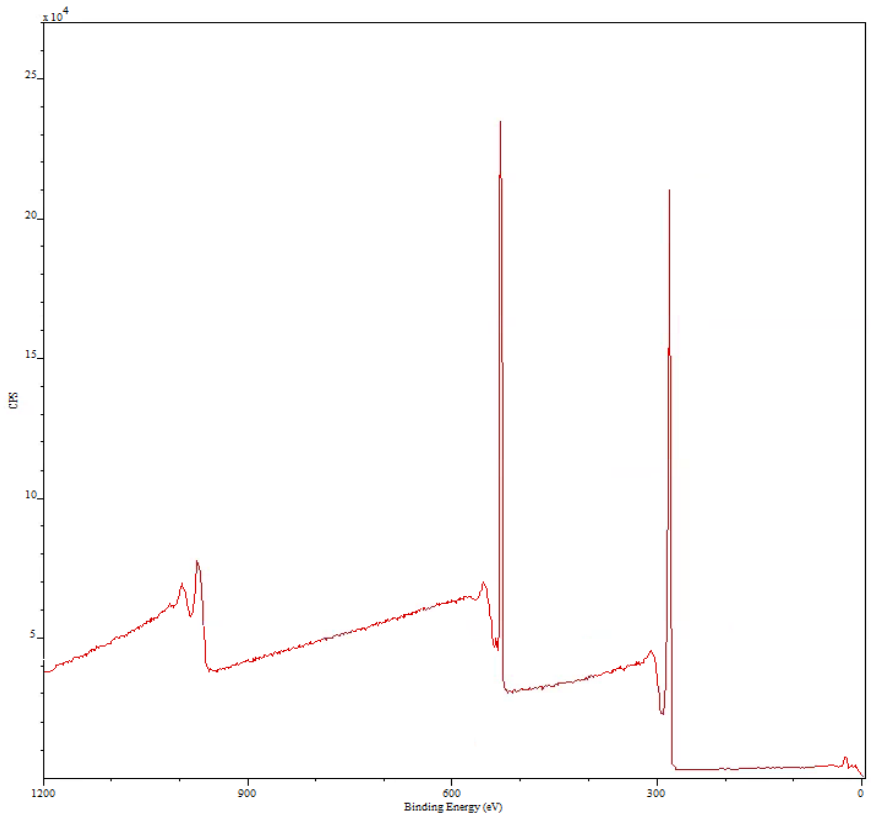

Figure 2.13 A typical XPS survey of PET

2.2.4.2 Experimental procedures and data processing

2.2.4.2.1 Experimental procedures

XPS measurements were carried out at the National EPSRC XPS Users' Service (NEXUS) in Newcastle University using a Kratos Analytical AXIS Nova x-ray photoelectron spectrometer. A monochromatic Al Kα x-ray with energy of 1486.6eV was applied to irradiate samples. The power of the x-ray gun is 225W. Pass energy for XPS survey and higher resolution scan were 160eV and 20eV, respectively.

Three different positions were selected on each sample with large analysis areas (a rectangle of 300μm x 700μm). For the PD-treated samples, analysis positions

were taken in the PD-degraded areas (the red area in figure 2.9) and always kept at the same distance from the edge of the electrode mark. While for the untreated samples, three random positions were taken on the sample surface. On each position a survey scan was acquired followed by higher resolution scans of C1s and O1s. The XPS survey scan of PET has been shown in figure 2.13, the higher resolution scans of C1s and O1s of PET are shown as below.

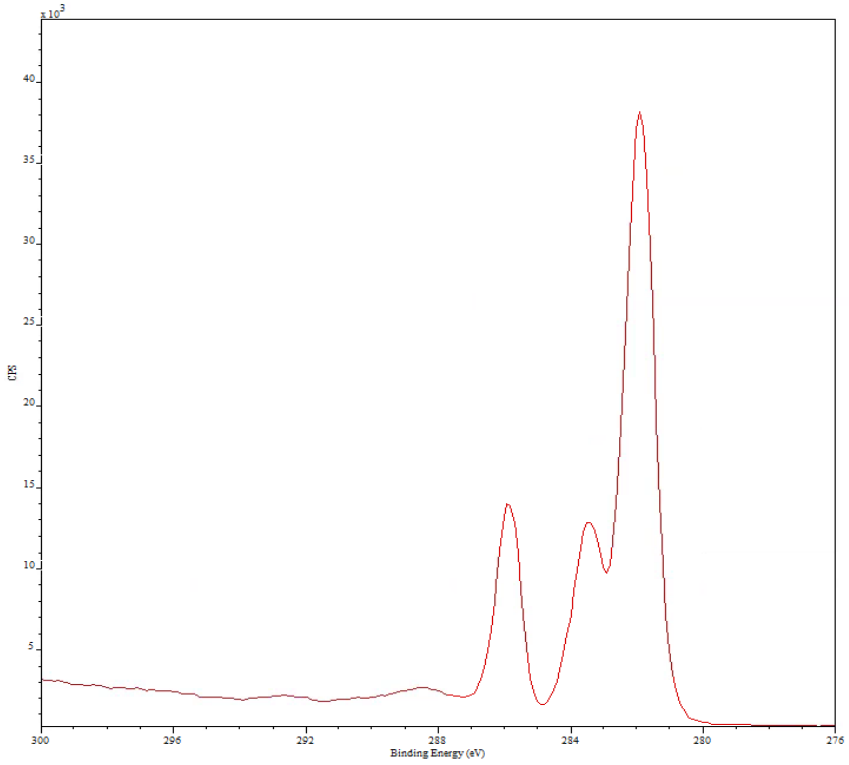

Figure 2.14 C1s scan of PET

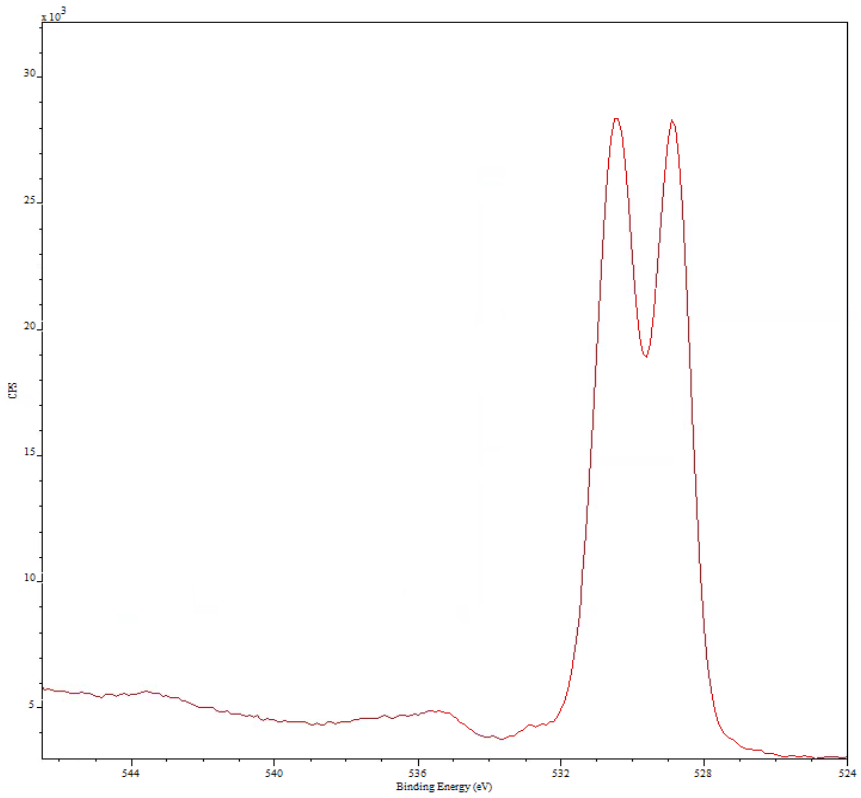

Figure 2.15 O1s scan of PET

According to the literature, the three peaks in the C1s scan of PET, which are at 284.80 eV, 286.41 eV and 288.78 eV are attributed to the carbon atom (underlined) in C-(C,H), C-O and O=C-O in PET, respectively. While the two peaks in the O1s scan, which are at 531.65 eV and 533.26 eV are attributed to the oxygen atom (underlined) in O-C=O and O-C=O in PET, respectively.

2.2.4.2.2 Data processing

CasaXPS software was utilised for data analysis and quantification. Element identification and percentages of samples can be obtained from the survey scans. For the higher resolution scans, peak fittings were carried out using a Gaussian-

Lorentzian line shape in order to investigate the PET surface chemistry changes due to PD in more detail. The peak-fitted C1s and O1s spectra of untreated PET are illustrated as below.

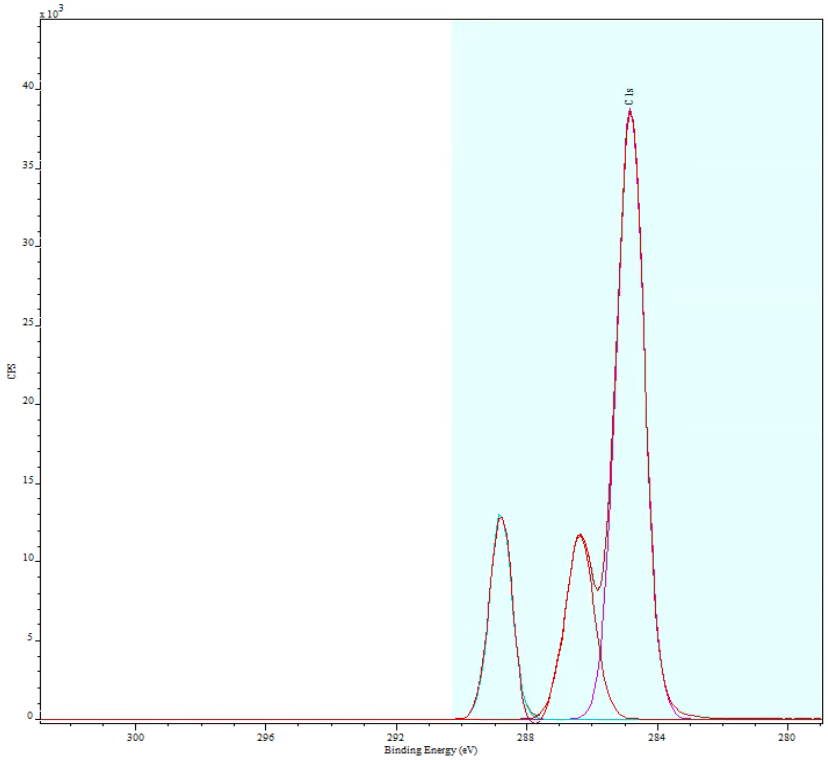

Figure 2.16 peak-fitted C1s spectrum of PET

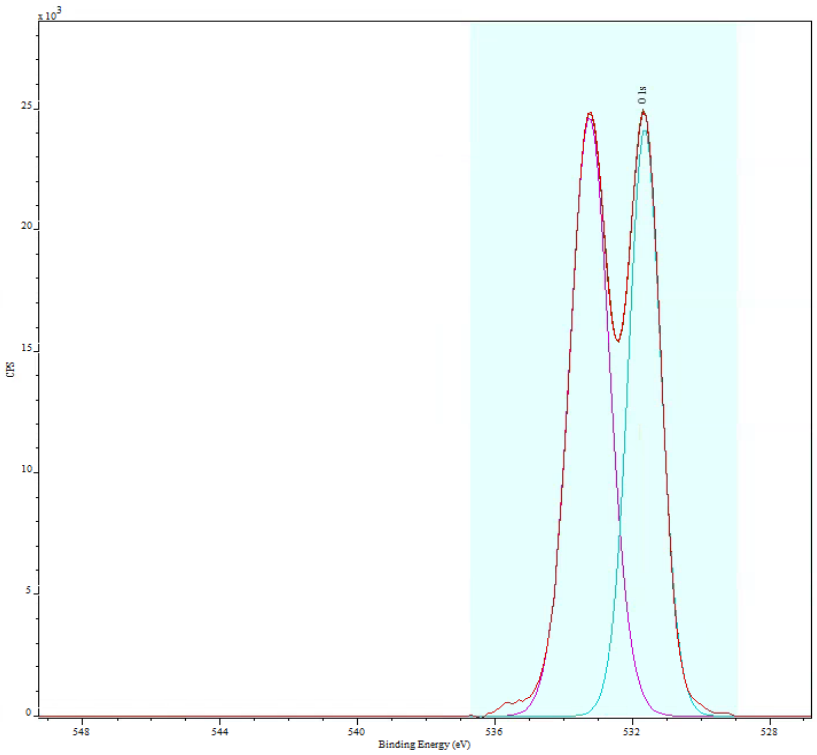

Figure 2.17 peak fitted O1s spectrum of PET

2.2.5 Differential scanning calorimetry

2.2.5.1 Introduction

Differential scanning calorimetry (DSC), which monitors the energy absorbed or released by a material as a function of temperature, is one of the most important thermal analytical tools. It has been widely used in industries such as polymers, food, manufacturing and pharmaceuticals. For polymers, DSC is used for example, to characterise glass transition (T_g), crystallization temperature (T_c), melting points (T_m), degree of crystallinity and oxidative stability.

There are two types of DSC systems, power compensation DSC and heat flux DSC. In power compensation DSC, the sample and reference are placed in two

identical furnaces separately. The temperatures of the sample and reference are kept exactly the same, hence the energy required to do this for the sample relative to the reference can be quantified. In heat flux DSC, the sample and reference are placed in the same furnace. For this type of DSC, the temperature difference between the sample and reference is recorded and the energy change in the sample can be obtained.

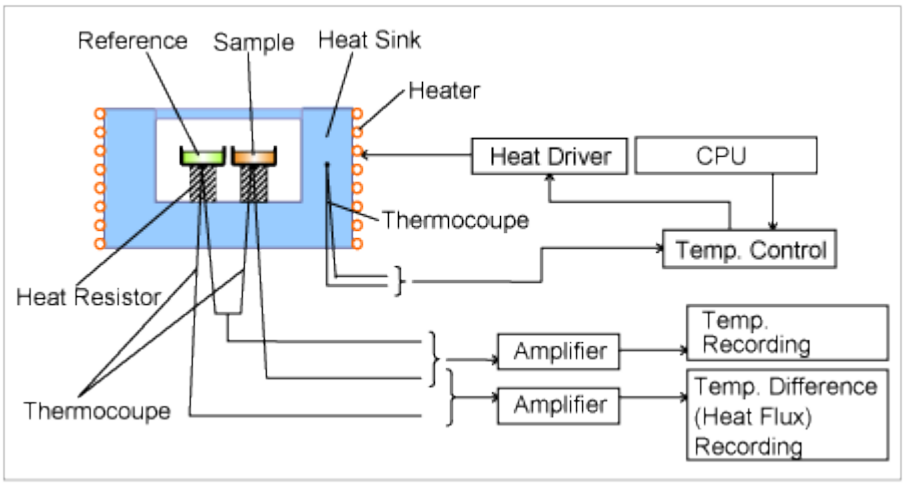

Figure 2.18 Schematic diagram of a heat flux DSC

2.2.5.2 Experimental procedures

DSC analyses were carried out using a TA instruments Q1000 DSC (figure 2.19). Samples were weighed by using a Mettler Toledo XS105 balance with a readability level of 0.01 mg. Samples between 1 to 15 mg, depending on the sample thickness, were encapsulated in PerkinElmer aluminium pans and an empty pan was selected as a reference. N_2 was used as purge gas with a flow rate of 40 mL min^{-1}.

DSC data were interpreted using the TA universal analysis software. Since all investigated polyester films in this project were biaxially-oriented, they are all in semicrystalline structures. A typical DSC curve of a PET sample of the project is shown in figure 2.20. As can be seen, a ‘cold-crystallization’ peak that usually occurs in the temperature range of 130°C - 150°C in amorphous PET is not present at all due to the semicrystalline structures of the samples.

Figure 2.19 TA instruments Q1000 DSC

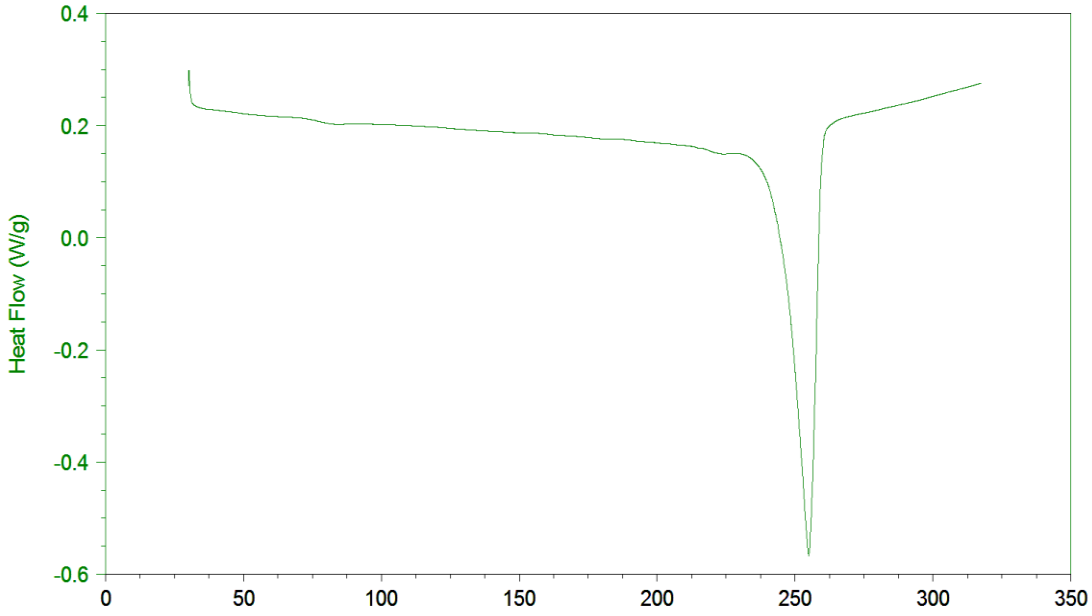

Figure 2.20 A typical DSC curve of a PET sample of the project

2.2.6 Optical and mechanical profilometers

As the extents of PD degradation of treated samples can be directly reflected by the PD erosion depths, this parameter is useful and straightforward tool to characterize the PD degradation effect. In this project, both optical and mechanical profilometers were used to quantify the erosion depths of the PD-treated samples.

2.2.6.1 Optical profilometer

A Veeco NT1100 optical profilometer (figure 2.21) was utilized to provide 3D surface profile measurements of samples without any contact. The instrument based on the technology of white light interferometry. The objective lens and field-of-view lens were set to 2.5X and 0.5X, respectively, to generate a scanning field size of 5mm x 3.7mm. The scanning mode of Vertical Scanning Interferometry (VSI) was used for

all samples. A typical 3D image of a PD-treated sample surface from the optical profilometer is illustrated in figure 2.22.

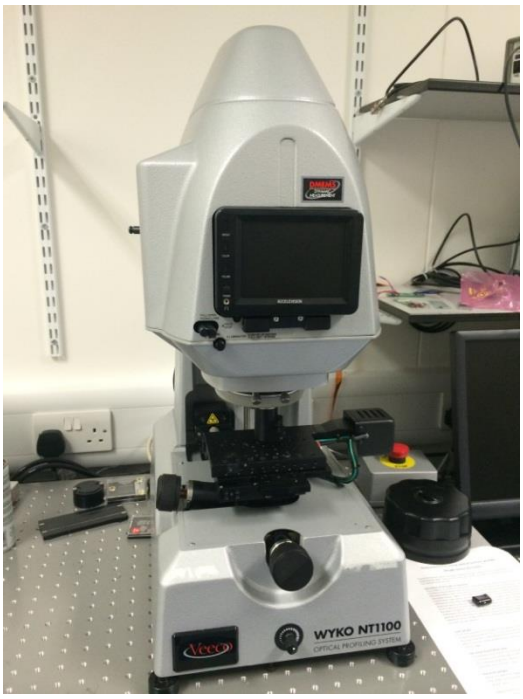

Figure 2.21 Veeco NT1100 optical profilometer

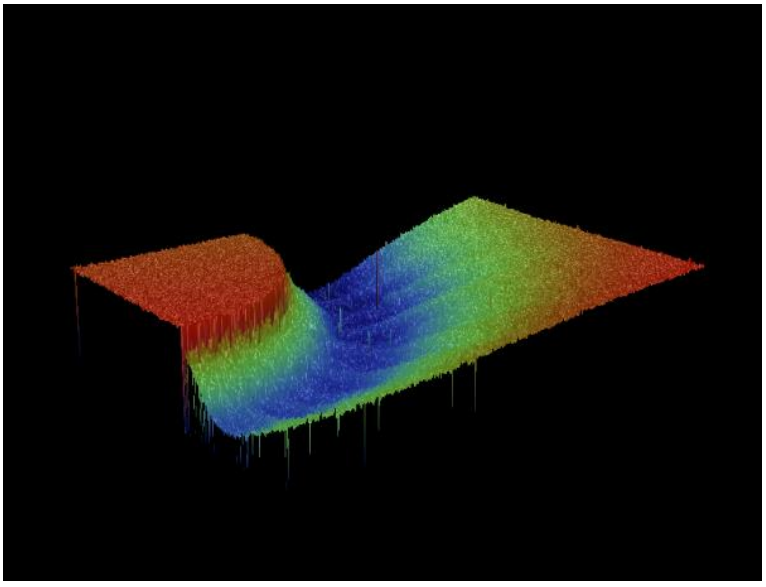

Figure 2.22 3D image of a PD-treated sample surface

2.2.6.2 Mechanical profilometer

It can be clearly seen that a valley due to PD-erosion is present on the PD-treated sample surface in figure 2.22. The erosion depths of treated samples were measured using a Veeco Dektak 6M stylus profilometer (figure 2.23). The profilometer is equipped with a diamond stylus with a radius of 12.5 µm. During each measurement, the system will drag the stylus across the sample surface and the vertical motion of the stylus is measured.

The starting point of the stylus for each scan was selected right at the middle of the white circle in figure 2.9. The scan length and scan speed were set to 7000 µm and 100 µm s^{-1}, respectively. In each scan, the profilometer dragged the stylus from the centre of the samples all the way to the end point. A typical measurement of erosion depth by the instrument is illustrated in figure 2.24. The erosion depth is defined as the height difference between the lowest point at the valley and the highest point at the untreated area. For each sample, five scans in different directions on the sample surface were measured and the average value of the erosion depths was taken as the final result for that sample.

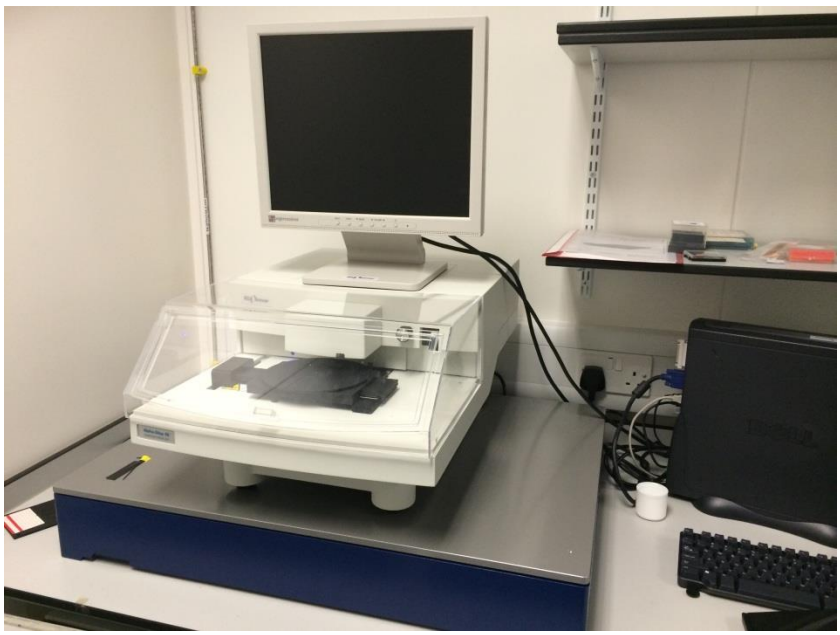

Figure 2.23 Veeco Dektak 6M stylus profilometer

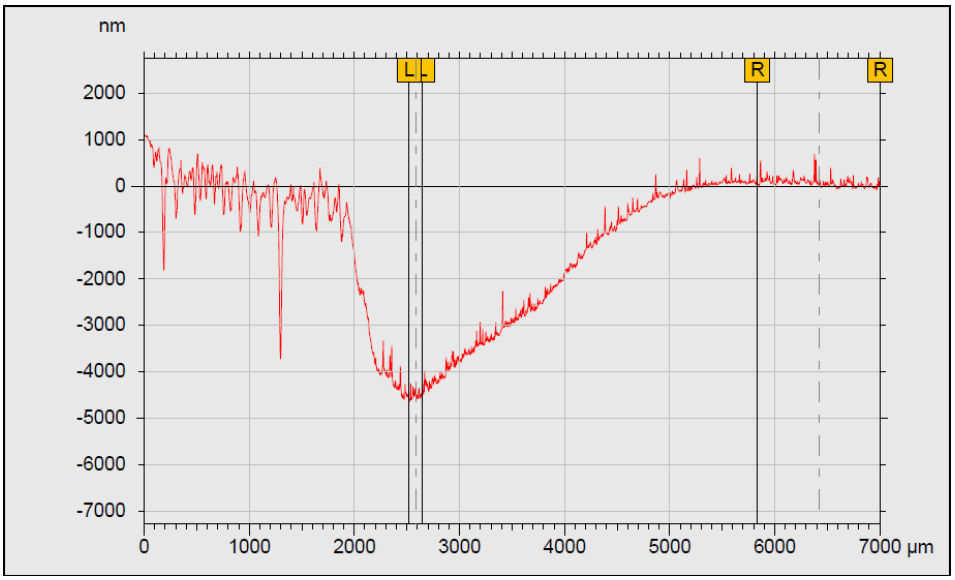

Figure 2.24 A measurement of erosion depth by the stylus profilometer

Chapter Three

3.Thickness and morphology effect on PD degradation of PET

3.1 Introduction

It is well known that crystallinity and morphology both play a very important role in many aspects of polymers such as mechanical property [59], gas permeability [64, 69], thermal [55, 56] and optical properties etc. Furthermore, the crystallinity can affect the UV and hydrolysis degradation rates of polymers as well [125-127]. However, the crystallinity and morphology effect on PD degradation of PET were seldom investigated. Although there are a few reports [27, 101] that polymers with higher crystallinity will show superior PD resistance as measured by PD-caused erosion depths, further research such as the chemistry changes and the effect of sample morphology have never been explored in detail.

Thickness is obviously the most important factor that will affect the PD and dielectric breakdown behaviour of polymers. The thickness effect of intrinsic electronic breakdown in PET films was well analysed by I. Vitellas [4]. The authors claimed that the dielectric strengths of PET films are inversely proportional to the sample thicknesses. Because the longest mean free path, which is reciprocal to the dielectric strength, is most likely to exist in the thickest sample. It is also interesting to find out how the sample thickness will affect the PD degradation.

In this chapter, the effect of morphology on PD degradation in PET films will be investigated chemically and physically by using a series of analytical techniques.

The mechanism of PD-induced degradation of PET films is explored using ATR-FTIR and XPS. Lastly, the thickness effect on PD lifetime of samples will be discussed.

3.2 Experimental

3.2.1 Samples

Mylar®A, a biaxially oriented, semicrystalline PET film from DuPont Teijin Films, with a thickness range from 36 to 300μm (to be specific, 36, 50, 100, 125, 190, 250 and 300μm), was used to investigate the effect of thickness and morphology on PD degradation and breakdown of PET films.

3.2.2 Experimental set-up of partial discharge and breakdown tests

It is no doubt that thicker samples will have less severe PD degradation and therefore longer PD-lifetimes than thin ones if they are subjected to the same voltage as a result of the lower electric field. Therefore, in order to investigate the 'real' thickness effect, sample stacks with identical thickness were used to make the overall electric fields constant, as a result, partial discharges with identical magnitude can be generated on the surface of each sample stack. By analysing the samples with different thickness on the top layers of each stack, the 'real' thickness effect can be explored.

Two sets of experiments were carried out to investigate the thickness and morphology effect on PD degradation of PET. The sample holder for the both sets has already been shown in figure 2.2 in chapter two. All samples were dried out in a desiccator at least for a week before any tests. Silica gel was used to keep the relative humidity within the chamber as low as possible during the experiments, as the relative humidity can reasonably affect the PD behaviours. Room temperature, which maintain at a quite stable level, 20±2°C, was not specifically controlled. For each experiment, seven sample stacks with identical thickness were subjected to PD in parallel for a period of time. After PD exposure, the samples on the top layers of each stack (black blocks in figure 3.1) were removed for further analysis.

3.2.2.1 Experimental set-up for 36µm - 300µm

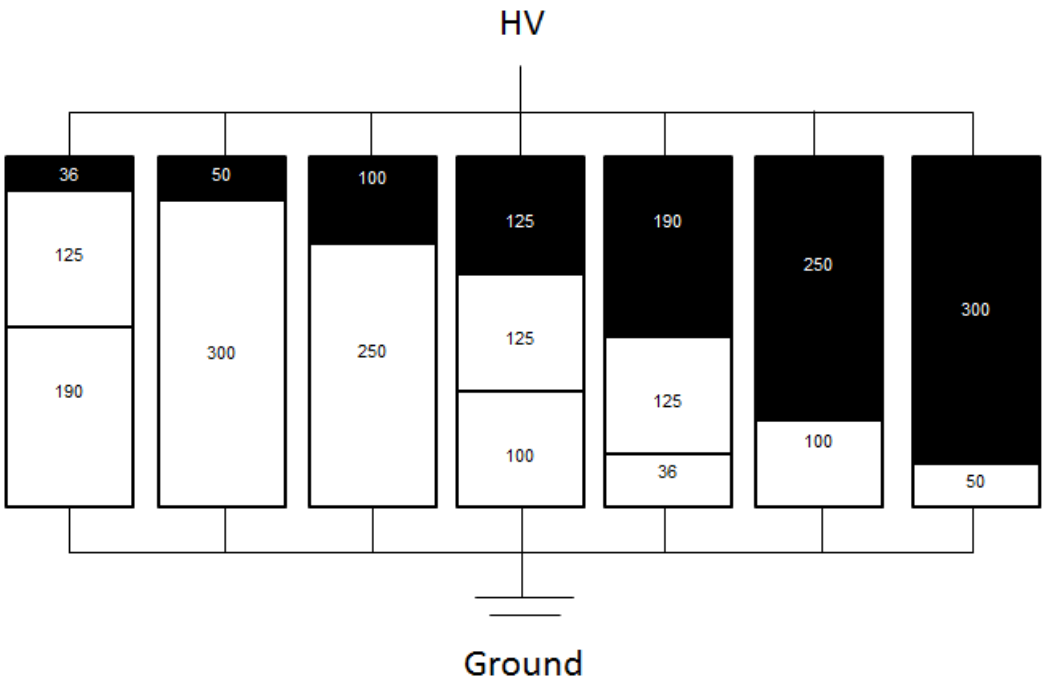

Figure 3.1 Schematic of set-up for samples 36 µm – 300 µm

For the sample with thickness from 36 µm to 300 µm, seven sample stacks with identical thickness (350 µm) were subjected to a 50 Hz AC high voltage of 3 kV for 24 hours. The structure of each stack is illustrated in figure 3.1.

3.2.2.2 Experimental set-up for breakdown test

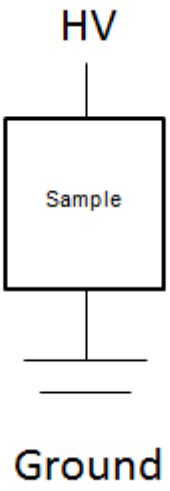

Figure 3.2 Schematic of set-up for breakdown tests due to PD degradation

Tests of sample breakdowns due to PD degradation were also carried out to investigate the practical thickness effect on PD degradation of PET. The sample holder and the sample lifetimes recording instruments have been previously described in chapter two. Single sheet of samples with various thickness from 36 µm to 300 µm were subjected to a 50 Hz AC high voltage of 4 kV until the sample breakdown due to PD erosion. For each thickness, at least five samples were tested and the average values of the PD lifetime of each thickness were calculated.

3.2.3 Experimental of analytical methods for sample characterisation

3.2.3.1 DSC

For each thickness, 1 – 15 mg virgin samples without any PD treatments, depending on the sample thickness, were cut from the sample bulk for DSC analyses. A single heating programme with a heating rate of 10°C/min was carried out in the temperature range between 30°C and 320°C for all samples in order to investigate the morphology of the samples.

3.2.3.2 Other analytical methods

Other analytical methods for sample characterisation have been previously described in chapter two.

3.3 Results and discussions

3.3.1 DSC analysis

The typical DSC response of a Mylar® A sample used in the project is shown in figure 3.3. Two melting endotherm peaks are seen to be located at 225 and 256°C. Multiple melting behaviours of PET were widely discussed in the literature [57-63]. A complex mechanism which is a combination of 'dual morphology' and 'melt-recrystallization-remelt' has been proposed for the explanation of multiple melting endotherm peaks [57,58]. The dual morphology mechanism suggests that two different populations of lamellae thickness could coexist in the polymer. Lamellae with low degree of perfection can melt during the DSC scan and recrystallize to form lamellae with higher degree of perfection and finally remelt. In figure 3.3, doublet peaks A and B thus can be associated with the melting of the thinner and thicker lamellae in the sample, respectively.

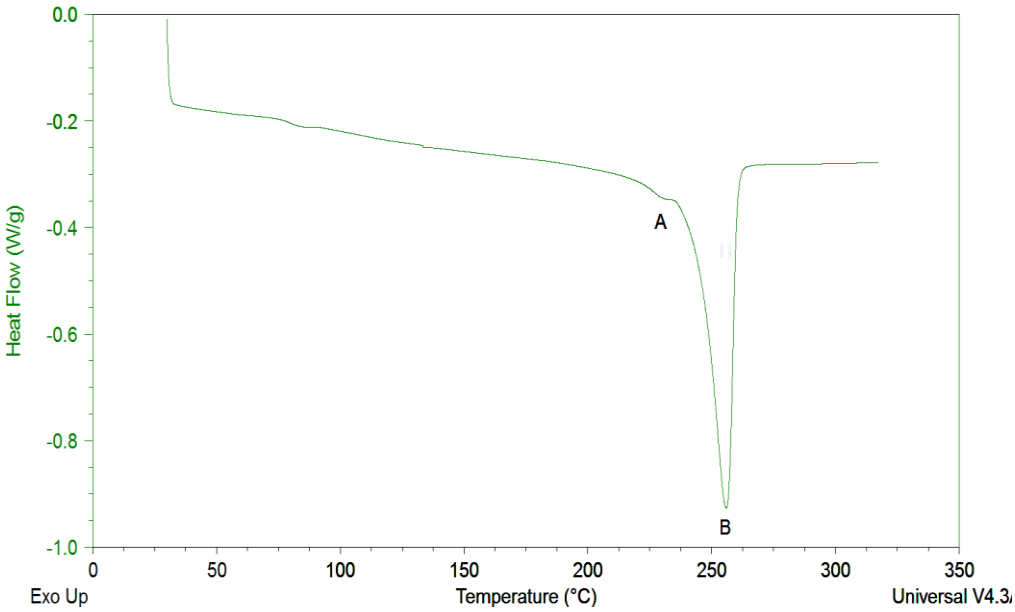

Figure 3.3 Two melting endotherm peaks of Mylar® A

The DSC traces of the melting of Mylar®A samples with 7 different thickness from 36μm to 300μm (from top to bottom with the top trace being the 36 μm) used for the PD degradation experiment are shown in figure 3.4. It can be clearly seen that doublet peaks are present in all samples. The locations of minor peaks vary from 214 up to 224°C while the locations of major peaks remain almost the same, around 255°C. The *Thomas-Gibbs* equation [61] was used to characterize the distribution of the lamellae thickness of the samples:

$$l_c(T_m) = [(1 - \frac{T_m}{T_m^0}) \cdot \frac{\Delta h_{mv}}{2\sigma_e}]^{-1} \quad (1)$$

where T_m is the melting temperature, T_m^0 (564 K) is the melting temperature of infinitely thick lamellae (equilibrium melting temperature), σ_e (0.106 Jm^{-2}) is the fold surface free energy, Δh_{mv} (2.1×10^8 Jm^{-3}) is the melting enthalpy per volume unit [61]. Table 3.1 represents the melting temperatures and the corresponding lamellae thickness for each sample with different thickness. It is somewhat surprising to note that even these are all Mylar®A sheets, they do exhibit some significant differences in morphology possibly due to different draw ratios in both machine direction (MD) and transverse direction (TD) in manufacturing processes. From table 3.1 it can be seen the thicknesses of the thinner lamellae L_c^1 vary greatly from samples to samples, for example, the L_c^1 and the crystallinity degree X_c% of the 100 μm sample

are 15% and 12% greater than that of the 300 μm sample, respectively. The crystallinity degrees of samples can be calculated by using the equation as follows:

$$X_c = \frac{\Delta H_m}{\Delta H_{100\%}} \quad (2)$$

where ΔH_m is the measured melting enthalpy of the sample and $\Delta H_{100\%}$ is the melting enthalpy of a 100% crystalline PET, which is 140 J/g.

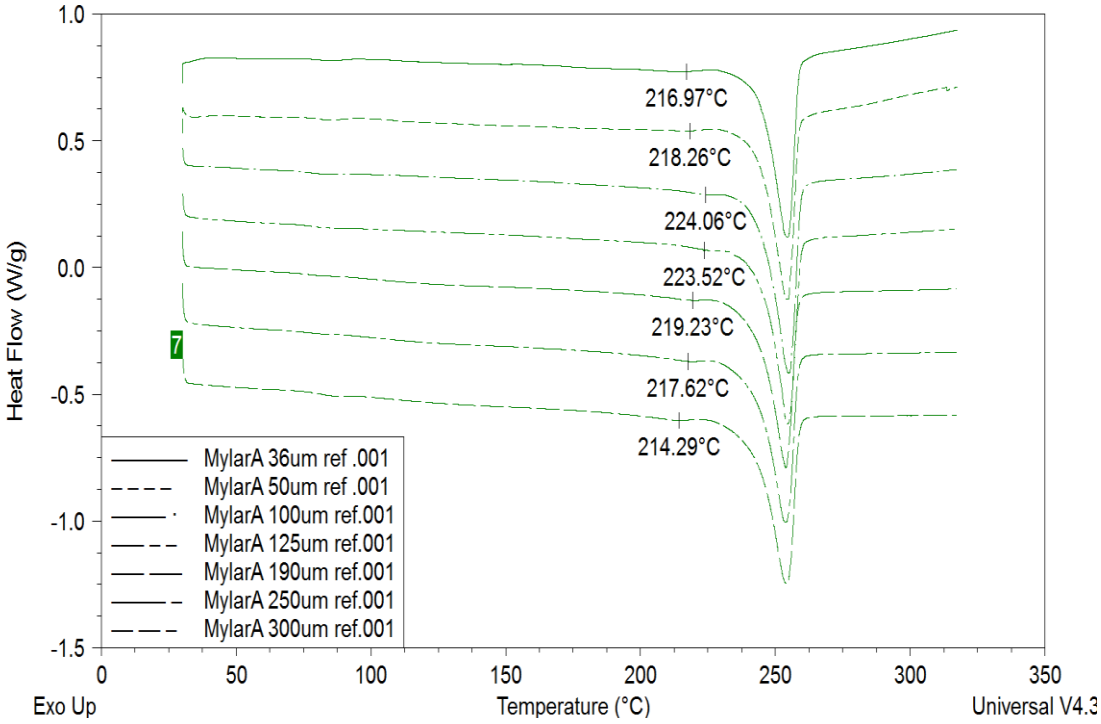

Figure 3.4 DSC analyses of the melting of Mylar®A samples with different thickness from 36μm to 300μm

Sample thickness	T_m^1(K)	L_c^1(Å)	T_m^2(K)	L_c^2(Å)	ΔH_m(J/g)	X_c%
36 µm	490±0.9	76.9±1.0	528.8±0.3	162.8±0.3	53.2	38
50 µm	491.4±1.1	78.4±1.2	527.7±0.1	156.9±0.1	55.73	39.81
100 µm	497.2±2.4	85.2±3.2	528.1±0.2	158.6±0.2	58.92	42.09
125 µm	496.7±1.2	84.6±1.4	527.7±0.3	156.9±0.3	55.96	39.92
190 µm	492.4±3.4	79.5±4.0	527.5	156.0	53.96	38.54
250 µm	490.8±1.3	77.8±1.4	526.8±0.3	153.1±0.3	53.05	37.89
300 µm	487.4±2.7	74.3±2.7	527.1±0.2	154.3±0.2	52.5	37.50

Table 3.1 DSC data of untreated Mylar®A samples

3.3.2 FTIR analysis

ATR-FTIR was used to investigate the surface morphology of untreated samples and the surface chemical changes of the partial discharge-treated samples.

Untreated samples

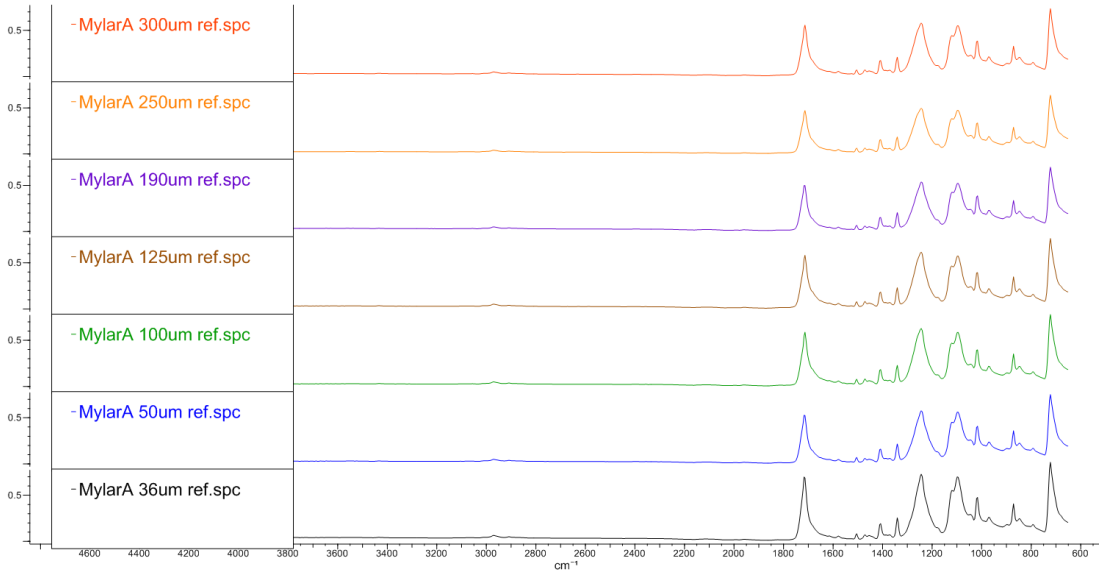

Figure 3.5 ATR-FTIR spectra of untreated samples with different thicknesses

Figure 3.5 represents the typical ATR-FTIR spectra of untreated Mylar®A samples with the bottom spectrum being the 36 µm and the top one being the 300 µm. Spectra are displayed in stack for clarity reason. According to Liang [85], Grime [86] and Chen [91], the main absorption bands of samples in figure 3.5 can be assigned as follows, 723 cm^{-1} to the C-H out-of-plane deformation, 1095 cm^{-1} and 1120 cm^{-1} to the stretching of amorphous and crystalline form of the (O–C) phases, respectively, 1245 cm^{-1} to the =C–O stretching in the ester group, 1340-1470 cm^{-1} to the wagging and bending of the CH_2, 1717 cm^{-1} to the carbonyl group stretching and 2970 cm^{-1} to the CH_2 stretching.

As already discussed in chapter 2, the two absorption peaks at 1473 cm^{-1} and 1455 cm^{-1} of PET are associated with the bending of the glycol CH_2 in amorphous and crystalline phases. These two peaks have been widely used to characterize the surface morphology of samples in literature [59] [61] [73] [88] [91], the crystallinity degree of sample surface can be calculated using the following equation:

$$X_c = \frac{A_c}{A_c + A_a} \quad (3)$$

where A_c and A_a are the crystalline and amorphous peak area, respectively. Deconvolution processes were carried out by using OriginPro 8.6 software, as discussed in chapter 2 and the typical result of the 'Peak fit' was shown in figure 2.11. The crystallinity degrees of untreated Mylar®A samples are shown in table 3.2. Compare the results with the same properties obtained by DSC in table 3.1, one can find that although the data of crystallinity degrees obtained by FTIR are smaller than the data by DSC, the data trends are highly consistent, with the 100 and 125 µm samples having the highest crystallinity degrees and the 300 µm one having the lowest.

Sample thickness	1455 cm^{-1}	1473 cm^{-1}	$\%X_c$
36 µm	78.98	21.02	21.02
50 µm	77.80	22.20	22.20
100 µm	76.41	23.59	23.59
125 µm	76.15	23.85	23.85
190 µm	77.67	22.33	22.33
250 µm	78.86	21.14	21.14
300 µm	79.55	20.45	20.45

Table 3.2 Crystallinity degrees of untreated Mylar®A samples by FTIR

PD exposed samples

Overlaid ATR-FITR spectra of untreated and PD exposed 100 µm samples were displayed in figure 3.6, spectra of samples in other six thicknesses are similar to the figure, hence only spectra of 100 µm sample are used in here as an example. Both spectra were normalized to the peak at 1410 cm^{-1}, which is assigned to C–C bond of aromatic stretching [86]. This peak is often selected as an internal reference peak for PET when quantitative characterization is needed as it is not sensitive to effects of crystallinity or orientation [88] [89] [91] [96] [98]. As seen from figure 3.6, once normalized and overlaid, absorption changes can be found between the two spectra. In order to characterize the PD degradation degree on each sample quantitatively, carbonyl bands (1610-1790 cm^{-1}, shown in figure 3.7) and 3000-3500 cm^{-1} absorption regions (shown in figure 3.8) were analysed via OriginPro 8.6 software.

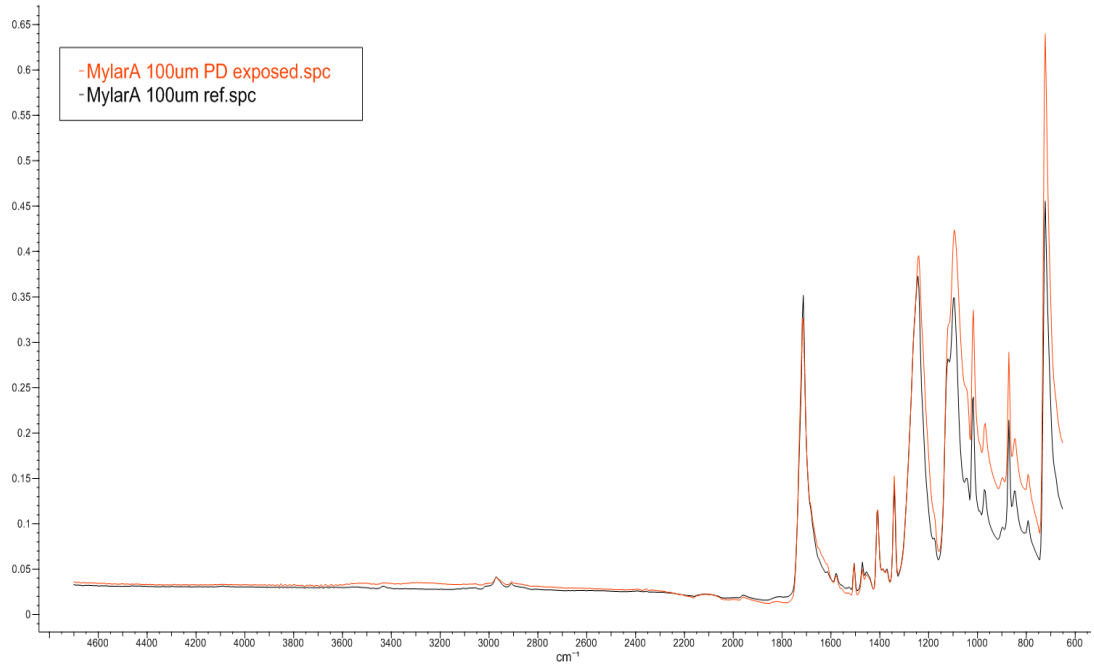

Figure 3.6 Overlaid ATR-FTIR spectra of 100 µm Mylar®A, untreated and PD exposed

The carbonyl band, which usually locates between 1610 and 1790 cm^{-1} in PET, has been used to characterize corona discharge treated PET samples. The band was reported to become broad after corona discharge treatment, according to Ding [33] and Barbaro [90]. From figure 3.7, one can see that the carbonyl band became broad after the PET film received PD degradation, which is consistent with the results from Ding and Barbaro. It is also important to note that after PD erosion, the intensity of the peak at 1717 cm^{-1} decreased, suggesting that the chemical structure of the ester component in the sample broke down due to the PD erosion, on the other hand, the increase of the peak at 1685 cm^{-1} implies that carboxylic acid and aldehyde could be produced [87].

As mentioned above, OriginPro 8.6 software was used to apply the 'Peak fit' function to the carbonyl bands to have a better understanding how PD degraded the materials quantitatively. The peak types were selected as 'Gaussian' and the peak centres of two peaks were fixed to 1717 and 1685 cm^{-1}. A typical deconvolution result of carbonyl peak is illustrated in figure 3.8, with the peak at 1717 and 1685 cm^{-1} assigned as the original C=O stretching in the ester component of PET and the C=O vibrational mode of carboxylic acid and aldehyde, respectively. Furthermore,

the IR absorption bands of C=O stretching in amides, N–H bending in amines and C=C stretching also fall into the region of 1610-1690cm^{-1} [92], which could also possibly attribute to the increase of the peak at 1685 cm^{-1} as substances like amides and amines are very likely to be produced during the PD degradation process.

Figure 3.9 represents the comparison of 3100-3650 cm^{-1} region of the samples. It is clear that a new wide band appear in this region after the samples were PD exposed. The new band can be assigned to the –OH group stretching in phenols and carboxylic acids as well as the N-H group stretching in amides and amines. In order to compare the 'real' peak intensities, the raw peak areas of the new generated bands were normalized to the internal standard peaks by dividing by the area of the peak at 1410 cm^{-1} in OriginPro 8.6.

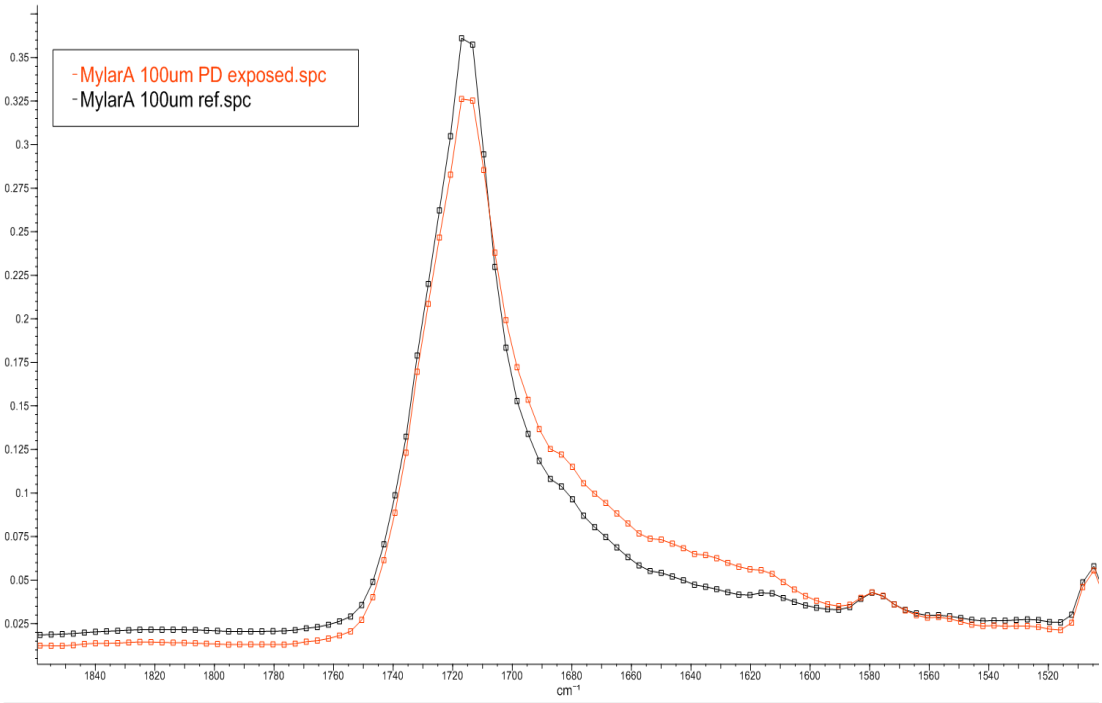

Figure 3.7 Overlaid carbonyl bands of 100 µm Mylar®A, untreated and PD exposed

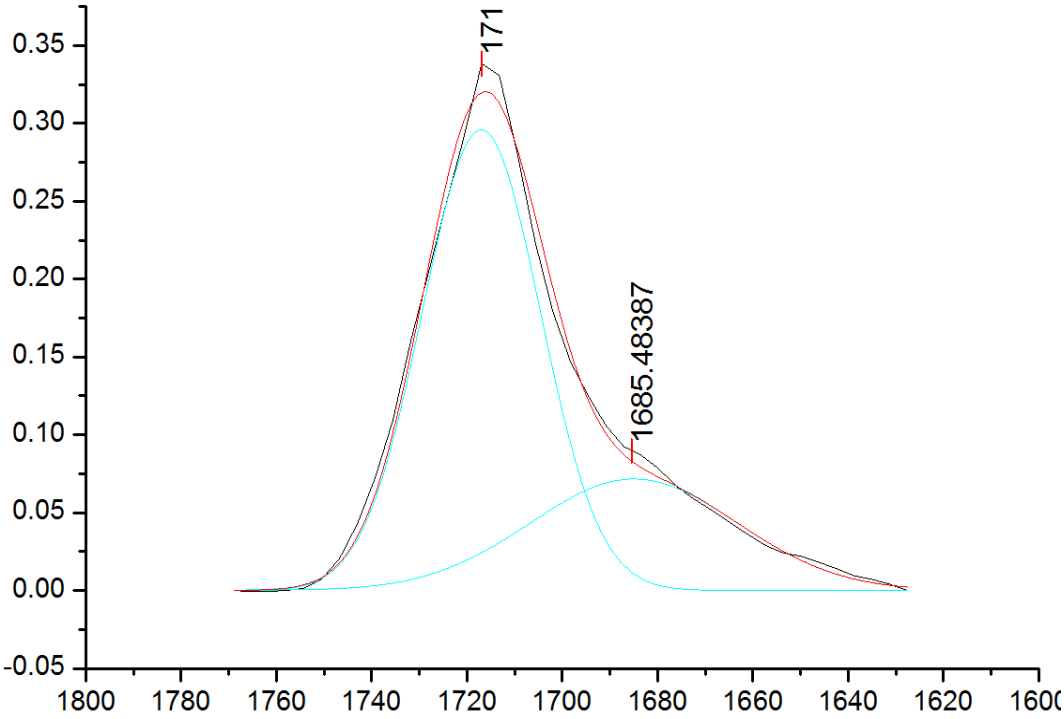

Figure 3.8 Deconvolution of carbonyl peak of PET

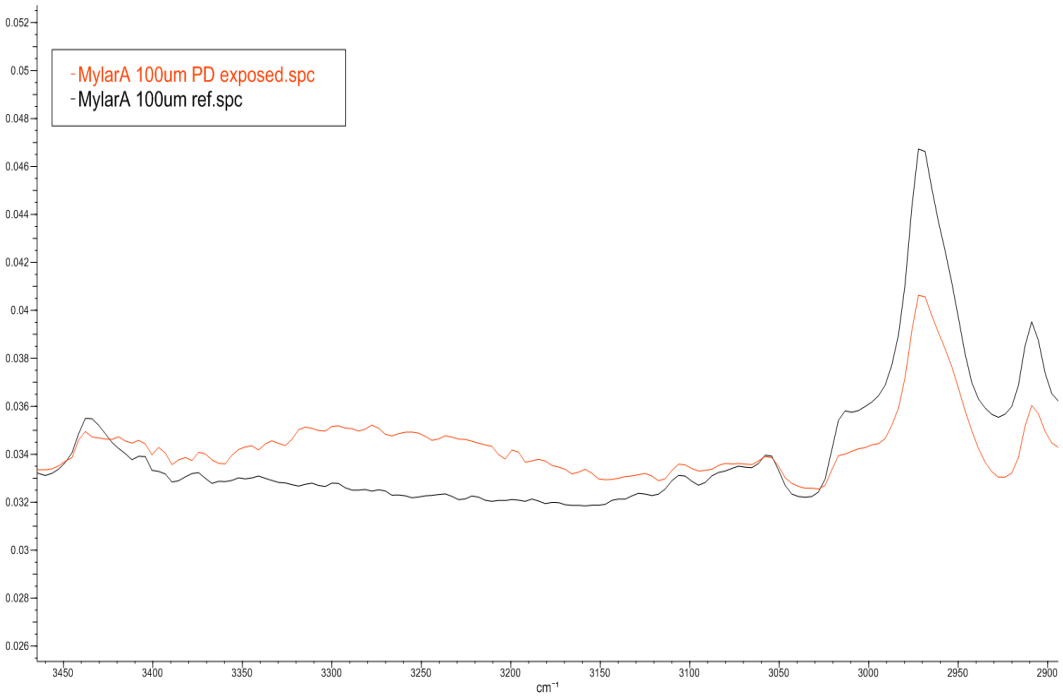

Figure 3.9 Overlaid 3000-3650 cm^{-1} region of 100 µm Mylar®A, untreated and PD exposed

Results of carbonyl peak fits are shown in table 3.3. The data shows that the peak area percentages of the 1717 cm^{-1} peaks for all the untreated samples are about 72.5%, however the numbers all decrease after the samples received PD degradation. Moreover, it is interesting to note that the peak area percentage of the 1717 cm^{-1} peaks for the 300 μm decrease to only 60.86%, which is the lowest value among all the samples, while the peak area percentage of the 1685 cm^{-1} peak, 39.14%, is higher than that of any other six samples. On the other hand, for the 100 μm sample, both peak area percentages, 70.34% and 29.66%, show the smallest changes among all the samples compared to the untreated data. Results of peak area ratios of 3100-3650 cm^{-1} and 1410 cm^{-1} are shown in table 3.4. Comparing the data in table 3.4 with the data in the third column of table 3.3, one can find that both sets of data follow the same trend where the peak intensities are greatest for the 300 μm sample and smallest for the 100 μm sample. The consistency of the two sets of data indicates that by-products such as carboxylic acids, phenols, amides and amines etc. could be generated during the PD degradation process, moreover, the 100 μm sample degraded less than the 300 μm sample in terms of the rate of decomposition of original functional groups in the polymers and generation of by-products.

From above, the PD-induced degradation degrees of Mylar®A samples with different thicknesses have been characterized quantitatively by ATR-FTIR. By correlating the data in table 3.3 and 3.4 to the data obtained by DSC and FTIR in both table 3.1 and 3.2, it is important to note that even the samples were made to receive identical electrical stresses from PD, the degradation extents were quite different for samples with different thicknesses and seems that the results are closely related to the morphology of the samples. Results reveal that samples with greater overall lamellae thickness and higher crystallinity degrees degraded less than samples with thinner lamellae structure and low crystallinity degrees.

Samples	Peak area % of 1717 cm^{-1}	Peak area % of 1685 cm^{-1}
Untreated	72.54±0.91	27.46±1.08
36 µm	65.24	34.76
50 µm	69.13	30.87
100 µm	70.34	29.66
125 µm	70.31	29.68
190 µm	63.8	36.16
250 µm	61.51	38.49
300 µm	60.86	39.14

Table 3.3 Peak fit results of Mylar®A, untreated and PD exposed

Samples	3100-3650 cm^{-1}/1410 cm^{-1}
Untreated	N/A
36 µm	8.32
50 µm	7.37
100 µm	7.20
125 µm	7.28
190 µm	8.56
250 µm	9.81
300 µm	12.35

Table 3.4 Peak area ratio of 3100-3650 cm^{-1} and 1410 cm^{-1} of Mylar®A, untreated and PD exposed

3.3.3 XPS analysis

As discussed above, surface chemical changes of PD exposed PET films have been semi-quantitatively analysed by using ATR-FTIR. In order to have a better understanding of the mechanism of PD degradation of PET films as well as explore the morphology effect on the PD erosion, XPS experiments were carried out for both the untreated and PD exposed samples. In this project, XPS surveys and higher resolution scans of C1s of samples were used for quantitative analysis.

Untreated samples

A typical XPS survey and higher resolution scan of C1s of an untreated Mylar®A sample have already been shown in figure 2.13 and 2.14 in chapter two. From the XPS survey, only carbon and oxygen are present as XPS technique could not detect hydrogen, the average carbon and oxygen concentrations in an untreated Mylar®A sample are 75.56% and 24.44%, respectively. Peak fit results of C1s using CasaXPS software was shown in figure 2.16, the three peaks in the spectrum, which locate at 284.80eV, 286.41eV and 288.78eV, are attributed to the carbon atom (underlined) in C-(C,H), C-O and O=C-O in PET, respectively [46, 48, 49]. The average concentrations of these three peaks are 62.83%, 19.92% and 17.26%.

PD exposed samples

The comparison of XPS survey scans of the untreated and PD exposed samples are shown in figure 3.10. As can be seen, for PD exposed samples, after PD degradation newly generated peaks are present and locate at 401.77 and 540.77eV, have been attributed to N1s and Sb3d, respectively. The presence of nitrogen atoms confirms that nitrogen-containing compounds such as amides and amines could be generated after the samples reacted with air discharge [31, 38]. On the other hand, the presence of antimony could be explained by the so-called 'corona etching' effect, which the PET resin degraded away and left behind the antimony-containing compounds such as Sb_2O_3 on the sample surface. The atomic concentrations of each element present on the sample surface are listed in table 3.5, for PD exposed samples, the concentrations of O1s increased from 24.44% to around 31% while the concentrations of C1s decreased from 75.56% to roughly 65%, indicates that the chemical structure of samples have been changed and oxygen-containing functional groups were implanted onto the samples due to surface oxidation. It is also important to note that even having low atomic concentrations (<1%), the concentration trends of N1s and Sb3d of the PD exposed samples with different thickness are nearly the same as the data trends in table 3.3 and 3.4, with the 100 µm degraded less than any other samples due to its thickest overall lamellae and highest crystallinity degree. For example, the concentrations of N1s and Sb3d of 300 µm are both more than twice that of the 100 µm.

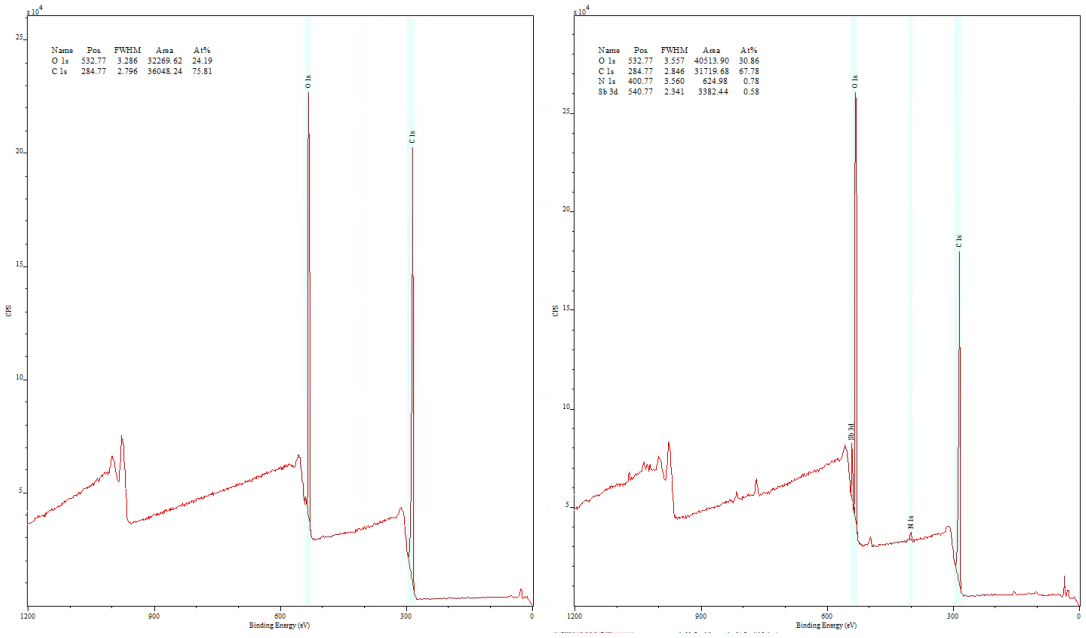

Figure 3.10 XPS surveys of Mylar®A, untreated and PD exposed

Samples	O1s (%)	C1s (%)	N1s (%)	Sb3d (%)
Untreated	24.44	75.56	0	0
36 µm	30.95	65.33	0.78	0.36
50 µm	30.13	66.48	0.58	0.25
100 µm	31.5	64.98	0.39	0.35
125 µm	31.2	65.45	0.4	0.36
190 µm	32.5	65.53	0.82	0.76
250 µm	30.51	67.88	0.83	0.57
300 µm	33.51	64.38	0.86	0.89

Table 3.5 XPS survey scan results of Mylar®A, untreated and PD exposed

More details about PD degradation mechanisms on PET films can be obtained by looking at higher resolution scans of C1s of the samples. Overlaid C1s spectra of PD exposed sample (use 250 µm as an example) are shown in figure 3.11, it is clear that the intensities of all the three absorption peaks decrease after samples were PD exposed, suggesting that chemical bond cleavages occurring for the

exposed samples. Moreover, one can note that the two peaks locating at 286.41 and 288.78eV become broad after PD degradation, indicates new peaks generated at 286.6 and 289.1eV, which are attributed to C-NH_x (amine), NH_x-C=O (amide), phenolic-OH and carboxylic acid, respectively [31-33,55]. Deconvolution of high resolution scans of C1s of samples were carried out by CasaXPS software, Gaussian/Lorentzian line-shapes were used for all the spectra, peak positions were set as 284.80, 286.41, 286.6, 288.78 and 289.1eV, no further constraints were set. A typical peak-fitting spectrum of C1s for the PD exposed samples is shown in figure 3.12 and the deconvolution results are shown in table 3.6. Although figure 3.11 has shown that all the peak intensities decrease after PD degradation, one can find out the concentrations of the peak at 284.80eV have not changed too much for all the samples. However, both concentrations of C-O and O=C-O, especially the C-O group, decrease markedly after PD degradation, implying that the ester group preferentially breaks down under the PD attacks. Comparing the data of samples with different thicknesses, once again, the loss rates of original functional groups and the growth rates of newly generated groups of samples follow the same trends as previous ATR-FTIR results.

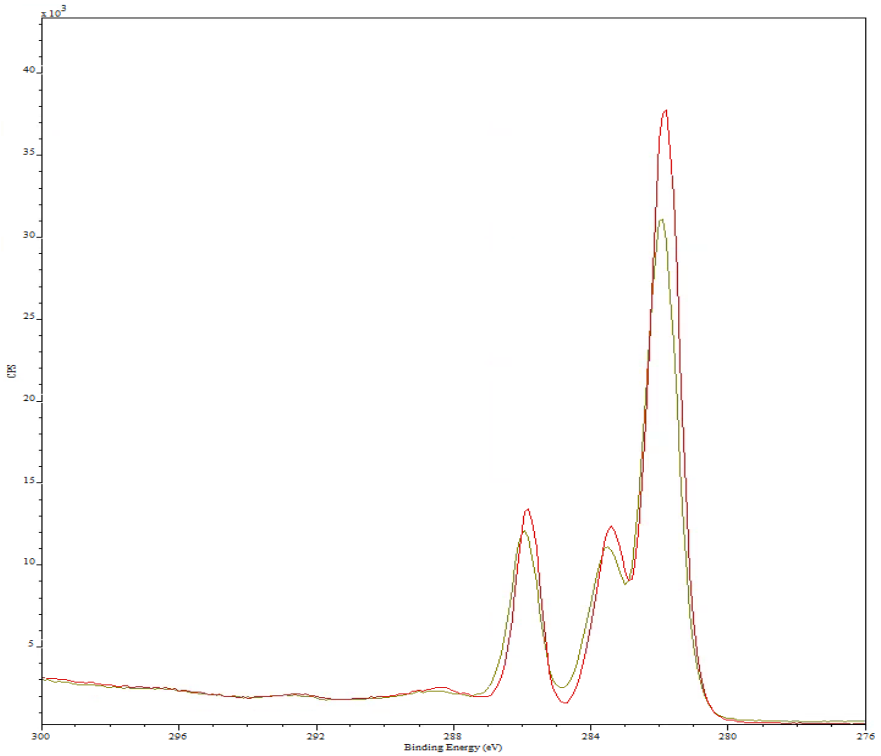

Figure 3.11 Overlaid C1s spectra untreated (red) and PD exposed (green)

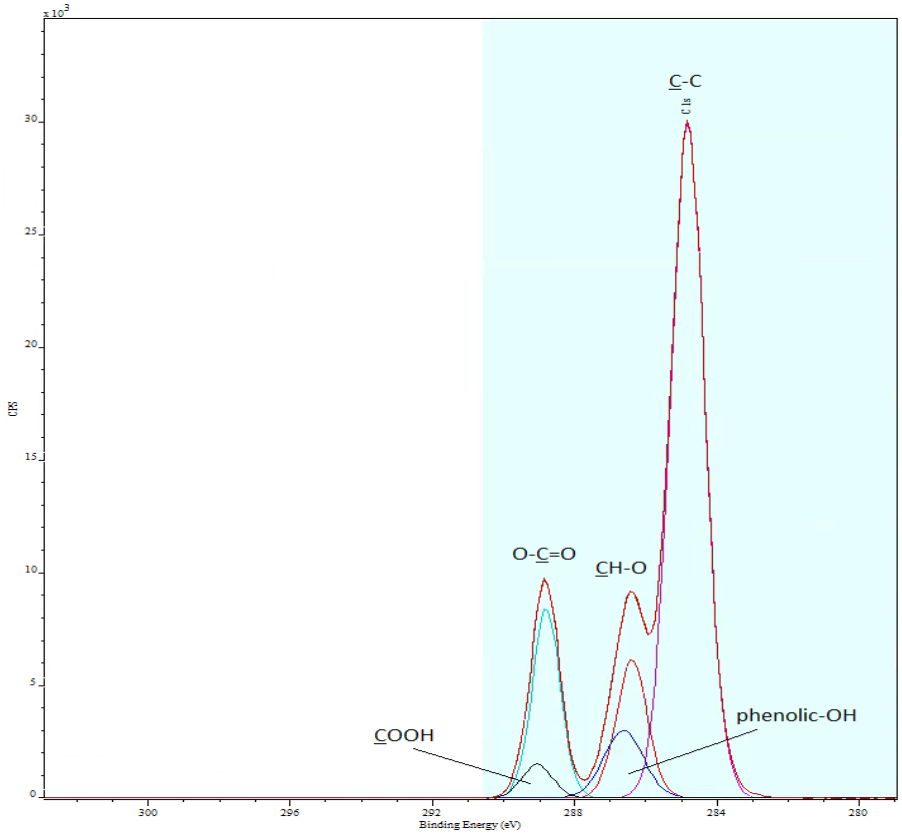

Figure 3.12 Deconvolution of C1s spectrum of PD exposed Mylar®A

Samples	C-C (284.80)	C-O (286.41)	O=C-O (288.78)	COH, C-NH_x, NH_x-C=O (286.6)	COOH, COH (289.1)
Untreated	62.83	19.92	17.26	N/A	N/A
36 µm	62.5	13.04	16.96	6.68	0.8
50 µm	62.16	15.84	16.94	4.33	0.73
100 µm	62.36	17.6	16.58	3.25	0.21
125 µm	62.64	16.61	16.41	4.02	0.32
190 µm	62.84	11.92	15.50	7.36	2.39
250 µm	63.73	13.08	15.68	6.47	2.04
300 µm	63.3	10.92	15.08	8.18	2.53

Table 3.6 High resolution C1s scan results of Mylar®A, untreated and PD exposed

3.3.4 Surface profilometer and SEM analysis

Surface profilometer

Surface profilometers were used to investigate the PD degradation of Mylar®A samples physically. A Veeco NT1100 optical profilometer was used to study the surface topology of samples and the images are shown in figure 3.13. The sample surfaces of untreated samples are plain and flat. However, a deep valley appeared around the electrode-sample contacting area after the samples were PD exposed, suggests that a portion of original materials decomposed by PD erosion. To measure the erosion depths of PD-treated samples, a Veeco Dektak 6M stylus profilometer was used. The measuring processes have been introduced in chapter two already and the results are plotted in figure 3.14. As can be seen, the figure shows a bowl-shape plot with the 100 µm sample having the lowest erosion depth and the depth values become greater as the sample thickness move towards 36 µm and 300 µm. Furthermore, it is interesting to note that the erosion depths of PD exposed samples follow the same trend as the chemistry data obtained by FTIR and XPS.

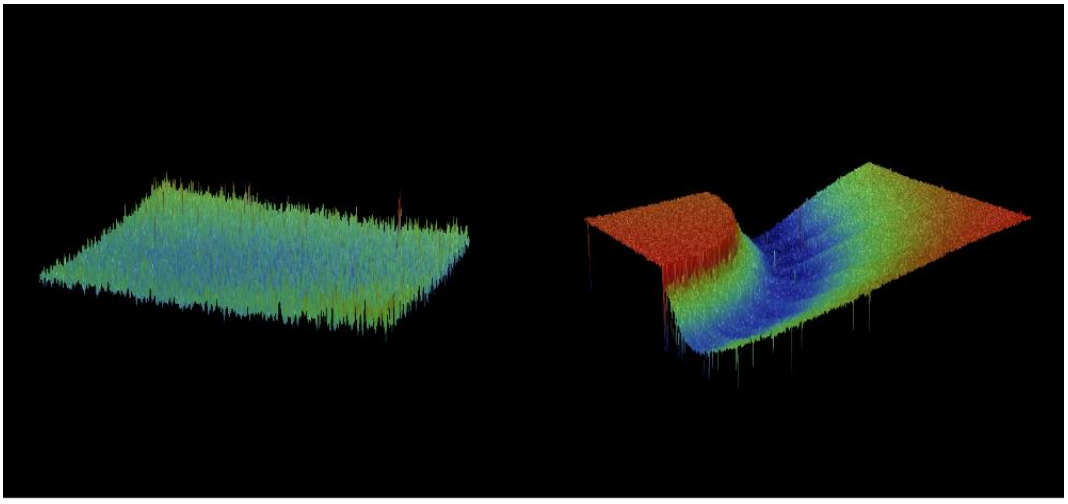

Figure 3.13 Sample surface images by Veeco NT1100, untreated and PD exposed

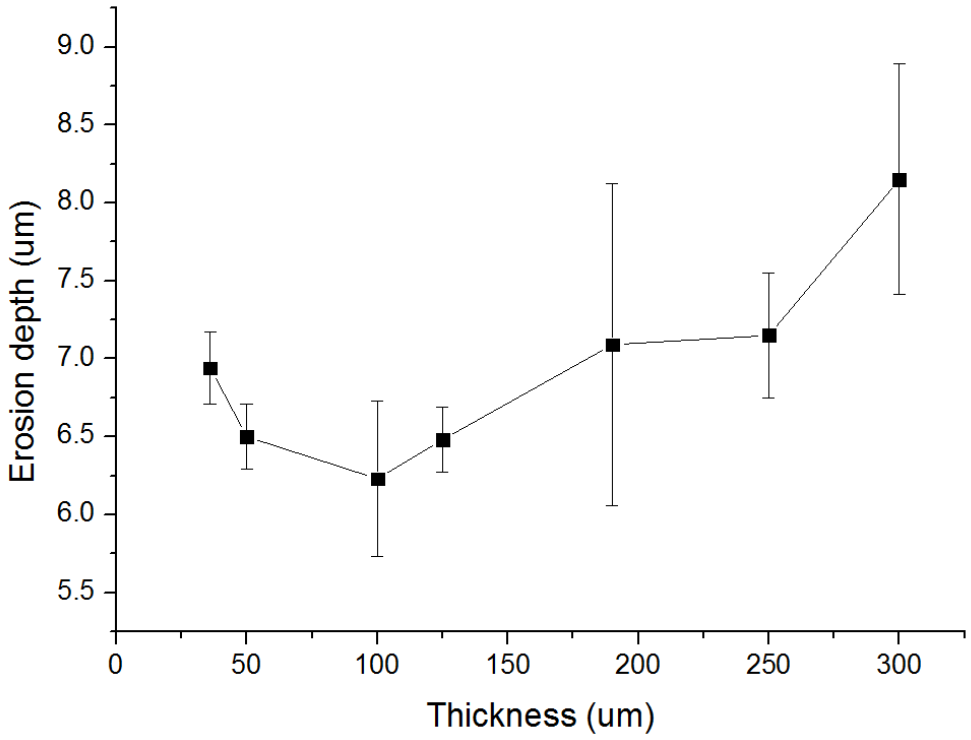

Figure 3.14 Erosion depth by Veeco Dektak 6M, untreated and PD exposed

SEM images

The SEM images of the untreated and PD exposed Mylar®A samples (use 50 µm as an example) are shown in figures 3.14-3.17. From figure 3.14 and 3.15, one can see that after PD degradation, the area outside the electrode-sample contacting circle become whiten, this could be due to the presence of antimony trioxide caused by PD erosion, as already mentioned in the XPS section. The cross-section images are shown in figure 3.16 and 3.17, by measuring the sample thicknesses, it is clear to directly witness the sample thickness reduction caused by PD – the thickness of the 50 µm sample has reduced by 6.6 µm, which is perfectly consistent with the erosion depth data shown in figure 3.14.

Figure 3.14 Untreated Mylar®A sample surface

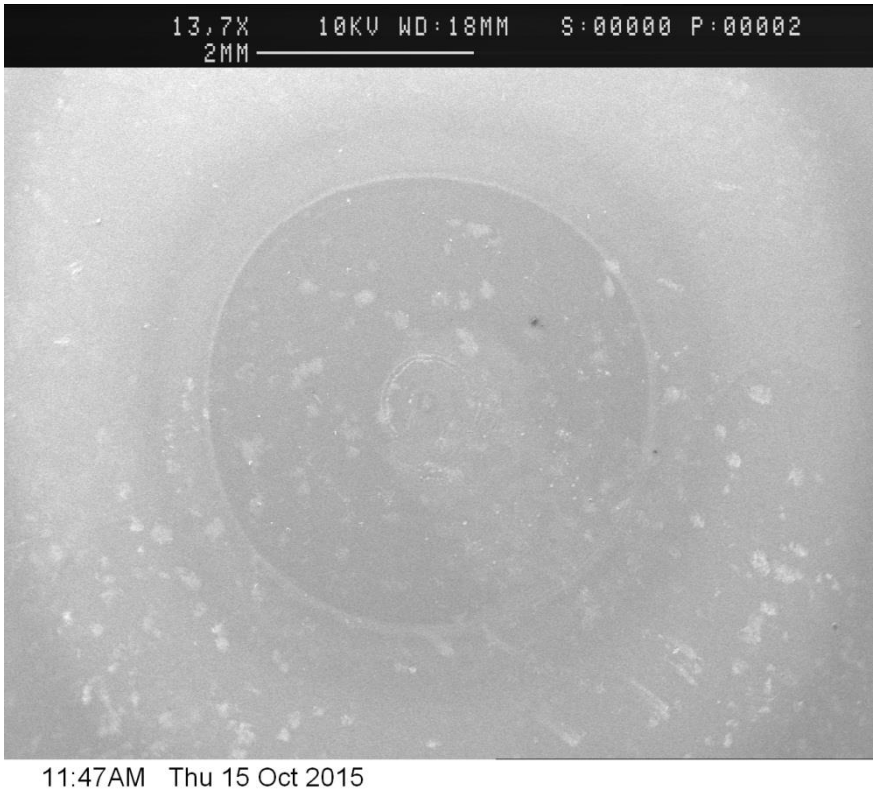

Figure 3.15 PD exposed Mylar®A sample surface

Figure 3.16 Cross-section of Untreated Mylar®A sample

Figure 3.17 Cross-section of PD exposed Mylar®A sample

3.3.5 Partial discharge lifetime analysis

Figure 3.18 represents the relation between PD lifetime and thickness of Mylar®A samples in a log-log plot. As can be seen the PD lifetimes seems to have a linear relation with sample thicknesses less than 200 µm on log-log scales. This is consistent with the data (represented in figure 3.19) obtained by Yotsuo and Hideo [1], where the authors used polyethylene with thicknesses between 50 and 200 µm as experimental materials. However, from figure 3.18, one can note that when the sample thickness is beyond 190 µm, the PD lifetimes of samples no longer follow the ideal linear relation (red dash line in figure 3.18) with thickness on log-log scales but deviate a lot, being much less than the ideal linear condition.

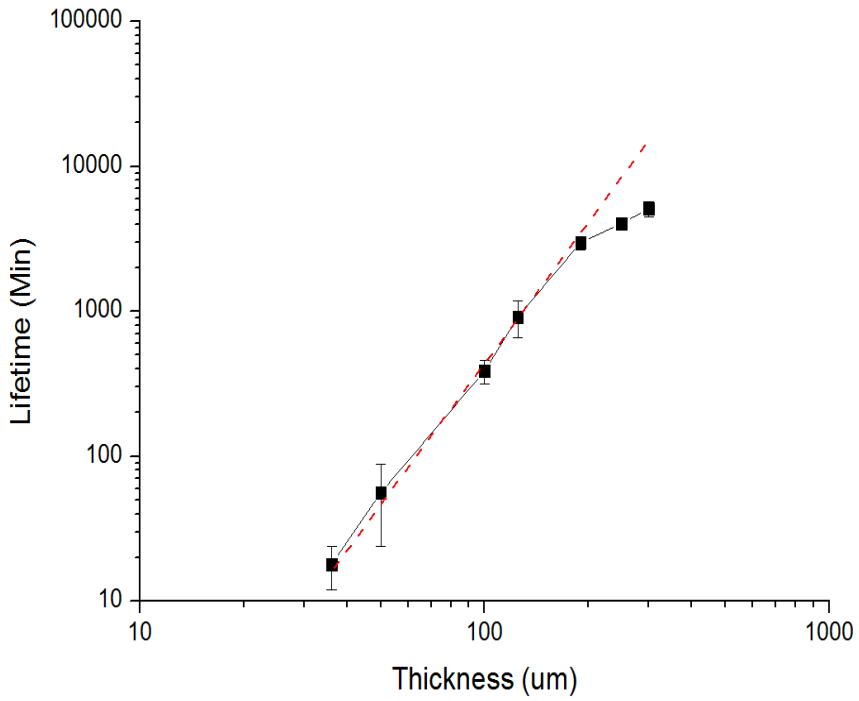

Figure 3.18 Relation between PD lifetime and thickness of Mylar®A samples

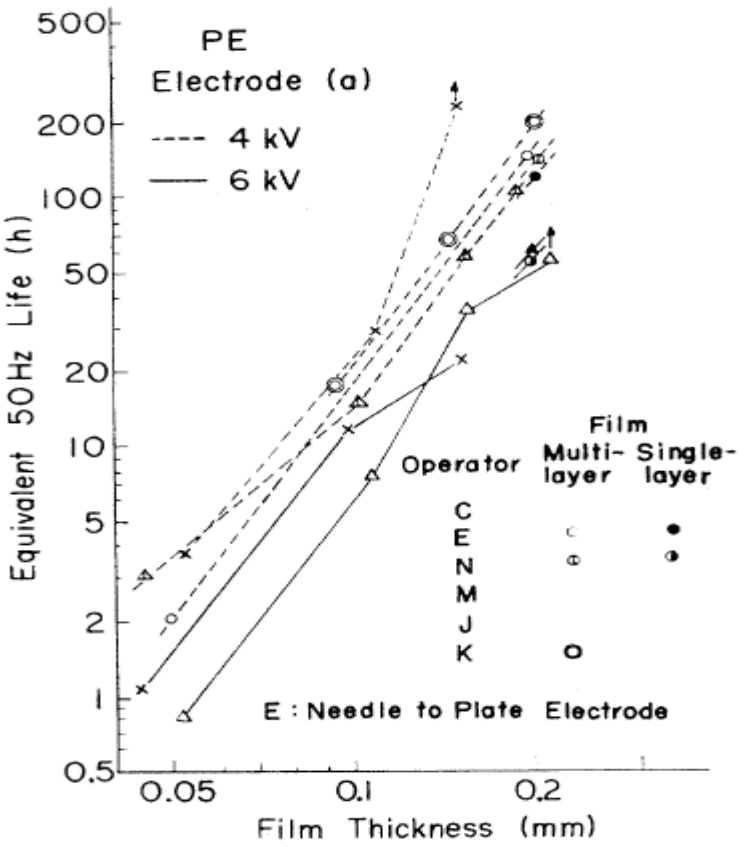

Figure 3.19 Relation between corona life and thickness of PE film [1]

3.4 Conclusions

Mylar®A samples with 7 different thicknesses from 36 to 300 μm were subjected to identical magnitudes of partial discharge to analyse the thickness and morphology effect on PD degradation of the samples. PD exposed samples have been investigated chemically and physically by using various analytical techniques. Both ATR-FTIR and XPS results show that surface chemistry have changed markedly after samples were subjected to PD degradation, the PD degradation mechanisms of PET materials are somewhat similar with the mechanisms of UV degradation [100], bond cleavage occur both in -O=C-O-C- and -O=C-O-C- groups of PET, CO and CO_2 were directly 'extracted' from the ester component of the polymer backbone and by-products such as carboxylic acid, aldehyde, phenol, amines and amides could be generated as well. Reaction details are demonstrated in figures 3.20-3.23.

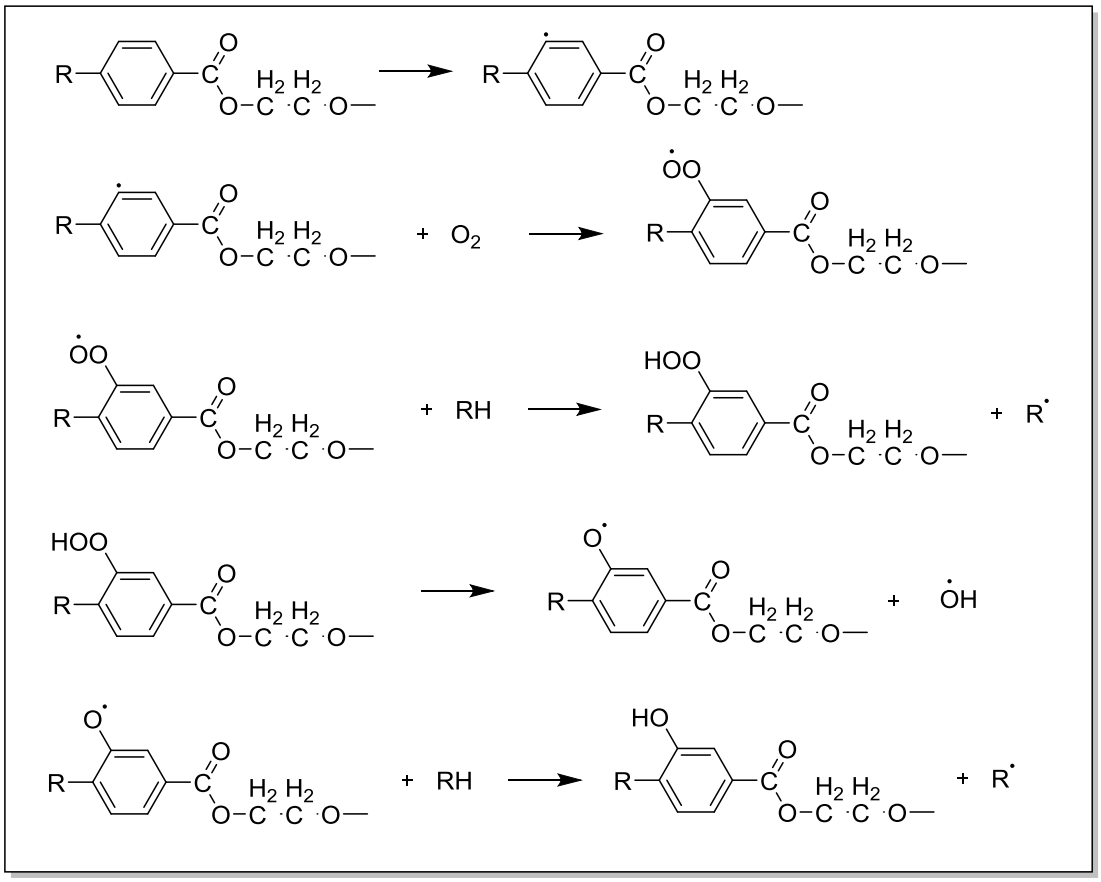

Figure 3.20 Reactions on aromatic rings [33, 99]

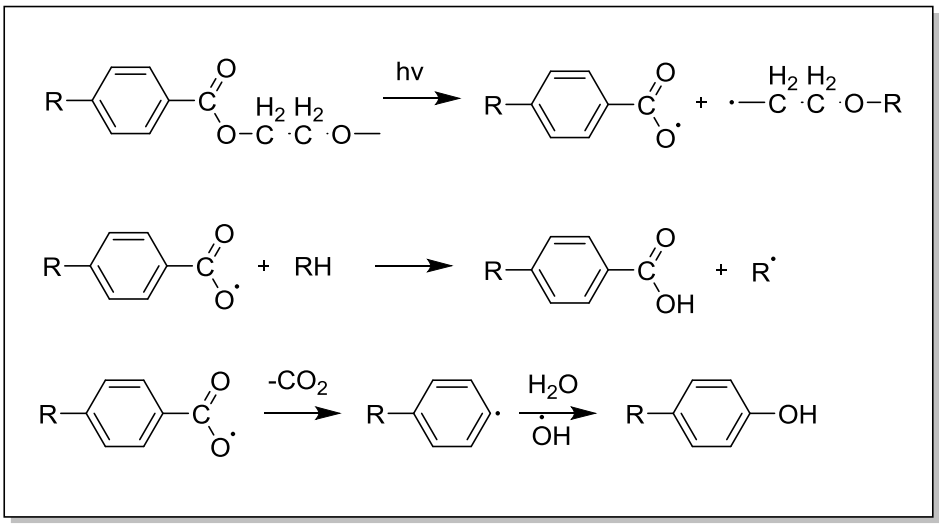

Figure 3.21 Cleavage of -O=C-O-C- group by PD (path A) [100]

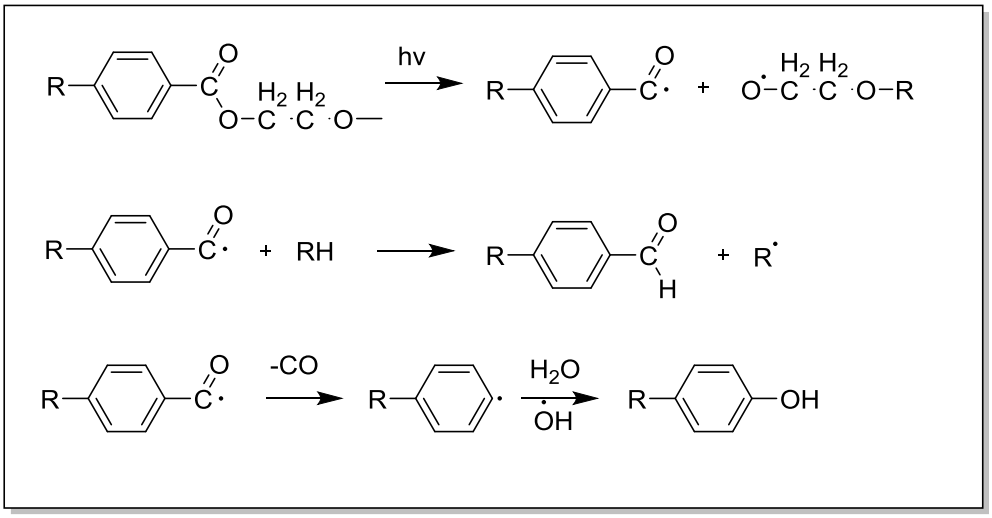

Figure 3.22 Cleavage of -O=C-O-C- group by PD (path B) [100]

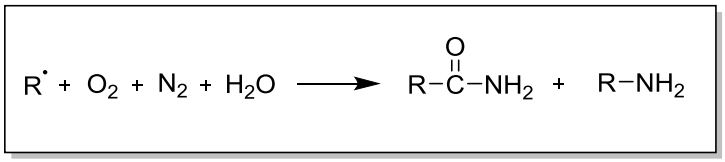

Figure 3.23 Reactions with nitrogen and oxygen [33]

DSC and FTIR results have proven that even the samples are all Mylar®A films, they do show considerable differences in morphology probably due to different draw ratios in both machine direction (MD) and transverse direction (TD) in manufacturing processes. Calorimetric and FTIR data show that the 100 and 125 μm samples have the highest crystallinity degrees among the samples, furthermore, DSC data also suggest that thickest lamellae structures and highest crystal perfection were present in the 100 and 125 μm. Quantitative analyses were carried out by using ATR-FTIR, XPS and surface profilometers to understand the effect of morphology and thickness further. It is found that samples with thicker lamellae structure, higher crystal perfection and crystallinity degree will have a better PD resistance in terms of degree of polymer backbone cleavage, amount of generated degradation by-products and physical erosion depth. As is well known, microvoids, in addition to the free volume, are inevitable in polymers and they usually appear in the amorphous regions of the materials. The permittivity of the crystalline regions should be higher than that of the amorphous regions, making electrical discharge concentrate more

on the crystalline regions. Hence, the thicker lamellae structure and higher crystal perfection degree will provide a better PD resisting ability than the thinner lamellae structure.

PD lifetime experiments were carried out to study the thickness effect of PD-induced breakdown behaviour. It is evident from the data that for the samples no thicker than 190 μm, the PD lifetime of the samples will have a linear relation with sample thickness on log-log scales. However, for the thicker samples, 250 μm and 300 μm namely, the PD lifetime of the samples are much less than the ideal condition, as can be seen from figure 3.18. This phenomenon could be explained by two aspects: first of all, the 250 μm and 300 μm have the thinnest lamellae structures among all the samples, making them most susceptible to PD degradation compared with the other samples, which have been proven both chemically and physically. Secondly, it can be expected that for a thicker sample, a larger void is more likely to exist in the polymer, hence the probability of internal discharge occurrence inside the polymer is higher, which will undoubtedly accelerate the PD degradation rate.

Chapter Four

4.Fillers and additives effect on PD degradation of PET

4.1 Introduction

Pigments, fillers and performance additives are usually utilized to modify and improve properties of polymers such as aesthetic appearance, mechanical, physical and electrical properties. Thanks to the excellent properties compared to the neat resin, polymer composites, especially nanocomposites, have drawn more and more attention in almost every field of our daily life such as food packaging, architecture, coatings, medical services and of course, electrical engineering [110]. According to T. Tanaka [114], in fact, the history of polymer nanocomposites being used as dielectrics is less than only 15 years. Partial discharge (PD) resistance can be significantly enhanced once the polymer was filled with nano-fillers, claimed by M. Kozako [101] firstly in 2004, by using polyamide (PA) as the basic resin and layered silicate as the nano-fillers, respectively. Afterwards, much work has been done to investigate the inorganic filler effect on PD as well as electrical treeing resistance of epoxy resin and polyimide [102-120]. The fillers mainly used were layered silicate, TiO_2, SiO_2 and Al_2O_3. Regardless the used filler type, all the results have shown that even with a small amount of fillers, the PD resistance of the polymer composites can be considerably improved compared to the neat resin.

In order to study the fillers and additives effect on PD degradation and breakdown of PET, five kinds of PET films filled with different additives namely, pure

PET, PET filled with TiO_2, PET filled with $BaSO_4$ (with and without UV stabilizer) and PET filled with phosphorus based flame retardant, were subjected to PD. It was surprisingly found that although the samples blended with inorganic fillers ($BaSO_4$ and TiO_2) showed best PD resistance, the sample functioned with phosphorus base flame retardant had the longest PD lifetime under the identical exposure conditions.

Various analytical methods were used to investigate the eroded sample surface, it was found that direct proportional relationship between the PD resistance and the PD lifetime does not exist, in other words, better PD resistance does not necessarily means longer PD lifetime. However, the PD lifetime has been proven to relate closely to the Erosion Depth At Breakdown (EDAB). Two different mechanisms of prolonged PD lifetime of the filled samples will be discussed in detail in this chapter.

4.2 Experimental

4.2.1 Samples

Five categories of biaxially oriented, semicrystalline PET films filled with different pigments and performance additives provided by Dupont Teijin Films and Mitsubishi Polyester Film were used to investigate the effect of fillers and additives on PD degradation and breakdown of PET films. All the samples have identical thickness of 50µm. Each sample category is described as below:

1. Universal PET without any additive used as a reference (PET).
2. PET filled with 18% $BaSO_4$ particles (PET- $BaSO_4$).
3. PET filled with 18% $BaSO_4$ particles and functioned with 1.0% Tinuvin 1577 UV stabilizer (PET-$BaSO_4$-UV).
4. PET filled with 13% TiO_2 particles (PET-TiO_2).
5. PET functioned with phosphorus based flame retardant which is chemically grafted to the PET chain (PET-FR).

4.2.2 Experimental set-up of partial discharge and breakdown tests

Two sets of experiments were carried out to investigate the additives effect on PD degradation and breakdown behaviours of PET films. The sample holders for the both sets have already been shown in chapter 2 (figure 2.2 and figure 2.3). The pre-experimental sample treatments and experimental environment conditions are the same as describe in 3.2.2 of chapter 3.

4.2.2.1 Experimental set-up for PD tests

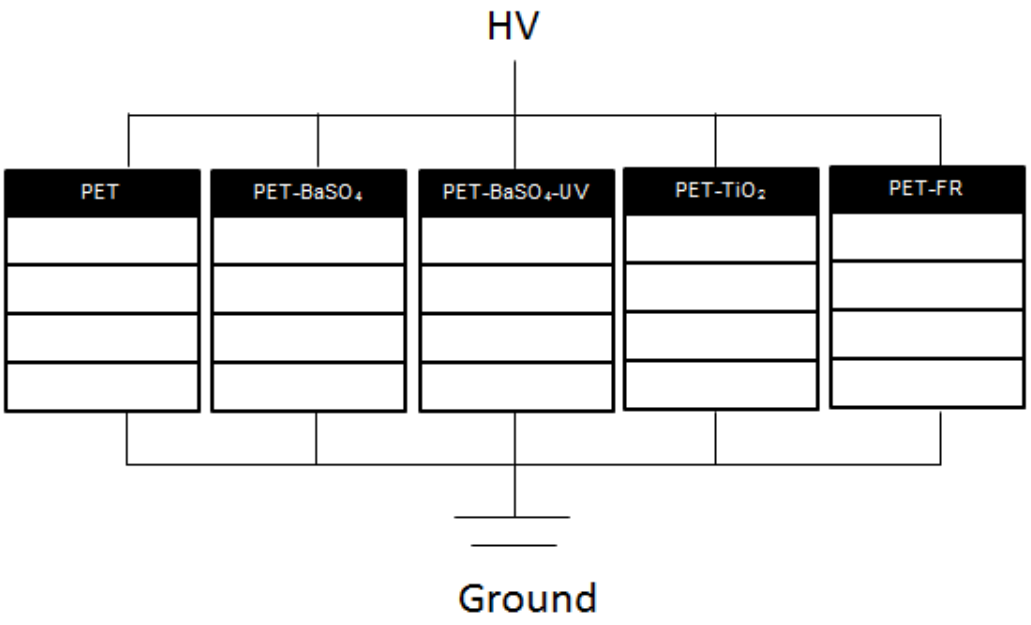

Figure 4.1 Schematic of set-up for samples with different additives

For the samples with different additives, five sample stacks with identical thickness (250 µm) were subjected to a 50 Hz AC high voltage of 3 kV for 12, 24 and 48 hours. The structure of each stack is shown in figure 4.1. After PD exposure, samples on the top layer of each stack (black block in figure 4.1) were removed for further analysis.

4.2.2.2 Experimental set-up for PD-lifetime test

The schematic of set-up for breakdown tests due to PD erosion has been shown in 3.2.2.2 of chapter 3. Single sheet of samples with different additives were subjected to a 50 Hz AC high voltage of 3 kV until the sample breakdown due to PD erosion. For each sample category, at least five samples were tested and the average values of the PD lifetime of each category were calculated.

4.2.3 Experimental of analytical methods for sample characterisation

All the analytical methods for sample characterisation have been introduced in chapter 2 and 3 already.

4.3 Results and discussions

4.3.1 Partial discharge lifetime analysis

PD lifetime experiments were firstly conducted for each kind of sample to compare the high voltage endurance of samples under the same conditions. The results are illustrated in figure 4.2, obviously the PD lifetime of each sample in this case are in the ranking of PET-FR >> PET-$BaSO_4$-UV > PET-TiO_2 > PET-$BaSO_4$ > PET, with the lifetime of PET-FR being much longer than that of the other samples and about four times as long as that of the pure PET.

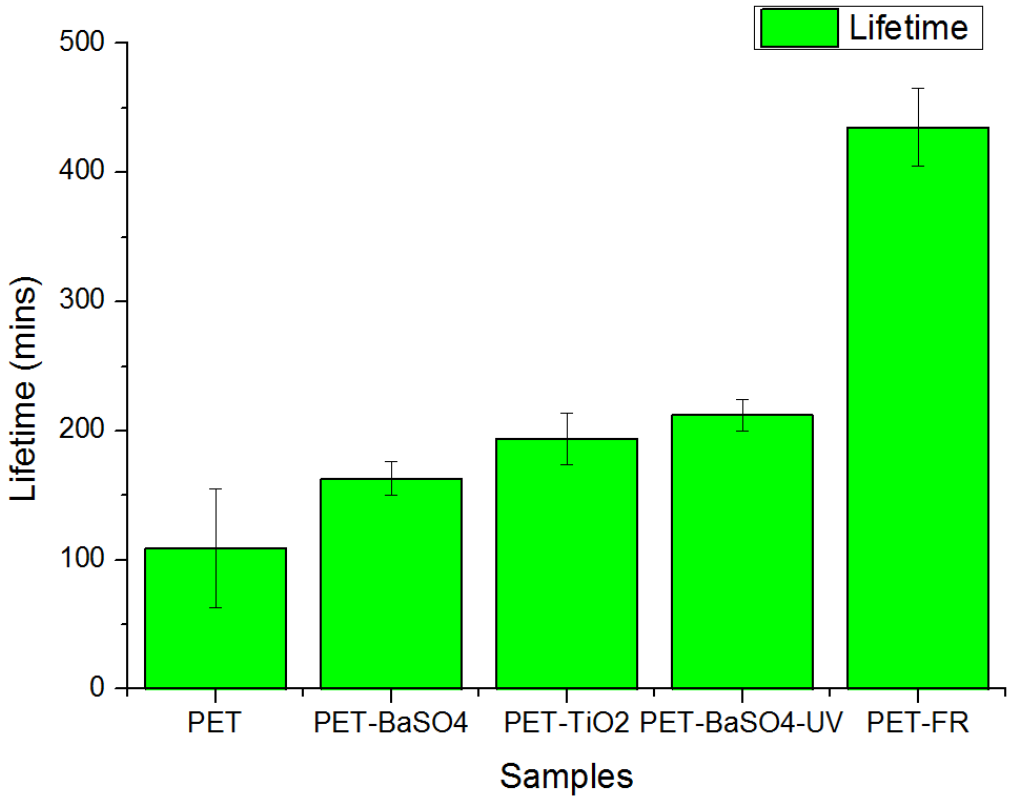

Figure 4.2 PD lifetimes of samples with different additives

4.3.2 Surface profilometer analysis

PD tests were then carried out using the experimental set-up in figure 4.1 to analyse the PD resistance of each kind of sample, samples on the top layer of each stack were removed for erosion depth and surface chemistry analysis after certain level of PD exposure. The erosion depth of each sample are shown in figure 4.3, it is clear that pure PET without any additive, eroded fastest under PD among all the samples while the samples filled with inorganic particles ($BaSO_4$ and TiO_2) have the best PD resistance. Further, it is very interesting to note that although having the longest PD lifetime, the PD resistance of PET-FR is far worse than expected — its PD resistance is only better than the pure PET and much worse than those samples filled with inorganic fillers. Obviously the enormous PD lifetime of PET-FR cannot be attributed to the PD resistance ability in this case, there must be some other mechanisms and explanations for the PET-FR, which will be discussed in detail later.

In order to study the relation between the PD lifetime and erosion depth further, the Erosion Depths At Breakdown (EDAB) were measured for those broken down samples that were already mentioned in 4.3.1. The EDAB is defined as the maximum erosion depth caused by PD that one sample can withstand before the breakdown occur. For each sample, five scans (avoid the breakdown point) in different directions across the sample surface were measured and the average value of the erosion depths was taken as the final result for that particular sample. The EDAB results of the samples are displayed in figure 4.4, it can be seen that EDAB and PD lifetime of samples follow exactly the same trend, i.e., PD lifetime of one sample is directly proportional to its EDAB. Discussions about how PD resistance and EDAB will influence the PD lifetime of one sample will be given later in this chapter.

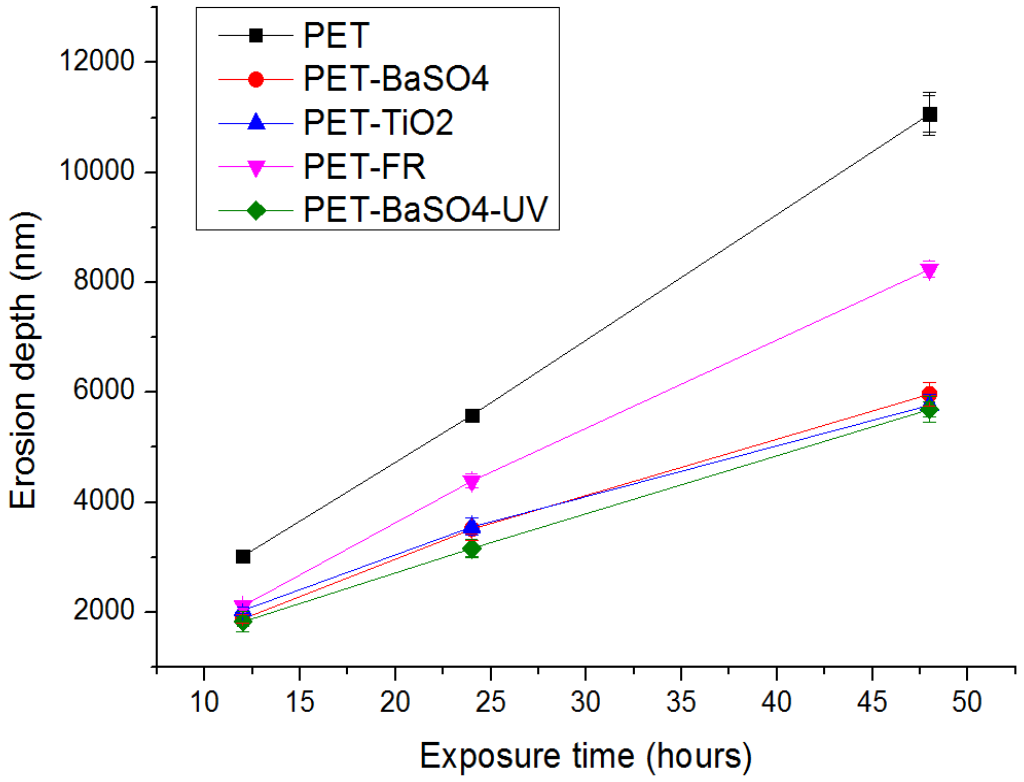

Figure 4.3 PD erosion depths of the samples exposed for 12, 24 and 48 hours

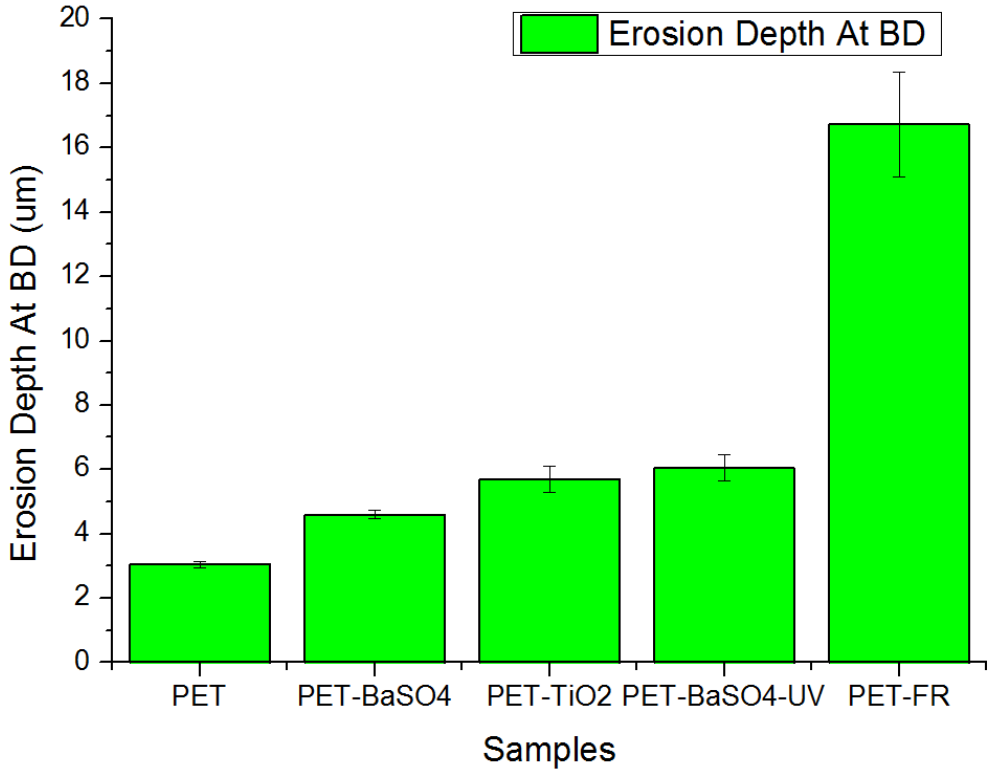

Figure 4.4 Erosion Depth At Breakdown (EDAB) of the samples

4.3.3 DSC analysis

The DSC traces of the first heating scans of samples with different additives are shown in figure 4.5. The main features of the DSC traces of the samples are listed in the Table 4.1. It can be seen that the DSC characteristics of PET-FR is quite different from the others, its melting point T_m and crystallinity degree X_c% are both much lower than that of the other samples, suggesting most parts of PET-FR are amorphous. Actually this is a common phenomenon which could happen in phosphorus-containing flame retardant copolyester [123-125]. The lower crystallinity degree of the sample can be attributed to the presence of bulky P-containing pendant group in the molecular chain, which can hinder the packing of the polymer chain [123-125].

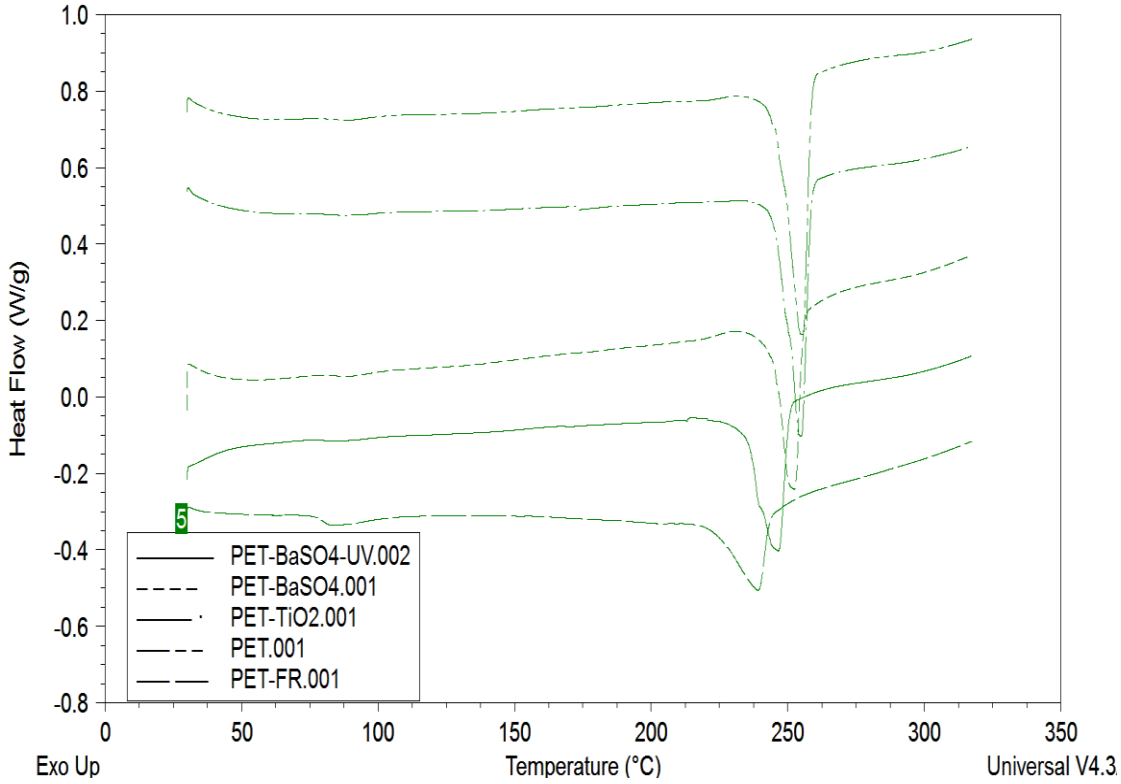

Figure 4.5 DSC first heating scans of samples with different additives

Samples	T_g(°C)	T_m(°C)	ΔH_m(J/g)	X_c%
PET	83.4	255.4	39.1	27.93
PET-TiO2	80.9	254.8	37.76	26.97
PET-$BaSO_4$	83.9	252.5	28.3	20.21
PET-$BaSO_4$-UV	80.8	246.6	32.7	23.36
PET-FR	79.9	239.1	16.73	11.95

Table 4.1 Main features of the DSC traces of samples with different additives

4.3.4 FTIR and XPS analysis

PET

Typical FTIR and XPS results and data analyses for universal biaxially-oriented PET films have been discussed in detail in chapter 3.

PET-$BaSO_4$ and PET- $BaSO_4$-UV

Untreated samples

The comparison of the ATR-FTIR spectra of PET and PET-$BaSO_4$ is illustrated in figure 4.6, here only IR spectra between 920 and 1360cm^{-1} are shown since the only differences between these two spectra lie in this region. Compared to the IR spectrum of pure PET, four additional absorption peaks can be observed at 1188, 1120, 1072 and 983 cm^{-1} for the PET-$BaSO_4$ spectrum. The three peaks at 1188, 1120 and 1072 cm^{-1} are attributed to the S-O stretching of the inorganic filler $BaSO_4$, while the peak at 983cm^{-1} can be attributed to the symmetrical vibration of SO_4^{2-} [127]. No other absorption peak shifts or changes can be observed for these two spectra.

The IR spectra of PET-$BaSO_4$ and PET-$BaSO_4$-UV are almost the same apart from an additional peak at 1530cm^{-1} is observed for PET-$BaSO_4$-UV, as shown in figure 4.7, this peak is due to the in-plane ring vibration of the triazine ring system in the Tinuvin 1577 UV stabilizer [128], whose chemical structure is shown in figure 4.8.

The results of XPS survey and higher resolution scans of C1s and O1s of pure PET sample have already been shown in figure 2.13, 2.14 and 2.15, respectively in chapter 2. For PET-$BaSO_4$ and PET-$BaSO_4$-UV, no absorption peak shifts can be observed in either C1s or O1s spectra (spectra not shown in here). It is also worth pointing out that only elements of carbon and oxygen are present, i.e., barium or sulphur cannot be detected in the survey for the untreated samples of PET-$BaSO_4$ and PET-$BaSO_4$-UV, possibly due to the short sampling depth of XPS (usually only a few nm, may not be deep enough to reach the inorganic fillers dispersed in the resin).

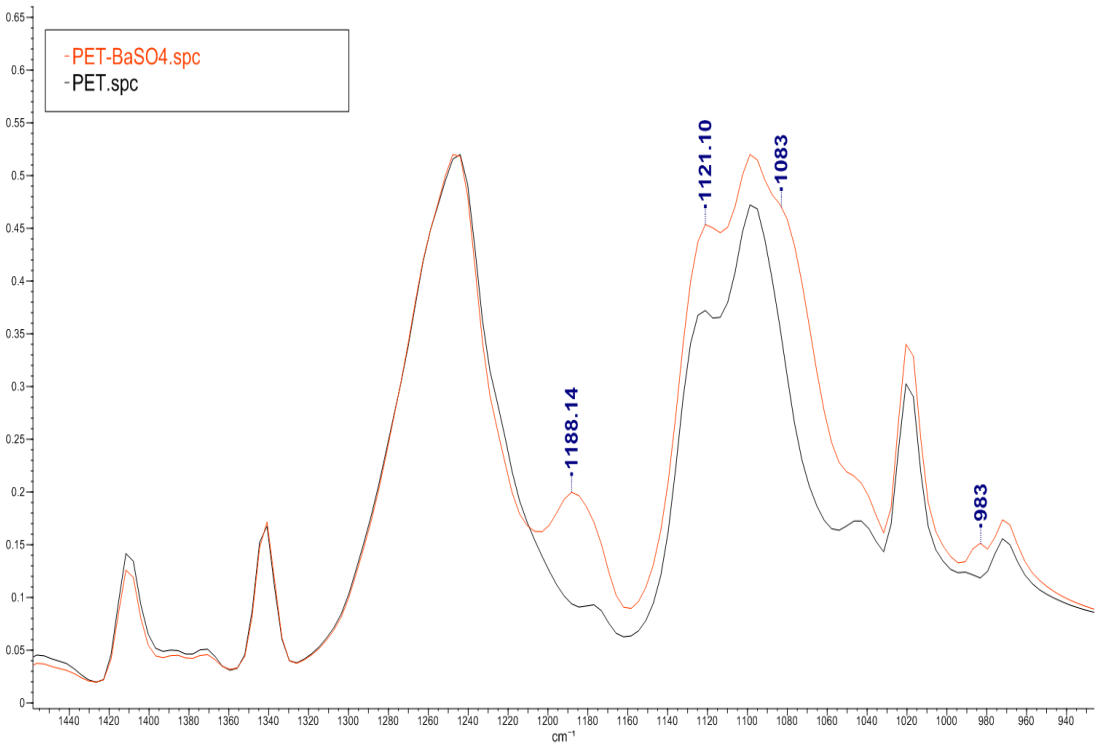

Figure 4.6 Overlaid spectra of PET and PET-$BaSO_4$

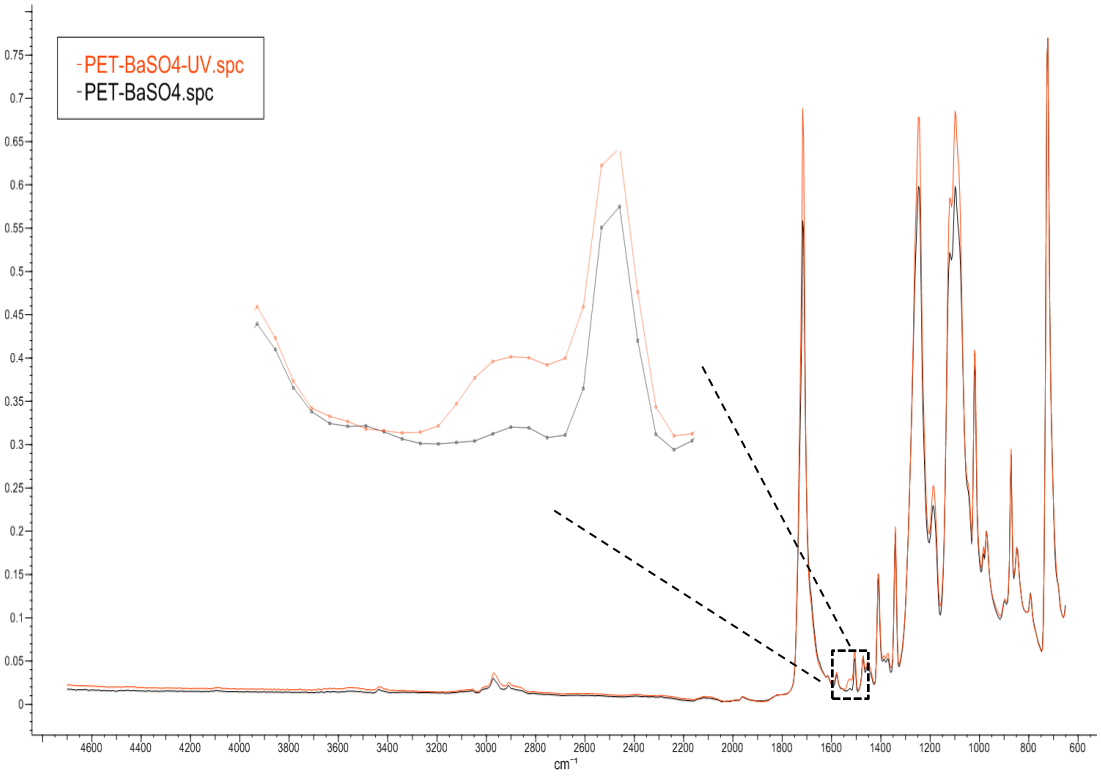

Figure 4.7 Overlaid spectra of PET-$BaSO_4$ and PET-$BaSO_4$-UV

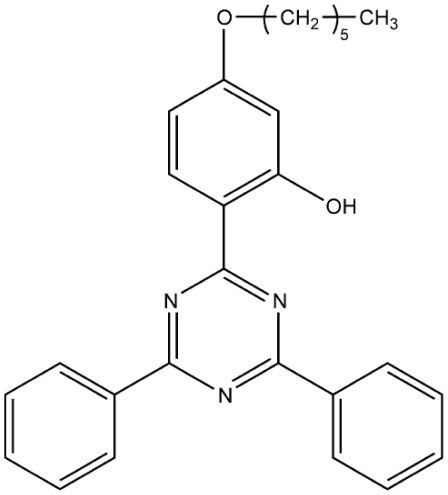

Figure 4.8 Chemical structure of Tinuvin 1577 in PET-$BaSO_4$-UV [126]

PD exposed samples

ATR-FTIR spectra of PET-$BaSO_4$ subjected to PD exposure for 0, 12, 24 and 48 hours are illustrated in figure 4.9, only spectra of PET-$BaSO_4$ are shown in here due to the extremely high similarity of the spectra of PET-$BaSO_4$ and PET-$BaSO_4$-UV (spectra of PET-$BaSO_4$-UV are shown in figure A.1 of appendix A). Obvious trends can be observed from the figure — the intensity of the band at 1245 cm^{-1}, which is due to the =C–O stretching in the ester group [91] decreased as the PD exposure time went on, on the other hand, the intensities of the main characteristic bands of $BaSO_4$ at 1188, 1072 and 983 cm^{-1} increased. This is the direct evidence of the accumulation process of the fillers $BaSO_4$ on the sample surface as PD exposure time increase. This so called 'filler pile-up' effect was also well discussed in the literature [103-105, 119]. Since the PD resistance of the inorganic fillers are much higher than that of the polymer, the originally embedded fillers will remain on the sample surface while the polymer is decomposing due to the PD degradation.

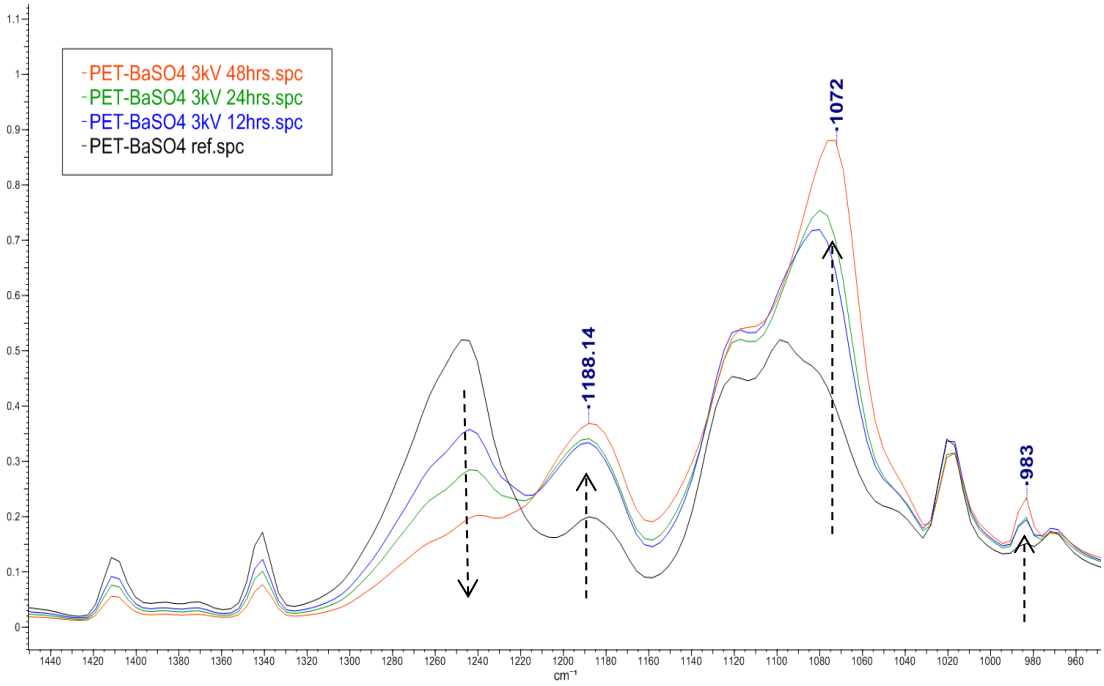

Figure 4.9 Overlaid ATR-FTIR spectra of PET-$BaSO_4$ subjected to PD for 0, 12, 24 and 48hrs

A series of XPS data of PET-$BaSO_4$ after 24 hours of PD exposure are shown in figure 4.10 – 4.13. For the same reason just mentioned above, only spectra of PET-$BaSO_4$ are shown for these figures. Figure 4.10 shows the XPS survey of PD exposed PET-$BaSO_4$ (the XPS survey data of PD exposed PET-$BaSO_4$-UV can be found in figure A.2 of appendix A), the spectrum become much more complicated compared to the data of untreated PET (figure 2.13) due to the presence of barium and sulphur peaks. The atomic concentration of each element present on the surface of the two samples are listed in table 4.2 (data of samples subjected to 3kV for 0, 12 and 24 hours are present), from the results it can be seen more quantitatively how the fillers $BaSO_4$ accumulate on the PD treated sample surface. It is also seen that both concentrations of barium and sulphur are nearly identical for the two samples for both exposure time of 12 and 24 hours, however, the concentrations of oxygen are higher for PET-$BaSO_4$ in both conditions, indicating that surface oxidation are more severe for PET-$BaSO_4$ than PET-$BaSO_4$-UV, possibly due to the presence of UV stabilizer in PET-$BaSO_4$-UV which could hinder the oxidation and UV degradation caused by the PD.

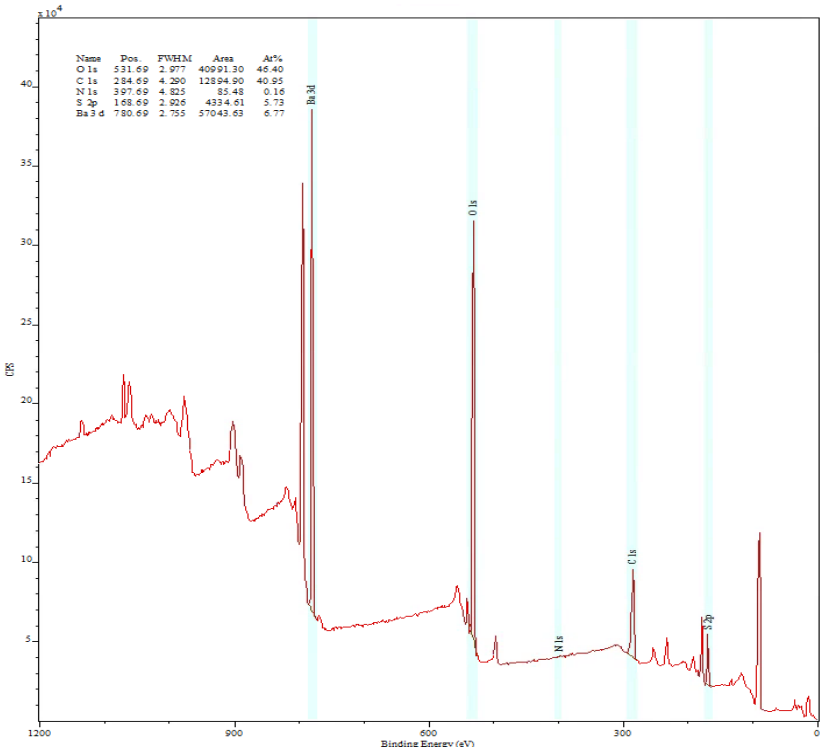

Figure 4.10 XPS survey of PET-$BaSO_4$ subjected to PD for 24 hrs

Samples	O1s (%)	C1s (%)	Ba3d (%)	S2p(%)	N1s(%)
Untreated	24.44	75.56	0	0	0
PET-$BaSO_4$ 12hrs	41.89	49.27	4.53	4.11	0.21
PET-$BaSO_4$-UV 12hrs	39.81	51.66	4.30	3.82	0.40
PET-$BaSO_4$ 24hrs	46.40	40.95	6.77	5.73	0.16
PET-$BaSO_4$-UV 24hrs	43.84	43.87	6.51	5.41	0.38

Table 4.2 XPS survey results of PET-$BaSO_4$ and PET-$BaSO_4$-UV

Overlaid O1s and C1s spectra of the untreated and PD exposed PET-$BaSO_4$ are shown in figure 4.11. In the O1s spectrum (left one), one can see that the original

doublet became one strong featureless peak at 531.5eV after PD treatment. For the C1s spectrum (right one), the intensities of all the carbon peaks decreased dramatically after PD exposure. It should be note that after PD exposure spectra became broad and shoulders in lower binding energy regions can be observed for both spectra, suggesting the formation of new peaks. The peak fitting results of both the O1s and C1s spectra of PD exposed PET-$BaSO_4$ are shown in figure 4.12 and 4.13, respectively. For the O1s spectrum, the peak B at 533.2eV is attributed to the oxygen atom O-C=O in PET, whose peak area is relatively small because of the presence of inorganic fillers and PET degradation. The biggest peak A at 531.6eV can be attributed to the oxygen atom O-C=O in PET and, the oxygen atom of the $–SO_4$ group in $BaSO_4$ [129-130]. Since these two peaks are highly superimposed, it is almost impossible to separate them individually. A new peak C appears as a shoulder locating at 530.2eV can be assigned to the presence of barium oxide, i.e., BaO, which could be the decomposition product of $BaSO_4$ when the temperature is as high as 1580°C [131]. According to T. Tanaka [119], even a tiny PD can raise the local temperature near the solid surface up to 1000°C for a very short period (0.1μs), hence it is not surprising that BaO could be detected on the sample surface in this case. For the C1s spectrum (figure 4.13), the three peaks locating at 284.8, 286.7 and 288.7eV are assigned to the carbon atom in C-(C,H), C-O and O=C-O in PET, respectively. Here in figure 4.13, the relative area of peak B at 286.7eV increase a bit after PD exposure, this could possibly be due to the adventitious carbon attached to the $BaSO_4$ surface. A new peak D appears at 288.0eV can be assigned to barium carbonate $BaCO_3$ since metal carbonates are usually observed on metal oxides (BaO in this case) [136]. Further, another newly generated peak E as a shoulder at 283.5eV can be attributed to the formation of barium carbide BaC_2 [132], which could be generated from barium oxide under the condition of local high temperature and electrical discharge like many other carbides.

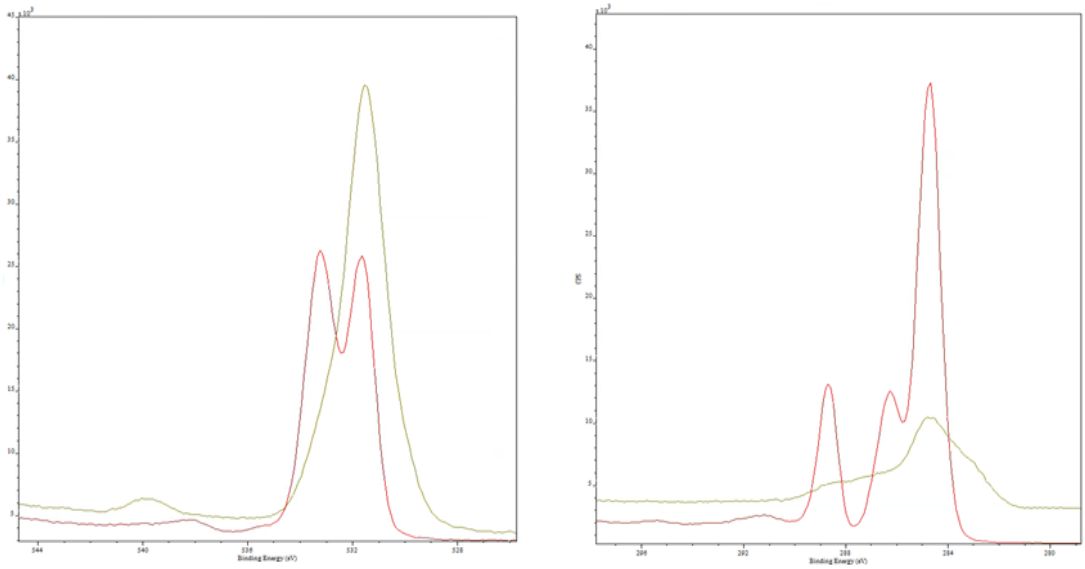

Figure 4.11 Overlaid O1s and C1s spectra of PET-$BaSO_4$ before (red) and after (green) PD exposure

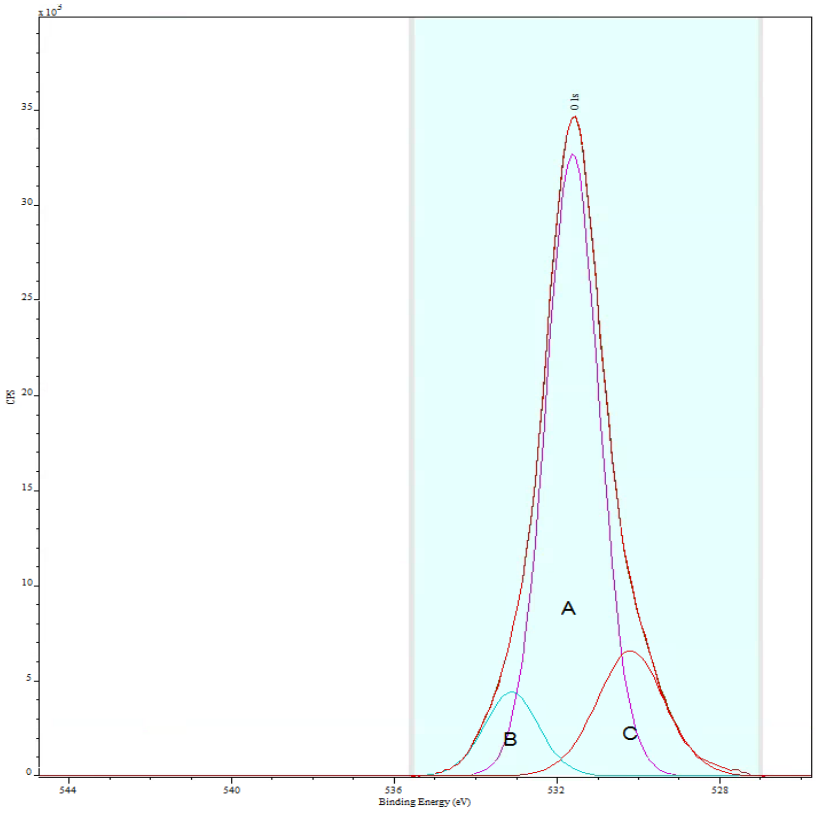

Figure 4.12 Deconvolution of O1s spectrum of PD exposed PET-$BaSO_4$

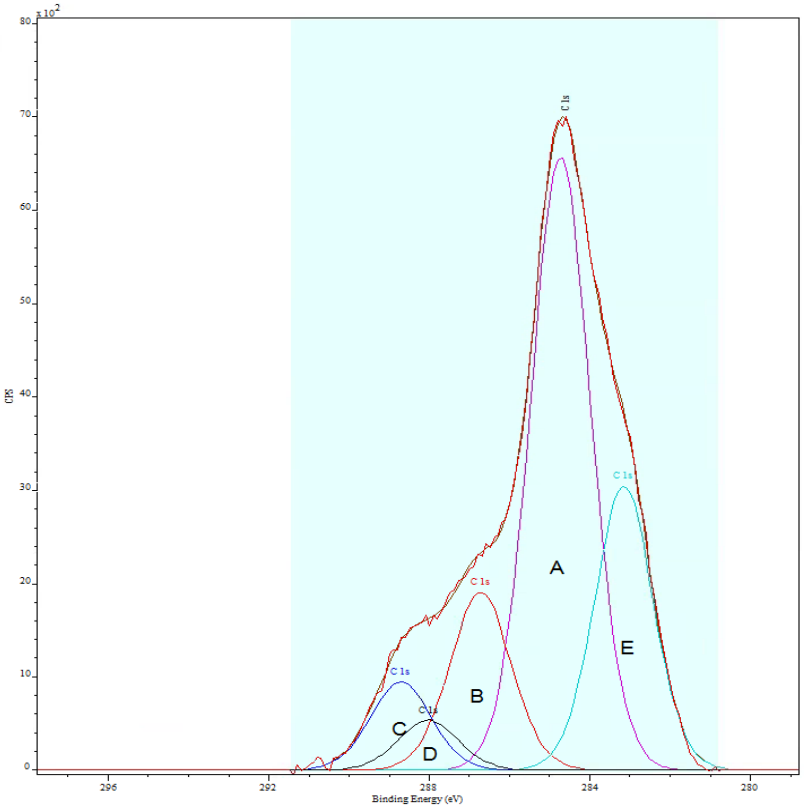

Figure 4.13 Deconvolution of C1s spectrum of PD exposed PET-$BaSO_4$

PET-TiO_2

Untreated samples

Figure 4.14 represents the overlaid ATR-FTIR spectra of PET and PET-TiO_2, only IR spectra between 650 and 940 cm^{-1} are shown here since the only differences between these two spectra lie in this region. A wide absorption band is observed in the wavenumber region lower than 800 cm^{-1} for PET-TiO_2, as shown in figure 4.14. This wide band can be assigned to the vibration of Ti-O of the TiO_2 fillers [133]. No other absorption peak shifts or changes can be observed for these two spectra.

Since no additional peaks or peak shifts can be observed compared to the data of pure PET, XPS data of untreated PET-TiO_2 will not be shown in here. Similar to the case of PET-$BaSO_4$ (PET-$BaSO_4$-UV), only elements of carbon and oxygen are present in the XPS survey of PET-TiO_2 due to the short sampling depth of XPS method.

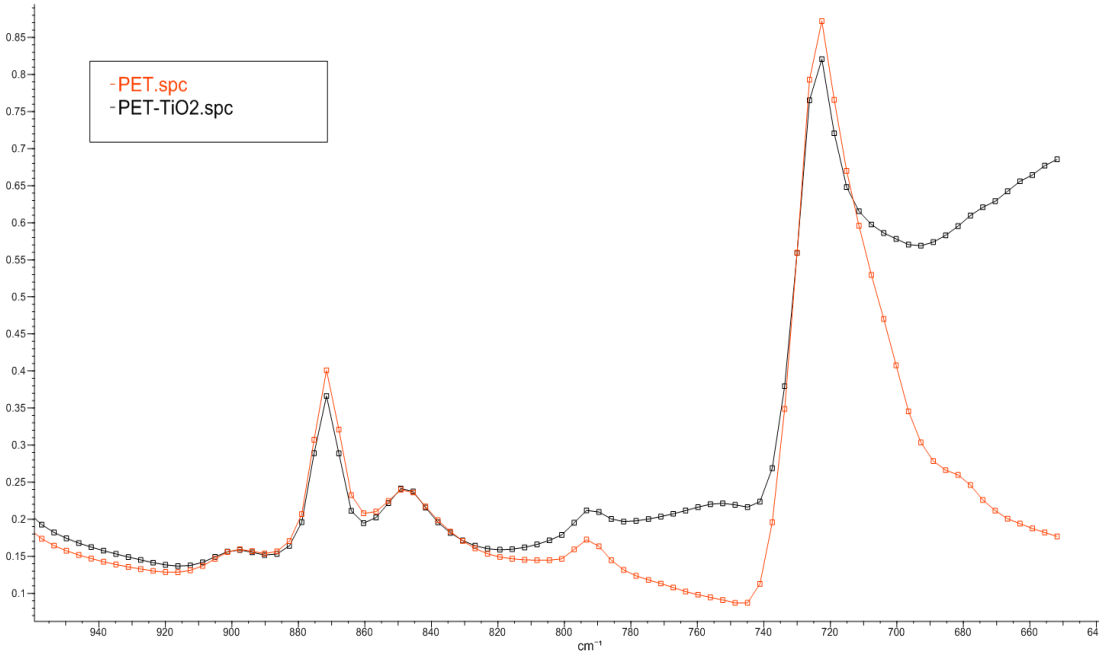

Figure 4.14 Overlaid spectra of PET and PET-TiO_2

PD exposed samples

Figure 4.15 shows the ATR-FTIR spectra of PET-TiO_2 after receiving PD exposure for 0, 12, 24 and 48 hours. It is clear that the characteristic absorption band of TiO_2, locating in the wavenumber region lower than 800 cm^{-1}, increased as the PD exposure time increased, indicating the 'pile-up' phenomenon of the TiO_2 fillers on the PD exposed samples, similar as PET-$BaSO_4$ (PET-$BaSO_4$-UV) that mentioned before.

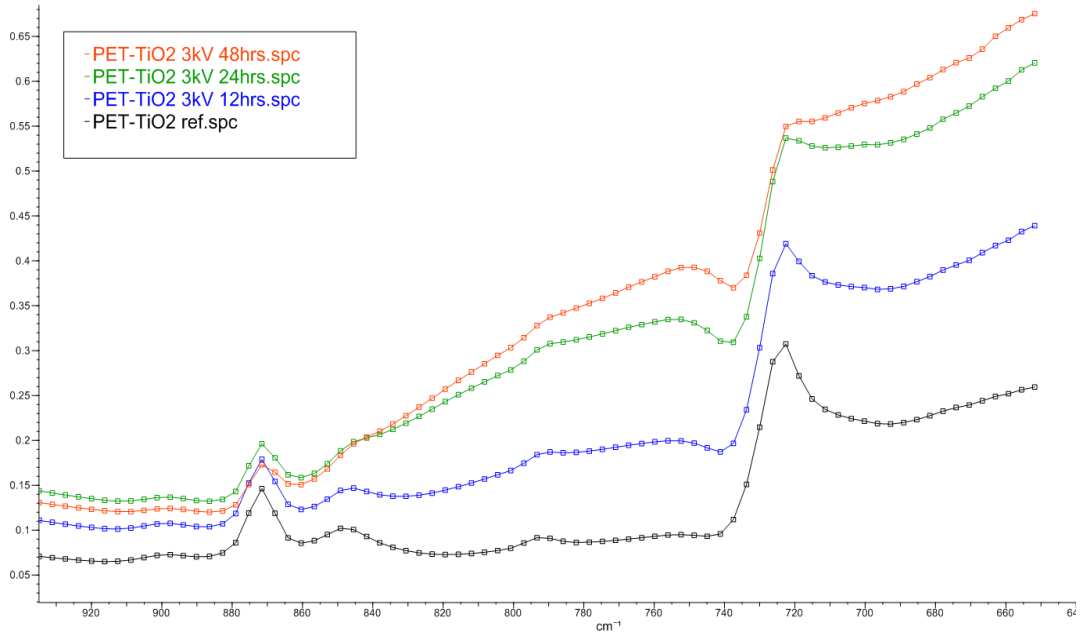

Figure 4.15 Overlaid ATR-FTIR spectra of PET-TiO_2 subjected to PD for 0, 12, 24 and 48hrs

The XPS survey of PD exposed PET-TiO_2 is given in figure 4.16, one can see that except for the big absorption peaks at 458.7 and 464.6eV which are due to Ti 2p, a series of peaks with small magnitudes can be seen in the region where binding energy (BE) is lower than 200eV. These tiny peaks are identified as Si 2p, Al 2p and P 2p. It is known that commercial TiO_2 will always have an inorganic coating such as aluminosilicate to provide the UV protection functionality [121], and elements like phosphorus and sodium could present on the surface of the aluminosilicate [135]. The atomic concentrations of each element present on the sample surface are listed in table 4.3 (data of samples subjected to 3kV for 0, 12 and 24 hours are present).

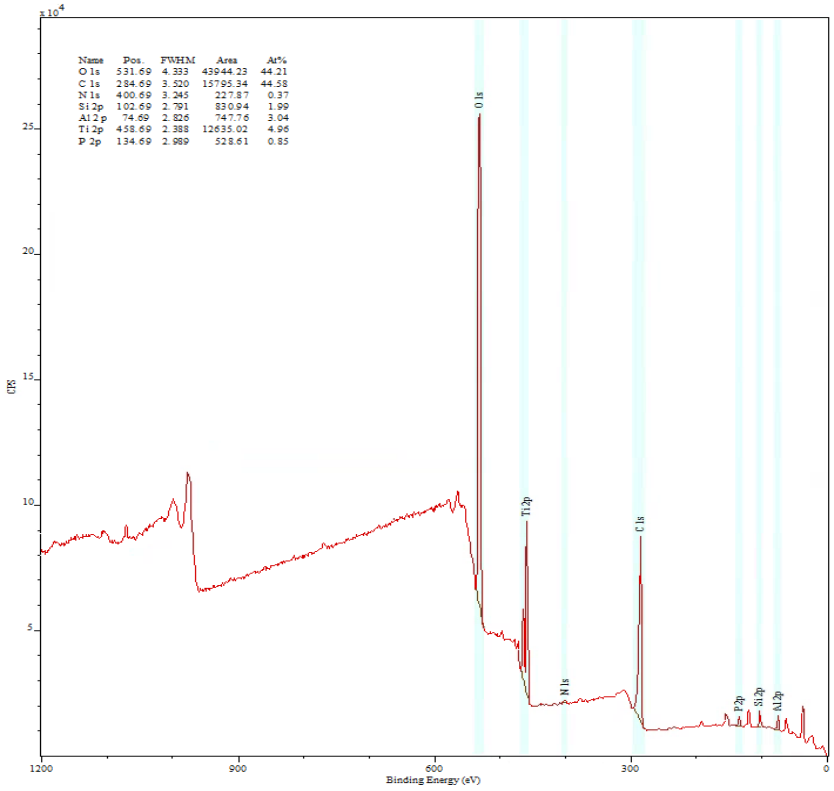

Figure 4.16 XPS survey of PD exposed PET-TiO_2

Samples	O1s	C1s	N1s	Si 2p	Al 2p	Ti 2p	P 2p
Untreated	24.44	75.57	0	0	0	0	0
PET-TiO2 12hrs	37.06	56.18	0.34	1.09	1.97	2.83	0.53
PET-TiO2 24hrs	44.21	44.58	0.37	1.99	3.04	4.96	0.85

Table 4.3 XPS survey results of PET-TiO_2

Overlaid O1s and C1s spectra of untreated and PD exposed PET-TiO_2 are illustrated in figure 4.17, one can see that in the O1s spectrum (left one), the original O1s doublet of PET turn into one strong band and the peak position shifts from 531.5 to 532.0eV after the samples were PD exposed. Furthermore, a distinct new peak is now observed at 529.8eV. For the C1s spectrum (right one), it can be seen that the intensities of all the C1s peaks drop significantly after PD degradation due to the filler 'pile-up' effect. The peak fitting results of both the O1s and C1s spectra

of PD exposed PET-TiO_2 are shown in figure 4.18 and 4.19, respectively. In figure 4.18, the strongest band A whose peak position is at 532.0eV is considered to be the superimposition of the peak at 531.5eV due to the oxygen atom O-C=O in PET and the peak at 532.0eV due to the presence of OH groups attached to the TiO_2 filler surface. The peak B is attributed to the oxygen atom O-C=O in PET. The distinct new peak C at 529.7eV can be assigned to the oxygen atom Ti-O in the TiO_2 lattice [134]. In the C1s spectrum shown in figure 4.19, the three main characteristic C1s peaks A, B and C for PET are still well defined, in addition, a new peak D at 287.5eV is observed, which could possibly due to the organic additives on the TiO_2 surface [121].

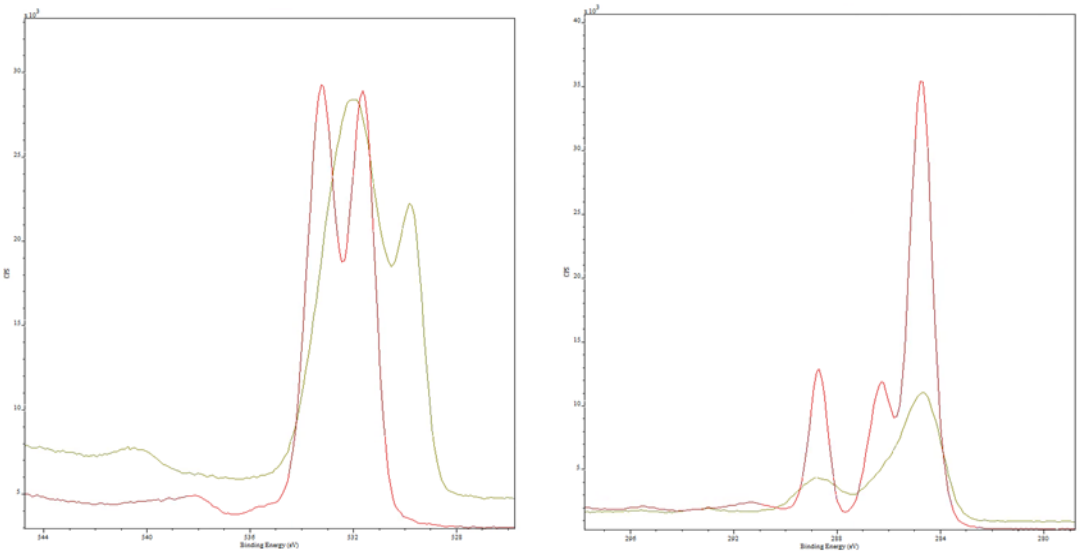

Figure 4.17 Overlaid O1s and C1s spectra of PET-TiO_2, before (red) and after (green) PD exposure

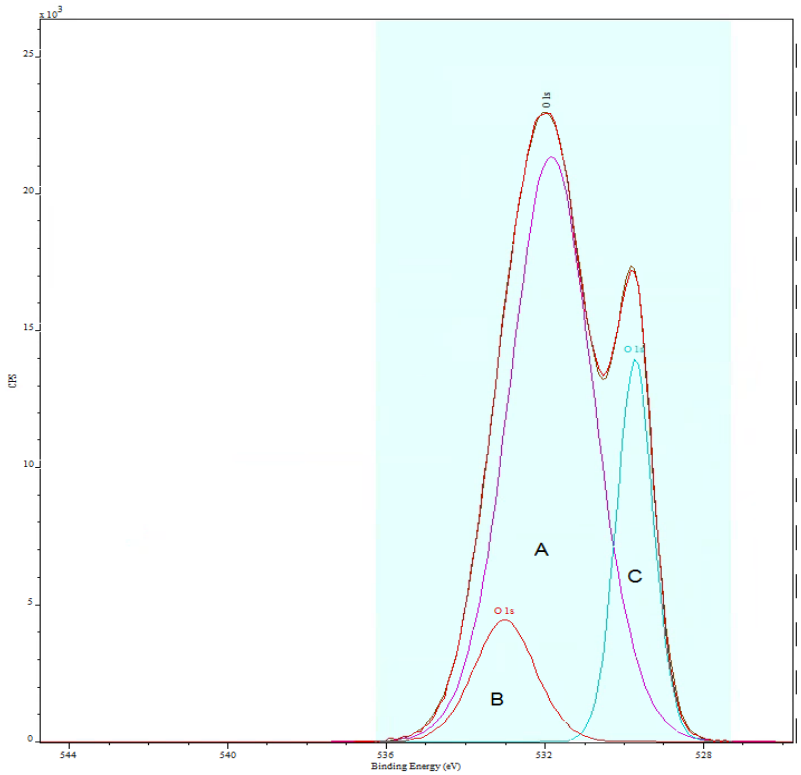

Figure 4.18 Deconvolution of O1s spectrum of PD exposed PET-TiO_2

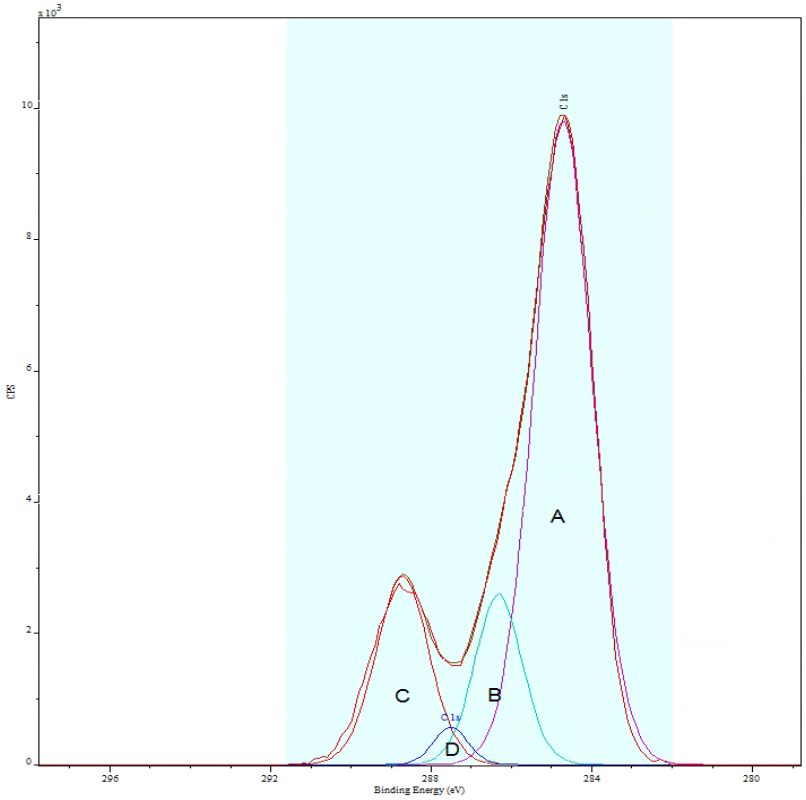

Figure 4.19 Deconvolution of C1s spectrum of PD exposed PET-TiO_2

PET-FR

Untreated samples

The ATR-FTIR spectra of PET and PET-FR (regions between 650 and 1800 cm-^{1}) are shown in figure 4.20. Four new peaks can be observed for the PET-FR at 759, 910, 1205 and 1597 cm^{-1} (all have been labelled in the figure). Since the PET-FR is a phosphorus-containing flame retardant copolyester, the peaks at 759 and 1205 cm^{-1} are attributed to the P-O and P=O stretching, respectively [138]. The absorption band at 910 cm^{-1} corresponds to the P-O-Ph stretching and the small peak at 1597 cm^{-1} is due to the P-Ph vibration [137]. In addition, it should be noted that the absorption ratio of the peaks at 1473 (bending of the glycol CH_2 in crystalline phase) and 1450 cm^{-1} (bending of the glycol CH_2 in amorphous phase) for the PET-FR is much smaller than that of the PET, suggesting the much lower crystallinity degree for the PET-FR, which agrees with the DSC results discussed before in this chapter. The spectrum is consistent with a flame-retardant PET of the type shown in figure 4.21 [183].

Unlike the samples containing inorganic fillers, apart from C 1s and O 1s peaks that belong to the PET resin, additional peak of Phosphorus P 2p can be observed for the XPS survey result of PET-FR (spectrum not shown here), due to the fact that the P-containing flame retardant is chemically grafted to the PET backbone. The peak center of P 2p of the untreated PET-FR locates at 133.2eV, which is assigned to P-O-C groups in the P-containing flame retardant [139].

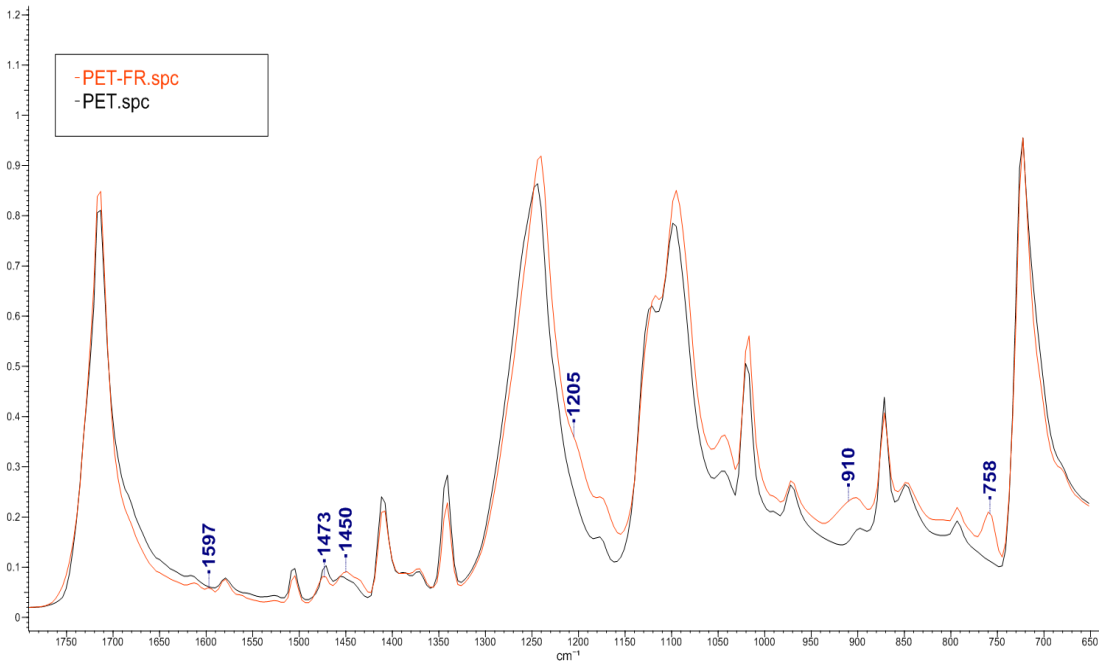

Figure 4.20 Overlaid spectra of PET and PET-FR

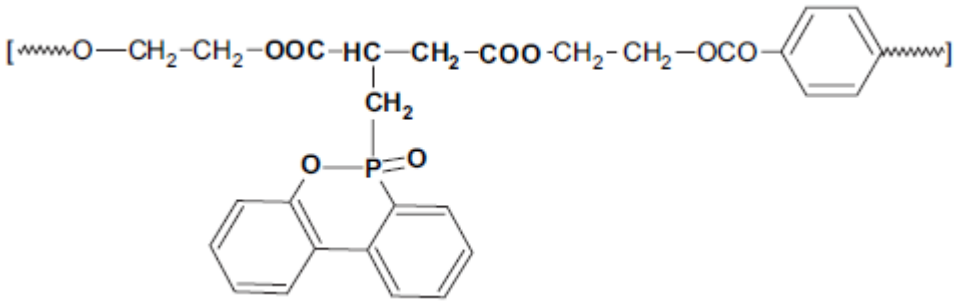

Figure 4.21 Chemical structure of a phosphorus based flame-retardant PET [183]

PD exposed samples

ATR-FTIR spectra of PET-FR subjected to PD exposure for 0, 12, 24 and 48 hours are demonstrated in figure 4.22. Some prominent changes are observed for the PD-treated samples as the degradation time increased. A very broad absorption band at 2600-3700 cm^{-1} is attributed to OH groups stretching. The band at 2160-2500 cm^{-1} is due to P-H vibration. The strong band appears as a shoulder of the original carbonyl peak at about 1665 cm^{-1} can be assigned to the existence of phosphinic

acids [142]. The increase of the band at 1205 cm^{-1} is due to the increment of P=O groups on the sample surface. The sharp increase of the band at 900-1050 cm^{-1} can be assigned to P-OH stretching vibration in O=P-OH groups, further, the general increment of the spectra at 1600-2000 cm^{-1} are also due to the P-OH vibration. From the above FTIR results, it can be concluded that large amount of phosphoric acid H_3PO_4 and phosphorus pentoxide P_2O_5, which are two common substances that can be produced in the oxidative degradation during the burning process of P-containing flame retardant PET [143], were produced during the PD degradation. Moreover, due to the detection of abundant P-H groups (2160-2500 cm^{-1}), it is believed that phosphorous acids and phosphinic acids were also produced during the PD degradation.

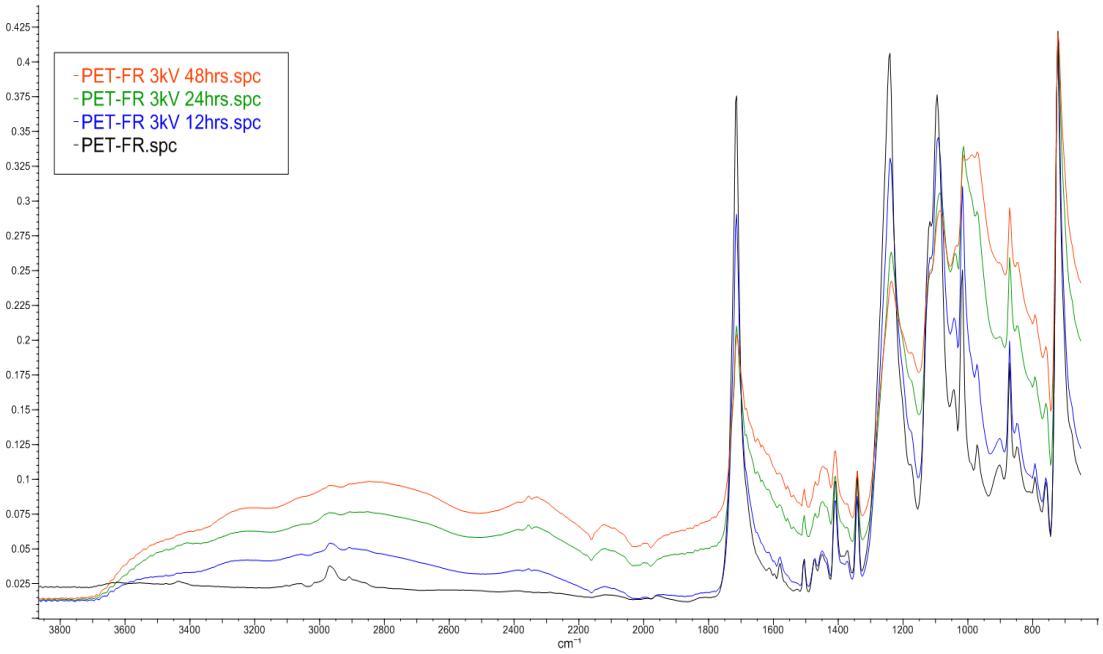

Figure 4.22 Overlaid ATR-FTIR spectra of PET-FR subjected to PD for 0, 12, 24 and 48hrs

XPS data of PD exposed PET-FR samples were shown in figures 4.23-4.25. Since no new absorption peaks could be found for the PD treated samples, the XPS survey data will not be shown in here. Figure 4.23 shows the overlaid P 2p spectra of the untreated and PD exposed PET-FR, one can see that not only the intensity of

the peak dramatically increased, but the peak position shifted from 133.2 to 134.6eV, indicating the large production of phosphate compounds such as phosphoric acid or P_2O_5 caused by PD. Higher resolution scans of O 1s and C 1s spectra of untreated and PD exposed PET-FR are shown in figure 4.24, for the O 1s spectra (left one), it can be seen that the peak intensity greatly enhanced and became featureless after PD degradation. Peak fitting result of the O 1s is given in figure 4.25, the bigger peak A at 533.2eV corresponds to the combination of C-O and P-OH groups, the peak B at 531.9eV is due to the groups of C=O and P=O [139]. The more significant intensity increment of the peak A than the peak B confirms the existence of P-containing acids such as H_3PO_4, H_3PO_3 and H_3PO_2.

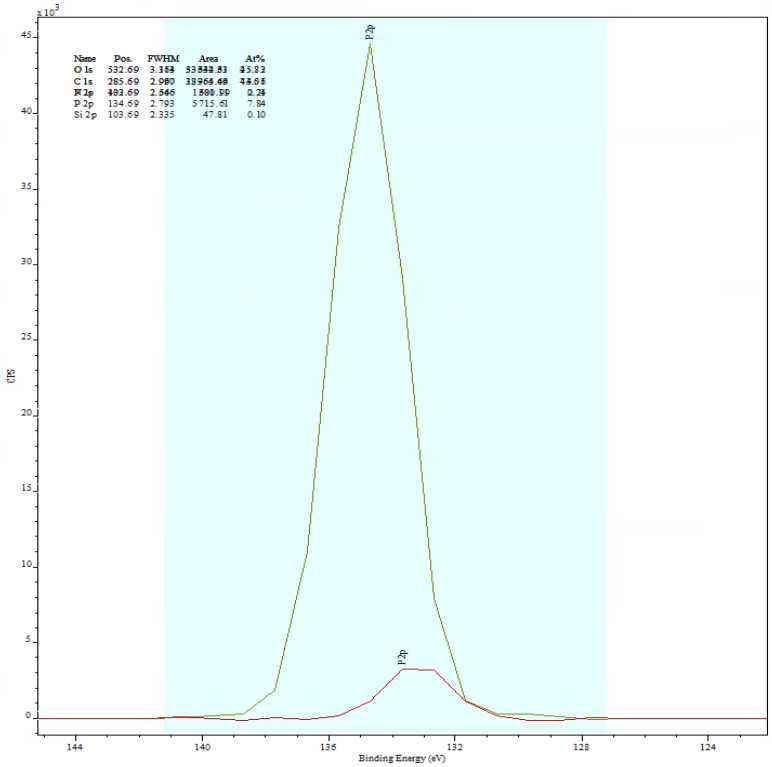

Figure 4.23 Overlaid P 2p spectra of PET-FR, before (red) and after (green) PD exposure

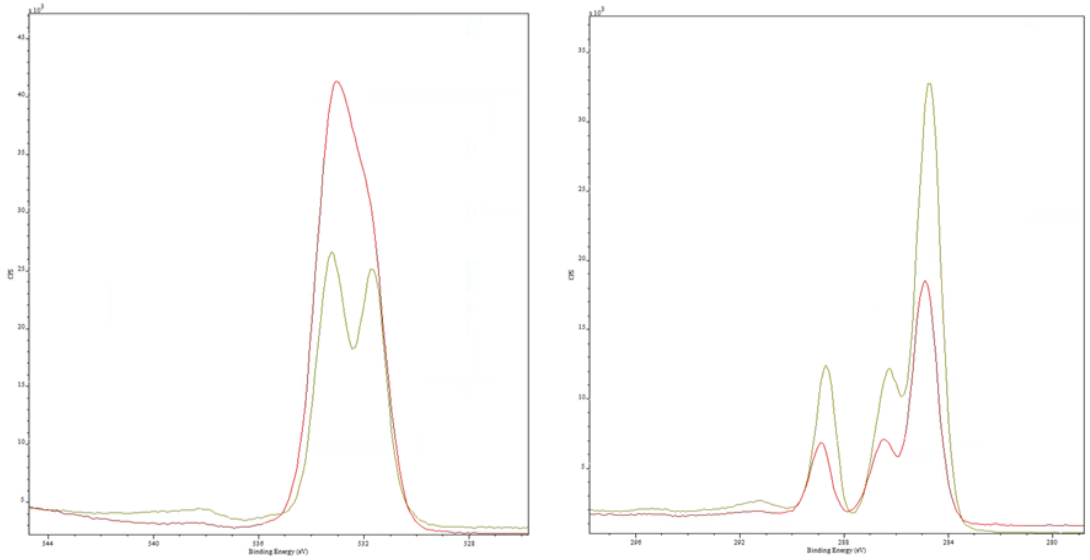

Figure 4.24 Overlaid O 1s and C 1s spectra of PET-FR, before (green) and after (red) PD exposure

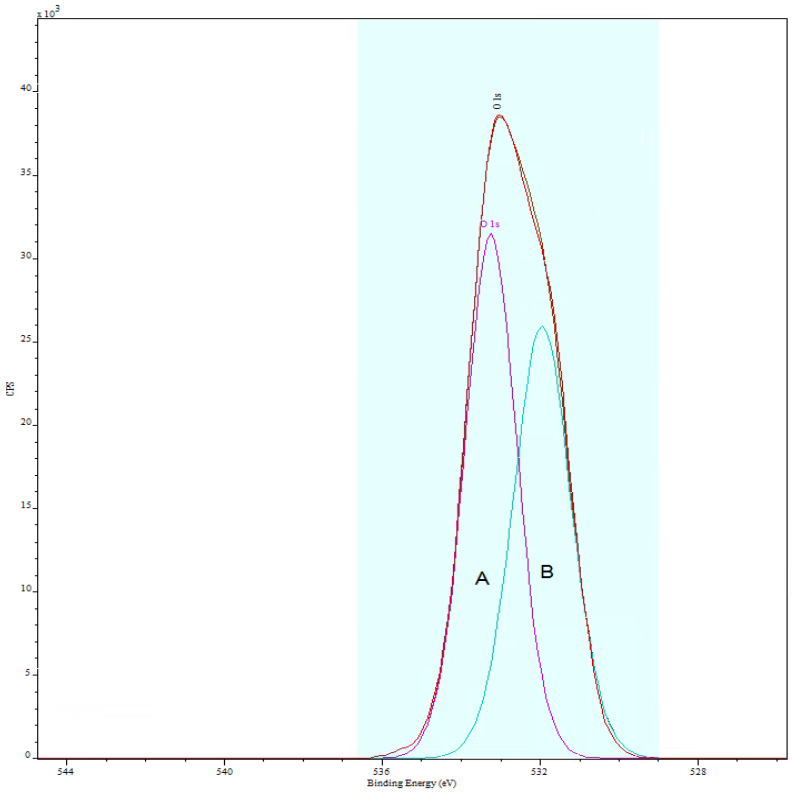

Figure 4.25 Deconvolution of O1s spectrum of PD exposed PET-FR

4.3.5 SEM analysis

SEM images of untreated and PD exposed PET samples with different inorganic fillers and additives are illustrated as below. Surface condition of an untreated PET film is shown in figure 4.26(F), it is plain and featureless as expected. Figure 4.26(D) and (E) show the surface of PD exposed PET filled with inorganic particles in low (15x) and high (388x) magnification, respectively. The filler 'pile-up' phenomenon can be directly observed from these two images, especially the figure 4.26(E), in which a well-defined interface between the PD eroded and unaffected area is observed. Surface images in further higher magnification (777x) of PD exposed pure PET, PET filled with inorganic particles and PET-FR are shown in figure 4.26(A), (B) and (C), respectively. Not much change could be found for the pure PET sample after PD degradation. In figure 4.26(B), one can clearly see that the white particles totally overwhelmed the PET resin, forming a thin filler layer on the resin surface after PD erosion. In the case of PET-FR (figure 4.26(C)), some micron-sized white particles (which should be P_2O_5 or H_3PO_4 as analysed by FTIR and XPS) but with much lower particle density than the PET filled with fillers, are found on the PD exposed sample surface. It is also interesting to note that 'ripple-shape' structures, especially around those particles, are seen on the sample surface after PD degradation, which could possibly be due to the trace of aqueous phosphoric acid.

The cross section of an untreated PET sample is shown in figure 4.27(A), it is intact as expected. The cross section images of PD exposed pure PET, PET filled with inorganic particles and PET-FR are shown in figure 4.27(B), (C) and (D), respectively, and structural changes can only be found near the sample top surface where the PD came from for all the samples. In the cases of pure PET and PET filled with inorganic particles, changes can barely be seen due to the absence and extremely fine particles in the resin. When it comes to PET-FR, a distinct thin and spiky particle layer can be observed on the sample surface.

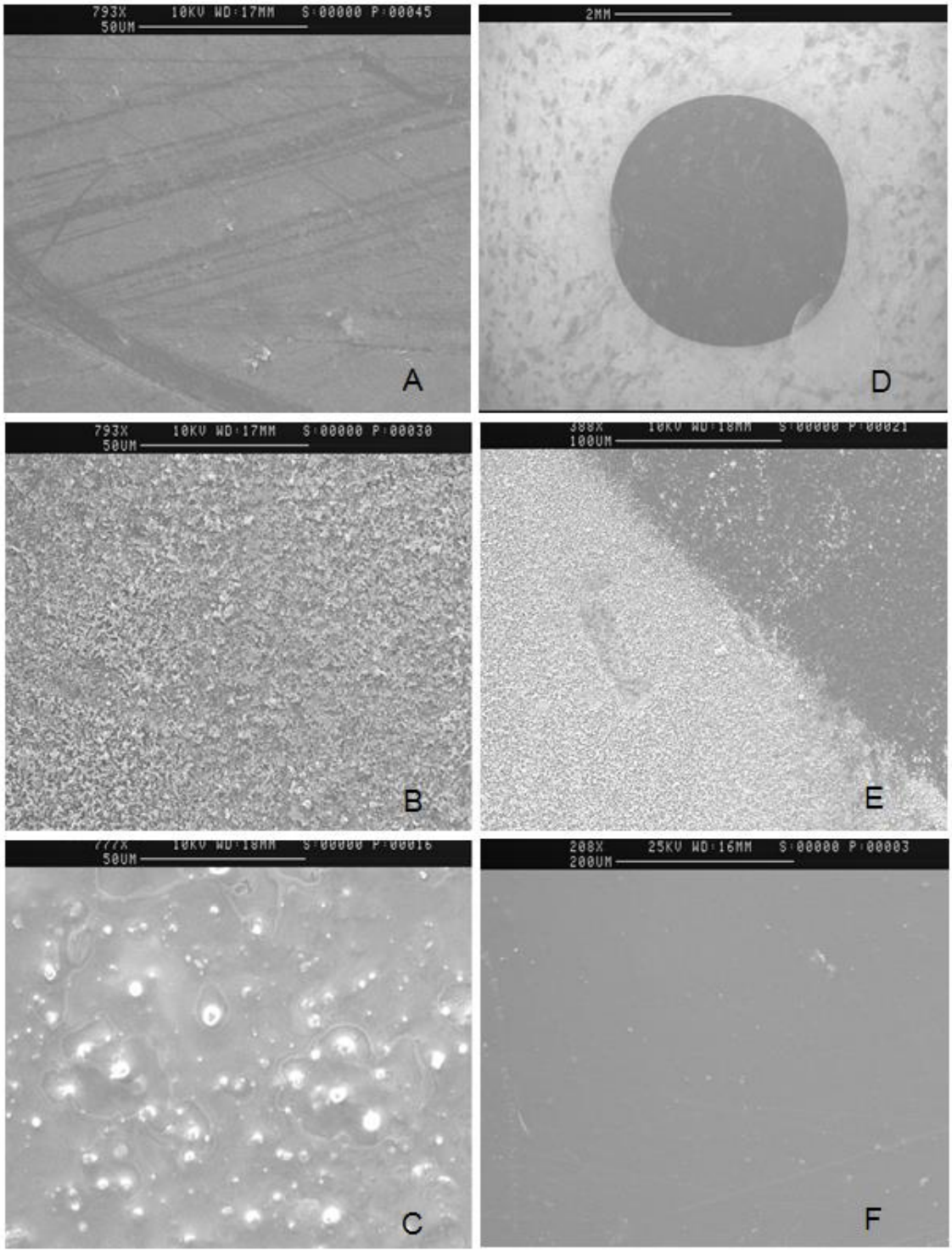

Figure 4.26 Surface of samples treated under 3kV for 48hrs, PET (A); PET filled with inorganic particles (B); PET-FR (C); Low magnification of PET filled with particles (D); High magnification of PET filled with particles, degradation interface (E); Untreated PET (F)

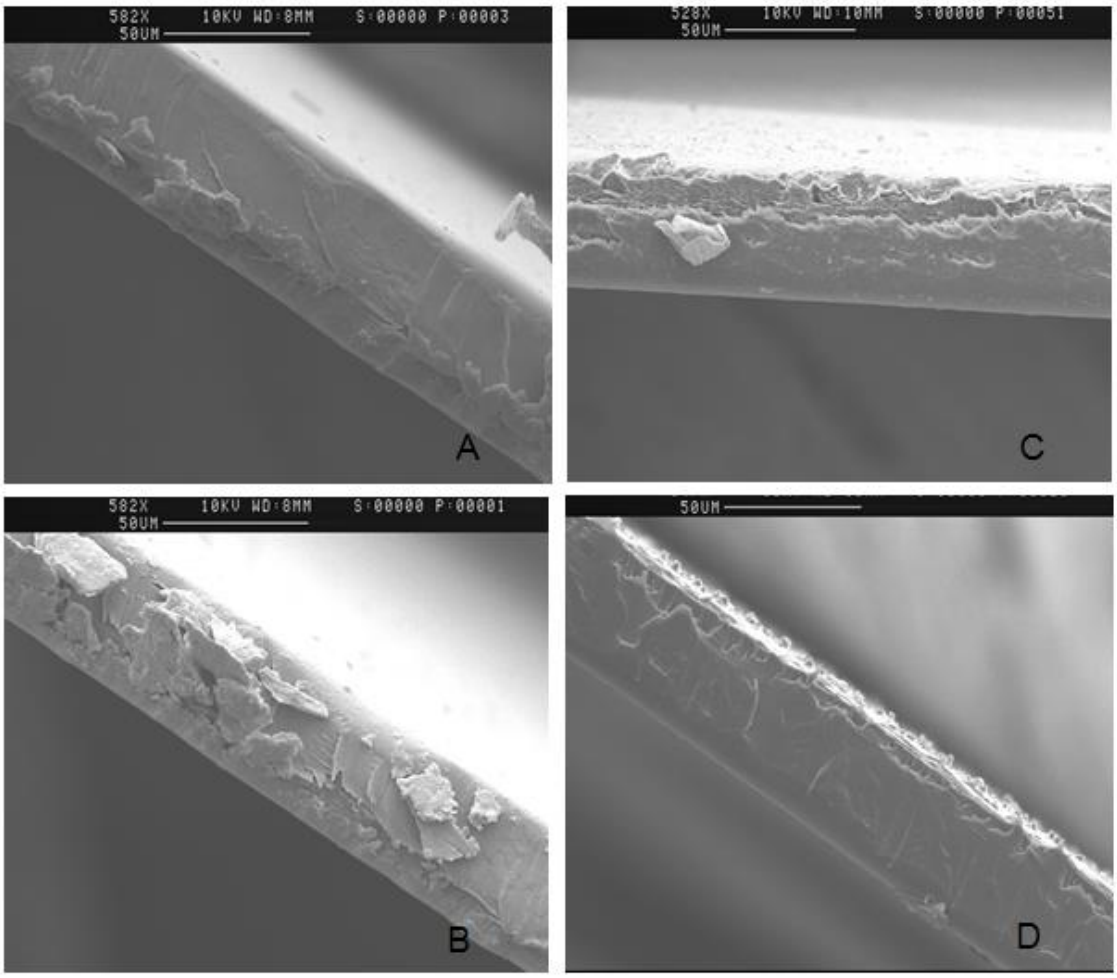

Figure 4.27 Cross section of samples treated under 3kV for 48hrs, Untreated PET (A); PET (B); PET filled with particles (C); PET-FR (D)

4.3.6 Discussions

It is well known that composites will have superior properties including PD resistance abilities to their basic resins. Researches have shown that PD resistances of polyimide and epoxy resin can be greatly enhanced once these polymers are filled with even a small amount of particles [101-120]. Furthermore, other composite structures such as polypropylene/silica and polyethylene/MgO were also investigated and positive results in terms of PD resistance of these composites have been confirmed too [119].

PD degradation and breakdown experiments of PET without and with different performance fillers/additives were carried out in this project. Data in figure 4.2 and

4.3 have shown that both PD resistance abilities (in terms of PD erosion depths) and PD lifetimes can be considerably enhanced once the PET resins are filled with inorganic fillers and P-containing flame retardant. However, it is surprising to note that the samples filled with particles which have the best PD resistances do not have the longest PD lifetimes as expected. In fact, the sample functioned with P-containing flame retardant, PET-FR, has the PD lifetime much longer than that of any other samples. It has been discussed in chapter 3 that for the same type of PET materials, samples with better PD resistance generally indicates the longer PD lifetime. However, this unexpected long PD lifetime of PET-FR suggests direct proportional relationship between PD resistance and PD lifetime of samples does not always exist, better PD resistance does not necessarily means longer PD lifetime. Therefore for the PET-FR sample, there must be another mechanism of PD resistance which can provide the extreme long PD lifetime for it.

From figure 4.3, one can see that the three samples filled with particles, namely, PET-$BaSO_4$, PET-$BaSO_4$-UV and PET-TiO_2 have nearly identical PD erosion depths and their erosion depths are much less than that of the PET and PET-FR under all PD exposure conditions. The excellent PD resistances of these particles filled PET can be explained by the mechanisms that have been established for the composites in the literature [119]. Since the pigments were physically blended with the PET resin in the extruder during the manufacturing process, it is reasonable to assume that no chemical coupling will occur between the fillers and PET resin. FTIR data confirm this assumption by showing that apart from the characteristic absorption bands of inorganic particles per se no other peak shift or change can be observed for either PET-$BaSO_4$ (PET-$BaSO_4$-UV) or PET-TiO_2, hydrogen bonds could possibly exist between the pigments and the PET resin but considering the bonds are usually very weak, the effect of it are negligible here. Therefore, the effect of coupling agent is ruled out for the samples.

The fillers pile-up phenomena have been directly observed by different analytical methods, the schematic of the effect is shown in figure 4.28. The inorganic pigments will remain on the eroded sample surface forming a protective layer, thanks to the excellent PD resistance of the inorganic pigments this protective layer will not only significantly slow down the PD erosion rate but also inhibit oxygen from entering the unaffected region, which will decrease the degradation process as well. Furthermore, since the PET resin is three-dimensionally segmented by the well dispersed fillers,

high energy ions bombardment will be partially blocked by these fillers which will decrease the erosion rate. This is the so called 'filler-segmentation' effect [118]. In addition, PD will concentrate more on the PD resistive inorganic fillers than the polymer resin because the permittivity of the fillers is usually higher than that of the polymer, causing the intensification of electric field on the inorganic fillers. In this case, the permittivity of PET resin, $BaSO_4$ and TiO_2 are 3.3, 11.5 and 110, respectively. Hence PD will concentrate even more on the fillers when the PET is filled with TiO_2 than $BaSO_4$, this can partially explain why PET-TiO_2 has a longer PD lifetime than PET-$BaSO_4$ (figure 4.2).

When polymer surface is subjected to PD, the sample surface will be bombarded by high energy ions such as electrons and positively charged particles that generated by the avalanche breakdown of the air, leading to chemical bond cleavage thus molecular mass decline. What's more, temperature of the PD activated region can easily rise to a few hundred °C and even beyond 1000°C for a very short moment [119] and this high temperature will undoubtedly cause local melting and decomposition of the material. Primary and secondary excited molecules such as activated oxygen and ozone, as well as UV radiation generated by PD will also chemically degrade the sample surface. All the above mentioned processes will gradually erode the sample surface and decrease the sample thickness and continuous decrease of the sample thickness will lead to the formation of pits (figure 4.28). Once pits are produced, electric field will be greatly intensified in these regions and eventually electrical trees can be initiated from the bottom of the pits. These electrical trees will propagate toward the ground electrode which can cause the final breakdown of the polymer. The whole process is illustrated in figure 4.29. The well dispersed particles inside the polymer are considered to be able to block the electrical tree propagation paths thus enhance the PD lifetime of the sample, as shown in figure 4.28. It should be noted that the environments around the particles could play an important role in electrical tree propagation. TiO_2, whose refractive index is higher than that of any other commercial pigments, is usually used as a whitener by purely pigment effect. On the other hand, $BaSO_4$, is usually used as a void initiator during orientation to increase the light scattering and toughness of the polymer [145]. Therefore, it is reasonable to believe that more voids and defects will present around $BaSO_4$ than TiO_2 when they are both used as pigments for PET. Electrical tree propagation will accelerate when a tree tip reaches the defects around $BaSO_4$ and speed up the whole breakdown

process, this is the main reason why PET-TiO_2 has a superior PD lifetime to PET-$BaSO_4$. PET-$BaSO_4$-UV has the longest PD lifetime among the three inorganic particles containing samples. XPS results (table 4.2) have shown that sample surface oxidation is less severe for PET-$BaSO_4$-UV than PET-$BaSO_4$, suggesting chemical degradation caused by primary and secondary excited molecules as well as UV radiation during PD erosion can be inhibited by the Tinuvin 1577 UV stabilizer for PET-$BaSO_4$-UV (as illustrated on the right paths in figure 4.29), hence PD resistance and lifetime of the sample can be enhanced.

The most important finding of this experiment is that PET-FR, whose PD resistance ability is just medium (better than pure PET but worse than inorganic particles filled PET), has astonishingly long PD lifetime and its PD lifetime is four times as long as that of the pure PET! This unexpected PD lifetime of PET-FR has suggested that PD lifetime cannot be fully attributed to PD resistance ability, on the other hand, it is the initiation and propagation of electrical trees caused by PD that dominate the PD lifetime. FTIR and XPS results have proven that abundant phosphoric acids H_3PO_4 and phosphorous pentoxide P_2O_5 were produced once the sample received PD degradation. H_3PO_4 which is the common product that could be produced in the thermal degradation during the combustion of P-containing flame retardant PET to promote the char formation, can easily form due to the high local temperature and oxidation process when PET-FR is subjected to PD. The massively produced phosphoric acids will be in viscous liquid form due to local high temperature, covering the PD affected area of the sample, as can be directly observed from the SEM results (figure 4.26(C)). The sample surface conductivity will therefore remarkably increase leading to the moderation of local electric field, as a result, the initiation process of electrical tree will be significantly delayed. In fact even after the formation of electrical trees, the produced aqueous phosphoric acids are capable of migrating into the electrical tree channels thus eliminate the PD inside the channels by moderating the internal electric field across the channels, similar as the way semiconducting organic liquids work [99]. In this way the propagation rate and widening of the electrical trees can be greatly inhibited. Lastly, the medium PD resistance of PET-FR can be attributed to the P_2O_5 particles produced during the PD degradation. These inorganic substances can block and slow down the PD erosion process in the same way as those white pigments do. However because of its large-size, as shown in figure 4.26(C), the inter-particle distances of PET-FR will be larger than that of those white pigments filled PET

samples and it was reported that smaller inter-particle distance can provide better PD resistance [105], therefore the apparent PD resistance of PET-FR will be better than pure PET resin but worse than inorganic particles filled PET.

It has been proven that PD lifetime of samples relate more closely with the electrical treeing behaviour than the PD resistance per se. Figure 4.2 and 4.4 confirm this by showing that the PD lifetime and EDAB of samples follow exactly the same trends. The EDAB of samples shown in figure 4.4, which is a parameter that define the maximum erosion depth that one sample can withstand before breakdown, is obviously depends on the electrical treeing behaviour especially the initiation time of the trees. Therefore, EDAB can be regarded as a useful tool to investigate the electrical treeing and PD-induced breakdown of polymers.

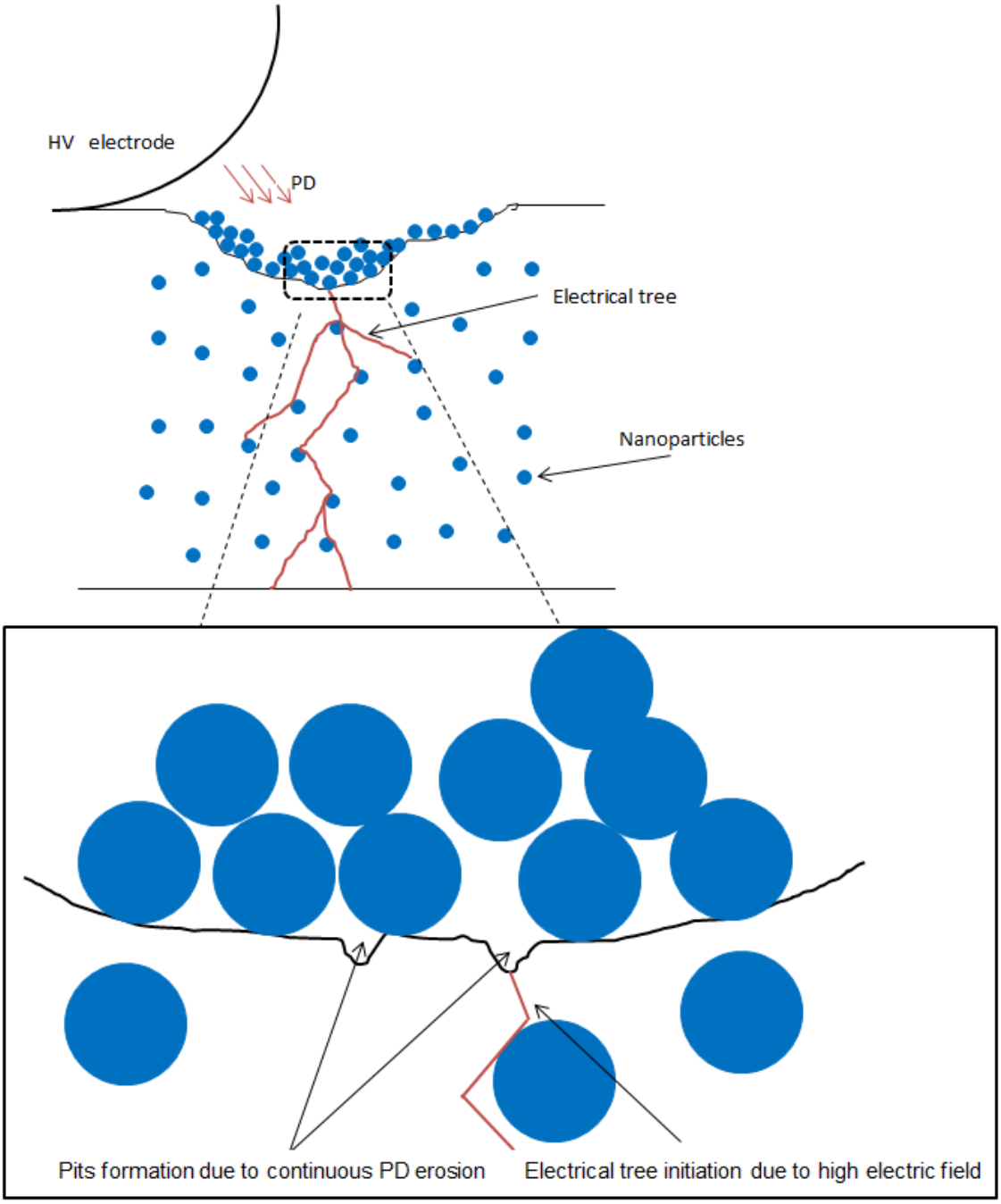

Figure 4.28 Pile-up effect of fillers and dielectric breakdown caused by PD-initiated electrical tree

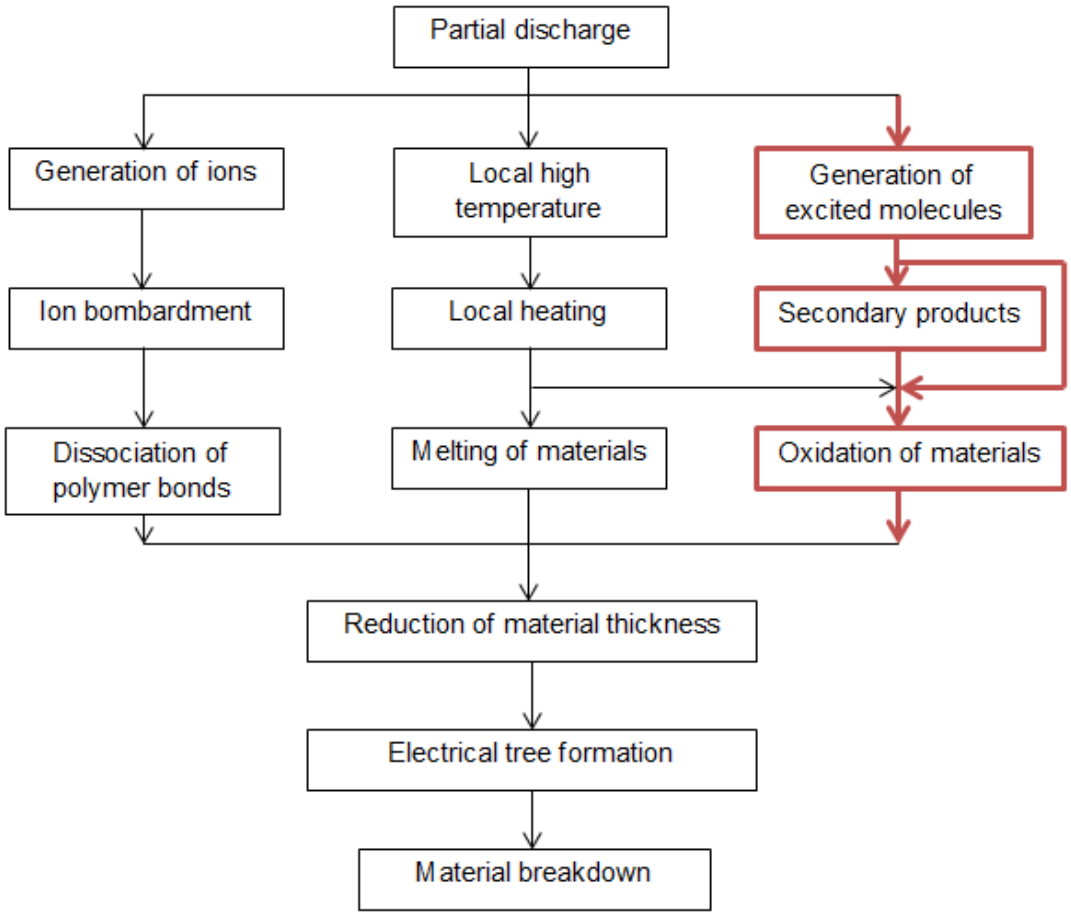

Figure 4.29 Physicochemical processes of polymer surface degradation caused by partial discharge [119]

4.4 Conclusions

Five categories of biaxially oriented, semicrystalline PET films filled with different pigments and performance additives, namely, Universal PET without any additive (pure PET), PET filled with 13% TiO_2 particles (PET-TiO_2), PET filled with 18% $BaSO_4$ particles plus functioned without and with Tinuvin 1577 UV stabilizer (PET-$BaSO_4$ and PET-$BaSO_4$-UV) and PET functioned with phosphorus-containing flame retardant (PET-FR), were subjected to identical voltage stresses to investigate the effect of fillers and additives on PD degradation and breakdown of PET films. A few conclusions are made as follows:

1. Proportional relationship between PD resistance and PD lifetime of samples does not always exist, better PD resistance does not necessarily means longer PD lifetime. In fact, PD lifetime of samples relate more closely with the electrical treeing behaviour than the PD resistance per se.
2. Inorganic pigments can significantly improve both the PD resistance and PD lifetime of samples by the filler pile-up effect and blocking the propagation paths of electrical trees.
3. Lower permittivity of $BaSO_4$ than TiO_2 and defects that were created around the $BaSO_4$ particles during orientation make PET-$BaSO_4$ more prone to PD induced breakdown than PET-TiO_2.
4. Further improvements on PD resistance and PD lifetime can be made once inorganic particles filled sample is functioned with UV stabilizer by reducing the sample surface oxidation caused by PD.
5. Although having the PD resistance that far from excellent, the P-containing flame retardant PET-FR can withstand the electrical stress much longer than any other sample. Unlike those inorganic particles filled samples whose PD lifetime can be extended mainly by slowing down the PD erosion rate, the enormous PD lifetime of PET-FR is attributed to the massively produced phosphoric acids onto the sample surface caused by PD. Electric fields across the whole sample and the electrical tree channels will be moderated by the high conductivity of the phosphoric acids and therefore both initiation and propagation of electrical trees inside the sample can be significantly suppressed.
6. EDAB has been proven as a useful tool to investigate the electrical treeing and PD-induced breakdown of polymers since the PD lifetime and EDAB of samples follow exactly the same trends.

Chapter Five

5.Annealing treatment effect on PD degradation of PET

5.1 Introduction

Crystallinity is unquestionably one of the most important parameters for polymers as it influences mechanical properties such as tensile strength, modulus, hardness and stiffness [55]. It has been discussed in chapter 3 that crystallinity can also affect the PD degradation rate of PET sample in terms of PD erosion depth and surface chemistry changes.

Isothermal crystallization/annealing is a simple way to not only increase the crystallinity of a polymer material but also thicken and perfect the lamellae of the polymer spherulites, thereby improving the material performance. For example, in order to improve the gas barrier properties of PET, samples are usually annealed at temperatures between the glass transition temperature T_g and the melting point T_m to increase the crystal size [64]. Therefore, whether the PD resistance and PD lifetime of PET materials can be improved via annealing treatment is of great interest since the lamellae size could be a potential factor in determining the PD lifetime as well.

5.2 Experimental

5.2.1 Samples

Three categories of biaxially oriented, semicrystalline PET films filled with various performance additives that were already discussed in chapter 4 were used to explore the annealing treatment effect on PD degradation and breakdown of PET films. The samples were provided by DuPont Teijin Films and Mitsubishi Polyester Film and all in 50 μm. The three sample categories are described as below:

1. Universal biaxially oriented PET without any additive (PET).
2. PET filled with 18% $BaSO_4$ and functioned with 1.0% Tinuvin 1577 UV stabilizer (PET-$BaSO_4$-UV).
3. PET functioned with phosphorus based flame retardant which is chemically grafted to the PET chain (PET-FR).

5.2.2 Annealing treatments of samples

Before any PD or dielectric breakdown test, the above mentioned samples were isothermally crystallized at various temperatures from 180 to 230°C (PET-FR was isothermally crystallized up to a temperature of 220°C because of its relatively low melting point) in a laboratory oven for one hour. After cooling down, all the samples thicknesses were measured by using a digital micrometer to ensure no sample thickness changes occur during the annealing processes.

5.2.3 Experimental set-up of partial discharge and breakdown tests

Two sets of experiments were carried out to investigate the annealing treatment effect on PD degradation and breakdown behaviours of PET films. The sample holders for the both sets have already been shown in chapter 2 (figure 2.2 and figure 2.3). The pre-experimental sample treatments and experimental environment conditions are the same as describe in 3.2.2 of chapter 3.

5.2.3.1 Experimental set-up for PD tests

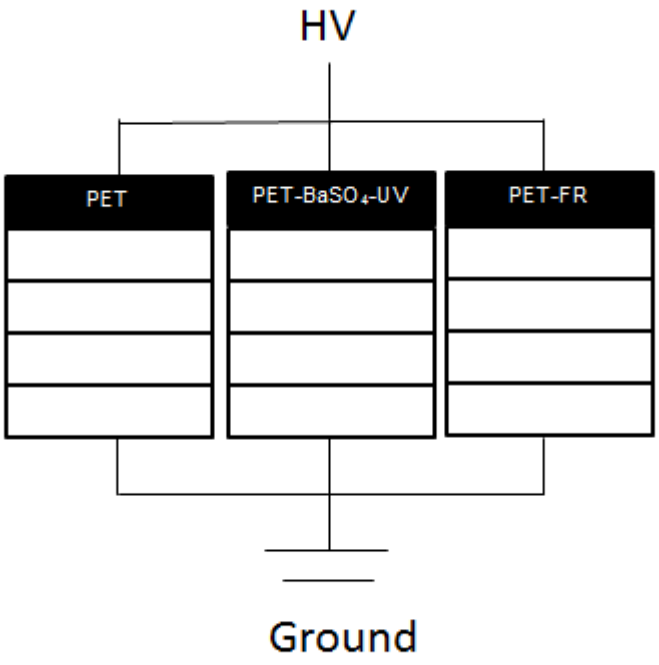

Figure 5.1 Schematic of set-up for PD exposure of samples after annealing treatment

For the samples with different additives, three sample stacks with identical thickness (250 µm) were subjected to a 50 Hz AC high voltage of 3 kV for 24 hours. The schematic of the whole experimental set-up is shown in figure 5.1, the annealed samples were placed on the top layer of each stack (black block in figure 5.1) while the other sheets of the stacks being the untreated samples. After PD exposure, the annealed samples on the top layers were removed for further analysis.

5.2.3.2 Experimental set-up for PD-lifetime test

The schematic of set-up for breakdown tests due to PD erosion has been shown in 3.2.2.2 of chapter 3. Single sheet of the annealed samples with different additives

were subjected to a 50Hz AC high voltage of 3kV until the sample breakdown due to PD erosion. For each sample category, at least five samples were tested and the average values of the PD lifetime of each category were calculated.

5.2.4 Experimental of analytical methods for sample characterisation

All the analytical methods for sample characterisation have been introduced in chapter 2 and 3 already.

5.3 Results and discussions

5.3.1 DSC analysis

The DSC thermograms of PET samples annealed at various temperatures from 180 to 230°C were shown in figure 5.2, with the top trace being the untreated PET. Double melting endotherms can be observed for all the isothermally crystallized samples and it is clear that the lower melting peak shifted to higher temperature as the crystallization temperature increased, indicating two distributions of lamellae thickness and the 'melt-recrystallization-remelt' phenomenon that has been discussed in chapter 3. Melting calorimetric parameters such as melting points T_m^n(K), lamellae thickness L_c^n(Å), percentage of each lamellae structure A_{Tmn}(%) and overall crystallinity degree X_c(%) are summarized in table 5.1. The lamellae thicknesses L_c^n(Å) were calculated using the *Thomas-Gibbs* equation [61] discussed in chapter 3. In order to further investigate the development of the dual lamellae thickness during the annealing treatment, a peak fitting process was applied to the melting doublets of each sample. The deconvolution processes were performed by the OriginPro 8.6 software and Gaussian-Lorentzian cross was selected as the peak types for the processes. Thicknesses and percentages of primary and secondary lamellae of PET annealed at different temperatures were plotted in figure 5.3 and 5.4, respectively. DSC thermograms, calorimetric results and data plots of PET-$BaSO_4$-UV and PET-FR can be found in figure A.3-A.8, table A.1 and A.4 in appendix A.

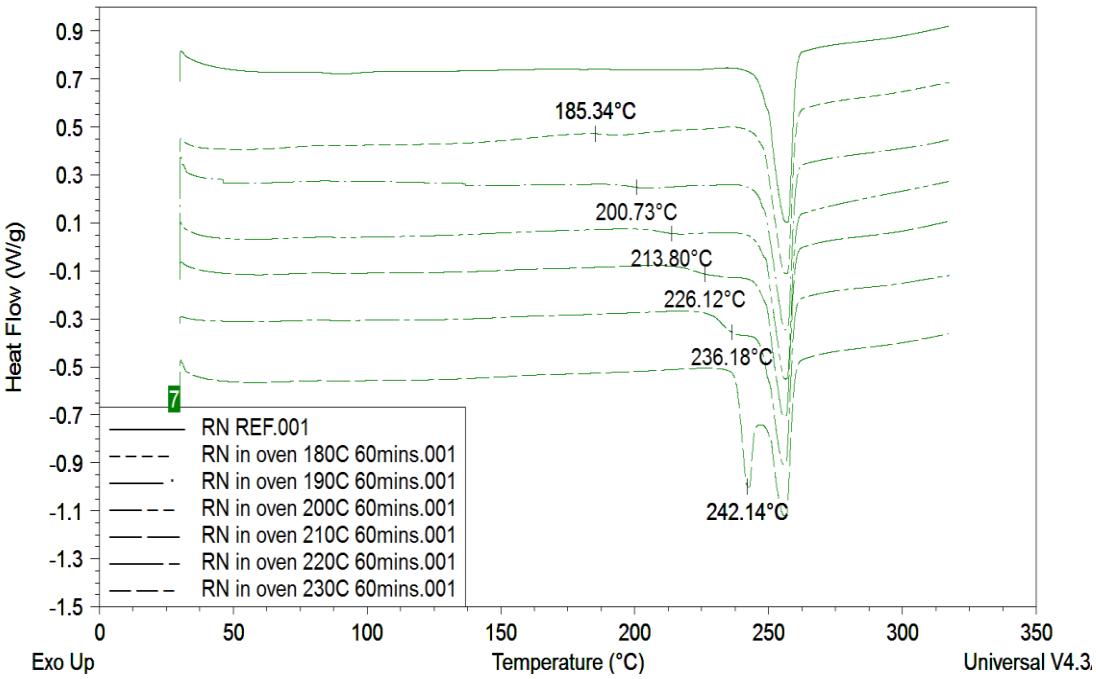

Figure 5.2 DSC analyses of the melting of PET after crystallization at different temperatures

Samples	T_m^1(K)	L_c^1(Å)	A_{Tm1}(%)	T_m^2(K)	L_c^2(Å)	A_{Tm2}(%)	ΔH_m(J/g)	X_c%
REF	N/A	N/A	N/A	530.2±0.2	168.4	N/A	47.17	33.69
180°C	458.5±1.2	54.0	4.1	530.0±0.3	167.4	95.9	48.45	34.61
190°C	473.9±1.1	63.2	5.4	530.0±0.2	167.4	94.6	51.08	36.49
200°C	487.0±0.8	74.0	12.0	529.8±0.4	166.7	88.0	51.20	36.57
210°C	499.3±2.4	88.0	16.7	529.4±0.2	164.6	83.2	53.70	38.36
220°C	509.3±1.7	104.1	36.4	529.3±0.4	164.6	63.6	54.22	38.73
230°C	515.3±1.5	116.9	43.8	529.4±0.2	164.6	56.2	57.83	41.30

Table 5.1 DSC data of PET annealed at various temperatures from 180 to 230°C for 60 mins

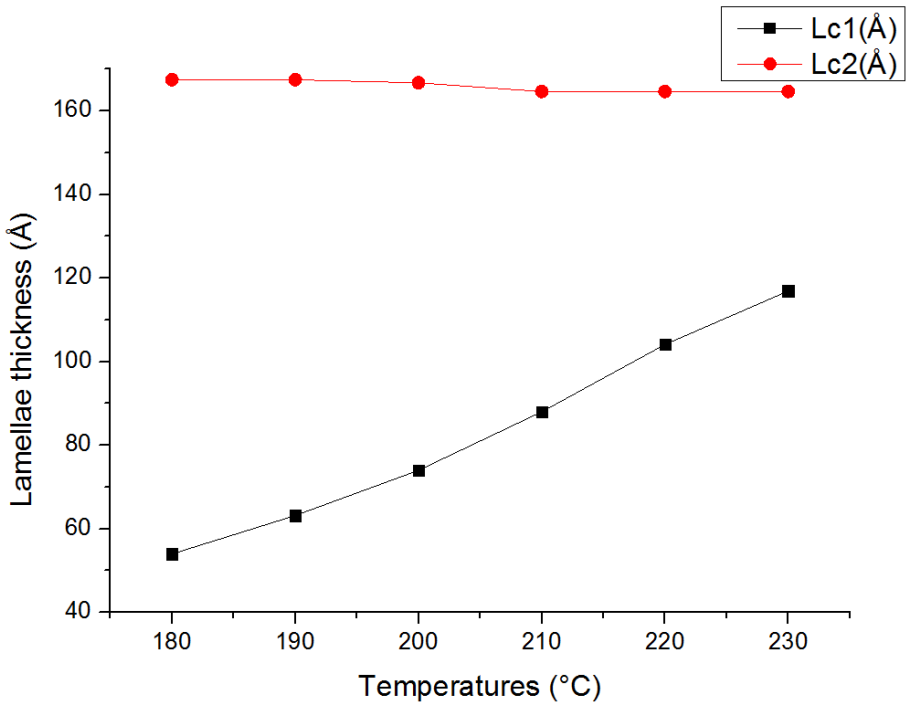

Figure 5.3 Thicknesses of primary and secondary lamellae of PET annealed at various temperatures from 180 to 230°C for 60 mins

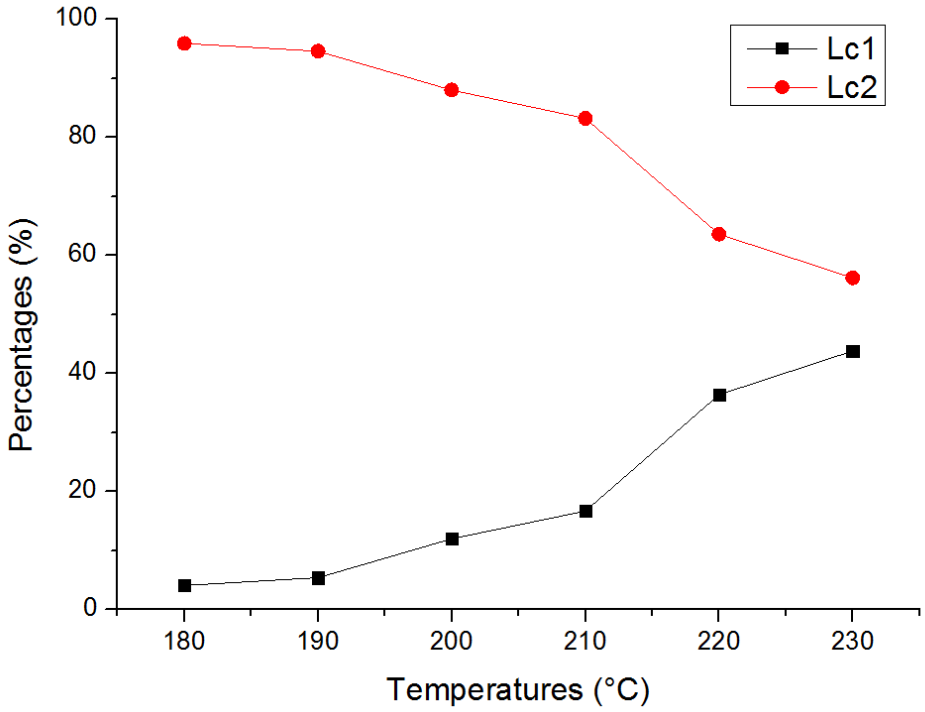

Figure 5.4 Percentages of primary L_c^1 and secondary L_c^2 lamellae of PET annealed at various temperatures from 180 to 230°C for 60 mins

5.3.2 FTIR analysis

As discussed in chapter 3, FTIR is a useful tool to analyse PET morphology and crystallinity degree, which can be achieved by measuring the ratio of absorption peaks at 1473 and 1455 cm^{-1} that are attributed to the bending of the glycol CH_2 in crystalline and amorphous phases, respectively [56, 61, 73]. The comparison of the doublets during the isothermal crystallization is shown in figure 5.5, one can see that after annealing treatment the peak at 1473 cm^{-1} increased while the peak at 1455 cm^{-1} decreased, suggesting the development of the crystalline portion of PET. The crystallinity degrees of the samples were calculated using the equation (3) in chapter 3 and the results of PET are shown in table 5.2 (FTIR data of PET-$BaSO_4$-UV and PET-FR are given in table A.2 and A.4, respectively in appendix A). It is seen that the data trends of the sample crystallinity degrees X_c% both in table 5.1 and 5.2 are highly consistent although the data obtained by DSC is a bit larger than the data by FTIR, which has been mentioned in chapter 3.

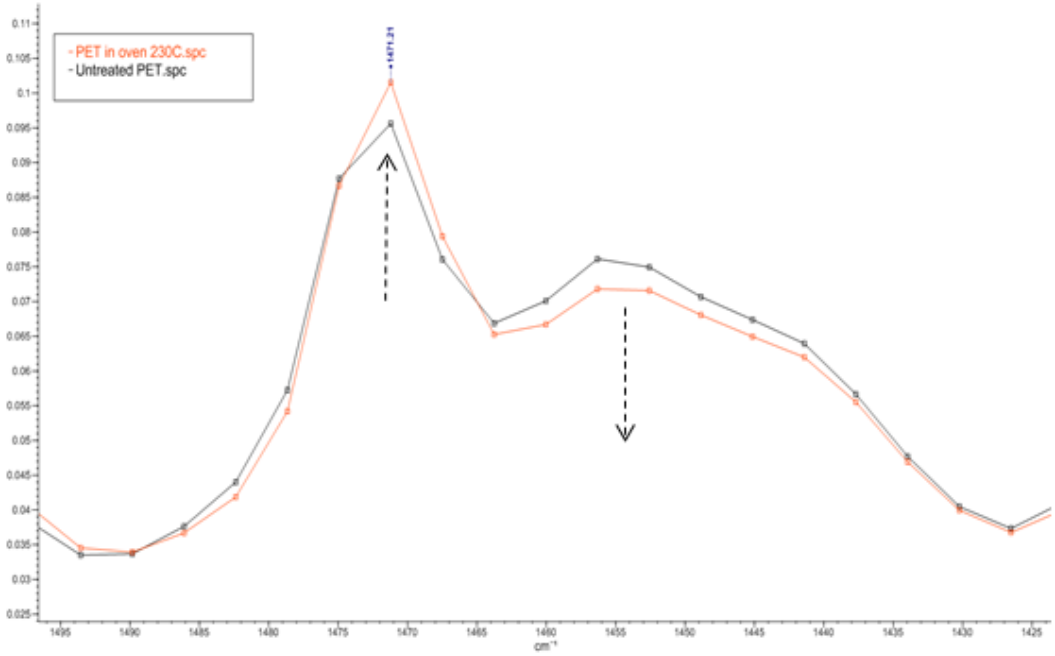

Figure 5.5 Overlaid 1430-1500 cm^{-1} regions of ATR-FTIR spectra of untreated and annealed at 230°C PET

Samples	1455 cm^{-1}	1473 cm^{-1}	$\%X_c$
Untreated PET	70.3	29.7	29.7
180°C	69.7	30.3	30.3
190°C	69.7	30.3	30.3
200°C	69.4	30.6	30.6
210°C	69.1	30.9	30.9
220°C	68.3	31.7	31.7
230°C	67.4	32.6	32.6

Table 5.2 Crystallinity degrees of untreated and annealed PET by FTIR

5.3.3 Surface profilometer and PD lifetime analyses

Surface profilometer

PD tests were carried out for the three different annealed samples, namely PET, PET-$BaSO_4$-UV and PET-FR by using the PD experimental set-up shown in figure 5.1. After PD exposure, samples on the top layer (the annealed one) of each stack were removed for erosion depth tests. The erosion depths of the samples are plotted in figure 5.6. It can be clearly seen that the erosion depths in general decreased with the increase of crystallization temperatures for each type of samples. To be more specific, the erosion depths of the samples decreased at a relatively slow rate when the crystallization temperatures are lower than 210°C (200°C for PET-FR), however once the crystallization temperatures are higher than 210°C, a sharp decrease of PD erosion depths could be found for all the annealed samples, suggesting a significant improvement of PD resistance. This phenomenon will be discussed in detail later.

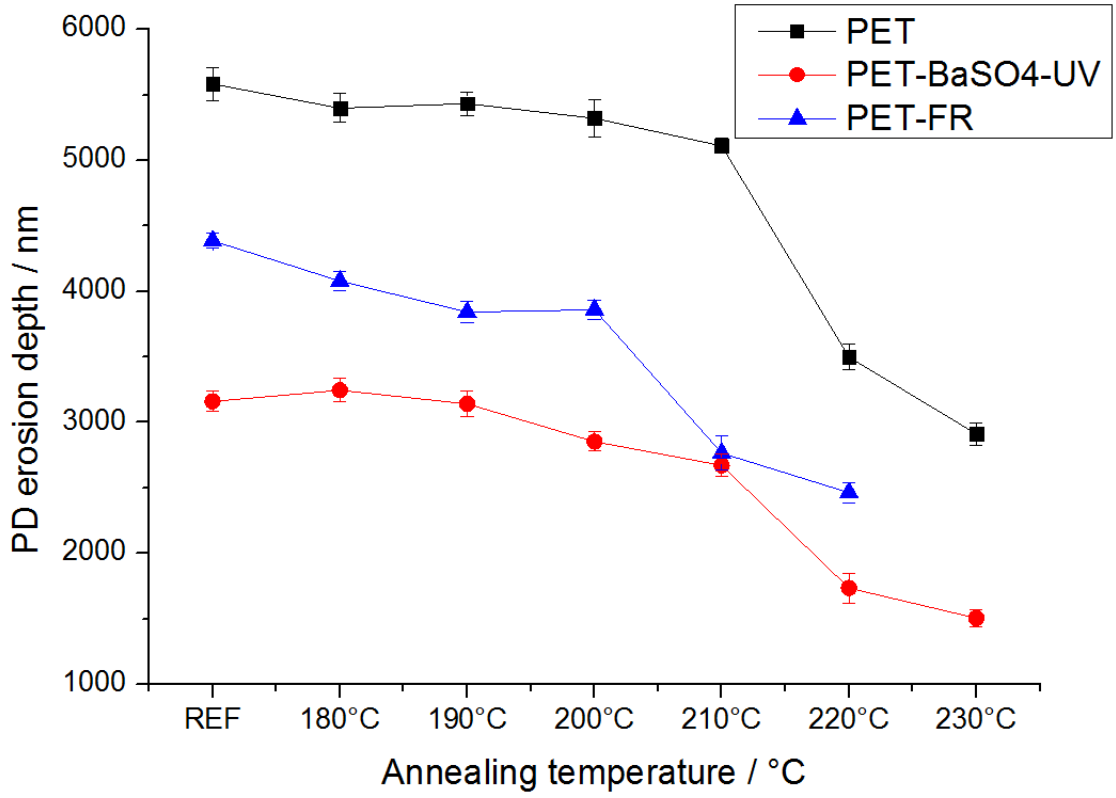

Figure 5.6 PD erosion depths of samples after crystallization at different temperatures

PD lifetime analysis

PD lifetime tests were also carried out for all the annealed samples and the results are illustrated in figure 5.7. Although in the last chapter it has been shown that better PD resistance does not always means longer PD lifetime for PET with various performance additives, it is logical to expect that the PD lifetime is directly proportional to PD resistance for the same type of polymeric materials. Therefore, similarly, the PD lifetimes of the annealed samples enhanced greatly when the crystallization temperatures are higher than 210°C (200°C for PET-FR), as shown in figure 5.7. From the figure it is seen that PD lifetime of each sample can be enhanced by a factor of 100% (70% for PET-FR when it was annealed at 220°C) when the sample was annealed at 230°C.

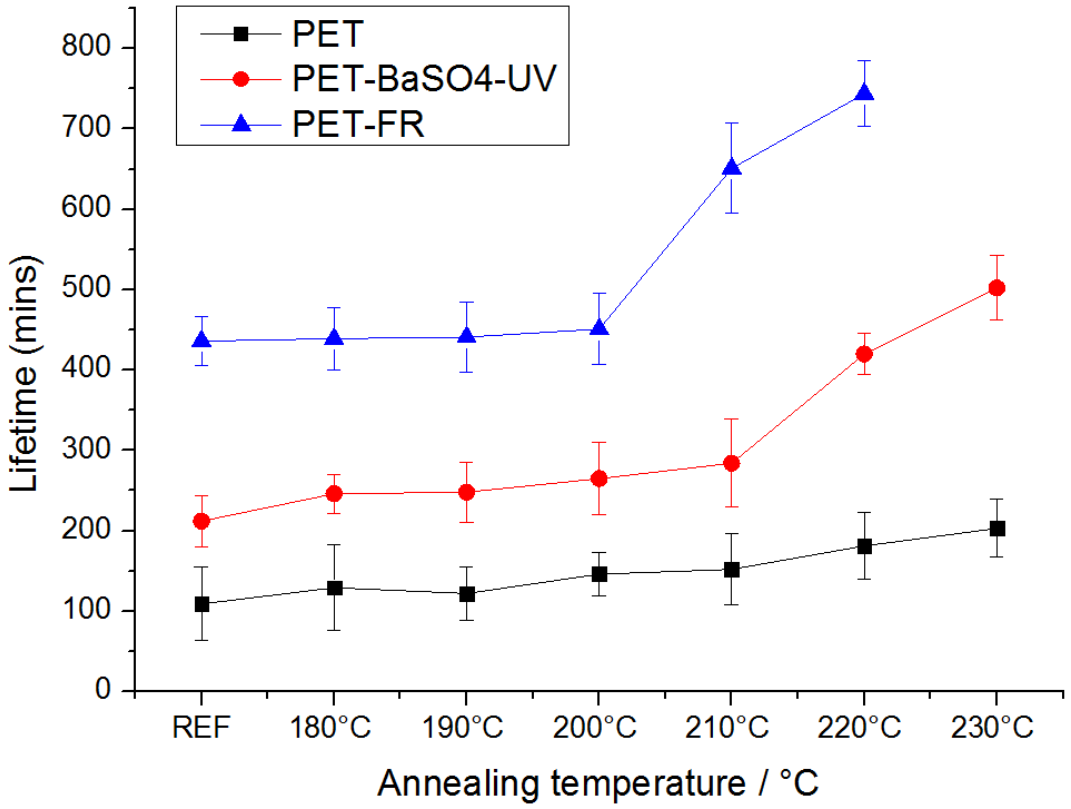

Figure 5.7 PD lifetimes of samples after crystallization at different temperatures

5.3.4 Discussions

Polymeric films with thicker lamellae structure and higher crystallinity degree will provide a better PD resistance to the polymers in terms of surface chemistry changes and physical erosion depths, as discussed in chapter 3. Lamellae thicknesses and crystallinity degrees of semicrystalline polymeric materials can be considerably enhanced by isothermal crystallization at temperatures between the glass transition temperatures T_g and the melting temperatures T_m [55-63], especially when close to the melting points.

DSC thermograms and the corresponding calorimetric results of PET annealed at various temperatures between 180°C to 230°C are shown in figures 5.2 – 5.4 (data of PET-$BaSO_4$-UV and PET-FR are shown in appendix A). Two well-defined melting peaks are observed in DSC thermograms for all the samples. The double melting

behaviour of isothermally crystallized PET have been widely discussed in the literature and dual distributions of lamellae thickness in the materials is usually used to explain this behaviour [55-62]. The lower ones which usually locate 10-20°C higher than the crystallization temperature T_c are attributed to the melting of defective and thinner secondary lamellae formed by the secondary crystallization of amorphous materials. These defective lamellae with relatively low thermal stability therefore will firstly melt away during the DSC heating scans [58, 67]. As can be seen in figure 5.2, the temperature and peak area of the lower melting peak increase as the crystallization temperature, indicating the thickening and perfection of secondary lamellae during the crystallization processes. The schematic of secondary lamellae growth of annealed PET at various temperatures is shown in figure 5.8 [60]. Three annealing temperature regions were defined according to the authors, namely, low temperature region (T_c<170°C), medium temperature region (180°C<T_c<210°C) and high temperature region (T_c>220°C). From the figure one can find out that no crystalline thickening can occur when the annealing temperature is lower than 170°C. However the secondary crystallization can occur once the annealing temperature is high enough to give sufficient mobility to the amorphous PET molecular chains between primary lamellae, which will facilitate these polymer chains to form more ordered structures thereby increasing the secondary lamellae thickness. Thickest lamellae structures can be obtained via crystal perfection when the crystallization temperature is very high and close to the melting point of the polymer. Calorimetric data in figure 5.3 and 5.4 are consistent with this theory, secondary lamellae thickness of PET increase with the annealing temperature, as shown in figure 5.3 and a sudden large increase of secondary lamellae population are seen when the annealing temperature is as high as 220°C (figure 5.4). Therefore, a much more uniform distribution of lamellae thicknesses can be achieved when the sample is subjected to high annealing temperatures, especially in the case of PET-$BaSO_4$-UV where two melting endotherms merge together and become one large sharp melting peak after annealed at 230°C (see figure A.3 in appendix A).

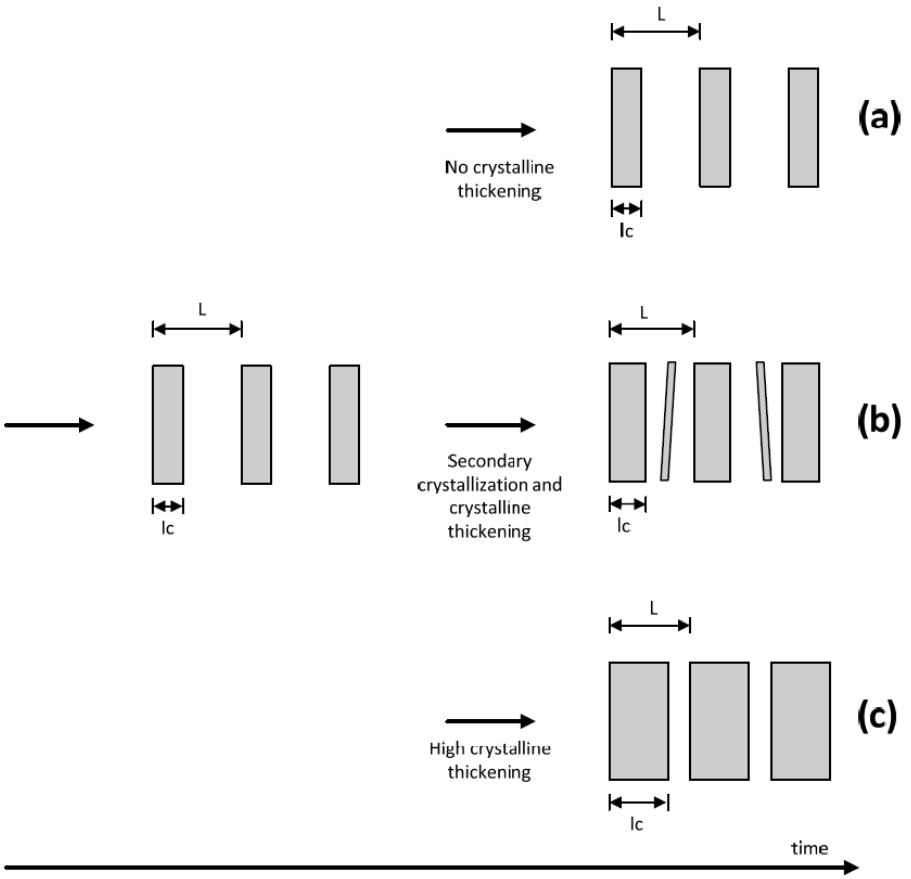

Figure 5.8 Developments of lamellae for PET annealed at various temperatures, (a) low temperature region (T_c<170°C), (b) medium temperature region (180°C<T_c<210°C) (c) high temperature region (T_c>220°C) [60]

PD and breakdown tests were carried out for the untreated and annealed PET. It was found that regardless of the PET film types, both PD resistances and PD lifetimes of the annealed samples were superior to that of the untreated samples, especially when the annealing temperature T_c is above 210°C. Significant improvements of the sample PD resistances are observed in the high annealing temperature region, as shown in figure 5.6. Similarly in figure 5.7, remarkable increases of the sample PD lifetimes can be achieved when the annealing temperature is higher than 210°C (200°C for PET-FR), all the PD lifetimes can be at least extended by a factor of 70% when the samples were crystallized at their highest annealing temperatures. However, it should be noted that when the annealing temperature is in the region of medium temperature (180°C<T_c<210°C), only inconspicuous increases of PD lifetimes can be found for all the samples. For

example, PD lifetime of PET-FR barely enhanced until the annealing temperature reached 210°C (figure 5.7). Schematics of electrical tree propagations caused by PD in untreated and annealed PET films are shown in figure 5.9. It is known that PD will selectively propagate through the 'weak points', namely the amorphous parts of the materials. In the case of untreated PET since only primary lamellae are present, the overall lamellae thickness of the untreated PET is the thinnest among the three conditions. Electrical trees will travel easily and quickly inside the polymer due to the relatively large amorphous area and thin lamellae structure, leading to a short PD lifetime of the material. When the sample is crystallized at a temperature below 210°C, secondary crystallization can occur due to the high mobility of molecular chains which can facilitate the polymer chains to form secondary lamellae. The thicknesses and portions of the secondary lamellae increased with the annealing temperature and time, as already demonstrated in the previous DSC results. These secondary lamellae are usually thin and defective, as a result although they can block the electrical tree propagation paths to a certain extent, the electrical trees are believed to be able to penetrate through the defective secondary lamellae (figure 5.9(b)). This could be the possible reason why the PD lifetime barely increases when the sample is annealed in the medium temperature region. Furthermore, 215°C has been widely reported to be the limit temperature of existence of the so called 'rigid amorphous fraction' (RAF) in PET materials [63] [78]. The RAF is defined as an interphase region between the traditional crystalline and amorphous sections whose chain mobility is usually hindered by the surrounding area [63]. According to J. Lin and S. Shenogin [69], vitrification of the RAF can occur at temperature above the glass transition temperature T_g and will be accompanied with the formation of extra excess-hole free volume. When encounter the defective excess-hole free volume, the propagation of electrical trees will undoubtedly accelerate leading to the shortening of PD lifetime. Lastly, when it comes to the high annealing temperature region (T_c>220°C), a much more uniform distribution of lamellae thickness and perfection of crystal are obtained due to the significant increase of the secondary lamellae thickness. The highly thickened lamellae structures of the PET samples can extend the tortuosity of the propagation paths of electrical trees, thereby increasing the sample PD lifetime, as demonstrated in figure 5.9(c). Furthermore, the absence of RAF and excess-hole free volume due to the high annealing temperature can also play an important role in the PD lifetime extension.

As shown in figure 5.7, PD lifetimes of PET-$BaSO_4$-UV and PET-FR also greatly increased after they had been crystallized at high temperatures, suggesting the synergistic effect of performance additives and annealing treatment. The voltage endurance ability of PET film can be tremendously improved, especially when the sample is functioned with phosphorus based flame retardant and high temperature annealed. From the figure it can be seen that after annealed at 220°C for one hour, the average PD lifetime of PET-FR went up to 744 mins — equivalent to 7 times the average PD lifetime of the untreated PET sample.

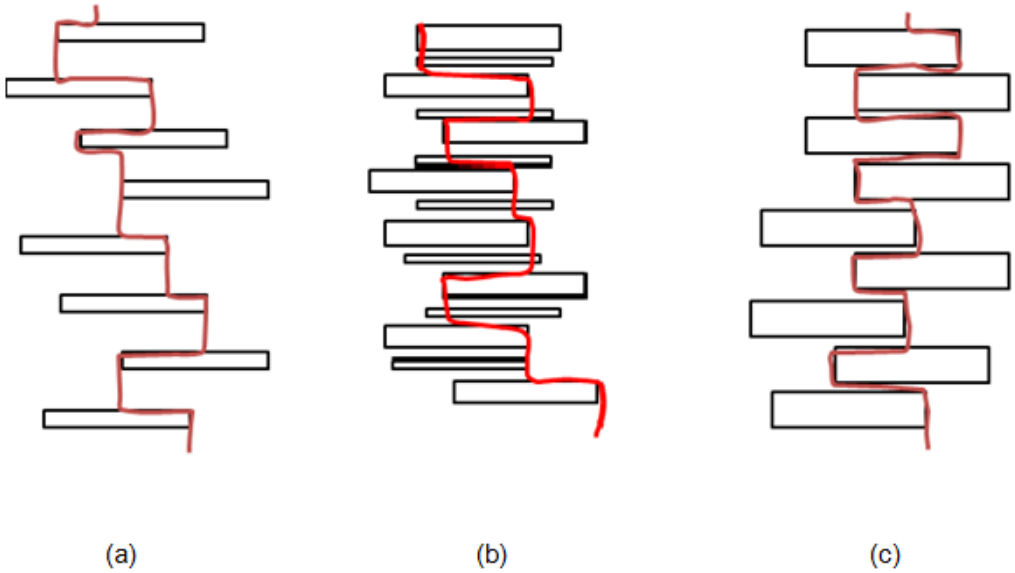

Figure 5.9 Propagation of PD-initiated electrical trees in (a) untreated PET (b) PET annealed at T_c<220°C (c) PET annealed at T_c>220°C

5.4 Conclusions

Three types of PET films with different performance additives, namely, pure PET, PET filled with 18% $BaSO_4$ particles plus Tinuvin 1577 UV stabilizer (PET-$BaSO_4$-UV) and PET functioned with phosphorus based flame retardant (PET-FR) that have been studied in chapter 3, were isothermally crystallized at various temperatures from 180 to 230°C (PET-FR was only annealed up to 220°C due to its low melting point). Afterwards the annealed samples were subjected to identical voltage

stresses to analyse the annealing treatment effect on PD resistances and PD lifetimes of the samples. Experimental conclusions can be made as below:

1. Thicknesses and portions of secondary lamellae of the samples increased with the annealing temperatures. A highly uniform distribution of lamellae thickness can be obtained when the samples were subjected to high annealing temperatures (T_c>220°C).
2. Both PD resistances and PD lifetimes can be remarkably improved when the samples were annealed at temperatures above 210°C (200°C for PET-FR). However the improvements became much slower in the medium annealing temperature region (180°C<T_c<210°C). This is because the thin and defective secondary lamellae produced in the low temperature region are not strong and firm enough to hinder either ion bombardment or electrical tree propagation. On the other hand, the highly thickened and perfected lamellae produced in high annealing temperatures can effectively increase the tortuosity of electrical tree propagation paths, thereby increasing the sample PD lifetimes. Moreover, the effect of the rigid amorphous fraction (RAF) and excess-hole free volume whose temperatures limit of existence are about 215°C must be taken into account as well.
3. Synergistic effect can be achieved when the additives functioned PET is annealed at temperatures above 210°C. For example, the average PD lifetime of the untreated PET-FR is 436 mins and the lifetime can be even further improved up to 744 mins after annealing treatment, which is 7 times the PD lifetime of the untreated PET. One explanation of the synergistic effect of the PET-FR is that there will be a tendency for the phosphorus parts of the polymer chains to be excluded from the crystalline regions. This means the amorphous regions will become increasingly rich in the phosphorus additives.

Chapter Six

6.Weathering and hydrolysis effects on PD degradation of PET

6.1 Introduction

Backsheet, as being the most important protection component of a PV module, not only provides insulation property for the module but also needs to protect the inner components from external stresses such as UV rays and moisture. The PV modules are expected to perform at least 25 years under long-term outdoor exposure and this would be impossible without proper backsheet material selection. Poor backsheet materials will deteriorate rapidly when they are subjected to harsh environments where strong UV radiation, moisture and high temperature are combined. Photodegradation and hydrolysis are known as the two main degradation processes for the backsheet materials that can lead to rapid decline of the module efficiency, loss of dielectric properties, formation of cracks on the backsheet and even delamination of backsheet layers.

Tedlar/PET/Tedlar is the only backsheet structure that has over 25 years field-proven lifetime thanks to excellent weathering and hydrolysis resistance of the poly(vinyl fluoride) (PVF) layer on the air side. Unstabilized standard PET is intrinsically vulnerable to photodegradation and hydrolysis, making it unsuitable for being the outermost layer of PV backsheets. However, nowadays PET is receiving more and more commercial attractions since it is much cheaper than the PVF

material. What's more, engineering-grade stabilized PETs show great UV and hydrolysis resistance compared to the standard ones [126, 147, 148] although there is no 25 years field-proven lifetime report for the PET-based backsheets yet only because the PET-based structures are quite new hence most of these products are still in service.

Both mechanisms of photodegradation and hydrolysis of PET have been extensively studied over the past few decades [51, 100, 126, 146-149, 151-159]. For photodegradation, two main schemes named Norrish type 1 and type 2 are illustrated in figure 6.1 [51]. As shown in the figure, the three possible paths for Norrish type 1 proceed via the cleavage of the ester functional group in PET molecule, subsequent reactions can include the generation of CO and CO_2, as well as chemical groups such as carboxylic acids, alcohols and hydroperoxides [100], while the Norrish type 2 reaction involves the intramolecular abstraction of a α-hydrogen [51]. Chemical degradation can lead to yellowing, loss of toughness, brittleness and formation of cracks on the material surface.

The mechanism of hydrolytic degradation of PET is shown in figure 6.2. From the figure, the ester group of PET is attacked by water and broke into two smaller chain segments. Subsequent reactions involve the generation of a carboxylic acid and an alcoholic end groups using one water molecule [156, 159]. There is ample evidence in the literature that hydrolysis will become much more significant when experimental temperatures are above the glass transition temperature (T_g) [156-161]. 'Chemicrystallization' is a well-accepted phenomenon for semicrystalline polymers that can occur in hydrolytic degradation. During the degradation water can merely diffuse into the amorphous regions therefore these are the only regions where chain scissions can take place. Smaller chain fragments caused by hydrolysis will have higher mobility to recrystallize [156-161].

As stated earlier, photodegradation and hydrolysis are the two main reasons for deteriorations of PV backsheets and hydrolysis seems to be the more significant one. Commercial backsheet products will need to pass the so-called 'UV preconditioning test' and 'Damp heat test' listed in IEC 61215 where the samples will subjected to a total UV irradiation of 15 kWh/m^2 in the wavelength between 280 to 385 nm and to an environment of 85°C and 85% relative humidity for 1000 hours, respectively before any qualification tests like wet leakage current test and mechanical load test [162]. According to M. Kontges and S. Kurtz [163], the damp

heat test is the most critical test which causes 17% and 22% failure rates for crystalline PV and thin-film modules, respectively. Some poor backsheets even lost their basic functionalities completely after the 1000-hour damp heat test due to high extent of hydrolysis.

The correlation between the weathering and hydrolysis effects and the PD-induced degradation of PET materials is still not well understood. In this chapter, the PD-induced breakdown behaviours of photolyzed and hydrolysed PET films will be investigated in detail. The effects of pigments, UV stabilizer and hydrolysis stabilized sample are also discussed. Before the final dielectric tests, the samples were treated by protocols even more critical than those in the IEC 61215. The extents of chemical degradation of the pre-treated samples were analysed using ATR-FTIR and DSC.

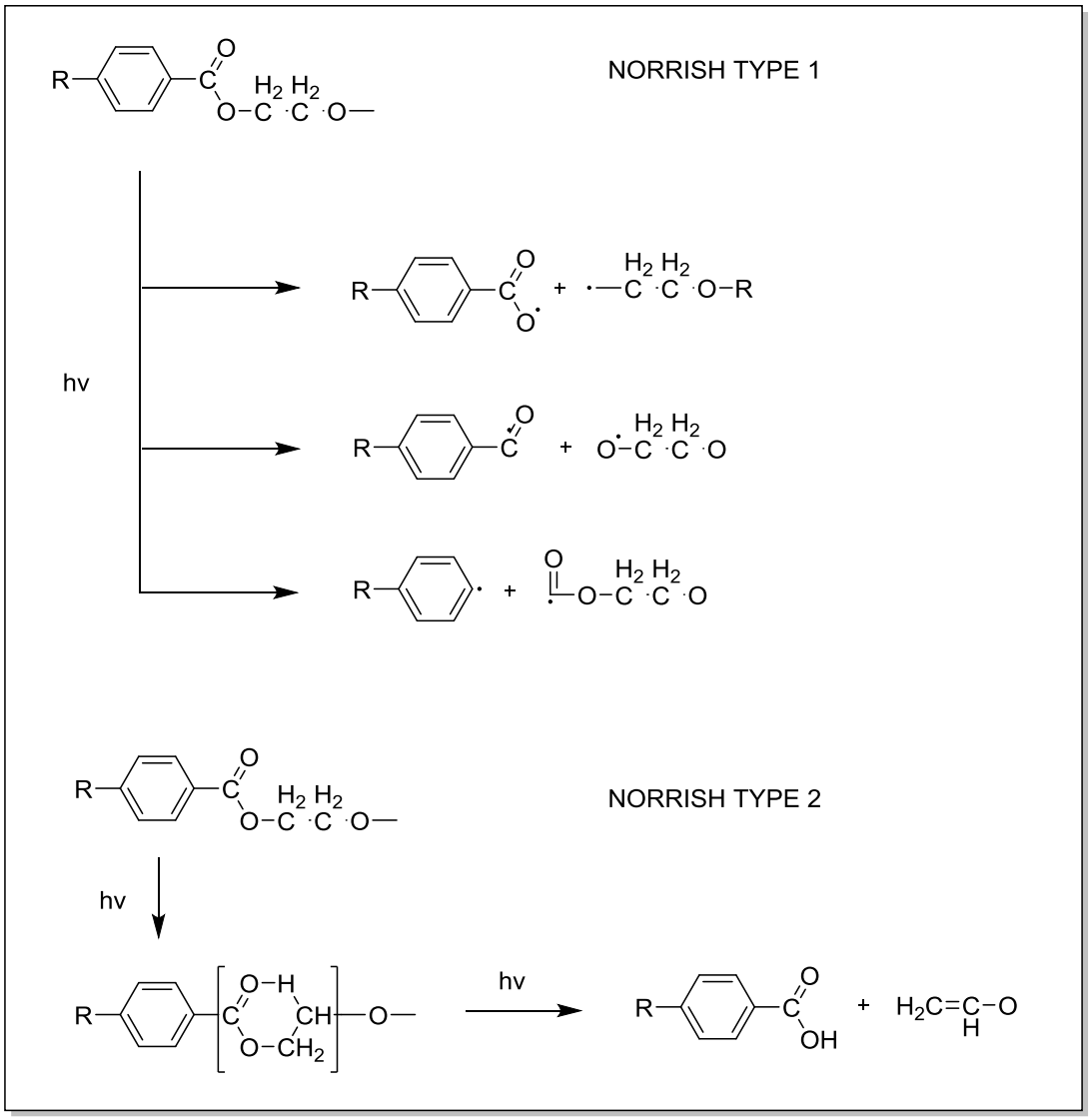

Figure 6.1 Mechanisms of PET photodegradation (schemes of Norrish type 1 and 2) [51]

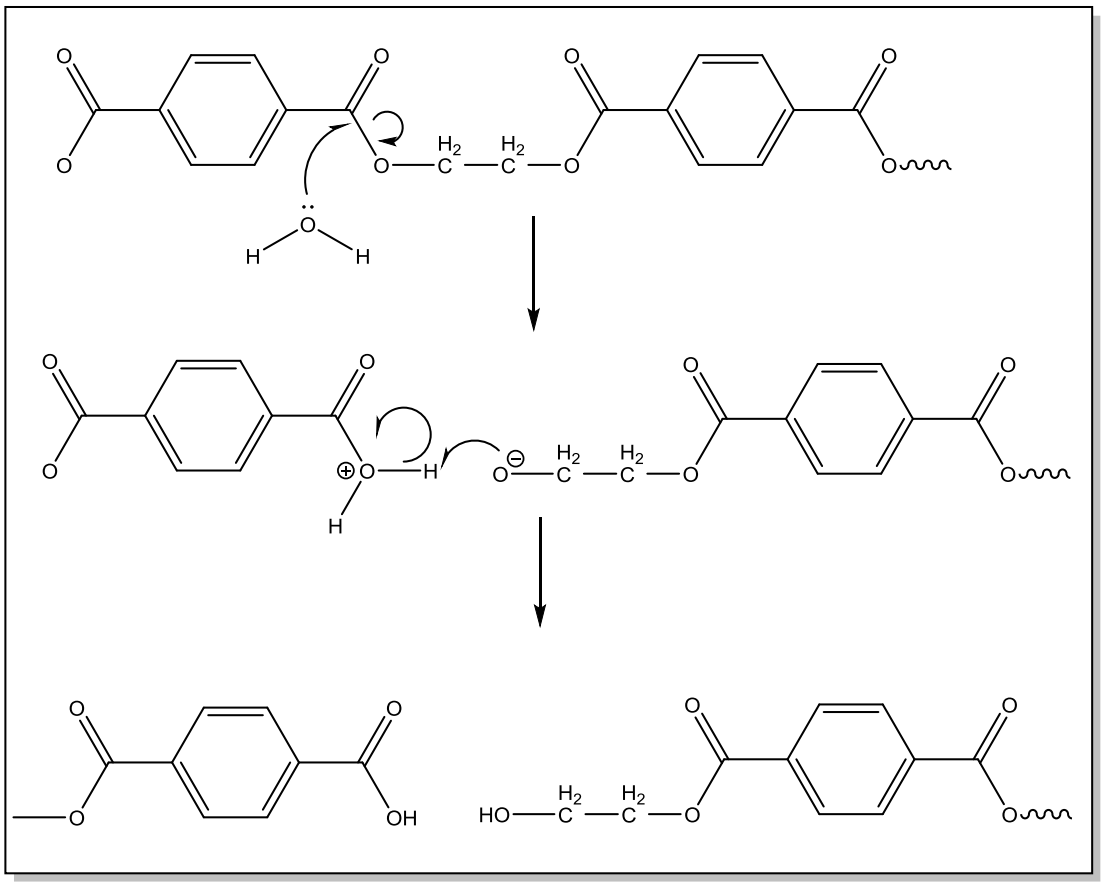

Figure 6.2 Mechanisms of PET hydrolysis [156]

6.2 Experimental

6.2.1 Samples

Three categories of biaxially oriented, semicrystalline PET films filled with various performance additives that were already discussed in chapter 4 were used to investigate the weathering and hydrolysis effect on PD degradation and breakdown of PET films. The samples were provided by DuPont Teijin Films and all in 50 µm thickness. The three sample categories are described as below:

1. Universal biaxially oriented PET without any additive (PET).
2. PET filled with 18% $BaSO_4$ (PET-$BaSO_4$).

3. PET filled with 18% $BaSO_4$ and functioned with 1.0% Tinuvin 1577 UV stabilizer (PET-$BaSO_4$-UV). According to the manufacturer, this sample has also improved to hydrolysis compared to universal PET films.

6.2.2 Weathering treatments of samples

Photodegradation experiments of the films were carried out in an Atlas Suntest XLS+ weatherometer using a xenon arc lamp that has been introduced in chapter 2. The sample films, namely, PET, PET-$BaSO_4$ and PET-$BaSO_4$-UV were aged for 2, 5, 9, 14, 20, 24 and 30 days. The light irradiance was set to 700 W/m^2 in the wavelength range between 300 to 800 nm. The black standard temperature (BST) was set to 65°C. In order to accelerate the degradation process even further, no dark/light period cycling was used during the experiments. The correlation between the artificial weathering experiments and real-time outdoor exposures can be calculated as below: 700 W/m^2 in the wavelength range 300 – 800 nm approximately equals to 0.7 W/m^2 at 340 nm, therefore the total UV dose at 340 nm the samples received after 30 days of exposure is 0.7 x 3600 x 24 x 30 = 1814 kJ/m^2. The annual mean UV dose at 340 nm in Florida is 2800 kJ/m^2 [150], hence 30 days of exposure in the weatherometer is equivalent to about 240 days exposure in Florida. Considering PV backsheet materials will only receive approximately 15% of the total UV radiation from the sun by ground reflection, therefore the actual equivalent exposure time in Florida will be 240/0.15 = 1600 days, which is nearly 4.5 years. For the exposed samples, the sides faced to the xenon arc lamp and the opposite sides are defined as side A and side B, respectively.

6.2.3 Hydrolysis treatments of samples

Hydrolytic degradation experiments were carried out by using the standard PET and hydrolysis resistive PET-$BaSO_4$-UV sample films. The samples were totally immersed in deionised water for 14, 21, 28, 35, 42 and 50 days. The temperature of the water was set to 90°C, which is well above the glass transition temperatures (T_g ≈ 83°C) of the samples. The water was changed every 7 days to make sure the pH value of the water was constant during the whole experiment.

6.2.4 Experimental set-up of dielectric breakdown caused by PD

The schematic of set-up for breakdown tests due to PD erosion has been shown in 3.2.2.2 of chapter 3. Single sheet of the treated samples with different additives were subjected to a 50Hz AC high voltage of 3kV until the sample breakdown due to PD erosion. For each sample category, at least five samples were tested and the average values of the PD lifetime of each category were calculated.

6.2.5 Experimental of analytical methods for sample characterisation

6.2.5.1 DSC

For all the samples, a heat-cool-reheat programme was used to record thermograms. The programme was designed as: (1) a heating run from 40 to 320°C, then the temperature was held at 320°C for 2 minutes to make sure the samples melt completely (2) a cooling run from 320 to 40°C and (3) a second heating run from 40 to 320°C. All the three runs were performed at a heating/cooling rate of 10°C/min and N_2 was used as purge gas with a flow rate of 40 mL/min.

6.2.5.2 Other analytical methods

Other analytical methods for sample characterisation have been previously described in chapter 2.

6.3 Results and discussions

6.3.1 FTIR analysis

Photodegradation

ATR-FTIR spectra of side A and side B of photolyzed PET in the weatherometer from 0 to 30 days are shown in figure 6.3 and 6.4, respectively. As expected, significant changes can be observed on the top sides (side A) of the exposed PET

samples (figure 6.3) where photodegradation took place due to the ultraviolet radiation from the xenon lamp. For the bottom sides (side B), ATR spectra are highly overlapped (figure 6.4) and very little spectral changes are seen, suggesting rare or no chemical change took place on the bottom sides of the exposed samples. Therefore, further ATR-FTIR data discussions will only focus on sides A of the samples. Very broad bands from 2200 to 3650 cm^{-1} with strong intensities were observed for the weathered PET, as shown in figure 6.3. The bands are attributed to hydroxyl (-OH) groups stretching in functional groups of carboxylic acids (2500-3300 cm^{-1}), alcohols and phenols (3200-3650 cm^{-1}) and aldehyde (2700-2850 cm^{-1}), which are common reaction products in photodegradation of PET [100]. It is obvious the peak intensity increased with the exposure time, as expected. However, the peak intensity became saturated after 20 days of exposure. This is possibly because the penetration depth of the evanescent wave of ATR-FTIR is usually very shallow i.e. less than 5 microns, as discussed in chapter 2. Carbonyl is a useful absorption band in FTIR spectrum for characterisation of PET photodegradation [146-155]. The high wavenumber regions (1300-1900 cm^{-1}) including carbonyl bands and fingerprint regions (650-1300 cm^{-1}) of the untreated and exposed PET are shown in figure 6.5 and 6.6, respectively. In figure 6.5, one can see that the strong absorption peak at 1714 cm^{1} which is assigned to the original carbonyl in ester group of PET, decreased with exposure time. This can be explained by the cleavage of original ester groups in PET via Norrish type 1 reaction of PET (figure 6.1). The newly generated strong peak at 1694 cm^{-1} is attributed to aromatic carboxylic acid [164] while the weaker peak at 1780 cm^{-1} can be assigned to hydroperoxide that can be produced by photo-oxidation of the glycol portion of PET molecule during photodegradation [100]. A new formed weak band at 1430 cm^{-1} is also observed for the exposed samples, which is due to the in-plane bending of OH groups. The two strong bands at 1244 and 1098 cm^{-1} that associated with O=(C-O)-C and O=C-(O-C) stretching (figure 6.6), decreased with exposure time due to ester functional groups break down, similar as the carbonyl band at 1714 cm^{-1}. On the other hand, the increases of the bands at 1200 and 1055 cm^{-1} are assigned to the vibrations of C-O groups in carboxylic acids, alcohols and phenols. In the lower regions of spectra, the new weak bands at 942 and 782 cm^{-1} can be assigned to the out-of-plane bending of OH groups in carboxylic acids, alcohols and phenols.

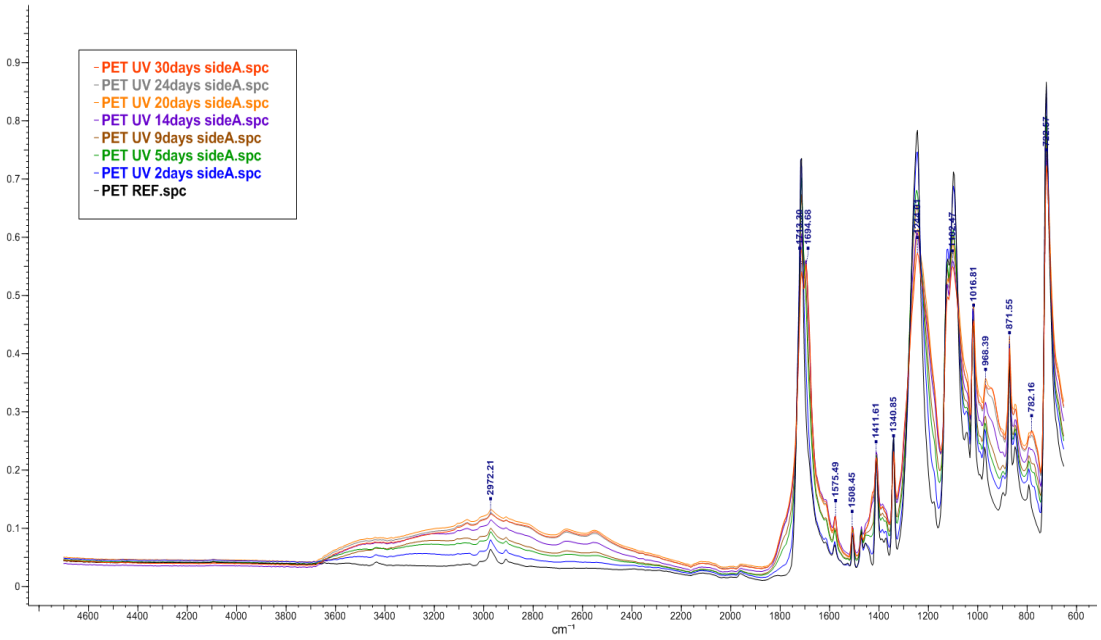

Figure 6.3 ATR-FTIR spectra of weathered PET from 0 to 30 days (side A)

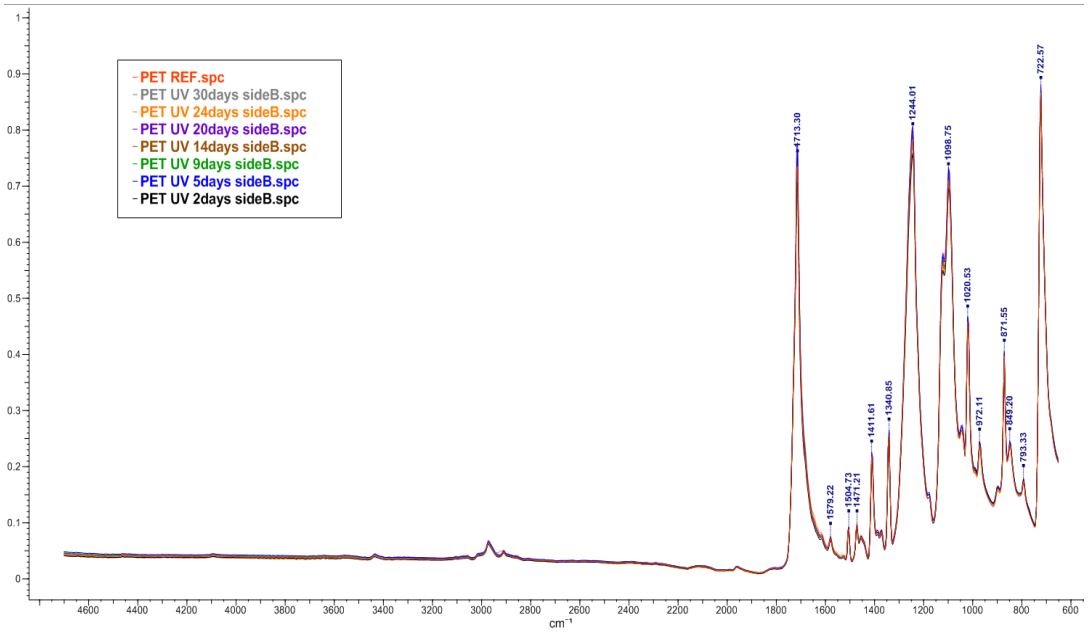

Figure 6.4 ATR-FTIR spectra of weathered PET from 0 to 30 days (side B)

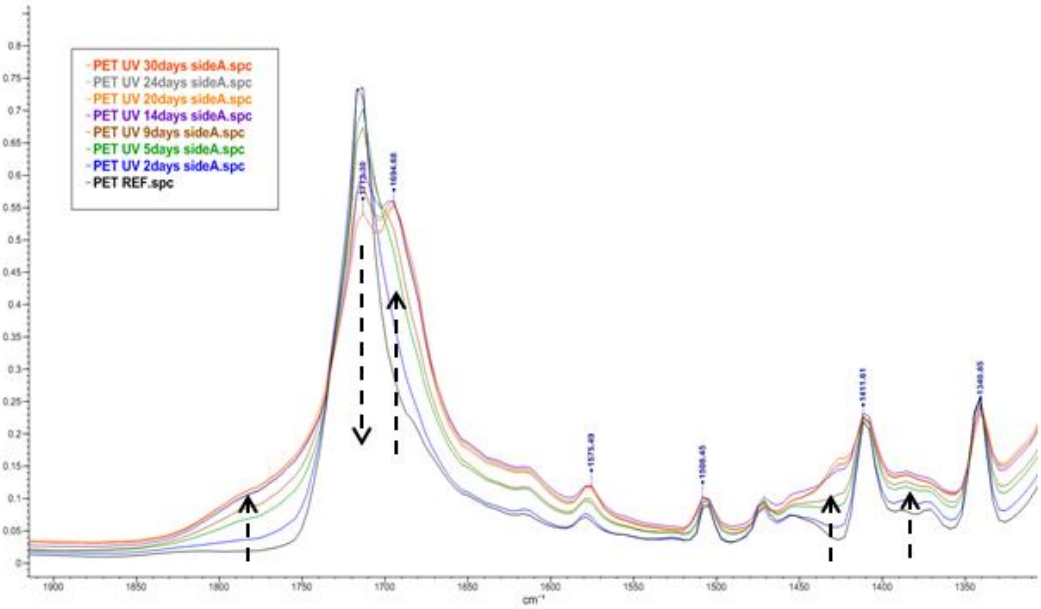

Figure 6.5 Carbonyl band changes of weathered PET from 0 to 30 days (side A)

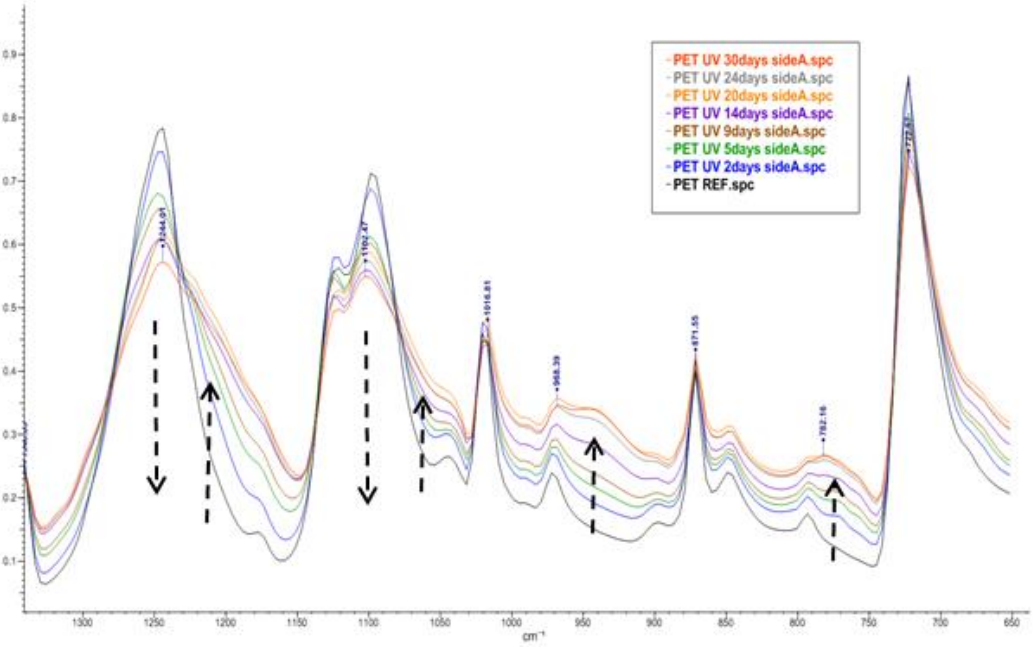

Figure 6.6 Fingerprint regions of weathered PET from 0 to 30 days (side A)

ATR-FTIR spectra of side A and side B of untreated and exposed PET-$BaSO_4$-UV from 0 to 30 days are shown in figure 6.7 and 6.8, respectively (spectra of PET-

$BaSO_4$ are similar with PET-$BaSO_4$-UV and shown in figure A.9 and A.10 in appendix A). Hydroxyl (-OH) broad bands from 2200 to 3650 cm^{-1} were also observed for the exposed PET-$BaSO_4$-UV but the intensities of the bands are much smaller than those of the exposed PET films, indicating the extents of chemical degradation on the PET-$BaSO_4$-UV films were weaker. The high wavenumber regions (1300-1900 cm^{-1}) including carbonyl bands and fingerprint regions (650-1300 cm^{-1}) of the untreated and exposed PET-$BaSO_4$-UV are shown in figure 6.9 and 6.10, respectively. Similar changes are seen for the carbonyl bands of PET-$BaSO_4$-UV where the original peak representing ester decayed while the new peaks due to oxidation products increased with exposure time. Furthermore, the two characteristic absorption bands of $BaSO_4$ at 1184 and 1080 cm^{-1} became stronger while the original ester bands of the polymer at 1244 and 1098 cm^{-1} decreased after weathering treatment, suggesting a 'filler pile-up' (discussed in chapter 4) like phenomenon had occurred caused by surface decomposition for the $BaSO_4$-based PET films.

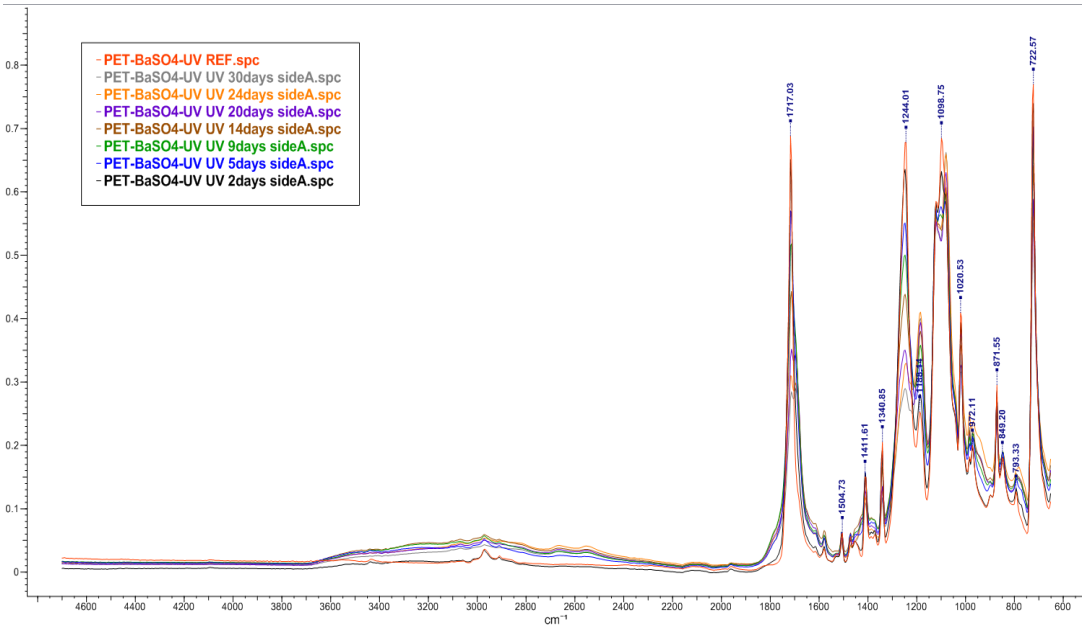

Figure 6.7 ATR-FTIR spectra of weathered PET-$BaSO_4$-UV from 0 to 30 days (side A)

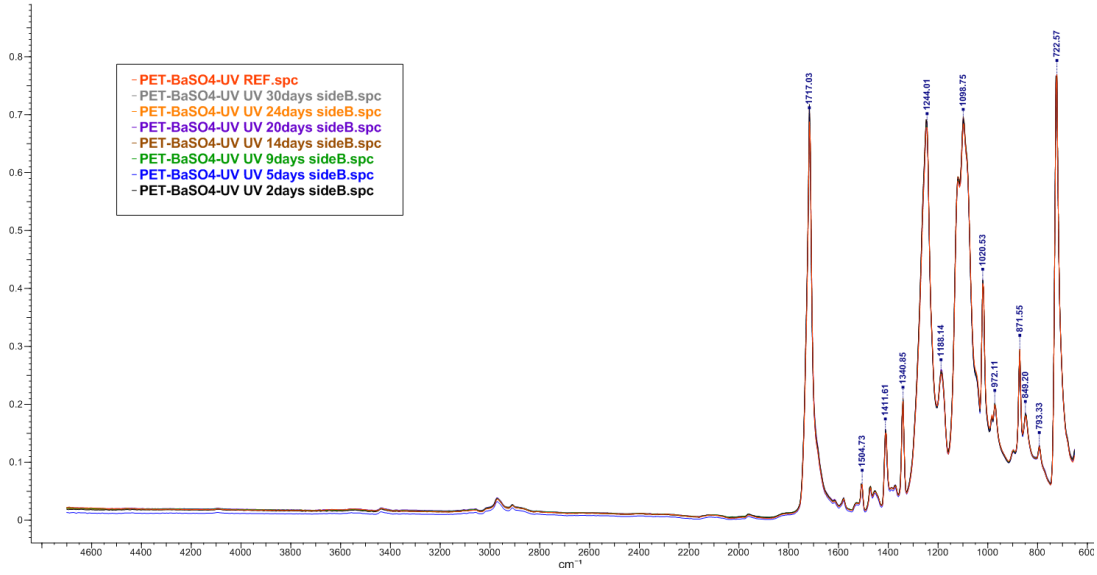

Figure 6.8 ATR-FTIR spectra of weathered PET-$BaSO_4$-UV from 0 to 30 days (side B)

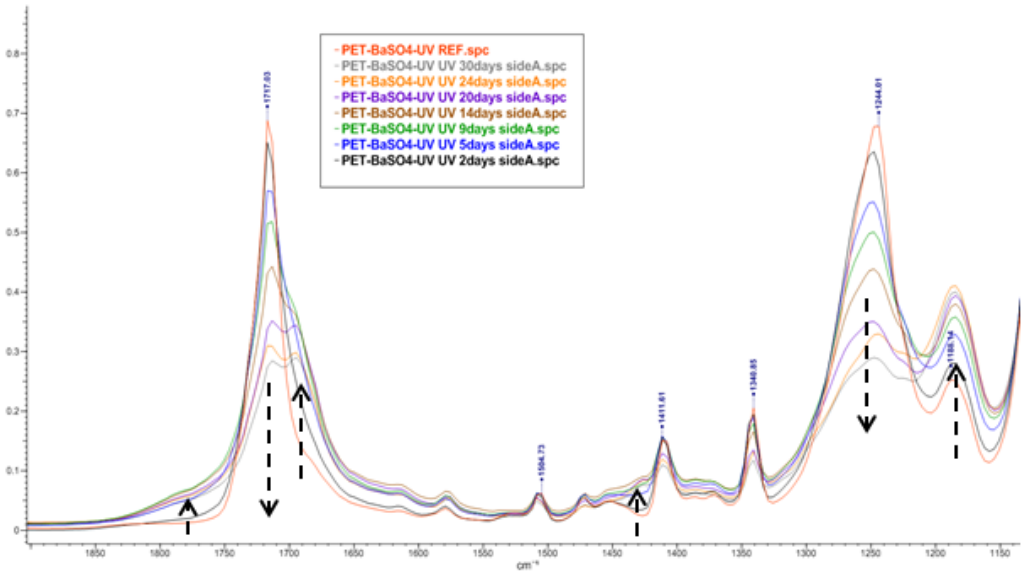

Figure 6.9 Carbonyl band changes of weathered PET-$BaSO_4$-UV from 0 to 30 days (side A)

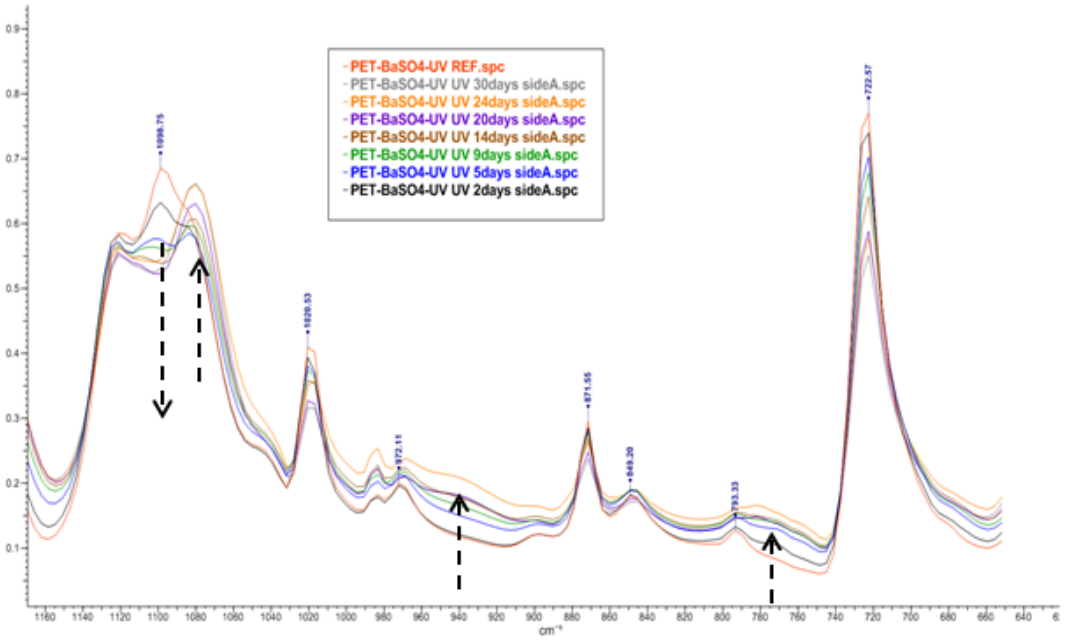

Figure 6.10 Fingerprint regions of weathered PET-$BaSO_4$-UV from 0 to 30 days (side A)

In order to characterize the extents of surface chemical degradation of the three samples quantitatively, peak areas of the hydroxyl groups (2250-3650 cm^{-1}) of the exposed samples were calculated and shown in figure 6.11. It is seen that hydroxyl group concentrations increased with exposure time at the early stages (T<9 days) for all types of samples and the increasing rate of unstabilized PET is clearly higher than that of PET-$BaSO_4$ and PET-$BaSO_4$-UV. Furthermore, it can also be seen the concentration for unstabilized PET kept increasing until 20 days and the peak intensity reached as high as 63 at the end of the experiment while in the cases of PET-$BaSO_4$ and PET-$BaSO_4$-UV, the hydroxyl group concentrations became saturated after only 9 days of weathering exposure and even started declining at a slow rate afterwards, after 30 days of exposure the hydroxyl group concentrations for these two samples are about only 22. This can be explained by screening effect caused by the pigment 'pile-up' phenomenon, when $BaSO_4$-containing samples were subjected to UV exposures, the sample surface would decompose and leave the white pigments on the top side of the samples, as evidenced by figure 6.9 and 6.10. These $BaSO_4$ particles with high UV reflectance in the range of 300-400 nm

are believed to be able to shield the remaining polymer from the UV light thereby preventing further photo-oxidation.

From figure 6.5 and 6.9 a strong peak at 1694 cm^{-1} representing aromatic carboxylic acids could be found for all types of exposed samples. A deconvolution procedure was performed via the OriginPro 8.6 software for the carbonyl band of each sample and acid/ester ratio was obtained by calculating the peak area ratio of the peak at 1694 and 1714 cm^{-1}, to further characterize the degree of photodegradation of each sample quantitatively and the result is given in figure 6.12. It is obvious the acid/ester ratio of unstabilized PET increased much faster than that of the other two samples while the UV stabilized PET-$BaSO_4$-UV showed the least increase.

It was discussed in chapter 4 that surface degradation extents of $BaSO_4$-based PET films caused by surface discharge erosion can be characterized by calculating the ratio of the characteristic band of $BaSO_4$ at 1184 cm^{-1} and the ester band of PET at 1247 cm^{-1}. Similar pigment 'pile-up' effects had been found for both PD treated and weathering treated samples, therefore the pigment/ester ratio (A_{1184}/A_{1247}) was also utilized to compare the photodegradation extents of the two $BaSO_4$-based PET samples in detail thereby evaluating the effect of UV stabilizer. The overlaid ATR-FTIR spectra and the pigment/ester ratios (A_{1184}/A_{1247}) of weathering treated PET-$BaSO_4$ and PET-$BaSO_4$-UV were shown in figure 6.13 and 6.14, respectively. Smaller pigment/ester ratios thereby slower photodegradation process were found for the UV stabilized samples at every exposure time, confirming the effectiveness of the UV stabilizer in preventing photodegradation from PET films.

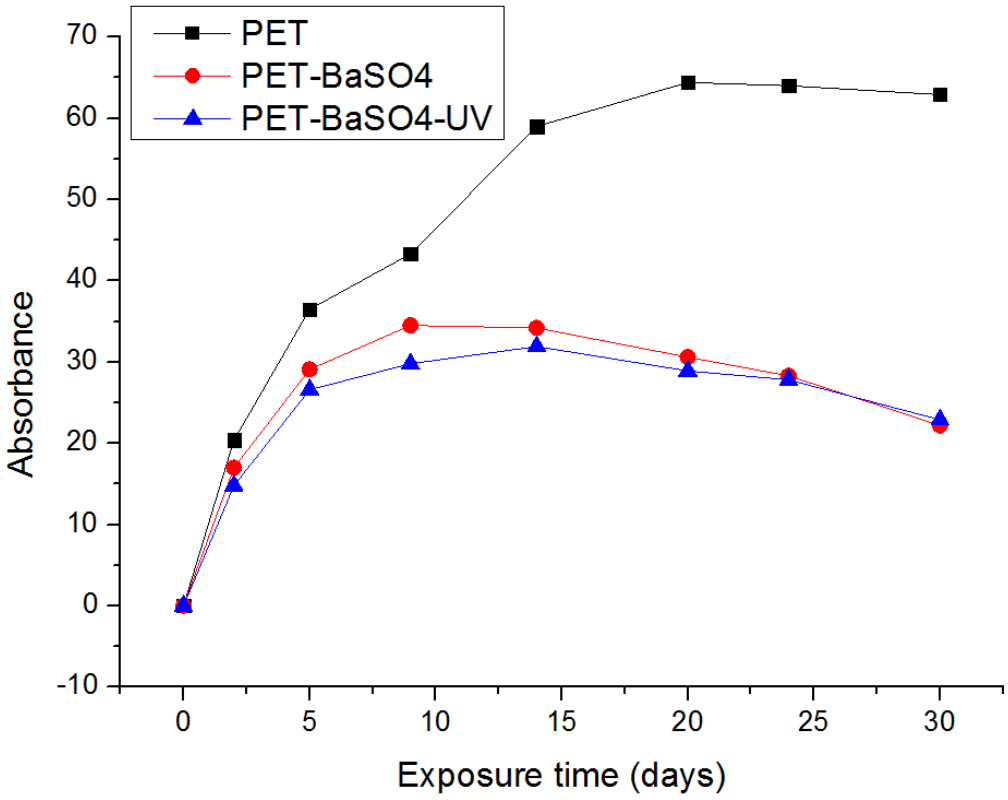

Figure 6.11 Peak areas of –OH groups (2250-3650 cm^{-1}) of the three different samples

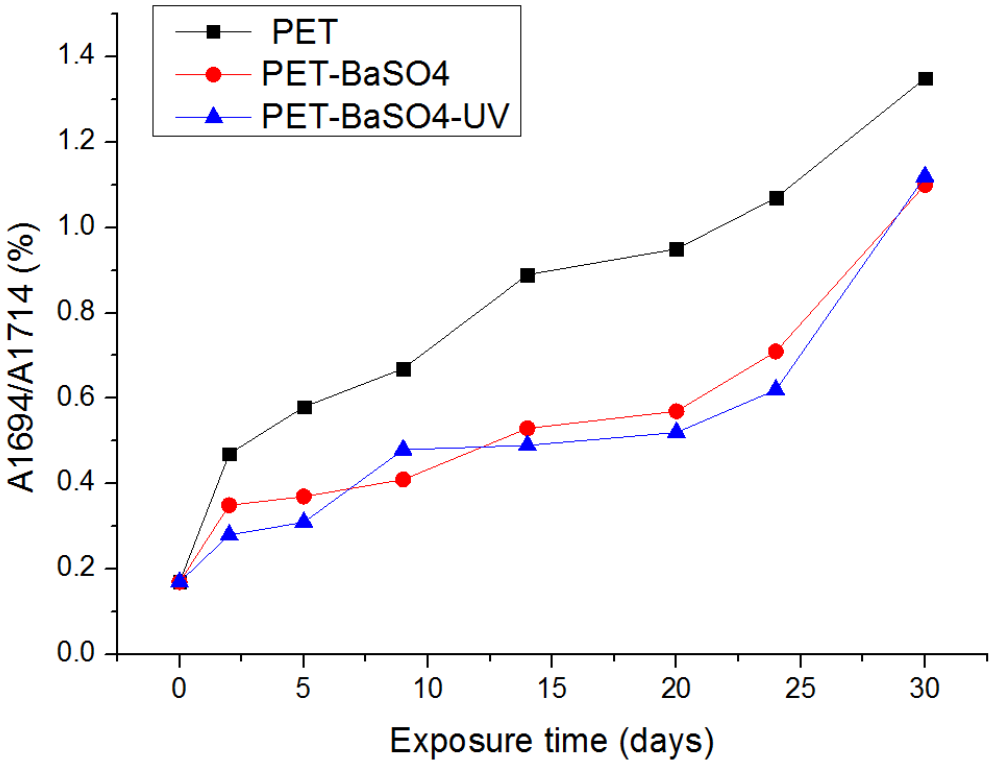

Figure 6.12 Ratio of acid and ester calculated from carbonyl bands of the three samples

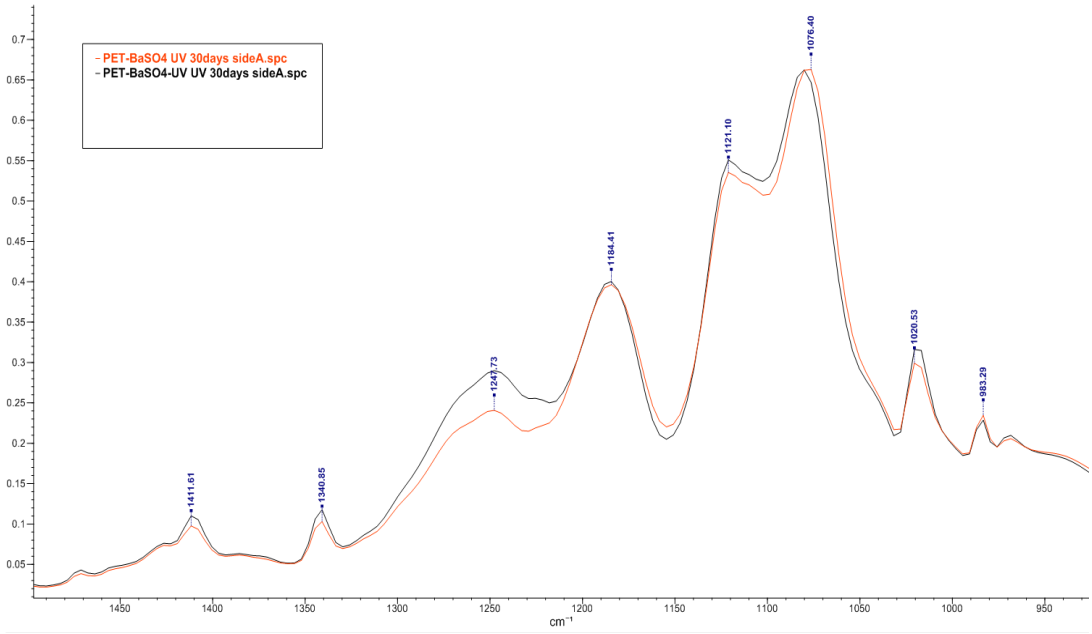

Figure 6.13 ATR-FTIR spectra of weathered PET-$BaSO_4$ and PET-$BaSO_4$-UV at 30 days

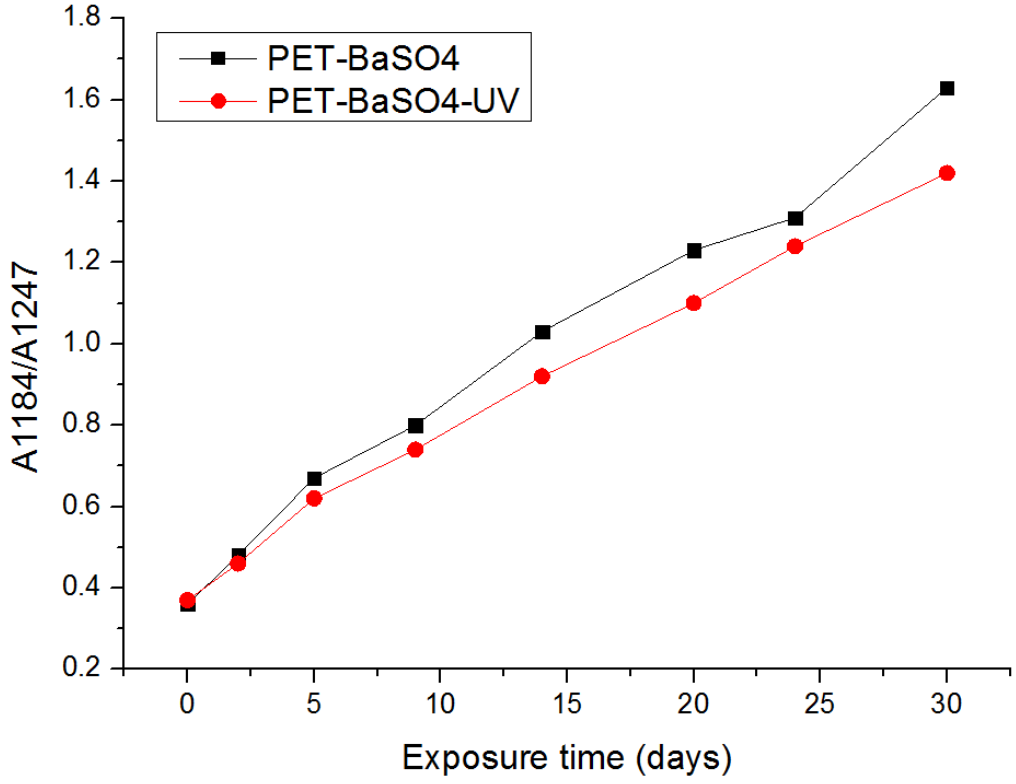

Figure 6.14 Ratios of the peaks at 1184 and 1247 cm^{-1} for PET-$BaSO_4$ and PET-$BaSO_4$-UV

Hydrolysis

The ATR-FTIR spectra of untreated and 50-day hydrolysed samples of unstabilized PET and hydrolysis stabilized PET are shown in figure 6.15 and 6.16, respectively. It can be seen that for both samples, overall spectral changes are much weaker compared to those of photodegraded samples and the only differences were observed in ester groups where the band intensities became weaker due to ester cleavages and in bands representing polymer crystallinity where the band intensities increased due to chemicrystallization in hydrolysis. This finding is consistent with the data obtained by F. Higgins and P. L. Tang [164], where the UV lights and oxygen were excluded during the experiments and hydroxyl free radical reactions being the only source of chemical changes. Therefore, further characterization of hydrolytic degradation of the samples will be performed via DSC analysis.

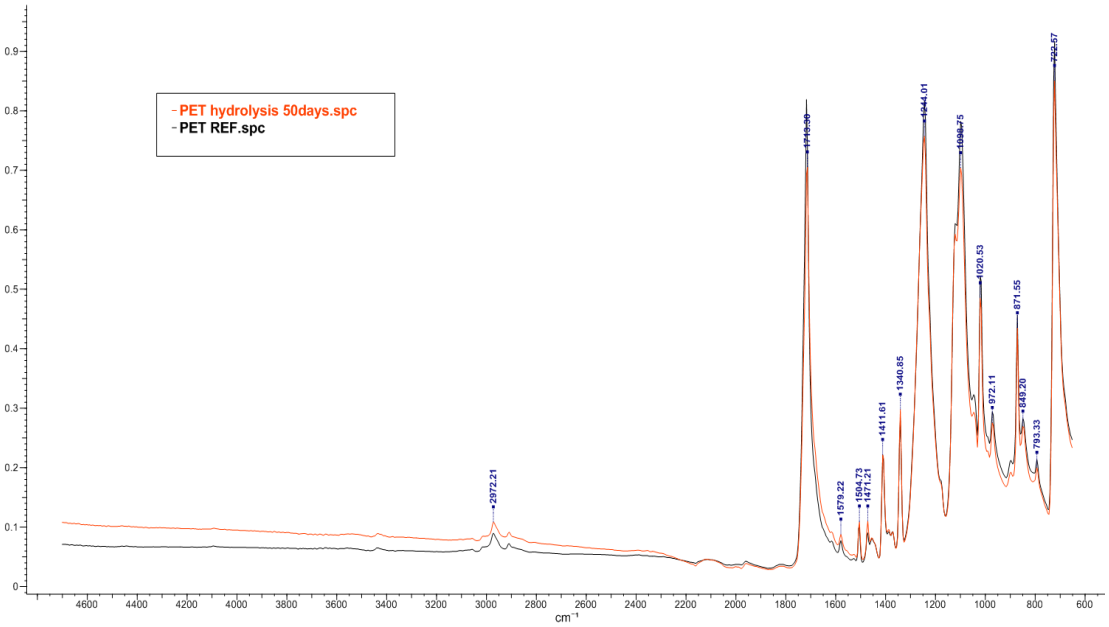

Figure 6.15 ATR-FTIR spectra of untreated and hydrolysed PET for 50 days

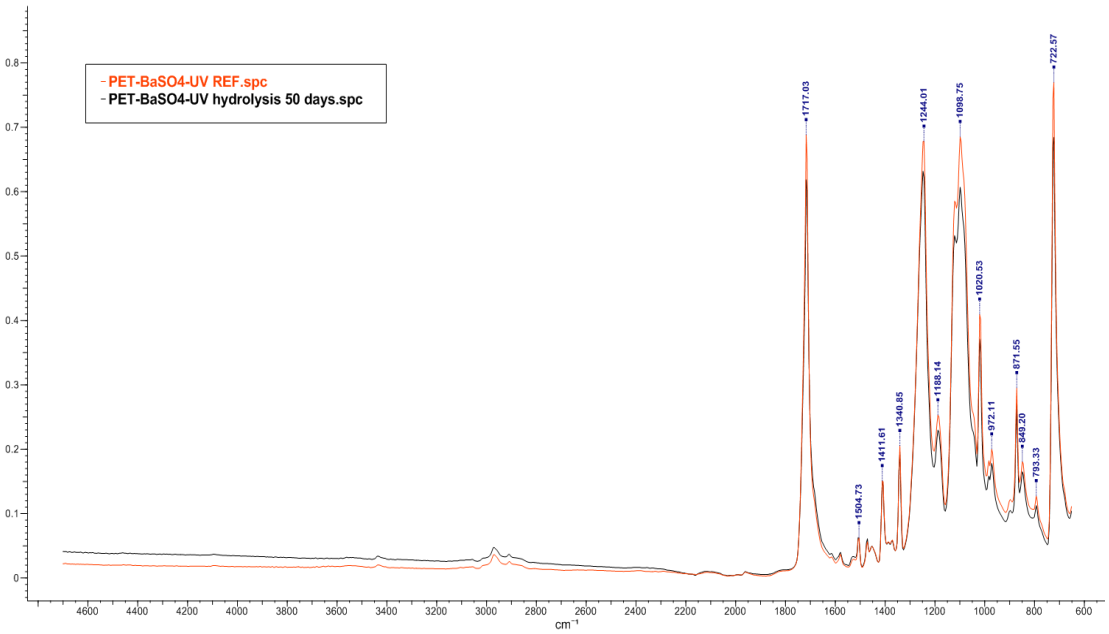

Figure 6.16 ATR-FTIR spectra of untreated and hydrolysed PET-$BaSO_4$-UV for 50 days

6.3.2 DSC analysis

Photodegradation

DSC thermograms of the three types of weathered samples are shown in figure 6.17 – 6.19. Some crucial changes can be readily observed for the thermogram of 30-day weathering treated unstabilized PET (figure 6.17). First of all, the melting endotherm became broader and the onset of the melting peak decreased to a much lower value, implying that original PET crystals were broken into smaller and thinner ones with lower melting temperatures by photodegradation, thus leading to the broadening of the whole melting endotherm [153]. Some of these lower melting peaks can be directly seen near the main melting peak (shown in the zoom in picture of the melting endotherm in figure 6.17). Secondly, the melting point of the unstabilized PET shifted to a lower temperature as well after weathering, indicating the crystal fold surfaces were also attacked, thereby increasing the crystal free energy [148]. Furthermore, a weak exothermic peak was observed at around 105°C for the degraded PET. The presence of this peak can be attributed to the cleavages of entangled polymer chains between the lamellae segments of PET where the broken chains will have enough mobility to crystallize during the DSC heating run [148].

For PET-$BaSO_4$ and PET-$BaSO_4$-UV, the changes of the DSC thermograms were much weaker and less visible compared to the unstabilized PET, melting endotherm broadening, melting point declining and the exothermic peak can be barely seen. Some important calorimetric parameters of the three different samples are summarized in table 6.1 – 6.3. Due to the presence of the exothermic peaks, the equation (2) in chapter 3 for the calculation of crystallinity degrees of the samples was modified as:

$$X_c = \frac{\Delta H_m - \Delta H_c}{\Delta H_{100\%}}$$

where ΔH_m is the measured melting enthalpy, ΔH_c is the measured crystallization enthalpy and $\Delta H_{100\%}$ is the melting enthalpy of a 100% crystalline PET, which is 140 J/g. From table 6.1 to 6.3, it can be seen that the overall crystallinity degrees almost did not change for all types of samples during photodegradation, implying the chemicrystallization did not occur for the photodegraded samples probably because the experimental temperature (65°C) is less than the glass transition temperature (T_g ≈ 83°C) of the PET samples, making the polymer chains lack of sufficient

mobility to crystallize during the degradation process. T_{m1}, T_{m1on} and T_{m2} denote the melting point in the first DSC heating run, the onset of the first melting peak and the melting point in the second DSC heating run, respectively. These are the three important parameters to describe the degradation extents of samples and it should be noted that T_{m2} was regarded as a more precise parameter than T_{m1} for degradation characterization, suggested by M. S. Rabello and J. R. White [149]. Compare the data in the tables, it is interesting to note that the decreases of T_{m2} were more significant than that of T_{m1} for all types of exposed samples indeed and largest declines of T_{m1}, T_{m1on} and T_{m2} are all found for the 30-day exposed unstabilized PET with the decline of the onset of the first melting peak T_{m1on} being the most prominent, where a drop of 11°C was found. In the case of PET-$BaSO_4$, except for T_{m1on}, both T_{m1} and T_{m2} had a very weak decline after 30 days of exposure while little changes can be observed for all three parameters and a drop of only 1°C was found in T_{m1on} of the 30-day exposed UV-stabilized PET-$BaSO_4$-UV sample, suggesting the crystal stability of this sample still remains at a high level even after 30 days of exposure.

From the above discussions, it can be easily concluded that after 30 days of exposure the crystal structure and stability of the unstabilized PET film had been severely damaged, original polymeric crystals were broken down into smaller and thinner ones, as indicated by the remarkable decreases of T_{m1}, T_{m1on} and T_{m2}. On the other hand, the crystal structures were more stable for the $BaSO_4$-based samples especially the UV-stabilized PET-$BaSO_4$-UV under photodegradation thanks to the presences of $BaSO_4$ pigments with high UV reflectance and UV stabilizers.

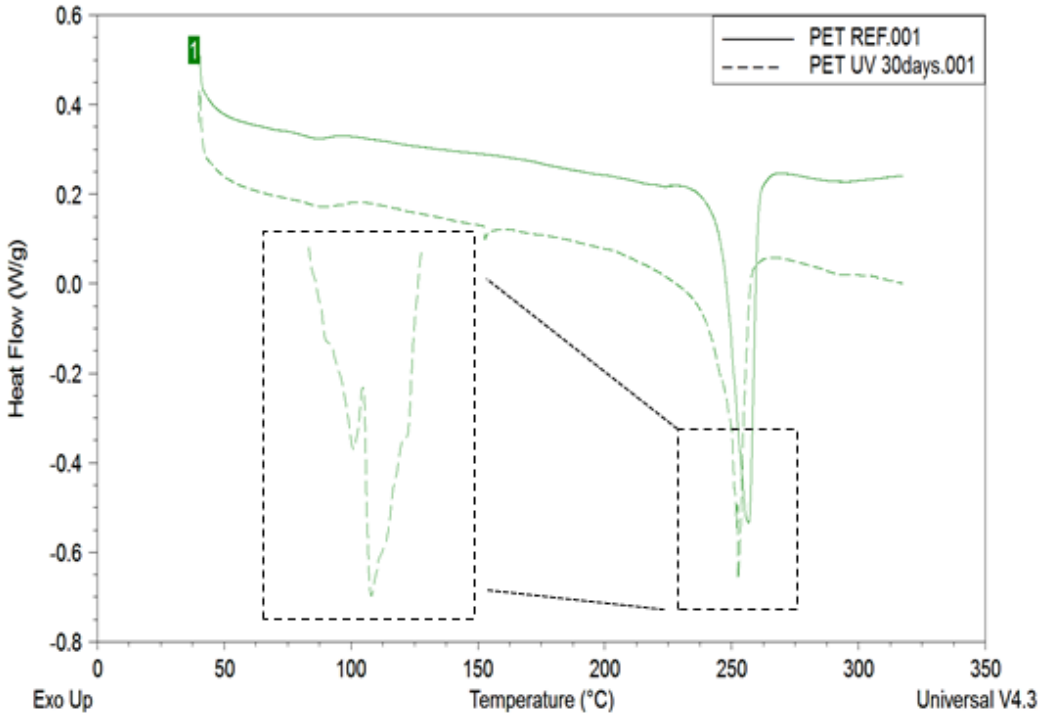

Figure 6.17 DSC thermograms of untreated and 30-day weathered PET

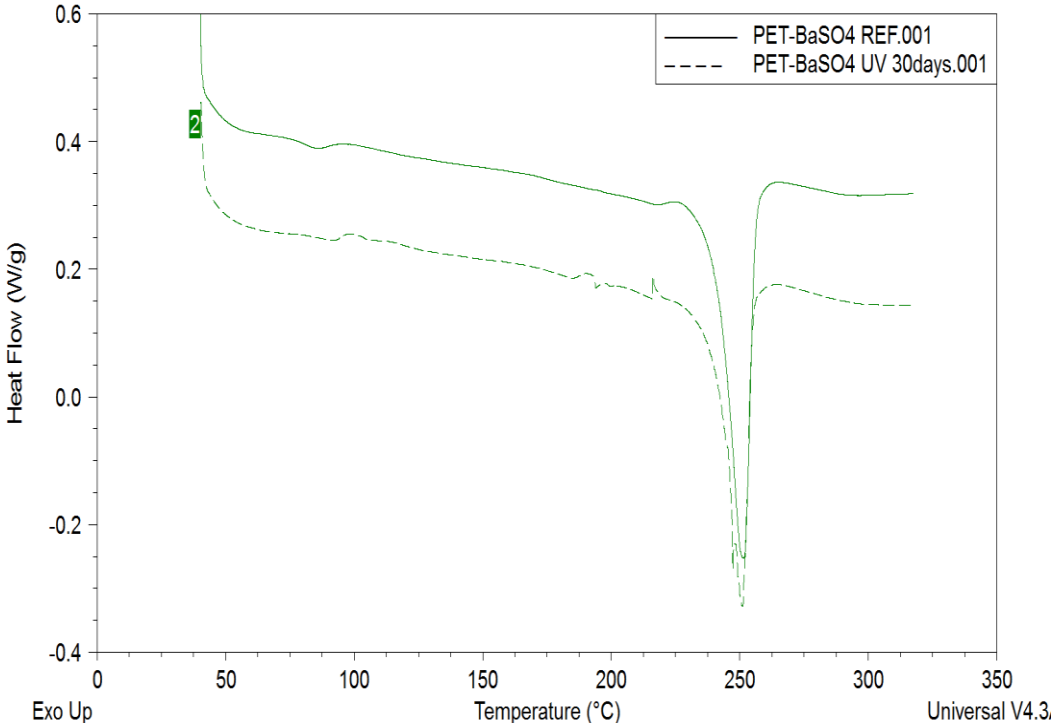

Figure 6.18 DSC thermograms of untreated and 30-day weathered PET-$BaSO_4$

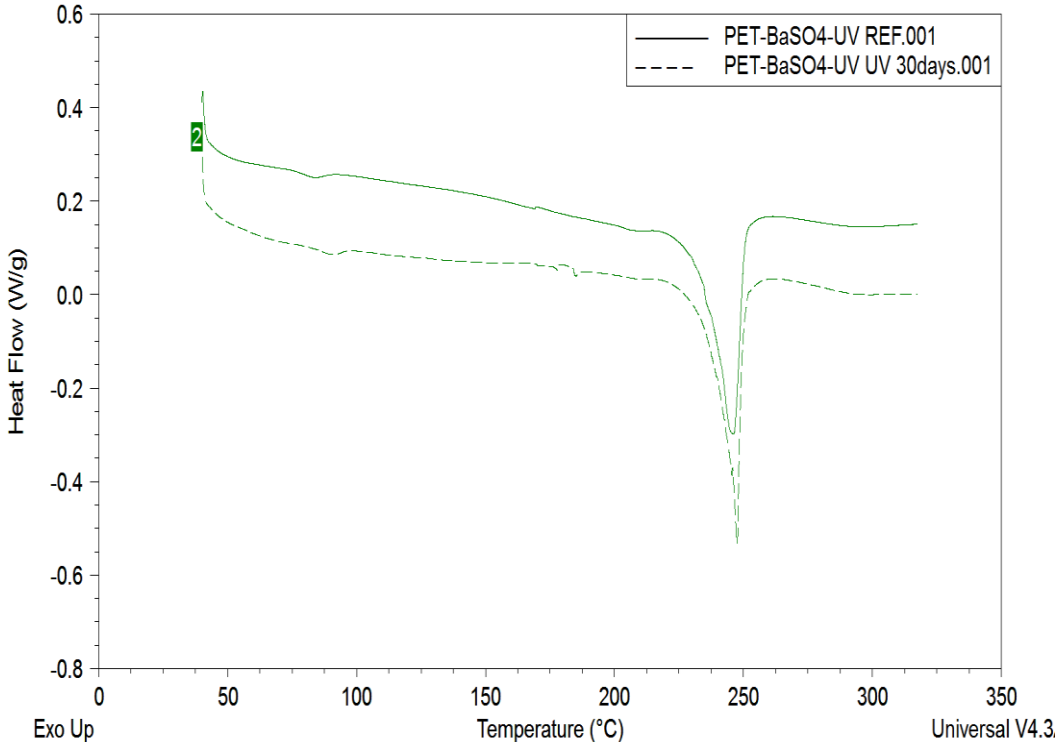

Figure 6.19 DSC thermograms of untreated and 30-day weathered PET-$BaSO_4$-UV

Samples	T_{m1}(°C)	T_{m1on}(°C)	T_{m2}(°C)	ΔH_m(J/g)	ΔH_c(J/g)	$\%X_c$
REF	256.6	244.5	255.2	45.5	0	32.5
2days	257.3	243.6	255.3	45.2	1.7	31.1
5days	257.3	243.8	254.7	45.5	1.1	31.3
9days	257.3	240.9	254.0	44.6	1.7	30.6
14days	255.1	238.7	252.0	47.8	3.3	31.8
20days	253.6	236.3	251.5	47.1	3.1	31.4
30days	252.6	233.6	249.3	48.7	3.5	32.3

Table 6.1 DSC data of untreated and weathered PET

Samples	T_{m1}(°C)	T_{m1on}(°C)	T_{m2}(°C)	ΔH_m(J/g)	ΔH_c(J/g)	$\%X_c$
REF	251.6	238.2	250.6	37.3	0	26.6
2days	252.1	237.6	250.8	36.6	0.5	25.8
5days	251.2	237.4	250.1	38.8	0.9	27.1
9days	252.7	236.9	250.5	37.4	1.4	25.7
14days	252.3	235.9	250.0	36.9	1.1	25.6
20days	251.4	233.4	249.7	36.6	0.7	25.6
30days	251.0	232.8	249.1	39.4	1.7	26.9

Table 6.2 DSC data of untreated and weathered PET-$BaSO_4$

Samples	T_{m1}(°C)	T_{m1on}(°C)	T_{m2}(°C)	ΔH_m(J/g)	ΔH_c(J/g)	$\%X_c$
REF	246.0	231.7	244.8	33.1	0	23.6
2days	246.7	231.7	244.6	33.2	0.3	23.5
5days	246.3	232.9	245.4	32.4	0.7	22.6
9days	246.7	231.2	244.5	33.3	1.1	23
14days	246.7	232.2	244.7	33.6	1.3	23.1
20days	247.0	230.8	244.8	31.4	0.8	21.9
30days	247.0	230.7	243.4	31.3	1.3	21.4

Table 6.3 DSC data of untreated and weathered PET-$BaSO_4$-UV

Hydrolysis

DSC thermograms of the first heating runs and the cooling runs of the unstabilized PET samples are displayed in figure 6.20 and 6.21, here only the results of the untreated, 14-day, 35-day and 50-day hydrolysed samples are shown for the sake of clarity since the changes of the thermograms with exposure time were subtle (DSC thermograms of the hydrolysis-stabilized PET-$BaSO_4$-UV are shown in appendix A). A weak endotherm peak at around 132°C whose intensity was unaffected by the exposure time was observed for all the exposed samples. The peak can be assigned to post-crystallization occurred in the amorphous regions [152]. Unlike the photodegraded samples, melting endotherm broadening and peak shifting were not observed for the hydrolysed samples even after 50 days of exposure, indicating the crystal structures of the exposed samples were not attacked by water throughout the

experiment. This is consistent with the ideas in the literature [156, 159, 160] that water molecules will be restricted to the amorphous regions where the molecules can diffuse into thereby leading to the occurrence of hydrolysis. The DSC cooling runs could be very helpful for characterizing the hydrolytic degradation of polyesters since the extent of chain cleavage in the amorphous regions can be reflected by parameters such as the crystallization temperature and enthalpy of crystallization [157].

Some useful calorimetric parameters such as the melting point (T_{m1}), crystallization temperature (T_{cc}), enthalpy of crystallization (ΔH_{cc}) and crystallinity ($\%X_c$) of the untreated and hydrolysed samples are summarized in table 6.4 and 6.5. It is obvious that chemicrystallization, which is a common phenomenon during the hydrolysis of semi-crystalline polymers especially when the experimental temperature is above the glass transition temperature of the samples, have been seen for both samples after hydrolysis treatment. Increases of T_{cc} and ΔH_{cc} due to hydrolysis can be observed for the both samples and it is seen that the increasing rates of the two parameters are higher for the unstabilized PET, for example, after 50 days of hydrolysis the increment of ΔH_{cc} is 9.5 for the unstabilized PET while the value for the hydrolysis-stabilized PET-$BaSO_4$-UV is only 4.2, less than half of that of the unstabilized PET. Higher increments of T_{cc} and ΔH_{cc} suggests the polymeric chain cleavage by hydrolysis was more significant for the unstabilized PET, leading to more newly produced shorter chains with higher mobility that can facilitate the crystallization and thus the higher crystallization temperature and enthalpy of crystallization.

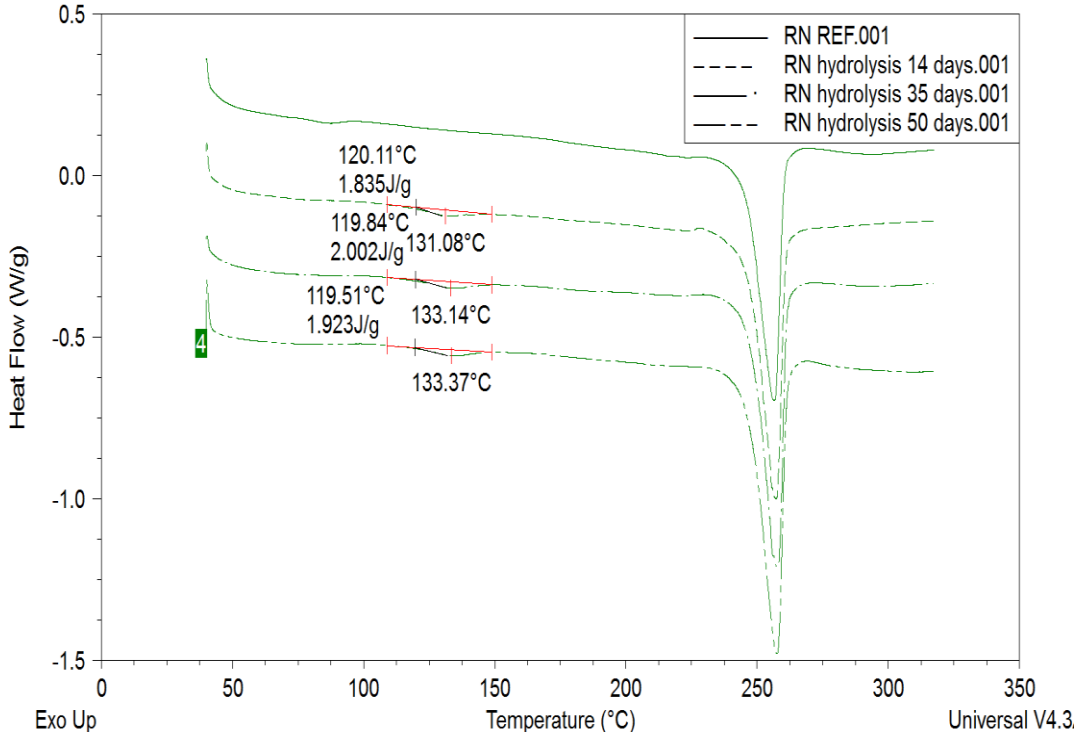

Figure 6.20 DSC thermograms of untreated and hydrolysed PET (14, 35 and 50 days)

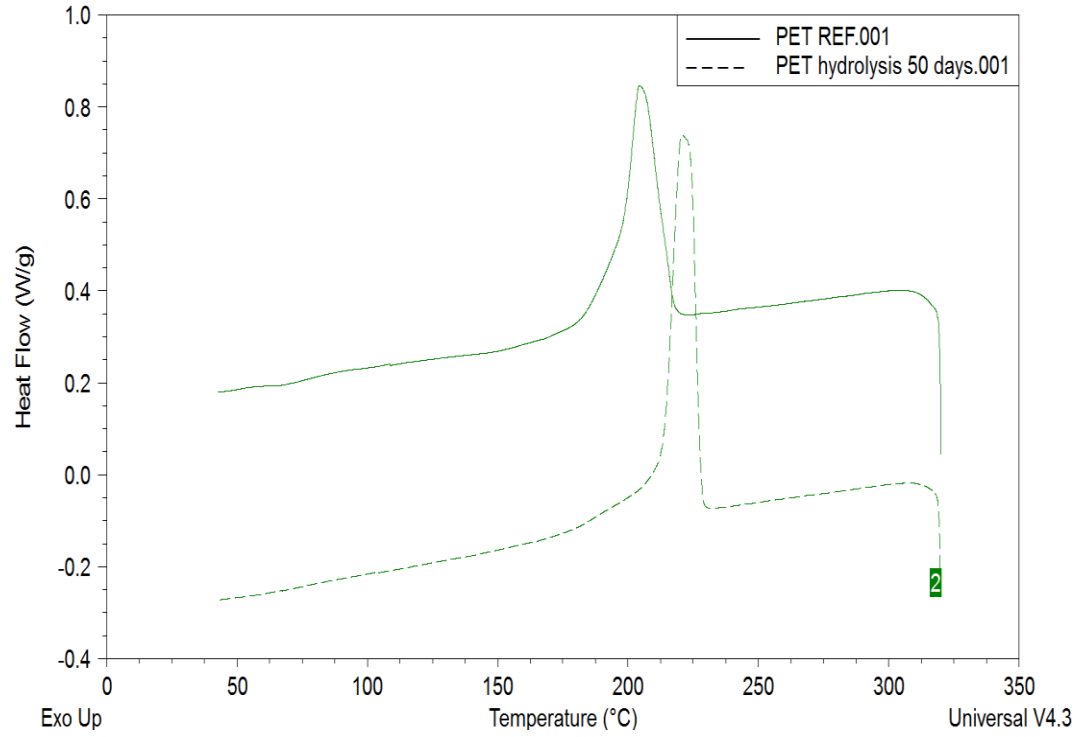

Figure 6.21 DSC thermograms (cooling run) of untreated and 50-day hydrolysed PET

Samples	T_{m1}(°C)	ΔH_m(J/g)	T_{cc}(°C)	ΔH_{cc}(J/g)	$\%X_c$
REF	256.6	45.7	204.5	51.6	32.6
14days	257.2	49.3	212.7	53.9	35.2
21days	257.2	48.3	213.2	55.5	34.5
28days	257.0	49.6	215.2	55.9	35.4
35days	257.9	50.5	217.6	57.4	36.1
42days	257.9	52.0	219.9	59.5	37.1
50days	257.7	53.5	220.7	61.1	38.2

Table 6.4 DSC data of untreated and hydrolysed PET

Samples	T_{m1}(°C)	ΔH_m(J/g)	T_{cc}(°C)	ΔH_{cc}(J/g)	$\%X_c$
REF	246.0	33.1	190.4	33.9	23.6
14days	246.3	33.7	198.6	34.7	24.1
21days	246.4	34.4	199.9	35.8	24.6
28days	246.6	34.2	200.3	36.4	24.4
35days	246.6	35.4	201.5	36.9	25.3
42days	247.0	36.5	202.4	36.8	26.1
50days	247.5	39.4	203.8	38.1	28.1

Table 6.5 DSC data of untreated and hydrolysed PET-$BaSO_4$-UV

6.3.3 SEM images

Photodegradation

SEM images of the untreated and photodegraded samples' surfaces are displayed in figure 6.22. It is obvious that after 30 days of exposure in the weatherometer the sample surface of the untreated PET have been significantly damaged as cracks can be observed on the exposed side (figure 6.22 (b)) as a result of long-term photodegradation. On the other hand, surface changes were much less visible for PET-$BaSO_4$ and PET-$BaSO_4$-UV and only the pigment 'pile-up' effect can be observed as more white particles appeared on the exposed surfaces (figure 6.22 (d) and (f)), similar as those inorganic pigments filled samples after PD exposure discussed in chapter 4.

In order to understand the photodegradation effect on the macroscopic structures of the exposed samples further, cross sections of the untreated and photodegraded samples were analysed as well and the images are shown in figure 6.23 and 6.24. One can see that before weathering exposure the cross sections were intact and perfect for all types of samples. However, severe damages can be found on the cross section area of the 30-day weathered unstabilized PET where fragmentary polymer crystals and air gap were seen, as shown in figure 6.23 (b-d), implying the complete destruction of the polymer crystal structures. A wide air gap has even been found in the middle of the sample (figure 6.23(b)) suggesting the partial delamination of the sample due to excess photodegradation. For PET-$BaSO_4$, the extent of polymer degradation was much weaker compared to the unstabilized PET as most of the material cross section remained intact. However a narrow air gap was still found near the exposed side of the sample (figure 6.24(b)). Figure 6.24(c) and 6.24(d) show the cross sections of PET-$BaSO_4$-UV before and after the weathering treatment, it is interesting to note that the macroscopic structure of the sample was almost unchanged and still perfect even after receiving 30 days of exposure.

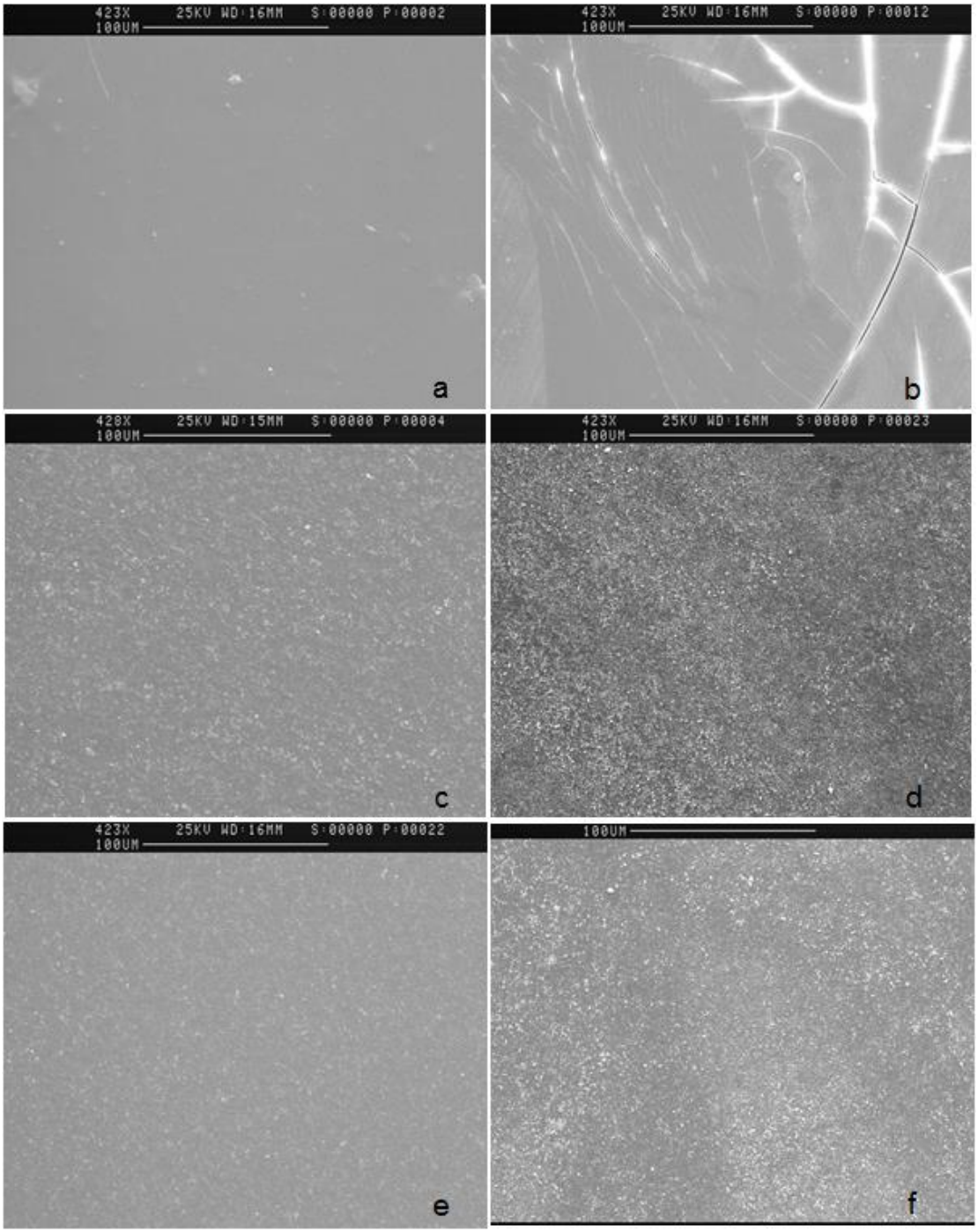

Figure 6.22 Sample surface conditions of untreated PET (a); 30-day weathered PET (b); untreated PET-$BaSO_4$ (c); 30-day weathered PET-$BaSO_4$ (d); untreated PET-$BaSO_4$-UV (e); 30-day weathered PET-$BaSO_4$-UV (f)

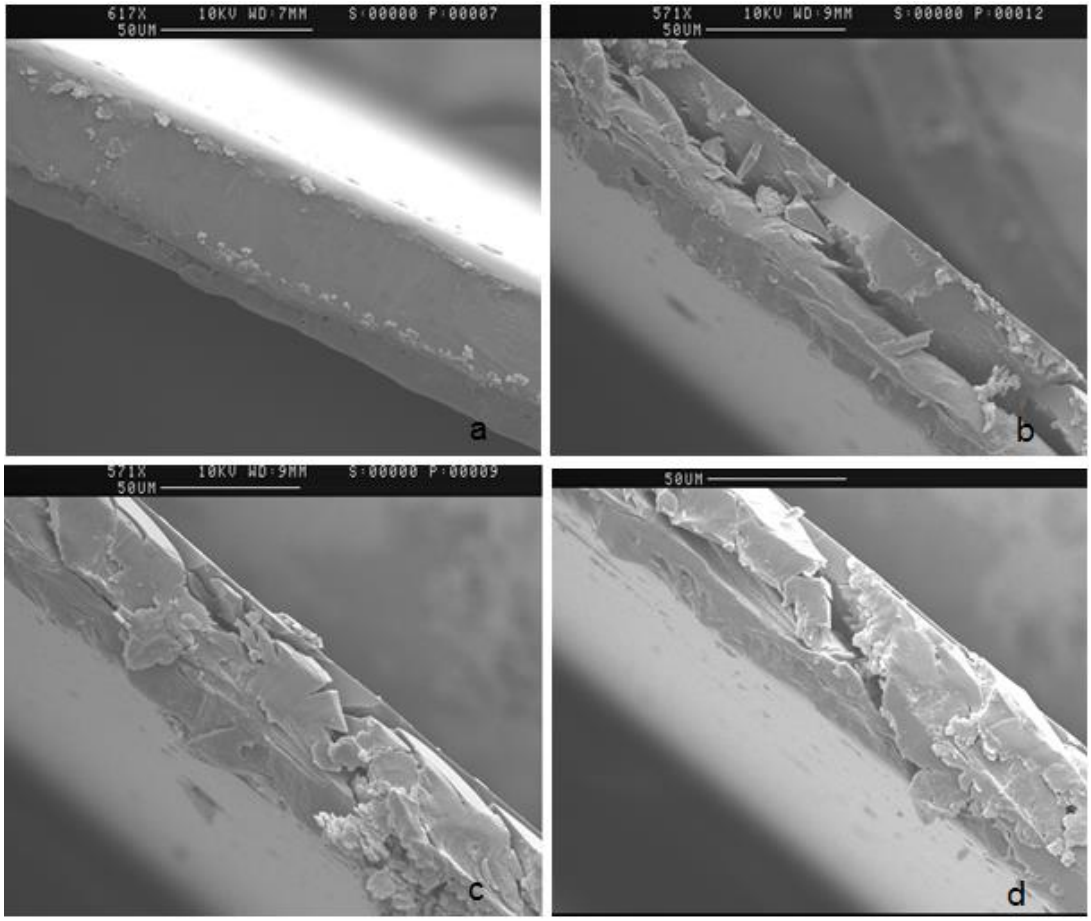

Figure 6.23 Cross sections of untreated PET (a); 30-day weathered PET (b-d)

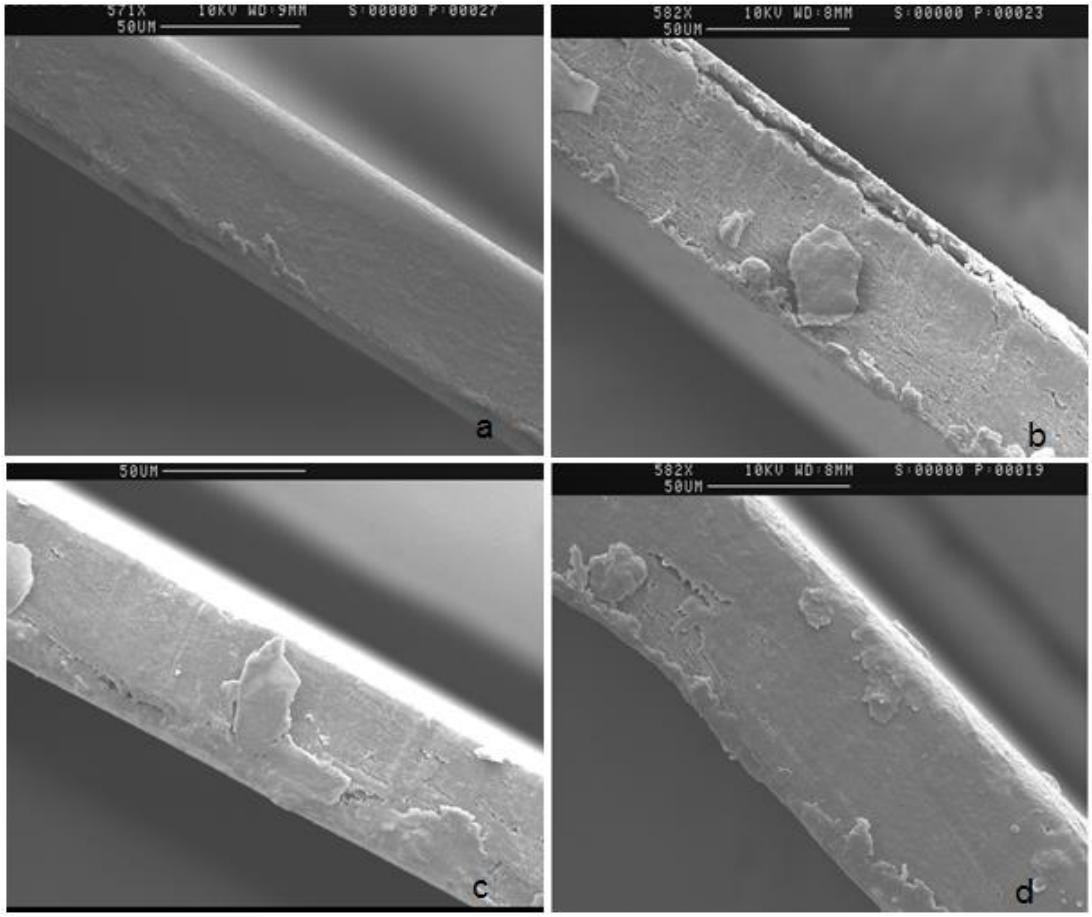

Figure 6.24 Cross sections of untreated PET-$BaSO_4$ (a); 30-day weathered PET-$BaSO_4$ (b); untreated PET-$BaSO_4$-UV (c); 30-day weathered PET-$BaSO_4$-UV (d)

Hydrolysis

SEM images of the untreated and hydrolysed samples' surfaces are illustrated in figure 6.25. No distinct difference can be found between the untreated and exposed samples throughout the experiment.

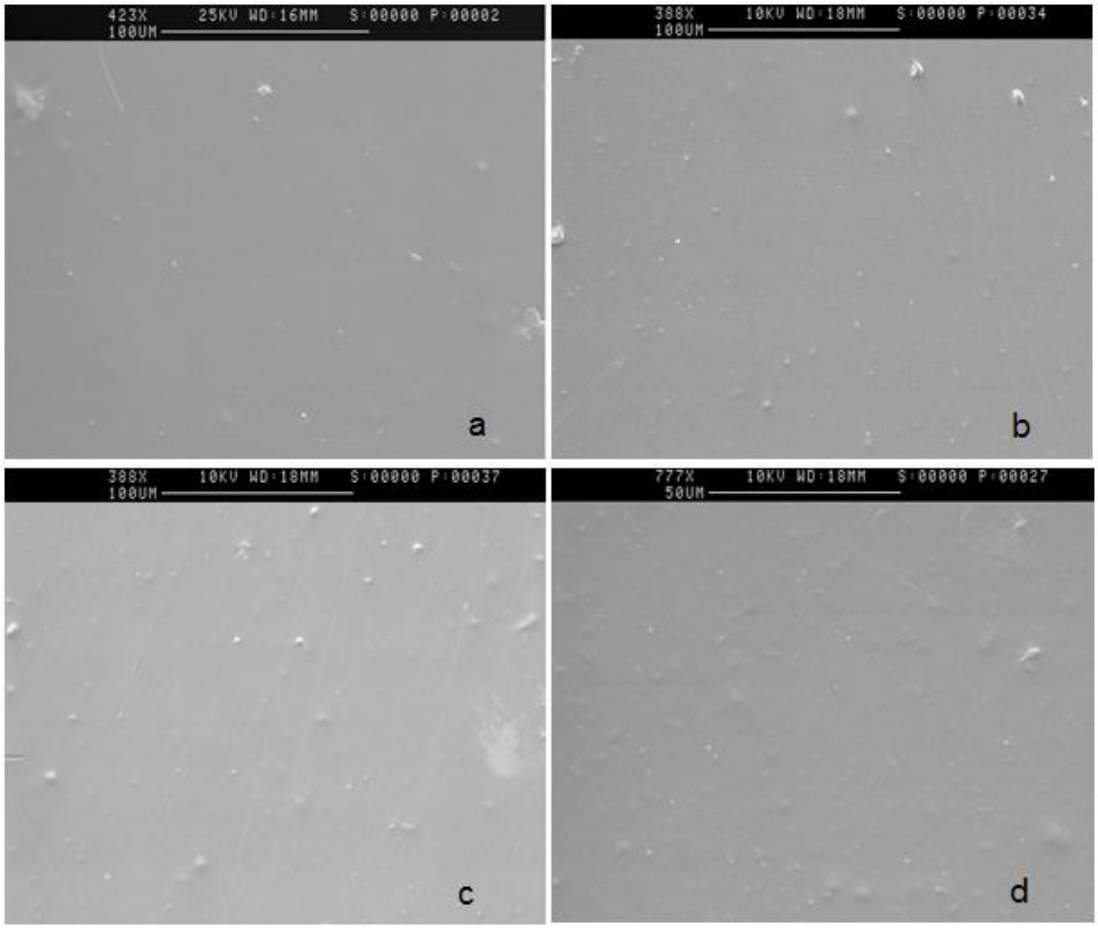

Figure 6.25 Sample surface conditions of untreated PET (a); 14-day hydrolysed PET (b); 35-day hydrolysed PET (c); 50-day hydrolysed PET (d)

6.3.4 PD lifetime analyses

The PD lifetimes of the photodegraded and hydrolysed samples are plotted and shown in figure 6.26 and 6.27, respectively. From figure 6.26 one can see that the PD lifetimes of the unstabilized PET and PET-$BaSO_4$ decreased with the exposure time and it is important to note that after 20 days of photodegradation in the weatherometer the PD lifetime of the unstabilized PET dropped to 0 (less than 1 minute), in other words, the sample would breakdown in no time once the experimental voltage (3kV) was applied. On the other hand, the PD lifetime of the UV-stabilized PET-$BaSO_4$-UV stayed at a high level throughout the experiment, no deterioration of the PD lifetime could be found even for the 30-day exposed sample compared to the untreated one.

For the hydrolysed samples, the PD lifetimes both increased slightly at the initial stages of the experiment and gradually dropped at a slow rate afterwards.

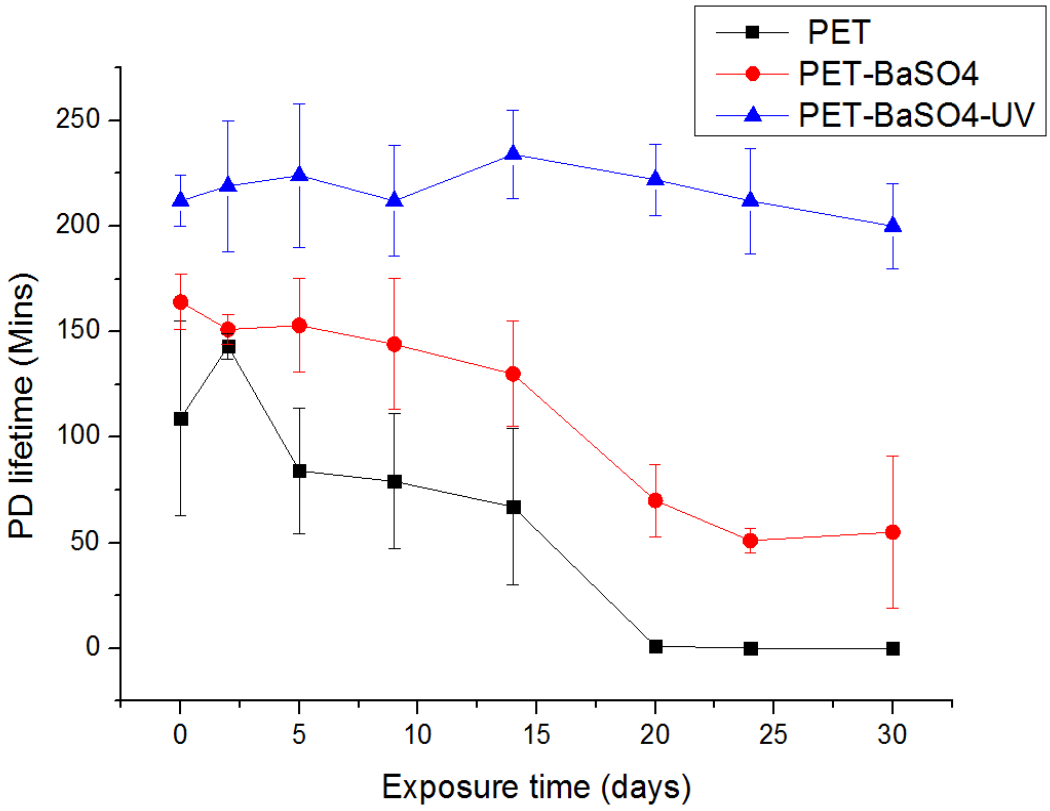

Figure 6.26 PD lifetimes of weathered PET, PET-$BaSO_4$ and PET-$BaSO_4$-UV

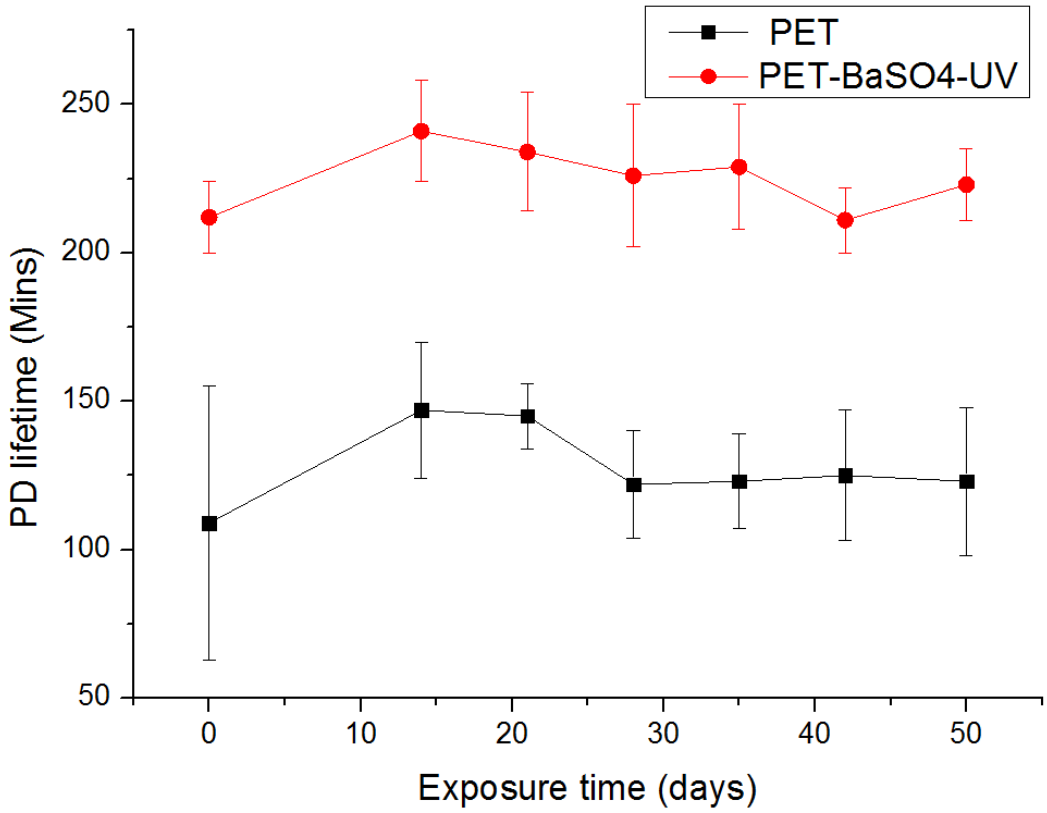

Figure 6.27 PD lifetimes of hydrolysed PET and PET-$BaSO_4$-UV

6.3.5 Discussions

In the previous sections, the surface chemical degradation of the photodegraded samples in the weatherometer were analysed by ATR-FTIR. The hydroxyl group concentrations, acid/ester ratios in the carbonyl bands were calculated to quantitatively characterize the extent of chemical degradation for each sample. From the FTIR data it can be easily concluded that the chemical degradation extents of the three samples were in the ranking of PET-$BaSO_4$-UV > PET-$BaSO_4$ > untreated PET. This is not surprising since the pigment 'pile-up' effect was seen for the $BaSO_4$-based samples and the exposed $BaSO_4$ particles with high UV reflectance in the range of 300 – 400 nm can surely screen the unaffected polymer and thus slow down the further photo-oxidation to a great extent. However, one can find out that the PD lifetimes of the photodegraded samples cannot be reflected by their surface chemical degradation extents precisely as no shortening of PD lifetime could be found for PET-$BaSO_4$-UV throughout the experiment while considerable

degrees of surface chemical degradation was still observed for the sample. On the other hand, although the surface chemical degradation of the unstabilized PET was more significant than that of the UV-stabilized PET-$BaSO_4$-UV (figure 6.11 and 6.12) the PD lifetime of the unstabilized PET declined much faster than expected and even dropped to 0 after 20 days of exposure.

The photodegradation extents of the samples were investigated via DSC and the first and second melting point (T_{m1}, T_{m2}) as well as the onset temperature of the first melting peak (T_{m1on}) were used to analyse the crystal structures and stability of the photodegraded samples. The three parameters decreased significantly with exposure time for the unstabilized PET, implying the breakage of the original polymer crystals and formation of massive defective and thinner ones. It has been discussed in chapter 3 and 5 that the thickness and perfection of crystals play a vital role in PD resistance and lifetime of the polymer. Therefore the severe destruction of the crystal structure is believed to be the main reason of the dramatic decrease in PD lifetime of the unstabilized PET. The dielectric property of the unstabilized PET dropped to an extremely low degree where the PD lifetime reached 0 after 20 days of photodegradation, suggesting the total deterioration of the polymer crystal structure. The crystal structure of the 30-day photodegraded unstabilized PET can be viewed macroscopically in figure 6.22 (b) and figure 6.23 (b-d) where multiple cracks were formed on the exposed side, furthermore defective and fragmentary polymer crystals and even wide air gaps are seen in the cross section area of the sample. Under this circumstance once the high voltage is applied electrical trees would form immediately then propagate along those pre-existing air channels and reach the opposite electrode very quickly, leading to the rapid dielectric breakdown of the sample (less than 1 minute as shown in figure 6.26). On the other hand, the crystal structure and stability of the UV-stabilized PET-$BaSO_4$-UV kept perfect in the photodegradation process as indicated by the three parameters of DSC that nearly remained unchanged (only a drop of 1°C was found for T_{m1on}) throughout the experiment. SEM images of both surface and cross section also revealed that the polymer crystal structure was intact and perfect after 30 days of exposure. As a result, the PD lifetime of the weathered PET-$BaSO_4$-UV did not show any deterioration during the experiment although considerable chemical degradation had been observed on the exposed surface. For PET-$BaSO_4$, even though the surface chemical degradation extent was nearly as the same as that of PET-$BaSO_4$-UV, the crystal stability of the sample was inferior, as indicated by a drop of 5.4°C in T_{m1on}

after receiving 30 days of exposure (table 6.2). Therefore local breakage of the polymer crystal might occur during the degradation process and this was confirmed by the cross section image of the sample where a small air gap could be observed beneath the exposed surface (figure 6.24(b)). As a result, decline of the PD lifetime was observed for PET-$BaSO_4$ as well but the decreasing rate is obviously lower than that of the unstabilized PET since except for partial destruction most of the polymer crystals were still intact and firm.

T_{m1on} of the untreated and photodegraded samples are plotted and shown in figure 6.28. Compared to the PD lifetimes of the samples (figure 6.26) it is seen that the data within the two figures follow the same trend where the fastest data decline could be found for the unstabilized PET while the data were almost unchanged for the PET-$BaSO_4$-UV. It can be concluded that T_{m1on} can be used as a useful parameter to predict the PD lifetime for chemically-degraded samples.

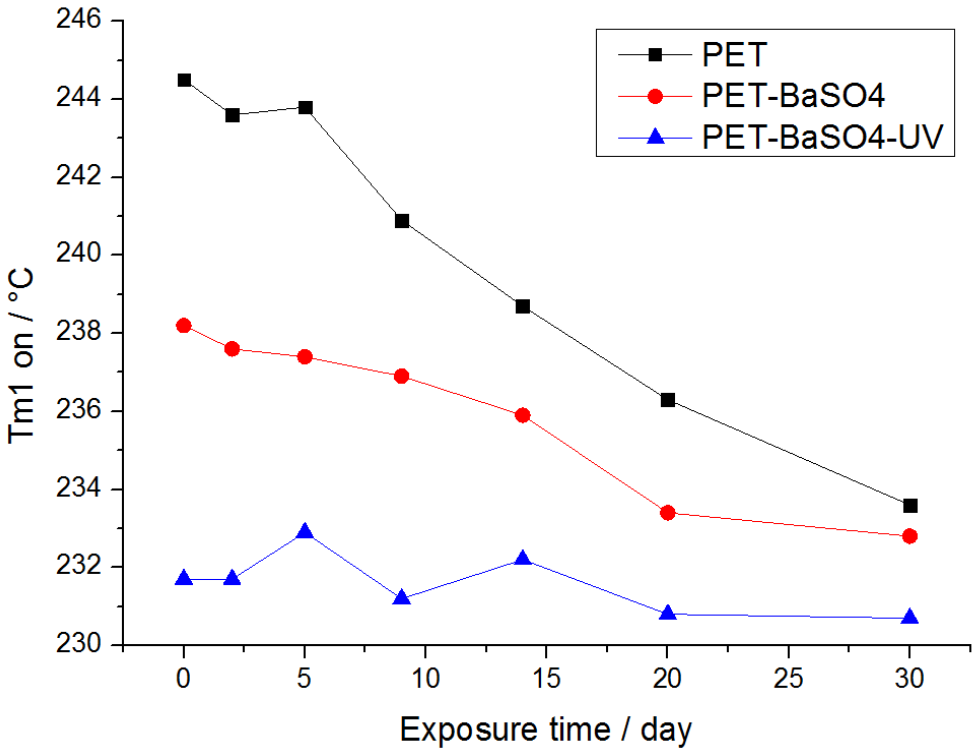

Figure 6.28 The onset temperatures of the melting peaks (T_{m1on}) of the three weathered samples

The hydrolysed samples were analysed via DSC and the hydrolytic degradation extents were characterized by the crystallization temperature (T_{cc}) and enthalpy of crystallization (ΔH_{cc}) in the DSC cooling runs for the samples. Results in the previous sections revealed that compared to the unstabilized PET the extent of chain scission in the amorphous regions was less significant for the hydrolysis-stabilized PET-$BaSO_4$-UV, which is expected. Melting endotherm broadening and peak shifting were not observed for the two types of hydrolysed samples, suggesting the crystalline regions of both samples were not affected during hydrolysis. Furthermore, chemicrystallization was observed for both samples after hydrolysis treatment.

Interesting results have been found for the PD lifetimes of the hydrolysed samples. The PD lifetimes of the samples did not decline rapidly after hydrolytic degradation as expected, on the contrary, they both increased initially in the beginning of the experiment (exposure time < 14 days) and then decreased at a slow rate as time went on. It should be noted that the longer PD lifetimes can be found for the exposed samples compared to the untreated one throughout the experiment even the sample had been subject to 50 days of hydrolysis. This can be explained by the mutual effect between chemicrystallization and hydrolysis on the exposed samples. It is already known that the PD resistance greatly depends on crystal stability and crystallinity degrees of the sample, as discussed in chapter 5. In the beginning of hydrolysis, the sample was not significantly degraded yet and it is believed this was the stage when the chemicrystallization effect dominated, shorter polymeric chains with sufficient mobility in the amorphous regions caused by hydrolysis can crystallize and this would locally inhibit the propagation of electrical trees thereby increasing the PD lifetime of the sample. In the later stage of hydrolysis, excess hydrolytic degradation would gradually offset the chemicrystallization effect and thus a slowly decline in PD lifetime was observed for both samples. However the PD lifetimes of the 50-day exposed samples were still found longer than that of the untreated ones, mainly due to the intact and perfect crystal structures (indicated by the DSC results) and high crystallinity degrees of the samples by long-term hydrolysis.

6.4 Conclusions

Samples with various additives were subjected to photodegradation in the weatherometer and hydrolytic degradation in hot deionised water before PD tests to investigate the weathering and hydrolysis effects on PD-induced breakdown behaviour of PET films used in photovoltaic devices. Samples have been treated in very harsh environments that were even more critical than those listed in the IEC 61215. A few conclusions are made as follows:

1. The photodegradation resistances of the samples were in the ranking of PET-$BaSO_4$-UV > PET-$BaSO_4$ > untreated PET, as proven by ATR-FTIR and DSC.
2. PD-induced breakdown behaviour is closely related to crystal stability and structure of the sample. After 20 days of exposure in the weatherometer the PD lifetime of the unstabilized PET dropped to 0 due to the nearly complete destruction of the crystal structure. On the other hand, the PD lifetime of PET-$BaSO_4$-UV remained unchanged throughout the experiment thanks to the effectiveness of $BaSO_4$ pigments and UV stabilizer to keep the polymer crystalline regions intact and perfect although considerable chemical degradation had been found on the exposed surface.
3. Since the polymer crystal stability and structure can be reflected by DSC results, DSC is a more precise tool than FTIR to predict the PD lifetimes for the photodegraded samples and the parameter T_{m1on}, the onset of the melting peak in the first DSC heating run, had been found very useful since the PD lifetimes and T_{m1on} display similar trends for the exposed samples.
4. Although subjected to long-term hydrolysis, PD lifetime deteriorations were not found for the highly degraded samples. Interestingly, the PD lifetimes of the samples increased slightly in the early stage of experiment and slowly decreased afterwards. This is because the crystalline regions of the polymers were not attacked during hydrolysis since water molecules can only diffuse into the amorphous regions where hydrolysis can take place. As a result, the intact polymer crystals can still effectively resist the high-energy ions bombardment as well as the propagation of electrical trees. The changes of PD lifetimes during the experiment can be explained by the mutual effect between chemicrystallization and hydrolysis.

Chapter Seven

7.Comparison of PD degradation and breakdown between PET and PEN

7.1 Introduction

It is well known that PET has become the most popular member in the polyester family over the past decades. Products based on PET can be found almost everywhere in daily life due to its excellent properties such as insulation property, high tensile strength, good gas barrier, thermal stability, light weight, high transparency and desirable price-performance ratio. However, some of the PET properties are still not good enough in many application fields where better properties including higher thermal resistance, better mechanical property and gas barrier are required. As a result an engineering-grade polyester material with superior properties to PET is needed.

Poly(ethylene 2,6-naphthalate) (PEN) is a type of polyester that has similar chemical structure (shown in figure 7.1) to PET. The only difference between these two polyesters is that PEN has naphthalene while PET has benzene in the polymer chain. The presence of the additional aromatic ring in the molecular chain of PEN is responsible for its superior properties including tensile strength, gaseous barrier and chemical resistance [100].

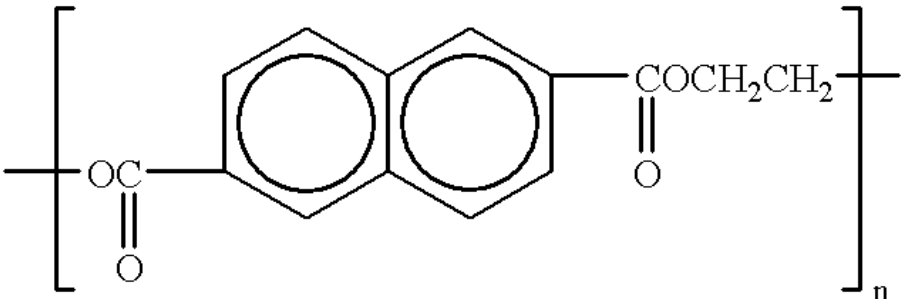

Figure 7.1 Chemical structure of poly(ethylene naphthalate) (PEN)

The comparisons of physical and chemical properties of PET and PEN are illustrated by the 'star diagrams' [100], as shown in figure 7.2. Some important parameters can be directly compared for the two polyester materials from this diagram. For instance, the glass transition temperature of PEN is as high as 122°C, about 40°C higher than that of PET, which allows it to work under a temperature much higher than that could be allowed for PET; the O_2 and CO_2 permeability of PEN is nearly 4 to 5 times lower than that of PET, makes it a better choice for storing beverages; the much lower wet and dry shrinkages compared to PET suggests the better dimensional stability of PEN, furthermore PEN is also much more UV and hydrolysis resistive than PET, therefore although PET is still the mainstream selection for PV backsheet materials today, PEN will be a perfect substitution thanks to its excellent properties.

The PD degradation and breakdown behaviour of PET have been comprehensively and thoroughly described in previous chapters. PEN, as an engineering-grade polyester, has shown superior properties to PET in many aspects. However, it is still unclear about the PD resisting ability of PEN compared to PET and very little information on PD-induced breakdown of PEN could be found in the literature. In this chapter, PD degradation extent of PEN compared to PET will be investigated chemically and physically by using ATR-FTIR and surface profilometer, respectively after the both samples had been treated under identical electrical stresses. The lifetimes of the two different polyester films with same thickness under high voltage were also studied.

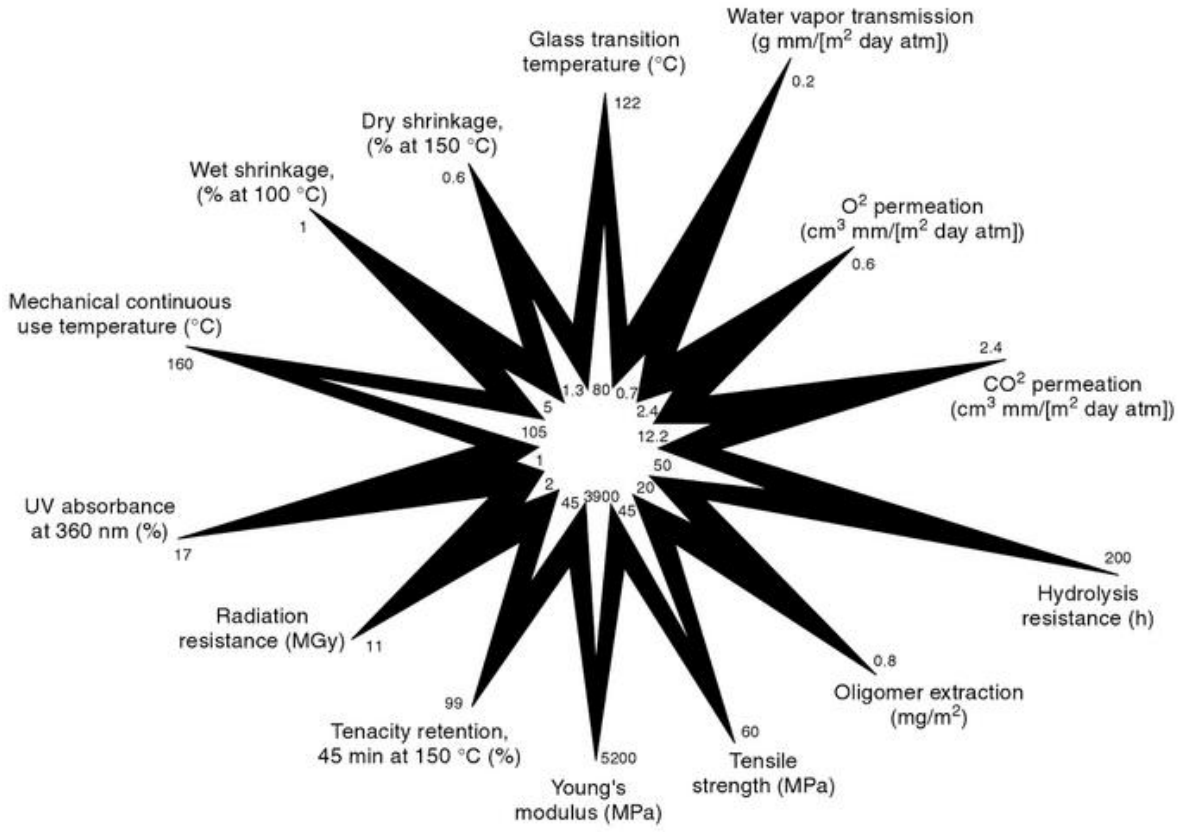

Figure 7.2 General properties comparisons of PET and PEN by the ‘star diagrams’, PEN, ‘black’; PET, ‘white’ [100]

7.2 Experimental

7.2.1 Samples

Universal biaxially oriented, semicrystalline PET and PEN films without performance additives provided by DuPont Teijin Films were used to compare the PD degradation and breakdown behaviours of these two polyester films. Both the samples are in 125 μm and can be described as below:

1. Universal PET without any additive used as a reference (PET).
2. Universal PEN without any additive (PEN).

7.2.2 Experimental set-up of partial discharge and breakdown tests

Two sets of experiments were carried out to investigate the PD degradation and breakdown behaviours of the polyester films. The sample holders for the both sets have already been shown in chapter 2 (figure 2.2 and figure 2.3). The pre-experimental sample treatments and experimental environment conditions are the same as describe in 3.2.2 of chapter 3.

7.2.2.1 Experimental set-up for PD tests

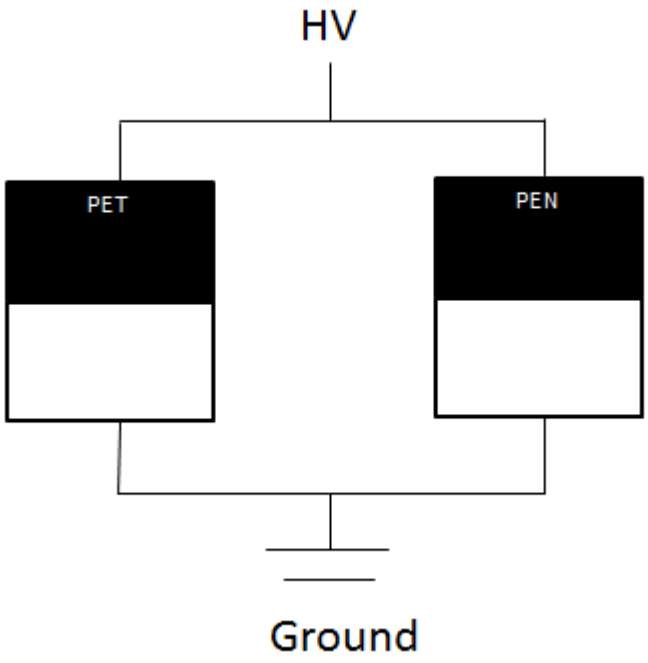

Figure 7.3 Schematic of set-up for PET and PEN

For both the polyester films, sample stacks with identical thickness (250 µm) were subjected to a 50 Hz AC high voltage of 4 kV for 24 hours. The structure of

each stack is shown in figure 7.3. After PD exposure, samples on the top layer of each stack (black block in figure 7.3) were removed for further analysis.

7.2.2.2 Experimental set-up for PD-lifetime test

The schematic of set-up for breakdown tests due to PD erosion has been shown in 3.2.2.2 of chapter 3. Single sheet of the polyester films were subjected to a 50Hz AC high voltage of 5kV until the sample breakdown due to PD erosion. For each sample category, at least five samples were tested and the average values of the PD lifetime of each category were calculated.

7.2.3 Experimental of analytical methods for sample characterisation

All the analytical methods for sample characterisation have been introduced in chapter 2 and 3 already.

7.3 Results and discussions

7.3.1 FTIR analysis

The ATR-FTIR spectrum of untreated PEN is shown in figure 7.4 and it is even more complicated than that of PET due to the presence of the additional aromatic ring in the molecular structure of PEN. The new peaks at 1132 and 1180 cm^{-1} compared to PET are assigned to the naphthalene ring vibration [165]. New absorption peaks with medium intensity at 1214 and 1601 cm^{-1} are due to aromatic ring vibration.

As discussed in previous chapters, the carbonyl band is very useful in characterizing surface chemical degradation of PET caused by PD and weathering. The carbonyl bands of PEN before and after PD treatment are shown in figure 7.5, it is seen that the changes were similar as those of PET where the band at 1714 cm^{-1} representing the original carbonyl group in the ester decreased and the band at 1685 cm^{-1} representing the carboxylic acid and aldehyde produced in degradation increased. The deconvolution of the carbonyl band was carried out via the OriginPro 8.6 software, the peak types were selected as ‘Gaussian’ and the peak centres of

two peaks were fixed to 1717 and 1685 cm^{-1}. The acid/ester ratios were thus calculated to compare chemical degradation extents of the two polyester samples and the results are listed in table 7.1. Greater changes were observed in the case of PET where the acid/ester ratio in the carbonyl band increased 10% after PD exposure while the number was only as low as 3% for PEN. This could be attributed to the better thermal-oxidative resistance of PEN due to the naphthalene in its molecular structure. Furthermore, the better resistance to the UV radiation produced in the discharge processes of PEN must be taken into account as well.

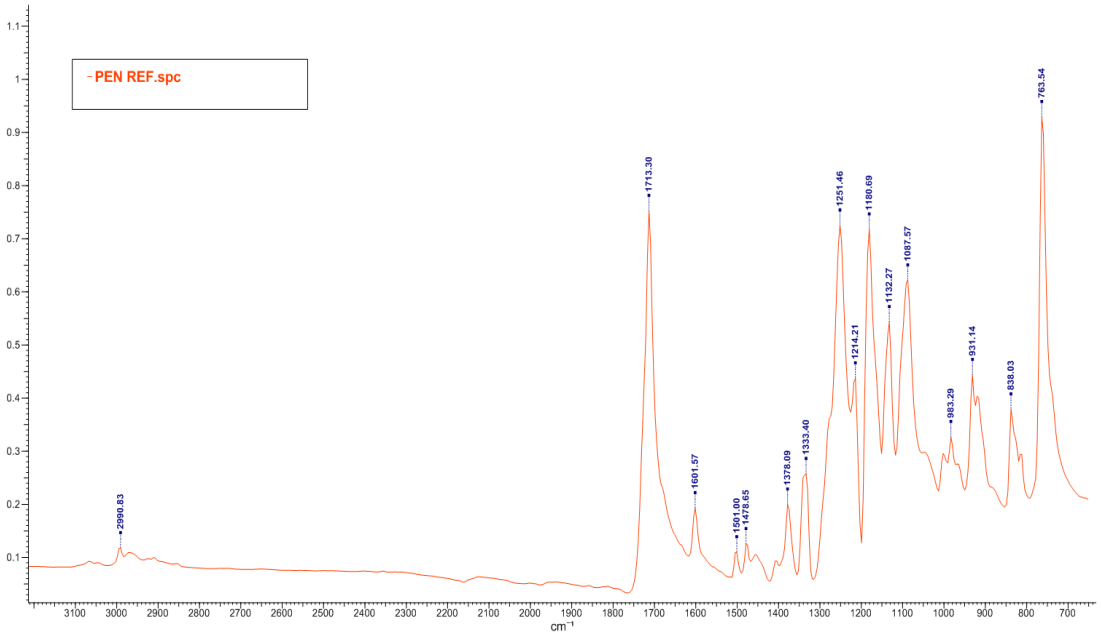

Figure 7.4 ATR-FTIR spectrum of untreated PEN

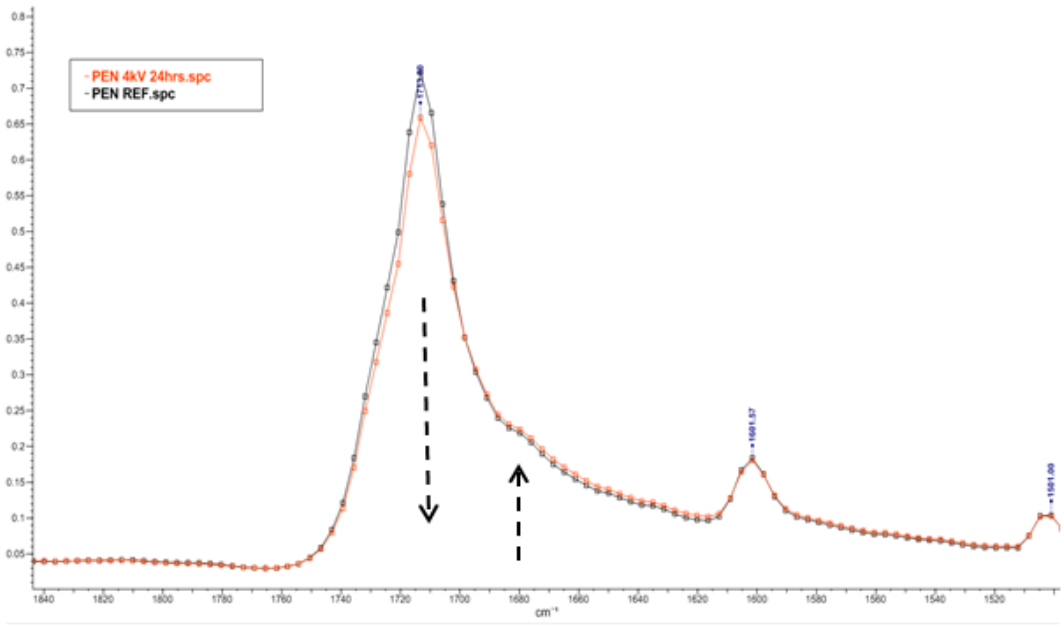

Figure 7.5 Overlaid carbonyl bands of PEN, untreated and PD exposed

Samples	$\%A_{1685}$	$\%A_{1714}$	$\%A_{1685}/A_{1714}$
Untreated PEN	31.5	68.5	46
PD exposed PEN	32.9	67.1	49
Untreated PET	27.5	72.5	38
PD exposed PET	32.6	67.4	48

Table 7.1 Peak fit results of PEN and PET, untreated and PD exposed

7.3.2 DSC analysis

The DSC thermograms of untreated PET and PEN are illustrated in figure 7.6. No glass transition region and cold-crystallization peak can be observed for the PEN sample due to its semicrystalline morphology by biaxial orientation. High melting point (262°C) was observed for PEN and the crystallinity of PEN can be calculated by using the equation (2) in chapter 3:

$$X_c = \frac{\Delta H_m}{\Delta H_{100\%}}$$

where ΔH_m is the measured melting enthalpy of the PEN sample and $\Delta H_{100\%}$ is the melting enthalpy of a pure crystalline PEN which according to G. Z. Papageorgiou and G. P. Karayannidis [83], should be 168 J/g. The DSC data of the two polyester films are summarized in table 7.2, one can see that the crystallinity degree of PEN is lower than that of PET, this is because the 2,6 distribution of the naphthalene ring in PEN makes the sample intrinsically difficult to crystallize compared to the PET, which has the 1,4 linear substitution of the benzene ring [100].

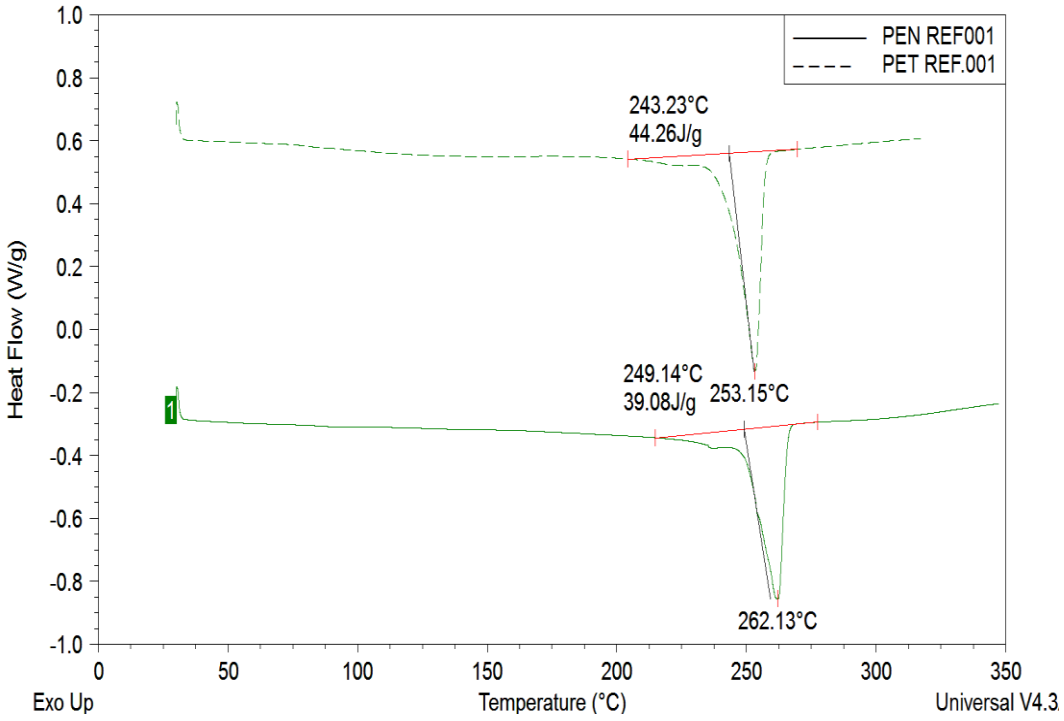

Figure 7.6 DSC endotherms of untreated PEN and PET

Samples	T_m(°C)	ΔH_m(J/g)	$\%X_c$
PEN REF	262.1	39.1	23.3
PET REF	253.2	44.3	31.6

Table 7.2 DSC data of untreated PEN and PET

7.3.3 Surface profilometer and PD lifetime analyses

Surface profilometer

PD tests were carried out using the experimental set-up in figure 7.3 to analyse the PD resistance of the two polyester samples, samples on the top layer of each stack were removed for PD erosion depth test. The erosion depths of both samples are shown in figure 7.7, one can find out the PD erosion depth of PEN was much lower than that of PET after both samples had been subjected to identical electrical stresses.

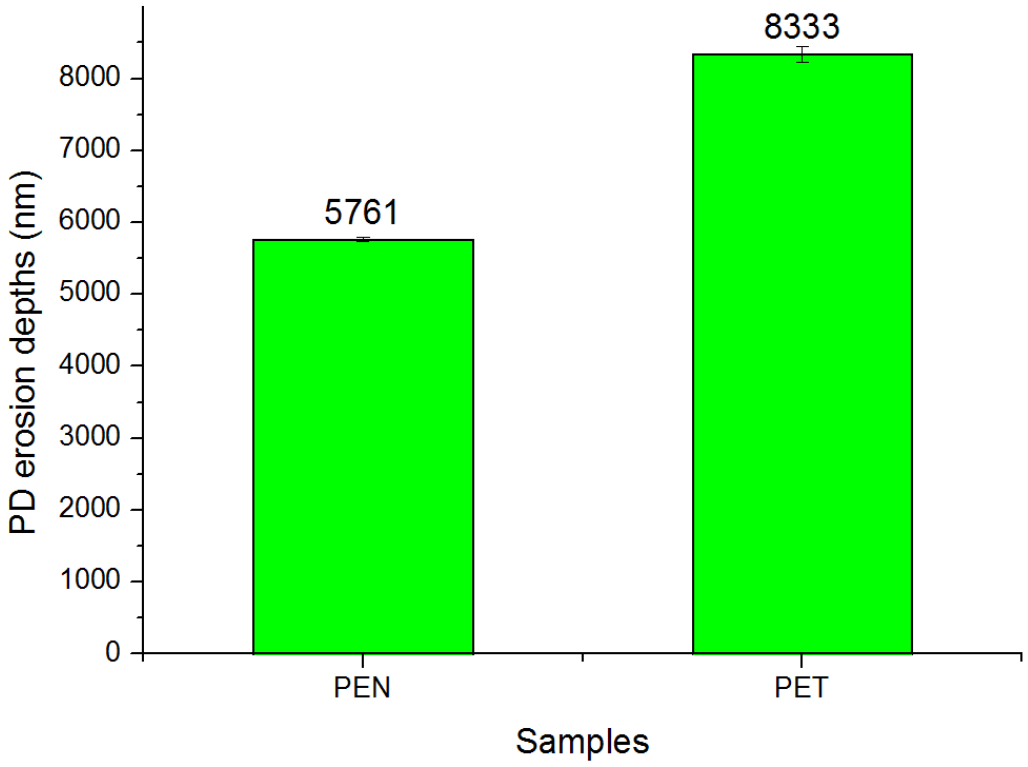

Figure 7.7 PD erosion depths of PD exposed PEN and PET

PD lifetime analysis

PD lifetime tests were also carried out for the two polyester samples and the results are shown in figure 7.8, surprisingly, the difference between the two samples in PD

lifetime is not as big as that in PD erosion depth. The average PD lifetime of PEN under a 50 Hz AC voltage of 5 kV is only about 30 mins longer than that of PET with a variation of ±60 mins.

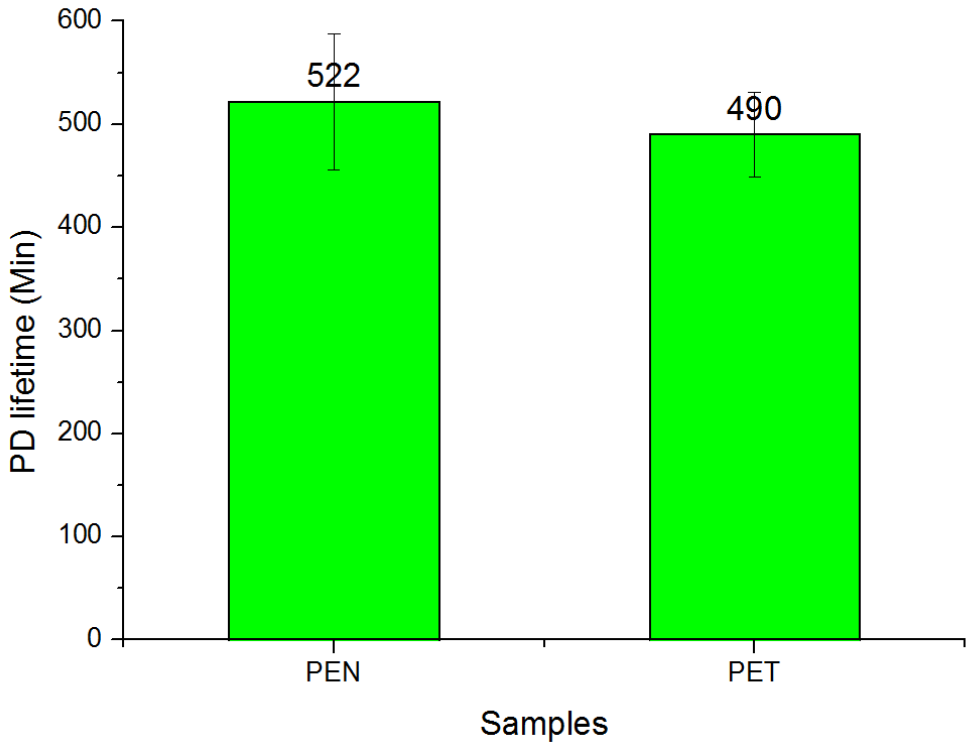

Figure 7.8 PD lifetimes of PEN and PET

7.3.4 Discussions

Superior PD resistance of PEN to PET has been confirmed chemically and physically by ATR-FTIR and surface profilometer where lower acid/ester ratio calculated from carbonyl band and lower PD erosion depth were observed for PEN. The results are not surprising since the rigid naphthalene ring of PEN is expected to resist the bombardment of ions and electrons more effectively than the benzene ring in PET. Thermal-oxidative and UV radiation degradation caused by PD will also be less significant for PEN due to the naphthalene ring in PEN molecular chain. Furthermore, the higher melting point of PEN is believed to be responsible for suppressing local melting of the polymer due to the local high temperature by PD.

As a result, the three main mechanisms of physicochemical degradation of polymer surface by PD (shown in figure 7.9) can be inhibited and thus the apparent material thickness reduction can be effectively suppressed. It was also reported by Y. Hasegawa and I. Isamu that polymers with higher melting point and weight ratio of aromatic rings would exhibit better PD resistance in terms of volume eroded [27].

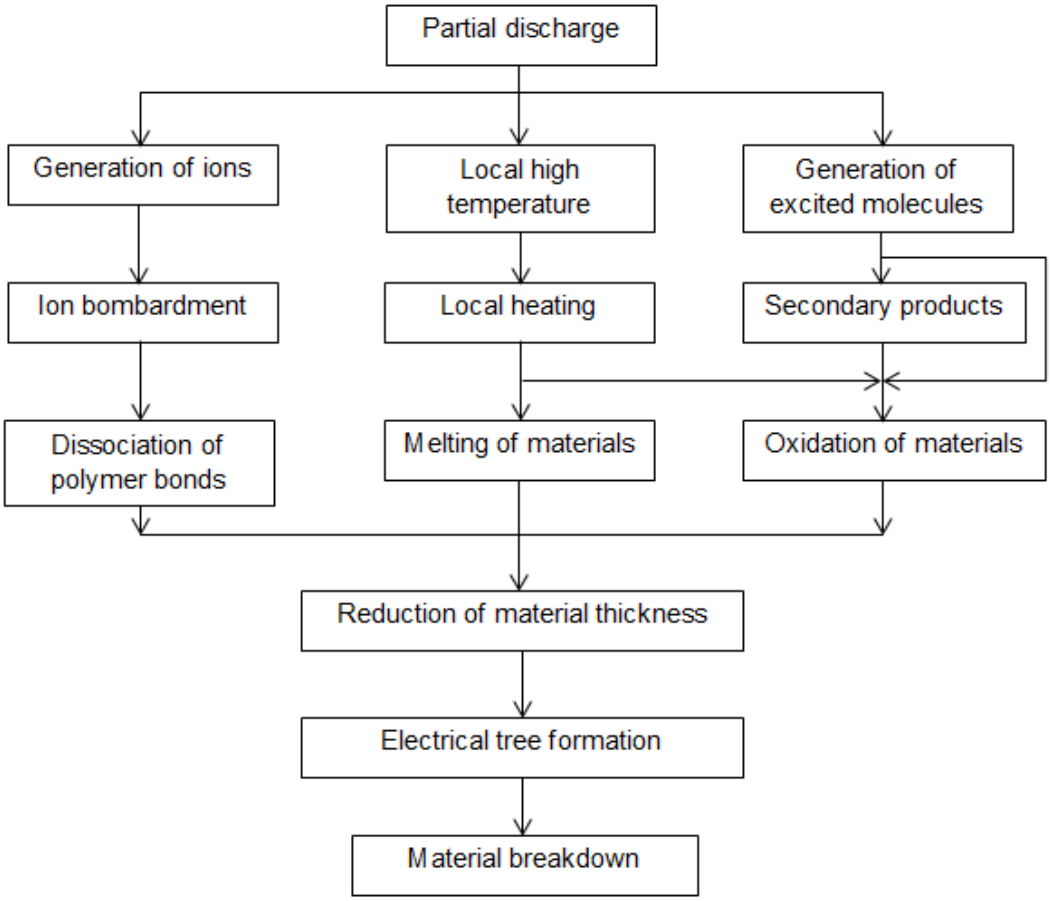

Figure 7.9 Physicochemical processes of polymer surface degradation caused by partial discharge [119]

However, the difference of PD lifetimes of the two polyester samples is much smaller than that of their PD erosion depths, as shown in figure 7.8. It has been discussed in chapter 4 that PD lifetime and PD erosion depth are sometimes not correlated with each other since PD lifetimes of polymers will also greatly depend on the initiation time and propagation rate of electrical trees in the polymers. Inorganic

particles especially phosphorus-based flame retardant can significantly reduce the propagation rate of electrical trees initiated by PD thereby increasing the PD lifetimes of the filled PET. In this chapter, both the polyester samples were unfilled hence the effect of performance additives can be ruled out. However, since PEN is chemically different to PET the effect of chemical structure on the initiation and propagation of electrical trees must be considered.

It was suggested by A. C. Ashcraft and R. M. Eichhron [167] that aromatic moieties could be very effective in enhancing the inception voltage (electric field) of electrical trees for polymers as the inception voltage of electrical trees was found correlated with the ionization potentials of the moieties. That is, the lower the ionization potential the higher the inception voltage of electrical trees. Because the ionization potentials of the aromatic moieties are much lower than that of the parts consisted with aliphatic hydrocarbons, therefore the aromatic moieties would be ionized more easily under the electric field making the energetic electrons react preferentially with the aromatic cation to reproduce the original aromatic ring rather than generating free radicals which can cause further degradation. Moreover, those aliphatic hydrocarbon radicals would be quenched by the aromatic moieties as well, as demonstrated in figure 7.10 [167, 99]. It should be also noted that under high electric field the aromatic moieties with low ionization potentials can ionize and increase the conductivity which will moderate the electric field to some extent and thus enhance the inception voltage of electric trees [99].

It is known that the ionization potential of naphthalene ring (8.12 eV) is lower than that of benzene ring (9.25 eV). From the above discussion it is expected that PEN is intrinsically more resistive in electrical tree initiation than PET as the naphthalene ring is more prone to ionize than the benzene ring under electric field thereby being more effective in preventing free radical degradation and in increasing the difficulty of electrical tree initiation by moderating the electric field.

M. N. Arbab and D. W. Auckland [166] proved that the propagation rate of electrical trees would be greatly influenced by the mechanical properties of the polymer. When polymeric materials are subjected to electric fields, internal mechanical stress will commence to build up inside the polymer due to the electrostatic forces of the electrodes. It is logical to believe that electrical trees would propagate more rapidly within the material when the polymeric molecules are subjected to tensile stress especially once microcracks are present due to excessive

stress [99]. It was found that polymers with lower Young's modulus would exhibit higher rates of electrical tree propagation because the build-up of Maxwell stresses by the AC electric field within these polymers were not so strong as those polymers with higher Young's modulus. It has been shown in figure 7.2 the modulus of PEN (5200 MPa) is much higher than that of PET (3900 MPa) and therefore it can be expected that higher Maxwell stress and thus faster growth of electrical trees would be generated in the case of PEN when both the polyester films were subjected to identical experimental voltage.

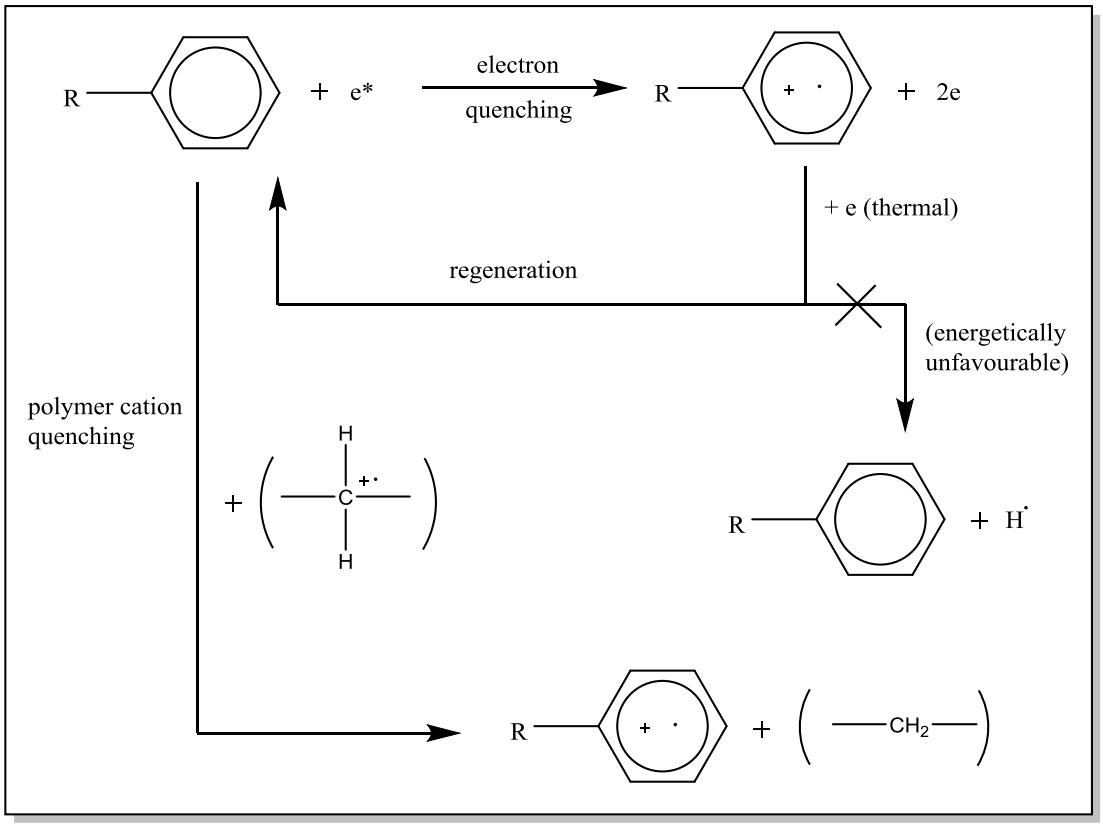

Figure 7.10 Mechanism of electron and polymer cation quenched by aromatic ring [167, 99]

Another important factor can influence the electrical tree propagate is obviously the polymeric morphology. In chapter 5, remarkable increase of PD lifetime could be found for those PET samples with high crystallinity due to high temperature

annealing. It has been proven that crystals can effectively increase the tortuosity of electrical tree propagation paths and thus improve the sample PD lifetime. From the DSC data shown in table 7.2, the overall crystallinity degrees of PEN and PET used in this experiment were 23.3% and 31.6%, respectively, possibly because the 2,6 distribution of the naphthalene ring in PEN makes the sample intrinsically difficult to crystallize compared to PET [100]. As a result, growth of electrical trees will be easier within PEN than the highly-crystalline PET.

7.4 Conclusions

Poly(ethylene 2,6-naphthalate) (PEN), a high quality engineering-grade polyester that exhibits superior properties to PET in many aspects such as mechanical properties, gaseous barrier, thermal stability, chemical resistance and weathering resistance, has been regarded as a perfection substitution of PET for the backsheet material used in PV modules. However the PD resistance and breakdown behaviour of PEN were seldom studied in the past. In this chapter PD degradation and PD-induced breakdown of PEN were investigated chemically and physically using standard PET film as a reference sample. The PD degradation extents and PD lifetimes of the two polyesters were compared with each other and conclusions can be made as below:

1. PEN exhibited much better PD resistance than PET both chemically and physically via ATR-FTIR and profilometer, respectively, as lower acid/ester ratio calculated from the carbonyl band and smaller PD erosion depth were observed for PEN.
2. Although PEN did exhibit longer apparent PD lifetime than PET, the difference of the two samples was not so big as expected since the PD lifetime of polymers greatly depends on the inception voltage (electric field) and propagation rate of electrical trees initiated by PD within the polymer which are determined by many factors such as polymer morphology, chemical structure, presence of performance additives and even mechanical properties. It was shown that although PEN is intrinsically more resistive in electrical tree initiation than PET due to low ionization potential of the naphthalene ring, the electrical tree propagation rate within PEN can be

accelerated because of its high Young's modulus and low tendency to crystallization, which will surely shorten the PD lifetime.

Chapter Eight

8.Conclusions and future work

8.1 Conclusions

This thesis has discussed the partial discharge induced degradation and breakdown of poly(ethylene terephthalate) (PET) used as the backsheet material in photovoltaic modules. Effects of experimental comparators such as morphology, additives, thickness etc. on degradation and breakdown behaviours of PET have been comprehensively and thoroughly investigated.

The surface chemistry of PD exposed PET samples was explored by using surface characterization techniques i.e. ATR-FTIR and XPS. It was found that the mechanism of PD degradation of PET is similar to that of Norrish type 1 reaction, where the ester functional group in PET molecule preferentially breaks down due to the surface bombardment by high energy ions and UV radiation produced during the discharge. Various by-products such as carboxylic acid, aldehyde, phenol and amines were found on the exposed sample surface.

A major contribution of this project is quantitative analysis of the morphology effect on PD degradation of PET films has been carried out chemically and physically by using surface-sensitive techniques such as ATR-FTIR, XPS and surface profilometers. Same type of PET samples with different morphology due to various draw ratios were used for the experiment. The morphology difference of the samples can be directly observed from DSC and ATR-FTIR. In DSC, locations and fusion enthalpies of the melting peaks for PET were measured and thus the lamellae thicknesses and crystallinities of the samples could be calculated. In FTIR,

crystallinities of the samples were calculated by the peak ratios of 1473 cm^{-1}/1455 cm^{-1}. The results of two methods exhibited high consistency. It was found samples with thicker lamellae and higher crystallinity will have a better PD resistance in terms of polymer bond cleavage rate, by-product amount and physical erosion depth.

Thickness effect was investigated using a wide thickness range from 36 μm to 480 μm. Linear relation between PD lifetime and thickness on log-log scale had been found until the sample thickness reached 190 μm. Samples with thickness greater than 190 μm exhibited PD lifetime much less than the ideal linear condition. This can be explained by the probability of presence of larger voids in thicker samples will be higher than that of thin samples, as a result the growth rate of PD-initiated electrical trees within the thicker samples will be accelerated and the apparent PD lifetime of the sample is thus decreased.

The performance additive effect was investigated in chapter 4 using PET films functioned with various additives i.e. white pigments (TiO_2 and $BaSO_4$), UV stabilizer and flame retardant. In this chapter, surprisingly, PD resistance and PD lifetime of samples had been found not necessarily correlated with each other as expected. The PD lifetime was found strongly influenced by the electrical treeing behaviour (including initiation and propagation) within the sample rather than the PD resistance per se. Once functioned with proper additives, PET film was able to withstand high voltage for a long time even significant thickness reduction due to PD erosion had been found. The PET film functioned with phosphorus based flame retardant (PET-FR) exhibited much longer PD lifetime than any other sample and the erosion depth at breakdown (EDAB) of the sample, was over a third of the original sample thickness, which is much higher than that of the rest samples as well. Results of ATR-FTIR, XPS and SEM revealed that after PD exposure, large amount of phosphoric acids were produced on the sample surface. These phosphoric acids with high conductivity would well cover the degradation area and might even migrate into the electrical tree channels. Therefore the electric fields across the whole sample and electrical trees can be strongly moderated and the initiation and propagation of electrical trees with the sample can thus be effectively suppressed. This is one of the most important contributions of this work as it has provided a basis of improving the PD lifetime of polymers to not only materials used in PV backsheets but also other insulation systems such as underground cables where PD-induced breakdown is a more common issue.

Best PD resistance have been found for the PET samples functioned with inorganic fillers which exhibited the lowest decomposition rates among all the samples. This could be attributed to the combination effect of the filler pile-up phenomenon and permittivity difference effect. The inorganic particles filled samples also showed superior PD lifetime to the untreated PET since the inorganic fillers can effectively slow down the growth of electrical trees by acting as physical barriers plus the PD initiation is expected to be inhibited due to the excellent PD resistance of the filled samples. An interesting result has been found for the TiO_2 filled PET sample which although having a lower filler content, showed longer PD lifetime than the $BaSO_4$ filled one. Explanations for this finding is that the $BaSO_4$ fillers are used specifically to generate voids between fillers and the polymer to scatter light and thus create the whiteness of the fillers, on the other hand, TiO_2 is simply used as a whitener by pure pigment effect as the refractive index of TiO_2 is higher than that of any other commercial pigments. Therefore it can be expected that more voids and defects will present around $BaSO_4$ than TiO_2 when they are both used as pigments for PET. As a result the difficulty of electrical tree propagation in PET-$BaSO_4$ will be lower and its PD lifetime is thus shorter. Furthermore, positive effect on enhancing both PD resistance and PD lifetime of PET has been found for UV stabilizer.

A straightforward technique for increasing both the PD resistance and PD lifetime of PET samples was described in this work. Significant improvements of PD resistance and PD lifetime of PET films were observed after the samples had been isothermally crystallized at temperatures above 210°C where highly thickened and perfected lamellae within the samples could be obtained. However, the effect was not obvious when the samples were annealed at temperatures below 210°C. Because the thin and defective lamellae produced at lower temperatures were not strong enough to suppress either ion bombardment or electrical tree growth. Additionally, annealing the samples at temperatures above 210°C can eliminate the extra excess-hole free volume which would be generated by the vitrification of the rigid amorphous region (RAF) in PET in lower temperatures, and thus the electrical tree propagation within the samples can be effectively inhibited.

Another important contribution of this work is the photodegradation and hydrolysis effects on PD-induced breakdown of PET films have been studied for the first time ever. PET films were subjected to photodegradation in weatherometer and hydrolysis in hot water, respectively prior to PD tests. Very different results have

been observed from the two sets of samples. For the photodegraded samples, rapid decline of PD lifetime was observed for the unstabilized PET due to the severe damage of polymer crystals by photodegradation; on the other hand, the sample functioned with $BaSO_4$ and UV stabilizer exhibited steady PD lifetime throughout the experiment as the crystal structure of the sample was well protected by the pigments and the UV stabilizer. For the hydrolysed samples, higher rate of hydrolysis was observed for the unstabilized sample. However when it came to the PD tests, similar changes of PD lifetimes have been found for both the unstabilized and hydrolysis-stabilized samples throughout the experiment where the PD lifetimes of the samples both increased slightly in the early stage of hydrolysis and gradually decreased afterwards. Compared to the untreated samples, no PD lifetime decline was found even for the 50-day treated samples. This is because the crystalline regions of the polymers were not attacked during hydrolysis and the changes of PD lifetimes during the experiment can be explained by the mutual effect between chemicrystallization and hydrolytic degradation. It could be concluded that the PD lifetime of the samples strongly depends on their crystal morphology. As a result, for all the weathering treated samples, DSC has been proven very powerful in predicting the PD lifetime as the crystal morphology of the samples can be directly reflected by the technique.

In this study, the PD degradation and breakdown behaviours of two members in the polyester family i.e. poly(ethylene terephthalate) (PET) and poly(ethylene 2,6-naphthalate) (PEN), were analysed and compared. It was found that PEN showed superior PD resistance to PET both chemically and physically. However, the difference of PD lifetimes between the two polyesters was much smaller than expected. Because despite PEN is intrinsically more resistive in electrical tree initiation than PET, its PD lifetime could be affected by mechanical properties and crystallinity.

8.2 Future work

8.2.1 AC vs DC

Since PV panels are working under DC voltage, one of the main issues of PD tests for PV backsheets is the correlation between the AC test and the DC test. AC has

been mostly used in both industry and academia including this work for the purpose of accelerating the test as the PD repetition rate of AC is usually orders of magnitude higher than that of DC [182]. Effort was made to determine the acceleration factor between DC and AC but failed since sample degradation was hardly seen after DC exposure [16]. Further study could be conducted by using higher voltage stress under DC condition to accelerate the test.

8.2.2 Longer UV test

In this study, a weathering test whose UV dose was equivalent to 4.5 years of outdoor exposure in Florida was carried out before PD tests. Significant declines of PD lifetimes have been found for the samples without UV stabilizer while the performance of the UV-stabilized sample was excellent and steady during the whole experiment. However the UV dose (4.5 years) used in this project was still far from enough to fully mimic the practical situation (25 years), longer UV test will be needed to further investigate the performance of PET-$BaSO_4$-UV.

8.2.3 PD degradation and breakdown of fluoropolymers

Today, fluoropolymers such as poly(vinyl fluoride) (PVF) and poly(vinylidene fluoride) (PVDF) are still playing as an important role in PV backsheet due to their excellent weatherability. In practical situation, PD is most likely to occur at the weak links of the backsheet i.e. adhesions between the fluoropolymer layer and the PET, where voids and air gap can be generated due to delamination. As a result, the fluoropolymer is potentially subjected to the PD-induced degradation as well. Therefore it is recommended that the PD degradation of the common fluoropolymers used in PV backsheets be studied to have a better understanding of PD-induced breakdown behaviour of the backsheet.

Reference

[1] Toriyama, Y., Okamoto, H. and Kanazashi, M., 1971. Breakdown of Insulating Materials by Surface Discharge. *IEEE Transactions on Electrical Insulation*, (3), pp.124-129.

[2] Mason, J.H., 1960. The resistance of sheet insulation to surface discharges. *Proceedings of the IEE-Part A: Power Engineering*, *107*(36), pp.551-563.

[3] Mason, J.H., 1978. Disharges. *IEEE Transactions on Electrical Insulation*, (4), pp.211-238.

[4] Vitellas, I., Theodosiou, K., Gialas, I. and Agoris, D.P., 2005. Mechanism of degradation and breakdown in PET films under high intensity AC fields. *The European Physical Journal Applied Physics*, *30*(2), pp.83-89.

[5] Bozzo, R., Centurioni, L. and Guastavino, F., 1993. Measuring the endurance of films in partial discharges. *IEEE transactions on electrical insulation*, *28*(6), pp.1050-1056.

[6] Guastavino, F. and Tiemblo, P., 1997. Models for life prediction in surface PD on polymer films. *IEEE transactions on dielectrics and electrical insulation*, *4*(2), pp.189-196.

[7] Földes, E., Tóth, A., Kálmán, E. and Fekete, E., 2000. Surface changes of corona-discharge-treated polyethylene films. *Journal of applied polymer science*, *76*(10), pp.1529-1541.

[8] Toriyama, Y., Okamoto, H., Kanazashi, M. and Horii, K., 1967. Degradation of polyethylene by partial discharge. *IEEE Transactions on Electrical Insulation*, (2), pp.83-92.

[9] Zaharudin, N., Arief, Y.Z., Izzati, W.A., Adzis, Z. and Makmud, M.Z.H., 2012, December. Effect of relative humidity on surface discharge characteristics of

polymeric material under AC stress. *2012 IEEE International Conference on Power and Energy (PECon)* (pp. 756-760). IEEE.

[10] Guastavino, F. and Tiemblo, P., 1998. Effect of humidity on the time to breakdown of polymers subject to partial discharges. *Polymer Engineering & Science*, *38*(1), pp.119-126.

[11] Sili, E., Cambronne, J.P., Naude, N. and Khazaka, R., 2013. Polyimide lifetime under partial discharge aging: effects of temperature, pressure and humidity. *IEEE Transactions on Dielectrics and Electrical Insulation*, *20*(2), pp.435-442.

[12] Tanaka, T. and Iizuka, T., 2010, October. Generic PD resistance characteristics of polymer nanocomposites. *2010 Annual Report Conference on Electrical Insulation and Dielectric Phenomena (CEIDP)* (pp. 1-4). IEEE.

[13] Rodehed, C., Gustafsson, A. and Gedde, U.W., 1990. Electrical strength and chemical surface analysis of polypropylene after exposure to external partial discharges. *IEEE transactions on electrical insulation*, *25*(6), pp.1066-1076.

[14] Iguchi, A., Hirabayashi, H., Hayashi, T., Yamada, K. and Nishimura, H., 2014. Evaluation of Degradation of PET Film by Partial Discharge Method. *Materials Sciences and Applications*, *2014, 5* (pp. 33-38).

[15] Gamez-Garcia, M., Bartnikas, R. and Wertheimer, M.R., 1987. Synthesis Reactions Involving XLPE Subjected to aartial Discharges. *IEEE Transactions on Electrical Insulation*, (2), pp.199-205.

[16] Phillips, N.H., Givot, B., O'Brien, B., Korba, G. and Loyd, J., 2012, June. Analytical techniques used to determine chemical degradation of polymeric materials used in PV modules after sustained exposure to partial discharge voltages. In *Photovoltaic Specialists Conference (PVSC), 2012 38th IEEE* (pp. 000714-000719). IEEE.

[17] Sekii, Y., 2010. Degradation of low-density polyethylene and cross-linked polyethylene by partial discharge. *IEEE Transactions on Dielectrics and Electrical Insulation*, *17*(1), pp.116-124.

[18] Miyata, K., Fujita, S., Ohki, Y. and Tanaka, T., 2007. Comparison of partial discharge resistance among several biodegradable polymers. *IEEE Transactions on Dielectrics and Electrical Insulation*, *14*(6), pp.1474-1476.

[19] Luo, Y., Wu, G., Liu, J., Zhu, G., Wang, P. and Cao, K., 2013, June. Damage processes of polyimide film caused by surface discharge. In *2013 IEEE International Conference on Solid Dielectrics (ICSD)* (pp. 325-328). IEEE.

[20] Matsushita, M., Maeno, Y., Kino, H., Fujita, S., Hirai, N., Tanaka, T., Ohki, Y., Tajitsu, Y., Kohtoh, M. and Okabe, S., 2005, June. Effects of glass transition on the dielectric breakdown and electrical conduction in several biodegradable polymers. In *Proceedings of 2005 International Symposium on Electrical Insulating Materials, 2005.(ISEIM 2005).* (Vol. 2, pp. 413-416). IEEE.

[21] Adhikari, D., Hepburn, D.M. and Stewart, B.G., 2012. Comparison of partial discharge characteristics and degradation in several polymeric insulators. *IET Science, Measurement & Technology*, *6*(6), pp.474-484.

[22] Rouha, N. and Beroual, A., 2013. Physico-chemical diagnosis of EPDM electrical aging by tree phenomenon. *IEEE Transactions on Dielectrics and Electrical Insulation*, *20*(5), pp.1577-1583.

[23] Yan, J., Liao, R., Yang, L. and Li, J., 2012. Study on microstructure and electrical properties of oil-impregnated paper insulation after exposure to partial discharge. *European Transactions on Electrical Power*, *22*(6), pp.733-746.

[24] Fuse, N., Fujita, S., Hirai, N., Tanaka, T., Kozako, M., Kohtoh, M., Okabe, S. and Ohki, Y., 2007. Partial discharge degradation of several biodegradable polymers. *IEEJ Transactions on Fundamentals and Materials*, *127*(8), pp. 459-466.

[25] Owens, D.K., 1975. The mechanism of corona and ultraviolet light-induced self-adhesion of poly (ethylene terephthalate) film. *Journal of Applied Polymer Science*, *19*(12), pp.3315-3326.

[26] Hudon, C., Bartnikas, R. and Wertheimer, M.R., 1995. Effect of physico-chemical degradation of epoxy resin on partial discharge behavior. *IEEE Transactions on Dielectrics and Electrical Insulation*, *2*(6), pp.1083-1094.

[27] Hasegawa, Y., Isamu, I. and Ohki, Y., 2012, July. Experimental study on the factors determining the partial discharge resistance of polymers. *2012 IEEE 10th International Conference on Properties and Applications of Dielectric Materials (ICPADM)* (pp. 1-4). IEEE.

[28] Hudon, C., Bartnikas, R. and Wertheimer, M.R., 1994, July. Chemical and physical degradation effects on epoxy surfaces exposed to partial discharges. *4th International Conference on Properties and Applications of Dielectric Materials* (Vol. 2, pp. 811-814). IEEE.

[29] Sekii, Y. and Yamauchi, K., 2008, April. Analysis of deterioration by partial discharge of XLPE using GCMS and FTIR. *International Conference on Condition Monitoring and Diagnosis, 2008.* (pp. 251-254). IEEE.

[30] Sekii, Y., Oguma, H., Takeo, H. and Yamauchi, K., 2005, October. GC-MS and FTIR analysis of LDPE and XLPE deteriorated by partial discharge. In *CEIDP'05. 2005 Annual Report Conference on Electrical Insulation and Dielectric Phenomena, 2005.* (pp. 237-240). IEEE.

[31] O'Hare, L.A., Smith, J.A., Leadley, S.R., Parbhoo, B., Goodwin, A.J. and Watts, J.F., 2002. Surface physico-chemistry of corona-discharge-treated poly (ethylene terephthalate) film. *Surface and interface analysis*, *33*(7), pp.617-625.

[32] Pandiyaraj, K.N., Selvarajan, V., Deshmukh, R.R. and Bousmina, M., 2008. The effect of glow discharge plasma on the surface properties of Poly (ethylene terephthalate)(PET) film. *Surface and Coatings Technology*, *202*(17), pp.4218-4226.

[33] Ding, L., Shao, L. and Bai, Y., 2014. Deciphering the mechanism of corona discharge treatment of BOPET film. *RSC Advances*, *4*(42), pp.21782-21787.

[34] Pandiyaraj, K.N., Selvarajan, V., Deshmukh, R.R. and Gao, C., 2008. Adhesive properties of polypropylene (PP) and polyethylene terephthalate (PET) film surfaces treated by DC glow discharge plasma. *Vacuum*, *83*(2), pp.332-339.

[35] De Geyter, N., Morent, R. and Leys, C., 2008. Influence of ambient conditions on the ageing behaviour of plasma-treated PET surfaces. *Nuclear Instruments and Methods in Physics Research Section B: Beam Interactions with Materials and Atoms*, *266*(12), pp.3086-3090.

[36] Cui, N.Y., Upadhyay, D.J., Anderson, C.A., Meenan, B.J. and Brown, N.M., 2007. Surface oxidation of a Melinex 800 PET polymer material modified by an atmospheric dielectric barrier discharge studied using X-ray photoelectron spectroscopy and contact angle measurement. *Applied surface science*, *253*(8), pp.3865-3871.

[37] Fang, Z., Wang, X., Shao, R., Qiu, Y. and Edmund, K., 2011. The effect of discharge power density on polyethylene terephthalate film surface modification by dielectric barrier discharge in atmospheric air. *Journal of Electrostatics*, *69*(1), pp.60-66.

[38] Dowling, D.P., Tynan, J., Ward, P., Hynes, A.M., Cullen, J. and Byrne, G., 2012. Atmospheric pressure plasma treatment of amorphous polyethylene terephthalate for enhanced heatsealing properties. *International Journal of Adhesion and Adhesives*, *35*, pp.1-8.

[39] Akishev, Y.S., Grushin, M.E., Drachev, A.I., Karalnik, V.B., Petryakov, A.V. and Trushkin, N.I., 2013. On Hydrophilicity Ageing of PP and PET Films Induced by Ultraviolet Radiation and Hydrogen Atoms. *The Open Plasma Physics Journal*, *6*, pp.19-29.

[40] Paun, I., Fréchette, M.F., Wertheimer, M.R. and Larocque, R.Y., 1998, October. Characterization of epoxy resin surfaces exposed to partial discharges in SF 6 and N 2-SF 6 mixtures. *Annual Report Conference on Electrical Insulation and Dielectric Phenomena* (pp. 706-709). IEEE.

[41] Strobel, M., Lyons, C.S., Strobel, J.M. and Kapaun, R.S., 1992. Analysis of air-corona-treated polypropylene and poly (ethylene terephthalate) films by contact-angle measurements and X-ray photoelectron spectroscopy. *Journal of adhesion science and technology*, *6*(4), pp.429-443.

[42] Peng, G., Yang, D., Liu, H. and He, S., 2008. Degradation of poly (ethylene terephthalate) film under proton irradiation. *Journal of applied polymer science*, *107*(6), pp.3625-3629.

[43] Vesel, A. and Mozetic, M., 2008. Modification of PET surface by nitrogen plasma treatment. In *Journal of Physics: Conference Series* (Vol. 100, No. 1, p. 012027). IOP Publishing.

[44] Kasahara, T., Shoji, S., and Mizuno, J., Surface modification of polyethylen-terephthalat (PET) by 172-nm eximer lamp, *Trans. Jpn. Inst. Electron. Pack.*, 2012, vol. 5, no. 1, pp. 47–54.

[45] Girardeaux, C., Zammatteo, N., Art, M., Gillon, B., Pireaux, J.J. and Caudano, R., 1996. Amination of poly (ethylene-terephthalate) polymer surface for biochemical applications. *Plasmas and Polymers*, *1*(4), pp.327-346.

[46] Doren, A., Genet, M.J. and Rouxhet, P.G., 1994. Analysis of poly (ethylene terephthalate)(PET) by XPS. *Surface Science Spectra*, *3*(4), pp.337-341.

[47] Dr. h .c. Robert Mathys Stifung, RMS Foundation. Chemical surface analysis with XPS, https://www.rms-foundation.ch/fileadmin/newsletter/newsletter_04_e.pdf, edition July 2011.

[48] Louette, P., Bodino, F. and Pireaux, J.J., 2005. Poly (ethylene terephthalate)(PET) XPS reference core level and energy loss spectra. *Surface Science Spectra*, *12*(1), pp.1-5.

[49] Tarek S. Salem, PET Surface Properties affected by low temperature plasma modification, http://www.uni-leipzig.de/~iom/muehlleithen/2009/Di_IV_1_Salem.pdf, Mühlleithen / Vogtland, 10-12, March 2009

[50] Pandiyaraj, K.N., Selvarajan, V. and Deshmukh, R.R., 2010. Effects of operating parameters on DC glow discharge plasma induced PET film surface. In *Journal of Physics: Conference Series* (Vol. 208, No. 1, p. 012100). IOP Publishing.

[51] Hurley, C.R. and Leggett, G.J., 2009. Quantitative investigation of the photodegradation of polyethylene terephthalate film by friction force microscopy, contact-angle goniometry, and X-ray photoelectron spectroscopy. *ACS applied materials & interfaces*, *1*(8), pp.1688-1697.

[52] Kormunda, M. and Pavlik, J., 2010. Characterization of oxygen and argon ion flux interaction with PET surfaces by in-situ XPS and ex-situ FTIR. *Polymer Degradation and Stability*, *95*(9), pp.1783-1788.

[53] EAG Laboratories, white paper: Surface and interface characterization of polymer films, 2015

[54] Le, Q.T., Pireaux, J.J. and Caudano, R., 1997. XPS study of the PET film surface modified by CO2 plasma: effects of the plasma parameters and ageing. *Journal of adhesion science and technology*, *11*(5), pp.735-751.

[55] Kong, Y. and Hay, J.N., 2002. The measurement of the crystallinity of polymers by DSC. *Polymer*, *43*(14), pp.3873-3878.

[56] Kong, Y. and Hay, J.N., 2003. The enthalpy of fusion and degree of crystallinity of polymers as measured by DSC. *European Polymer Journal*, *39*(8), pp.1721-1727.

[57] Woo, E.M. and Ko, T.Y., 1996. A differential scanning calorimetry study on poly (ethylene terephthalate) isothermally crystallized at stepwise temperatures: multiple melting behavior re-investigated. *Colloid and Polymer Science*, *274*(4), pp.309-315.

[58] Kong, Y. and Hay, J.N., 2003. Multiple melting behaviour of poly (ethylene terephthalate). *Polymer*, *44*(3), pp.623-633.

[59] Rastogi, R., Vellinga, W.P., Rastogi, S., Schick, C. and Meijer, H.E.H., 2004. The three-phase structure and mechanical properties of poly (ethylene terephthalate). *Journal of Polymer Science Part B: Polymer Physics*, *42*(11), pp.2092-2106.

[60] Baldenegro-Perez, L.A., Navarro-Rodriguez, D., Medellin-Rodriguez, F.J., Hsiao, B., Avila-Orta, C.A. and Sics, I., 2014. Molecular weight and crystallization temperature effects on poly (ethylene terephthalate)(PET) homopolymers, an isothermal crystallization analysis. *Polymers*, *6*(2), pp.583-600.

[61] Badia, J.D., Strömberg, E., Karlsson, S. and Ribes-Greus, A., 2012. The role of crystalline, mobile amorphous and rigid amorphous fractions in the performance of recycled poly (ethylene terephthalate)(PET). *Polymer degradation and stability*, *97*(1), pp.98-107.

[62] Medellin–Rodriguez, F.J., Phillips, P.J., Lin, J.S. and Campos, R., 1997. The triple melting behavior of poly (ethylene terephthalate): Molecular weight effects. *Journal of Polymer Science Part B: Polymer Physics*, *35*(11), pp.1757-1774.

[63] Righetti, M.C., Laus, M. and Di Lorenzo, M.L., 2014. Rigid amorphous fraction and melting behavior of poly (ethylene terephthalate). *Colloid and Polymer Science*, *292*(6), pp.1365-1374.

[64] Natu, A.A., Lofgren, E.A. and Jabarin, S.A., 2005. Effect of morphology on barrier properties of poly (ethylene terephthalate). *Polymer Engineering & Science*, *45*(3), pp.400-409.

[65] Menczel, J.D. and Jaffe, M., 2007. How did we find the rigid amorphous phase?. *Journal of thermal analysis and calorimetry*, *89*(2), pp.357-362.

[66] Androsch, R. and Wunderlich, B., 2005. The link between rigid amorphous fraction and crystal perfection in cold-crystallized poly (ethylene terephthalate). *Polymer*, *46*(26), pp.12556-12566.

[67] Wang, Z.G., Hsiao, B.S., Sauer, B.B. and Kampert, W.G., 1999. The nature of secondary crystallization in poly (ethylene terephthalate). *Polymer*, *40*(16), pp.4615-4627.

[68] Righetti, M.C., Di Lorenzo, M.L., Tombari, E. and Angiuli, M., 2008. The low-temperature endotherm in poly (ethylene terephthalate): Partial melting and rigid amorphous fraction mobilization. *The Journal of Physical Chemistry B*, *112*(14), pp.4233-4241.

[69] Lin, J., Shenogin, S. and Nazarenko, S., 2002. Oxygen solubility and specific volume of rigid amorphous fraction in semicrystalline poly (ethylene terephthalate). *Polymer*, *43*(17), pp.4733-4743.

[70] Righetti, M.C., Laus, M. and Di Lorenzo, M.L., 2014. Temperature dependence of the rigid amorphous fraction in poly (ethylene terephthalate). *European Polymer Journal*, *58*, pp.60-68.

[71] Differential Scanning Calorimetry; First and Second Order Transitions in PETE, http://www.colby.edu/chemistry/PChem/lab/DSCPETE.pdf

[72] Huang, J.M., Chu, P.P. and Chang, F.C., 2000. Conformational changes and molecular motion of poly (ethylene terephthalate) annealed above glass transition temperature. *Polymer*, *41*(5), pp.1741-1748.

[73] Karagiannidis, P.G., Stergiou, A.C. and Karayannidis, G.P., 2008. Study of crystallinity and thermomechanical analysis of annealed poly (ethylene terephthalate) films. *European Polymer Journal*, *44*(5), pp.1475-1486.

[74] Arnoult, M., Dargent, E. and Mano, J.F., 2007. Mobile amorphous phase fragility in semi-crystalline polymers: Comparison of PET and PLLA. *Polymer*, *48*(4), pp.1012-1019.

[75] Tan, S., Su, A., Li, W. and Zhou, E., 1998. The crystallization behavior of the metastable melts of poly (ethylene terephthalate) from the multiple melting process. *Macromolecular rapid communications*, *19*(1), pp.11-14.

[76] Lu, S.X. and Cebe, P., 1996. Effects of annealing on the disappearance and creation of constrained amorphous phase. *Polymer*, *37*(21), pp.4857-4863.

[77] Righetti, M.C., Tombari, E., Angiuli, M. and Di Lorenzo, M.L., 2007. Enthalpy-based determination of crystalline, mobile amorphous and rigid amorphous fractions in semicrystalline polymers: Poly (ethylene terephthalate). *Thermochimica Acta*, *462*(1), pp.15-24.

[78] Di Lorenzo, M.L., Righetti, M.C., Cocca, M. and Wunderlich, B., 2010. Coupling between crystal melting and rigid amorphous fraction mobilization in poly (ethylene terephthalate). *Macromolecules*, *43*(18), pp.7689-7694.

[79] Lu, X.F. and Hay, J.N., 2001. Isothermal crystallization kinetics and melting behaviour of poly (ethylene terephthalate). *Polymer*, *42*(23), pp.9423-9431.

[80] Minakov, A.A., Mordvintsev, D.A. and Schick, C., 2004. Melting and reorganization of poly (ethylene terephthalate) on fast heating (1000 K/s). *Polymer*, *45*(11), pp.3755-3763.

[81] Song, M., 2001. Rigid amorphous phase and low temperature melting endotherm of poly (ethylene terephthalate) studied by modulated differential scanning calorimetry. *Journal of applied polymer science*, *81*(11), pp.2779-2785.

[82] Keith, H.D. and Padden Jr, F.J., 1964. Spherulitic crystallization from the melt. I. Fractionation and impurity segregation and their influence on crystalline morphology. *Journal of Applied Physics*, *35*(4), pp.1270-1285.

[83] Papageorgiou, G.Z., Karayannidis, G.P., Bikiaris, D.N., Stergiou, A., Litsardakis, G. and Makridis, S.S., 2004. Wide-angle X-ray diffraction and differential scanning calorimetry study of the crystallization of poly (ethylene naphthalate), poly (butylene

naphthalate), and their copolymers. *Journal of Polymer Science Part B: Polymer Physics*, *42*(5), pp.843-860.

[84] Ma, Q., Georgiev, G. and Cebe, P., 2011. Constraints in semicrystalline polymers: Using quasi-isothermal analysis to investigate the mechanisms of formation and loss of the rigid amorphous fraction. *Polymer*, *52*(20), pp.4562-4570.

[85] Liang, C.Y. and Krimm, S., 1959. Infrared spectra of high polymers: Part IX. Polyethylene terephthalate. *Journal of molecular spectroscopy*, *3*(1), pp.554-574.

[86] Grime, D. and Ward, I.M., 1958. The assignment of infra-red absorptions and rotational isomerism in polyethylene terephthalate and related compounds. *Transactions of the Faraday Society*, *54*, pp.959-971.

[87] Hollauer, E., Mondragon, M.A. and Castaño, V.M., 2001. Fourier transform infrared and Raman spectra, vibrational assignment and ab initio calculations of terephthalic acid and related compounds. *Spectrochimica Acta Part A: Molecular and Biomolecular Spectroscopy*, *57*(5), pp.993-1007.

[88] Cole, K.C., Ajji, A. and Pellerin, E., 2002. New insights into the development of ordered structure in poly (ethylene terephthalate). 1. Results from external reflection infrared spectroscopy. *Macromolecules*, *35*(3), pp.770-784.

[89] Kirov, K.R. and Assender, H.E., 2005. Quantitative ATR-IR analysis of anisotropic polymer films: surface structure of commercial PET. *Macromolecules*, *38*(22), pp.9258-9265.

[90] Barbaro, G., Galdi, M.R., Di Maio, L. and Incarnato, L., 2015. Effect of BOPET film surface treatments on adhesion performance of biodegradable coatings for packaging applications. *European Polymer Journal*, *68*, pp.80-89.

[91] Atkinson, J.R., Biddlestone, F. and Hay, J.N., 2000. An investigation of glass formation and physical ageing in poly (ethylene terephthalate) by FT-IR spectroscopy. *Polymer*, *41*(18), pp.6965-6968.

[92] Novák, I.G.O.R., Chodák, I.V.A.N., Sedliačik, J., ŠTEVIAR, M., POPELKA, A. and Kopný, J., 2010. Investigation of poly (ethylene terephthalate) treated by low-temperature plasma. *Annals of Warsaw University of Life Sciences–SGGW Forestry and Wood Technology*, *72*, pp.83-89.

[93] Sikka, S.S. and Kausch, H.H., 1979. Study of stress-induced changes in poly (ethylene terephthalate) through Fourier transform infrared spectroscopy. *Colloid and Polymer Science*, *257*(10), pp.1060-1067.

[94] Chen, Z., 2013. *The crystallization of Poly (ethylene terephthalate) studied by thermal analysis and FTIR spectroscopy* (Doctoral dissertation, University of Birmingham).

[95] Adhikari, D., Hepburn, D.M. and Stewart, B.G., 2011, June. Analysis of deterioration of PET insulation with multiple voids due to electrical stressing. In *2011 Electrical Insulation Conference (EIC).* (pp. 146-150). IEEE.

[96] Donelli, I., Freddi, G., Nierstrasz, V.A. and Taddei, P., 2010. Surface structure and properties of poly-(ethylene terephthalate) hydrolyzed by alkali and cutinase. *Polymer Degradation and Stability*, *95*(9), pp.1542-1550.

[97] Hepburn, D.M., Kemp, I.J., Shields, A.J. and Cooper, J., 2000. Degradation of epoxy resin by partial discharges. *IEE Proceedings-Science, Measurement and Technology*, *147*(3), pp.97-104.

[98] Florián, Š., Novák, I., Popelka, A., Chodák, I., Špírková, M., Chehimi, M.M. and Kleinová, A., SURFACE PROPERTIES OF POLY (ETHYLENE TEREPHTHALATE) MODIFIED BY BARRIER PLASMA.

[99] Dissado, L.A. and Fothergill, J.C., 1992. *Electrical degradation and breakdown in polymers* (Vol. 9). IET.

[100] Scheirs, J. and Long, T.E. eds., 2005. *Modern polyesters: chemistry and technology of polyesters and copolyesters*. John Wiley & Sons.

[101] Kozako, M., Fuse, N., Ohki, Y., Okamoto, T. and Tanaka, T., 2004. Surface degradation of polyamide nanocomposites caused by partial discharges using IEC (b) electrodes. *IEEE Transactions on Dielectrics and Electrical Insulation*, *11*(5), pp.833-839.

[102] Tanaka, T., Montanari, G.C. and Mulhaupt, R., 2004. Polymer nanocomposites as dielectrics and electrical insulation-perspectives for processing technologies, material characterization and future applications. *IEEE Transactions on Dielectrics and Electrical Insulation*, *11*(5), pp.763-784.

[103] Tanaka, T., Ohki, Y., Ochi, M., Harada, M. and Imai, T., 2008. Enhanced partial discharge resistance of epoxy/clay nanocomposite prepared by newly developed organic modification and solubilization methods. *IEEE Transactions on Dielectrics and Electrical Insulation*, *15*(1), pp.81-89.

[104] Li, Z., Okamoto, K., Ohki, Y. and Tanaka, T., 2010. Effects of nano-filler addition on partial discharge resistance and dielectric breakdown strength of Micro-Al 2 O 3 Epoxy composite. *IEEE Transactions on Dielectrics and Electrical Insulation*, *17*(3), pp.653-661.

[105] Maity, P., Basu, S., Parameswaran, V. and Gupta, N., 2008. Degradation of polymer dielectrics with nanometric metal-oxide fillers due to surface discharges. *IEEE Transactions on Dielectrics and Electrical Insulation*, *15*(1), pp.52-62.

[106] Maity, P., Kasisomayajula, S.V., Parameswaran, V., Basu, S. and Gupta, N., 2008. Improvement in surface degradation properties of polymer composites due to pre-processed nanometric alumina fillers. *IEEE Transactions on Dielectrics and Electrical Insulation*, *15*(1), pp.63-72.

[107] Tanaka, T., Matsuo, Y. and Uchida, K., 2008, October. Partial discharge endurance of epoxy/SiC nanocomposite. In *2008 Annual Report Conference on Electrical Insulation and Dielectric Phenomena* (pp. 13-16). IEEE.

[108] Zhao, X., Yin, J.H., Jin, R. and Dong, J.Y., 2013. Effect of Content and Layer Thickness on the Corona-Resistance of PI/TiO2 Nanocomposite Films. In *Applied Mechanics and Materials* (Vol. 395, pp. 133-137). Trans Tech Publications.

[109] Meichsner, C., Clark, T., Groeppel, P., Winter, B., Butz, B. and Spiecker, E., 2012. Formation of a protective layer during IEC (b) test of epoxy resin loaded with silica nanoparticles. *IEEE Transactions on Dielectrics and Electrical Insulation*, *19*(3), pp.786-792.

[110] Danikas, M.G. and Tanaka, T., 2009. Nanocomposites-a review of electrical treeing and breakdown. *IEEE Electrical Insulation Magazine*, *25*(4), pp.19-25.

[111] Zha, J.W., Song, H.T., Dang, Z.M., Shi, C.Y. and Bai, J., 2008. Mechanism analysis of improved corona-resistant characteristic in polyimide/TiO2 nanohybrid films. *Applied Physics Letters*, *93*(19), p.192911.

[112] Tanaka, T., Kozako, M., Fuse, N. and Ohki, Y., 2005. Proposal of a multi-core model for polymer nanocomposite dielectrics. *IEEE Transactions on Dielectrics and Electrical Insulation*, *12*(4), pp.669-681.

[113] Guastavino, F., Ratto, A., Della Giovanna, L., Gómez-Elvira, J.M. and Garcìa, N., 2012, September. Surface partial discharges aging on thin polymeric nanocomposite films. In *Electrical Machines (ICEM), 2012 XXth International Conference on* (pp. 1836-1840). IEEE.

[114] Tanaka, T. and Imai, T., 2013. Advances in nanodielectric materials over the past 50 years. *IEEE Electrical Insulation Magazine*, *1*(29), pp.10-23.

[115] Seiler, J. and Kindersberger, J., 2014. Insight into the interphase in polymer nanocomposites. *IEEE Transactions on Dielectrics and Electrical Insulation*, *21*(2), pp.537-547.

[116] Tanaka, T., 2010. Interface properties and surface erosion resistance. In *Dielectric Polymer Nanocomposites* (pp. 229-258). Springer US.

[117] Li, S., Yin, G., Chen, G., Li, J., Bai, S., Zhong, L., Zhang, Y. and Lei, Q., 2010. Short-term breakdown and long-term failure in nanodielectrics: a review. *IEEE Transactions on Dielectrics and Electrical Insulation*, *17*(5), pp.1523-1535.

[118] Tanaka, T., 2009, July. Similarity between treeing lifetime and PD resistance in aging mechanisms for epoxy nanocomposites. In *2009 IEEE 9th International Conference on the Properties and Applications of Dielectric Materials* (pp. 741-744). IEEE.

[119] Tanaka, T. and Iizuka, T., 2010, October. Generic PD resistance characteristics of polymer nanocomposites. In *Electrical Insulation and Dielectric Phenomena (CEIDP), 2010 Annual Report Conference on* (pp. 1-4). IEEE.

[120] Tanaka, T., Kuge, S.I., Kozako, M., Imai, T., Ozaki, T. and Shimizu, T., 2006. Nano effects on PD endurance of epoxy nanocomposites. *Proc. ICEE, No. ME1-01*, p.4.

[121] Rothon, R. ed., 2003. *Particulate-filled polymer composites*. iSmithers Rapra Publishing.

[122] Bianchi, F., Lazzeri, A., Pracella, M., D'Aquino, A. and Ligeri, G., 2004, November. Physical-Mechanical and Thermal Properties of Polyethylene Toughened with Submicron BaSO4 Particles. In *Macromolecular Symposia* (Vol. 218, No. 1, pp. 191-200). WILEY-VCH Verlag.

[123] Chen, H.B., Chen, L., Zhang, Y., Zhang, J.J. and Wang, Y.Z., 2011. Morphology and interference color in spherulite of poly (trimethylene terephthalate) copolyester with bulky linking pendent group. *Physical Chemistry Chemical Physics*, *13*(23), pp.11067-11075.

[124] Lin, C.H., Huang, C.M., Wang, M.W., Dai, S.A., Chang, H.C. and Juang, T.Y., 2014. Synthesis of a phosphinated acetoxybenzoic acid and its application in enhancing Tg and flame retardancy of poly (ethylene terephthalate). *Journal of Polymer Science Part A: Polymer Chemistry*, *52*(3), pp.424-434.

[125] Chang, S.J., Sheen, Y.C., Chang, R.S. and Chang, F.C., 1996. The thermal degradation of phosphorus-containing copolyesters. *Polymer degradation and stability*, *54*(2), pp.365-371.

[126] Fechine, G.J.M., Rabello, M.S. and Souto-Maior, R.M., 2002. The effect of ultraviolet stabilizers on the photodegradation of poly (ethylene terephthalate). *Polymer Degradation and Stability*, *75*(1), pp.153-159.

[127] Ramaswamy, V., Vimalathithan, R.M. and Ponnusamy, V., 2010. Synthesis and characterization of BaSO4 nano particles using micro emulsion technique. *Adv. Appl. Sci. Res*, *1*(3), pp.197-204.

[128] Zheng, Z., Liu, B.W., Ting Yang, S., Cui, X. and Wang, H., 2015. Preparation of a novel phosphorus-and nitrogen-containing flame retardant and its synergistic effect in the intumescent flame-retarding polypropylene system. *Polymer Composites*, *36*(9), pp.1606-1619.

[129] Schmitz, P.J., 2001. Characterization of the Surface of BaSO4 Powder by XPS. *Surface Science Spectra*, *8*(3), pp.195-199.

[130] Lai, B. and Ni, X., 2008. Rheological Behavior and Interaction of Polycarbonate/Barium Sulfate Composites. *Journal of Macromolecular Science, Part B*, *47*(5), pp.1028-1038.

[131] Jerndal, E., Mattisson, T. and Lyngfelt, A., 2006. Thermal analysis of chemical-looping combustion. *Chemical Engineering Research and Design*, *84*(9), pp.795-806.

[132] Majjane, A., Chahine, A., Et-tabirou, M., Echchahed, B., Do, T.O. and Mc Breen, P., 2014. X-ray photoelectron spectroscopy (XPS) and FTIR studies of vanadium barium phosphate glasses. *Materials Chemistry and Physics*, *143*(2), pp.779-787.

[133] Jensen, H., Soloviev, A., Li, Z. and Søgaard, E.G., 2005. XPS and FTIR investigation of the surface properties of different prepared titania nano-powders. *Applied Surface Science*, *246*(1), pp.239-249.

[134] Salarian, M., Xu, W.Z., Biesinger, M.C. and Charpentier, P.A., 2014. Synthesis and characterization of novel TiO 2-poly (propylene fumarate) nanocomposites for bone cementation. *Journal of Materials Chemistry B*, *2*(32), pp.5145-5156.

[135] Todea, M., Vanea, E., Bran, S., Berce, P. and Simon, S., 2013. XPS analysis of aluminosilicate microspheres bioactivity tested in vitro. *Applied Surface Science*, *270*, pp.777-783.

[136] Majjane, A., Chahine, A., Et-tabirou, M., Echchahed, B., Do, T.O. and Mc Breen, P., 2014. X-ray photoelectron spectroscopy (XPS) and FTIR studies of vanadium barium phosphate glasses. *Materials Chemistry and Physics*, *143*(2), pp.779-787.

[137] Qian, X., Song, L., Bihe, Y., Yu, B., Shi, Y., Hu, Y. and Yuen, R.K., 2014. Organic/inorganic flame retardants containing phosphorus, nitrogen and silicon: preparation and their performance on the flame retardancy of epoxy resins as a novel intumescent flame retardant system. *Materials Chemistry and Physics*, *143*(3), pp.1243-1252.

[138] Shi, Y. and Wang, G., 2016. Influence of PEPA-containing polyether structure on fire protection of transparent fire-resistant coatings. *Journal of Coatings Technology and Research*, *13*(3), pp.457-468.

[139] Tsai, K.C., Kuan, C.F., Chen, C.H., Kuan, H.C., Hsu, S.W., Lee, F.M. and Chiang, C.L., 2013. Study on thermal degradation and flame retardant property of halogen-free polypropylene composites using XPS and cone calorimeter. *Journal of Applied Polymer Science*, *127*(2), pp.1084-1091.

[140] Puziy, A.M., Poddubnaya, O.I., Socha, R.P., Gurgul, J. and Wisniewski, M., 2008. XPS and NMR studies of phosphoric acid activated carbons. *Carbon*, *46*(15), pp.2113-2123.

[141] Gaan, S., Sun, G., Hutches, K. and Engelhard, M.H., 2008. Effect of nitrogen additives on flame retardant action of tributyl phosphate: phosphorus–nitrogen synergism. *Polymer Degradation and Stability*, *93*(1), pp.99-108.

[142] Daasch, L. and Smith, D., 1951. Infrared spectra of phosphorus compounds. *Analytical Chemistry*, *23*(6), pp.853-868.

[143] Levchik, S.V. and Weil, E.D., 2005. Flame retardancy of thermoplastic polyesters—a review of the recent literature. *Polymer International*, *54*(1), pp.11-35.

[144] Morshuis, P.H., 2005. Degradation of solid dielectrics due to internal partial discharge: some thoughts on progress made and where to go now. *IEEE Transactions on Dielectrics and Electrical Insulation*, *12*(5), pp.905-913.

[145] Wu, H. and Cao, Y.M., 2012. A study of Polyvinyl chloride modified by Barium sulfate. In *Applied Mechanics and Materials* (Vol. 117, pp. 1402-1405). Trans Tech Publications.

[146] Zhu, Z. and Kelley, M.J., 2005. IR spectroscopic investigation of the effect of deep UV irradiation on PET films. *Polymer*, *46*(20), pp.8883-8891.

[147] Fechine, G.J.M., Rabello, M.S., Maior, R.S. and Catalani, L.H., 2004. Surface characterization of photodegraded poly (ethylene terephthalate). The effect of ultraviolet absorbers. *Polymer*, *45*(7), pp.2303-2308.

[148] Fechine, G.J.M., Souto-Maior, R.M. and Rabello, M.S., 2002. Structural changes during photodegradation of poly (ethylene terephthalate). *Journal of materials science*, *37*(23), pp.4979-4984.

[149] Rabello, M.S. and White, J.R., 1997. The role of physical structure and morphology in the photodegradation behaviour of polypropylene. *Polymer Degradation and Stability*, *56*(1), pp.55-73.

[150] McGreer, M., 2001. Atlas weathering testing guidebook. *Chicago: Atlas Material Testing Technology LLC*.

[151] Haillant, O., 2011. Accelerated weathering testing principles to estimate the service life of organic PV modules. *Solar Energy Materials and Solar Cells*, *95*(5), pp.1284-1292.

[152] Oreski, G. and Wallner, G.M., 2005. Aging mechanisms of polymeric films for PV encapsulation. *Solar Energy*, *79*(6), pp.612-617.

[153] Arrieta, C., Dong, Y., Lan, A. and Vu-Khanh, T., 2013. Outdoor weathering of polyamide and polyester ropes used in fall arrest equipment. *Journal of Applied Polymer Science*, *130*(5), pp.3058-3065.

[154] Guadagno, L., Naddeo, C., Vittoria, V., Camino, G. and Cagnani, C., 2001. Chemical and morphologial modifications of irradiated linear low density polyethylene (LLDPE). *Polymer degradation and stability*, *72*(1), pp.175-186.

[155] Fechine, G.J.M. and Demarquette, N.R., 2008. Cracking formation on the surface of extruded photodegraded polypropylene plates. *Polymer Engineering & Science*, *48*(2), pp.365-372.

[156] Sammon, C., Yarwood, J. and Everall, N., 2000. An FT–IR study of the effect of hydrolytic degradation on the structure of thin PET films. *Polymer Degradation and Stability*, *67*(1), pp.149-158.

[157] Turnbull, L., Liggat, J.J. and MacDonald, W.A., 2012. Ageing of poly (ethylene terephthalate) and poly (ethylene naphthalate) under moderately accelerated conditions. *Journal of Applied Polymer Science*, *124*(6), pp.4517-4529.

[158] Krehula, L.K., Hrnjak-Murgić, Z., Jelenčić, J. and Andričić, B., 2009. Evaluation of poly (ethylene-terephthalate) products of chemical recycling by differential scanning calorimetry. *Journal of Polymers and the Environment*, *17*(1), pp.20-27.

[159] Pirzadeh, E., Zadhoush, A. and Haghighat, M., 2007. Hydrolytic and thermal degradation of PET fibers and PET granule: The effects of crystallization, temperature, and humidity. *Journal of applied polymer science*, *106*(3), pp.1544-1549.

[160] Hosseini, S.S., Taheri, S., Zadhoush, A. and Mehrabani-Zeinabad, A., 2007. Hydrolytic degradation of poly (ethylene terephthalate). *Journal of Applied Polymer Science*, *103*(4), pp.2304-2309.

[161] Golike, R.C. and Lasoski Jr, S.W., 1960. Kinetics of hydrolysis of polyethylene terephthalate films. *The Journal of Physical Chemistry*, *64*(7), pp.895-898.

[162] International Electrotechnical Commission, 1993. IEC-61215. *Crystalline Silicon Terrestrial Photovoltaic (PV) Modules-Design Qualification and Type Approval. IEC: Geneva*.

[163] Köntges, M., Kurtz, S., Packard, C., Jahn, U., Berger, K.A., Kato, K., Friesen, T., Liu, H. and Van Iseghem, M., 2014. Review of Failures of Photovoltaic Modules, 2014, International Energy Agency. *Report IEA-PVPS T13-01*.

[164] F.Higgins, P. L. Tang and A. Rein 2014 Analysis of Artificially Weathered PET and a Separate PET Hydrolysis Evaluation Using the 4300 Handheld FTIR http://www.agilent.com/cs/library/applications/5991-4859EN.pdf

[165] Ju, M.Y., Huang, J.M. and Chang, F.C., 2002. Crystal polymorphism of poly (butylene-2, 6-naphthalate) prepared by thermal treatments. *Polymer*, *43*(7), pp.2065-2074.

[166] Arbab, M.N., Auckland, D.W. and Varlow, B.R., 1988, June. Mechanical processes in the long term degradation of solid insulation. In *Dielectric Materials, Measurements and Applications, 1988., Fifth International Conference on* (pp. 231-233). IET.

[167] Ashcraft, A.C., Eichhorn, R.M. and Shaw, R.G., 1976, June. Laboratory studies of treeing in solid dielectrics and voltage stabilization of polyethylene. In *1976 IEEE International Conference on Electrical Insulation* (pp. 213-218). IEEE.

[168] PVPS, I., 2016. 2015 Snapshot of Global PV Markets. *Report IEA PVPS T1-29*.

[169] Luque, A. and Hegedus, S. eds., 2011. *Handbook of photovoltaic science and engineering*. John Wiley & Sons.

[170] Voronko, Y., Eder, G.C., Knausz, M., Oreski, G., Koch, T. and Berger, K.A., 2015. Correlation of the loss in photovoltaic module performance with the ageing behaviour of the backsheets used. *Progress in Photovoltaics: Research and Applications*, *23*(11), pp.1501-1515.

[171] Leadbitter, J., Tice, P., Ottenio, D., Escabasse, J.Y. and Podd, B., 2000. Packaging materials: 1. Polyethylene terephthalate (PET) for food packaging

applications.-(v. 3): Polypropylene as a packaging material for foods and beverages.-(v. 4): Polyethylene for food packaging applications.-(v. 5): Polyvinyl chloride (PVC) for food packaging applications.-(v. 6): Paper and board for food packaging applications.

[172] Labde, R.K., 2010. *Preparation and characterization of polyethylene terephthalate/montmorillonite nanocomposites by in-situ polymerization method* (Doctoral dissertation, University of Toledo).

[173] Wohlgemuth, J., 2011, February. How Standards Control Module Design for Better or Worse. In *NREL 2011 PV Module Reliability Workshop, Golden*.

[174] Standard, I.E.C., 2005. 61215. *Crystalline silicon terrestrial photovoltaic (PV) modules–Design qualification and type approval*.

[175] Standard, I.E.C., 2008. 61646. Thin-Film Terrestrial Photovoltaic (PV) Modules–Design Qualification and Type Approval. *International Electrotechnical Commission*.

[176] International Electrotechnical Commission, 2008. IEC 61730-2 Photovoltaic (PV) Module Safety Qualification-Part 2: Requirements for Testing. *International Electrotechnical Commission: Geneva*.

[177] Kuffel, J. and Kuffel, P., 2000. *High voltage engineering fundamentals*. Newnes.

[178] Morshuis, P.H., 1993. Degradation of Solid Dielectrics due to Internal Partial Discharge: Some thoughts on progress made and where to go now. *IEEE Transactions on Dielectrics and Electrical Insulation Vol*, *12*.

[179] Kreuger, F.H., 1989. *Partial discharge detection in high-voltage equipment*. Butterworth-Heinemann.

[180] Izzati, W.A., Arief, Y.Z., Adzis, Z. and Shafanizam, M., 2014. Partial discharge characteristics of polymer nanocomposite materials in electrical insulation: A review of sample preparation techniques, analysis methods, potential applications, and future trends. *The Scientific World Journal*, *2014*.

[181] Phillips, N.H., Givot, B., O'Brien, B., Hardy, L.C., Loyd, J., Schoeppel, W., Jaeger, C., Humpert, C., Schumacher, R. and Knoll, C., 2011, June. Study of Partial

Discharge effects of PV backsheet component films. Structure property relationships, and measurement consistency. In *Photovoltaic Specialists Conference (PVSC), 2011 37th IEEE* (pp. 003609-003613). IEEE.

[182] Morshuis, P.H. and Smit, J.J., 2005. Partial discharges at DC voltage: their mechanism, detection and analysis. *IEEE Transactions on Dielectrics and Electrical Insulation*, *12*(2), pp.328-340.

[183] Lecomte, H.A. and Liggat, J.J., 2008. Commercial fire-retarded PET formulations–Relationship between thermal degradation behaviour and fire-retardant action. *Polymer Degradation and Stability*, *93*(2), pp.498-506.

Appendix A:

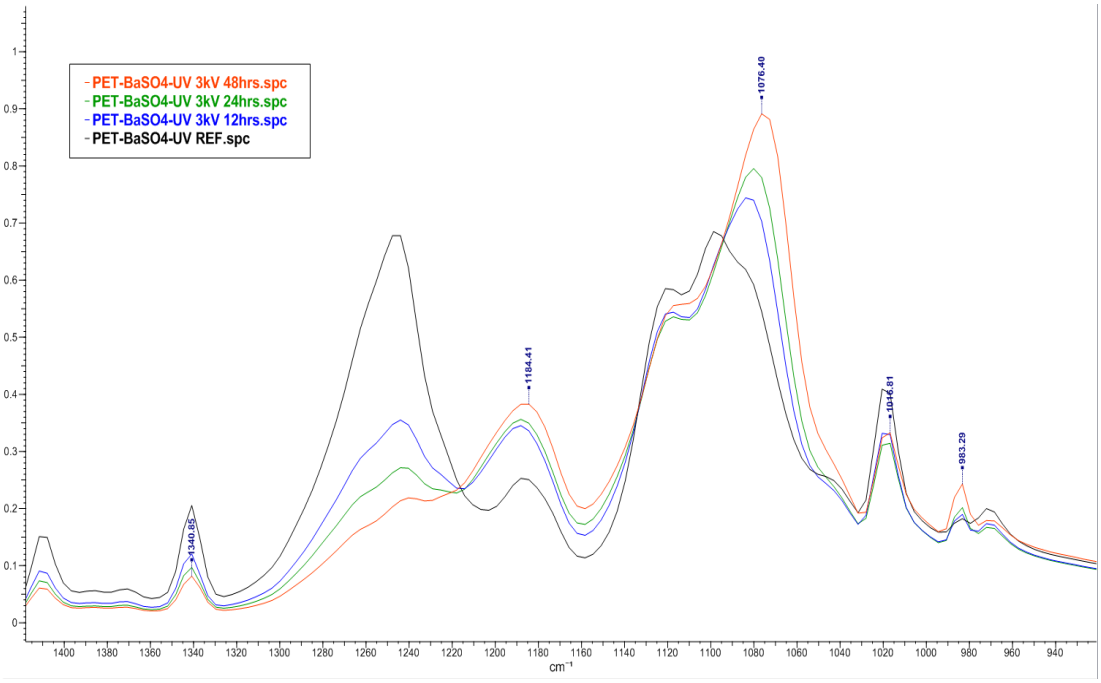

Figure A.1 Overlaid ATR-FTIR spectra of PET-$BaSO_4$-UV subjected to PD for 0, 12, 24 and 48hrs

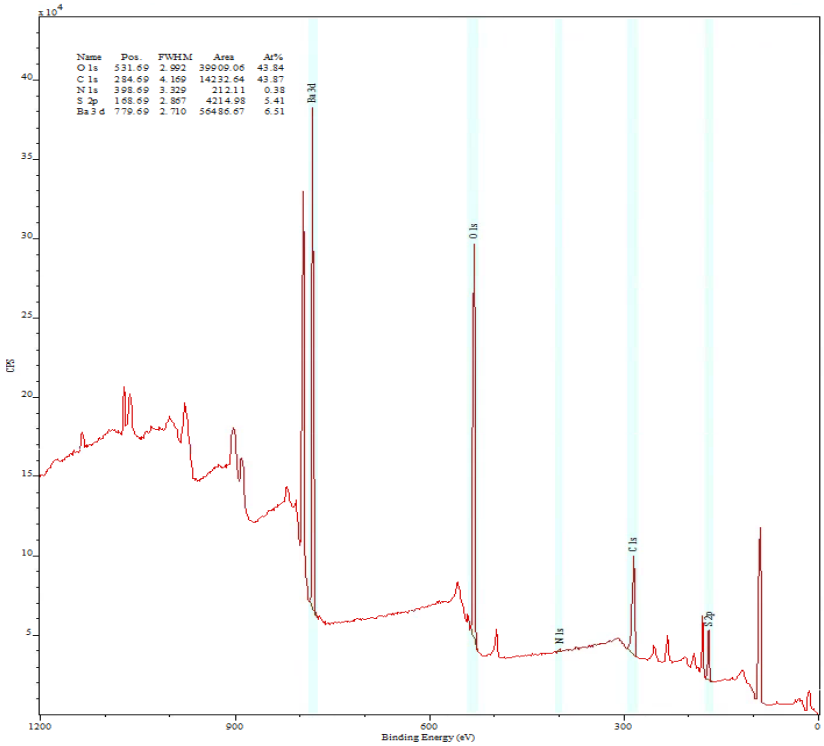

Figure A.2 XPS survey of PET-$BaSO_4$-UV subjected to PD for 24 hrs

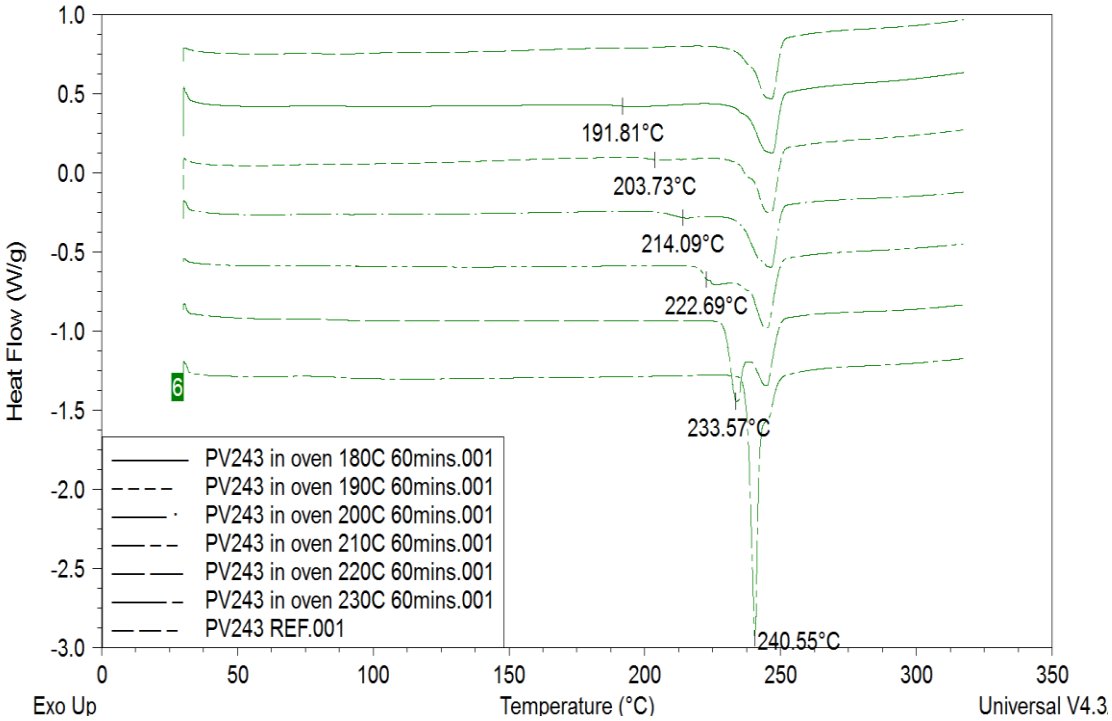

Figure A.3 DSC analyses of the melting of PET-$BaSO_4$-UV after crystallization at different temperatures

Samples	T_m^1(K)	L_c^1(Å)	A_{Tm1}(%)	T_m^2(K)	L_c^2(Å)	A_{Tm2}(%)	ΔH_m(J/g)	X_c%
REF	N/A	N/A	N/A	519.8±0.4	128.8	N/A	33.87	24.19
180°C	465.0±0.6	57.5	9.9	520.0±0.3	129.4	90.1	36.66	26.18
190°C	476.9±1.4	65.4	16.7	519.5±0.4	127.9	83.3	35.65	25.46
200°C	487.2±1.1	74.1	20.5	519.6±0.4	128.0	79.5	38.73	27.66
210°C	495.8±0.9	83.5	37.1	519.6±0.2	128.0	62.9	41.90	29.93
220°C	506.7±1.3	99.4	46.5	518.2±0.4	124.3	53.5	42.72	30.51
230°C	513.7±1.6	113.2	89.8	518.2±0.3	124.3	10.2	43.27	30.91

Table A.1 DSC data of PET-$BaSO_4$-UV annealed at various temperatures from 180 to 230°C for 60 mins

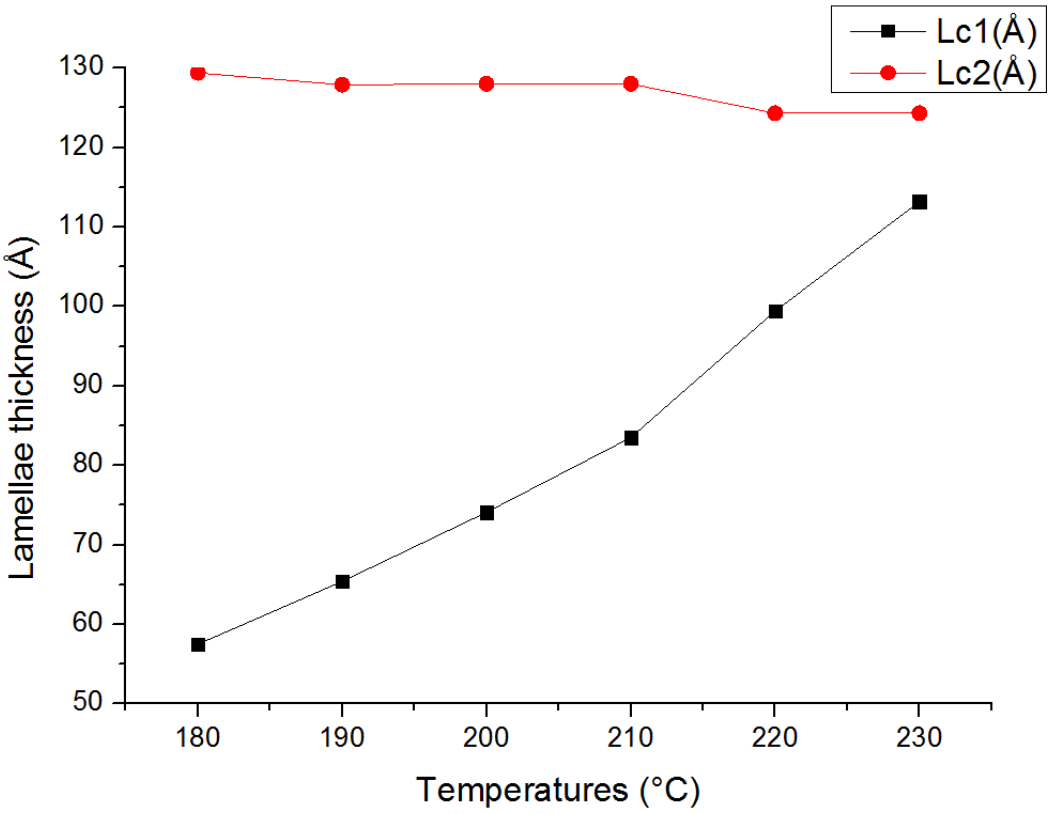

Figure A.4 Thicknesses of primary and secondary lamellae of PET-$BaSO_4$-UV annealed at various temperatures from 180 to 230°C for 60 mins

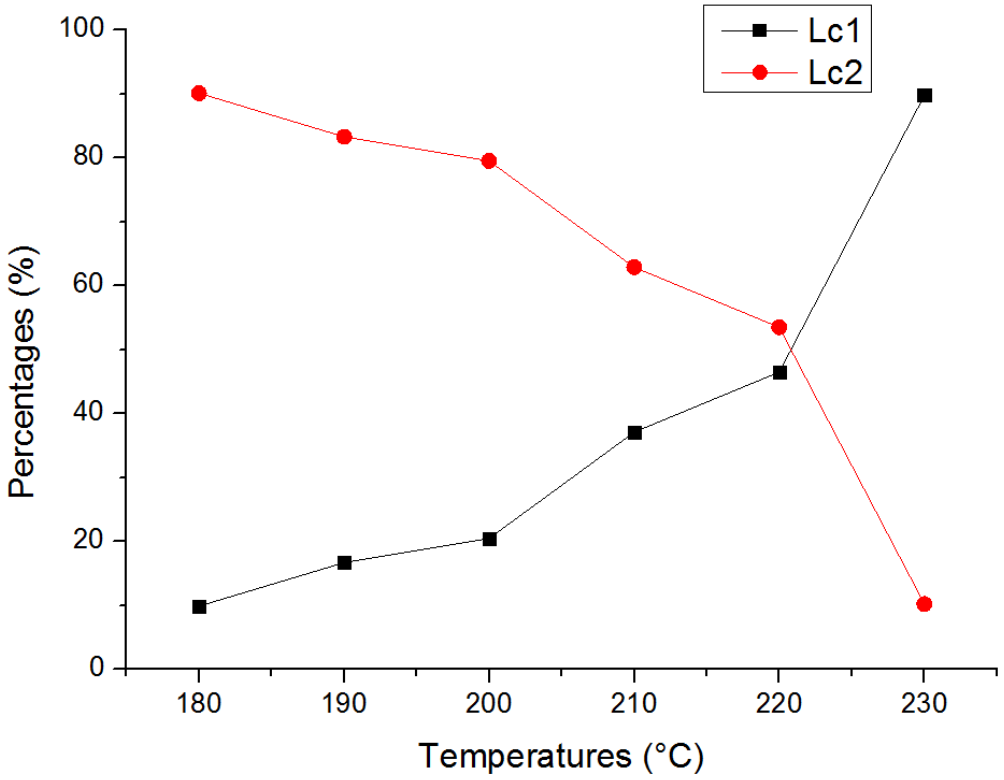

Figure A.5 Percentages of primary L_c^1 and secondary L_c^2 lamellae of PET-$BaSO_4$-UV annealed at various temperatures from 180 to 230°C for 60 mins

Samples	1455 cm^{-1}	1473 cm^{-1}	$\%X_c$
Untreated PET-$BaSO_4$-UV	68.3	31.7	31.7
180°C	67.4	32.6	32.6
190°C	66.9	33.1	33.1
200°C	66	34	34
210°C	66	34	34
220°C	64.5	35.5	35.5
230°C	64.1	35.9	35.9

Table A.2 Crystallinity degrees of untreated and annealed PET-$BaSO_4$-UV by FTIR

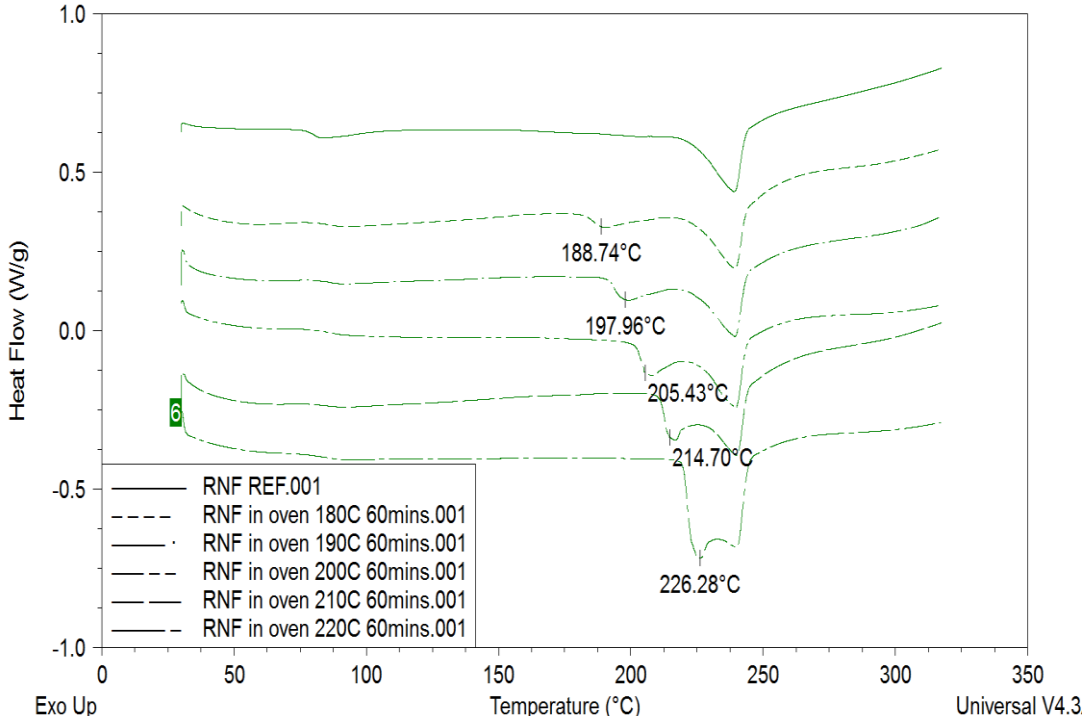

Figure A.6 DSC analyses of the melting of PET-FR after crystallization at different temperatures

Samples	T_m^1(K)	L_c^1(Å)	A_{Tm1}(%)	T_m^2(K)	L_c^2(Å)	A_{Tm2}(%)	ΔH_m(J/g)	X_c%
REF	N/A	N/A	N/A	512.2±0.3	109.9	N/A	19.73	14.09
180°C	463.2±0.9	56.5	26.3	512.5±0.5	110.6	73.7	31.32	22.37
190°C	472.2±1.1	62.0	32.6	512.5±0.4	110.6	67.4	32.54	23.24
200°C	481.2±1.6	68.8	41.3	512.7±0.4	110.9	58.7	33.08	23.63
210°C	490.0±0.8	76.9	52.3	513.0±0.2	111.6	47.7	33.19	23.71
220°C	499.4±1.1	88.1	61.4	513.0±0.3	111.6	38.6	39.24	28.03

Table A.3 DSC data of PET-FR annealed at various temperatures from 180 to 220°C for 60 mins

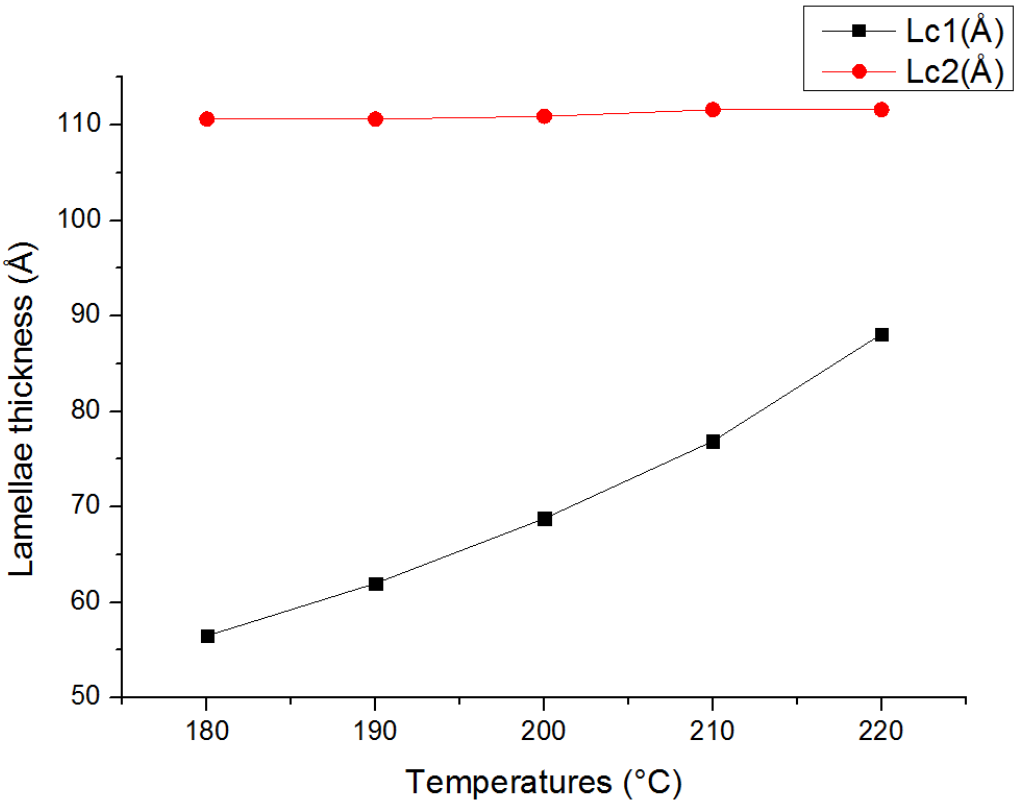

Figure A.7 Thicknesses of primary and secondary lamellae of PET-FR annealed at various temperatures from 180 to 220°C for 60 mins

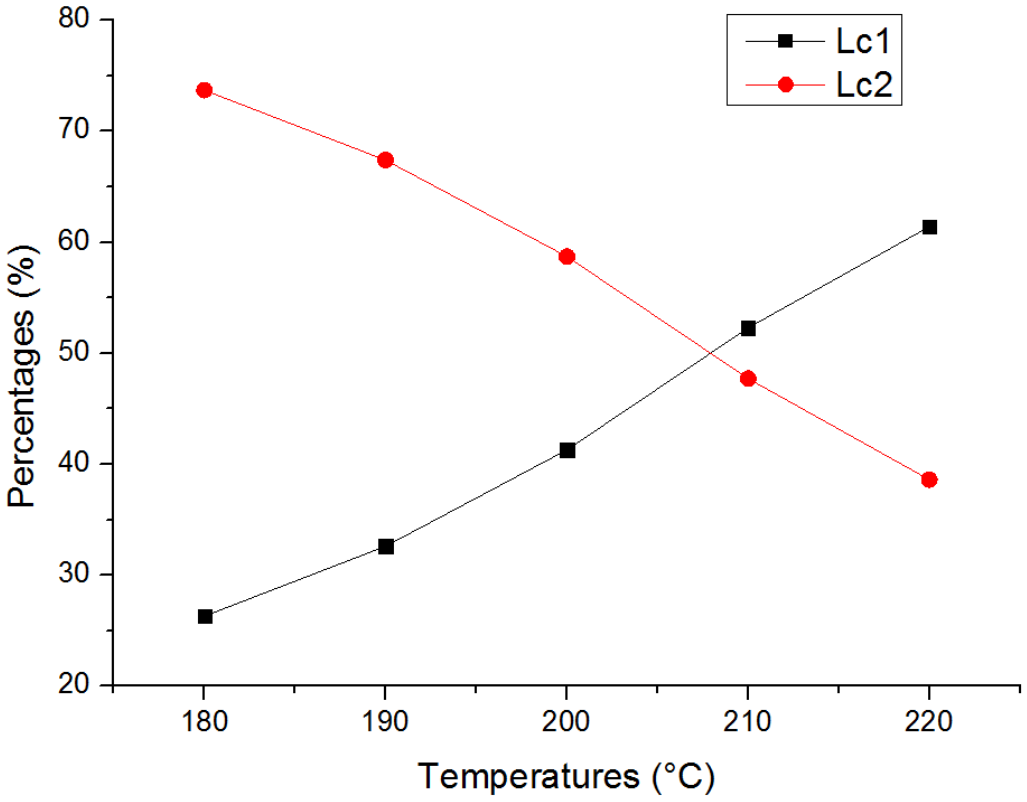

Figure A.8 Percentages of primary L_c^1 and secondary L_c^2 lamellae of PET-FR annealed at various temperatures from 180 to 220°C for 60 mins

Samples	1455 cm^{-1}	1473 cm^{-1}	$\%X_c$
Untreated PET-FR	69.6	30.4	30.4
180°C	64.3	35.7	35.7
190°C	63.6	36.4	36.4
200°C	63.1	36.9	36.9
210°C	63.0	37.0	37.0
220°C	62.8	37.2	37.2

Table A.4 Crystallinity degrees of untreated and annealed PET-FR by FTIR

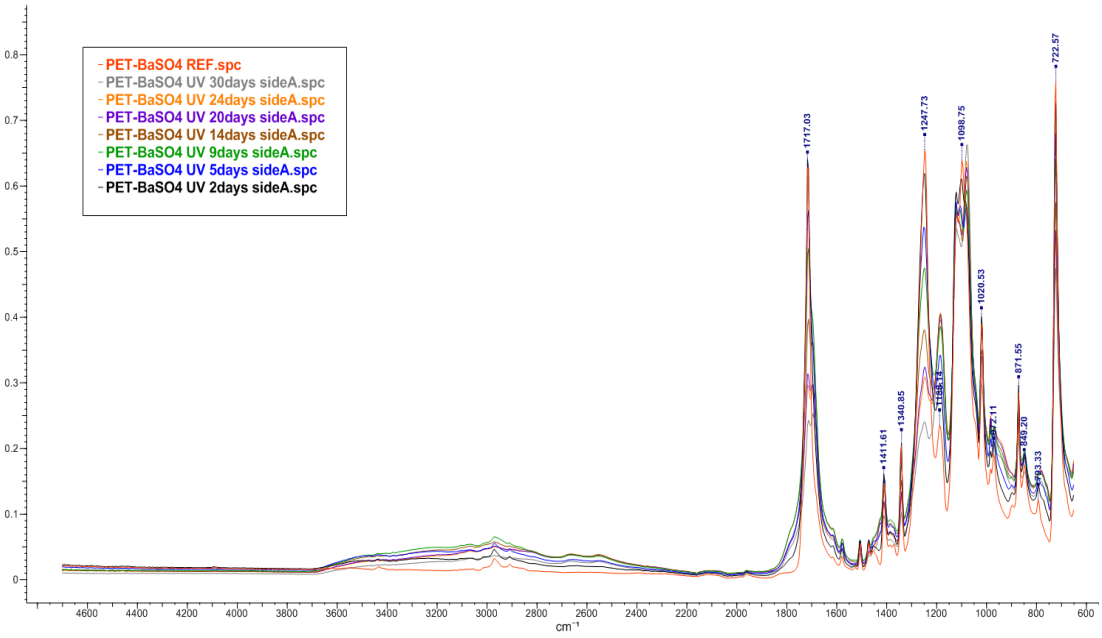

Figure A.9 ATR-FTIR spectra of weathered PET-$BaSO_4$ from 0 to 30 days (side A)

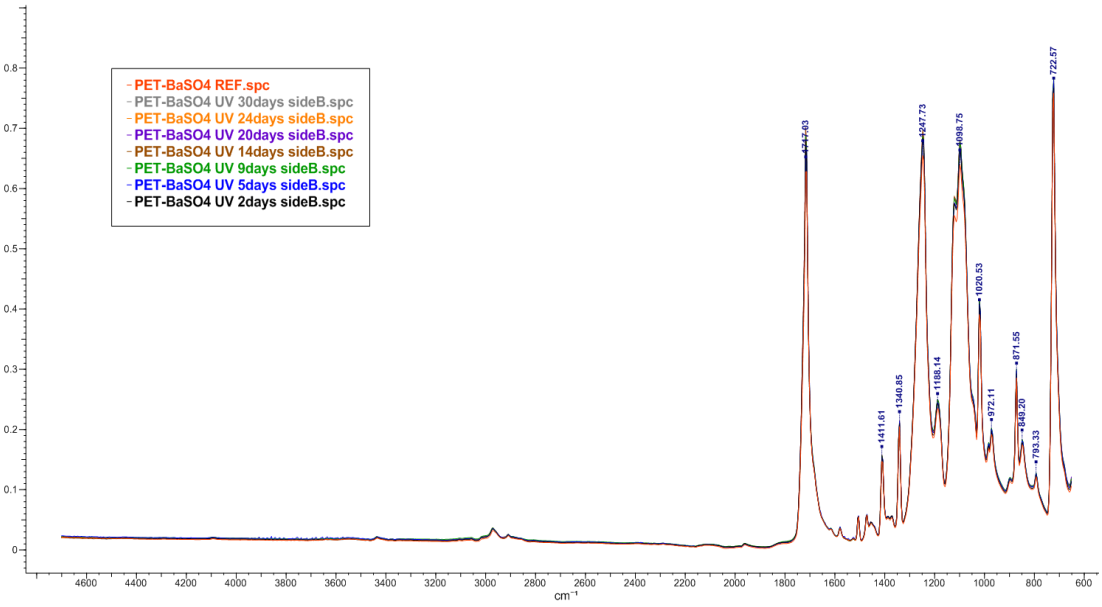

Figure A.10 ATR-FTIR spectra of weathered PET-$BaSO_4$ from 0 to 30 days (side B)

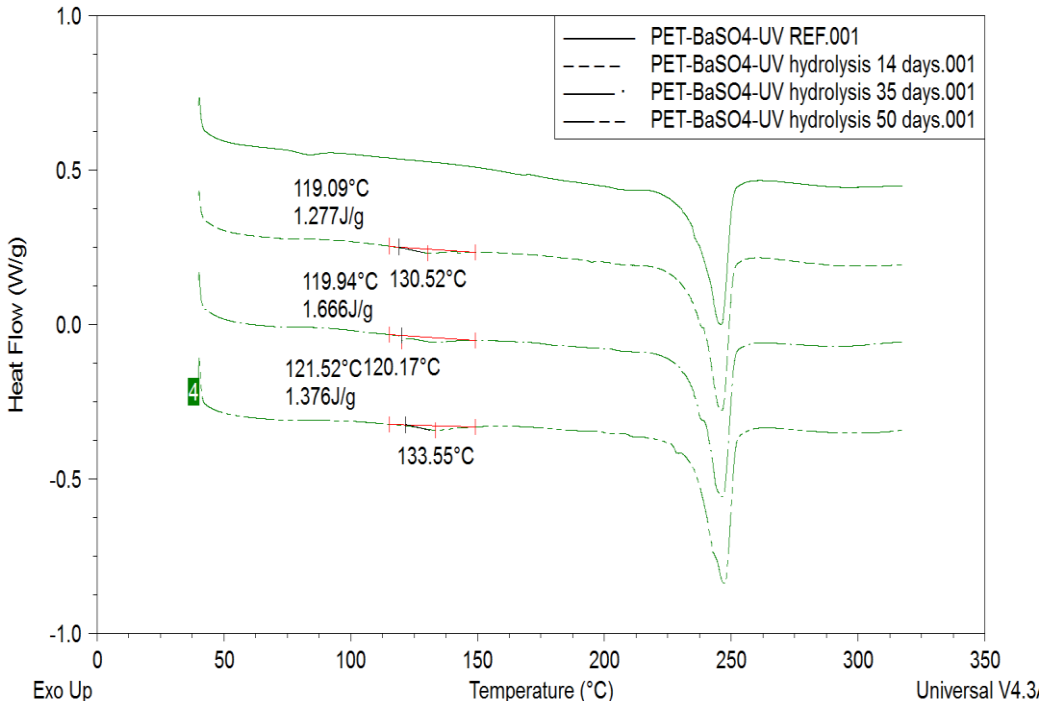

Figure A.11 DSC thermograms of untreated and hydrolysed PET-$BaSO_4$-UV (14, 35 and 50 days)

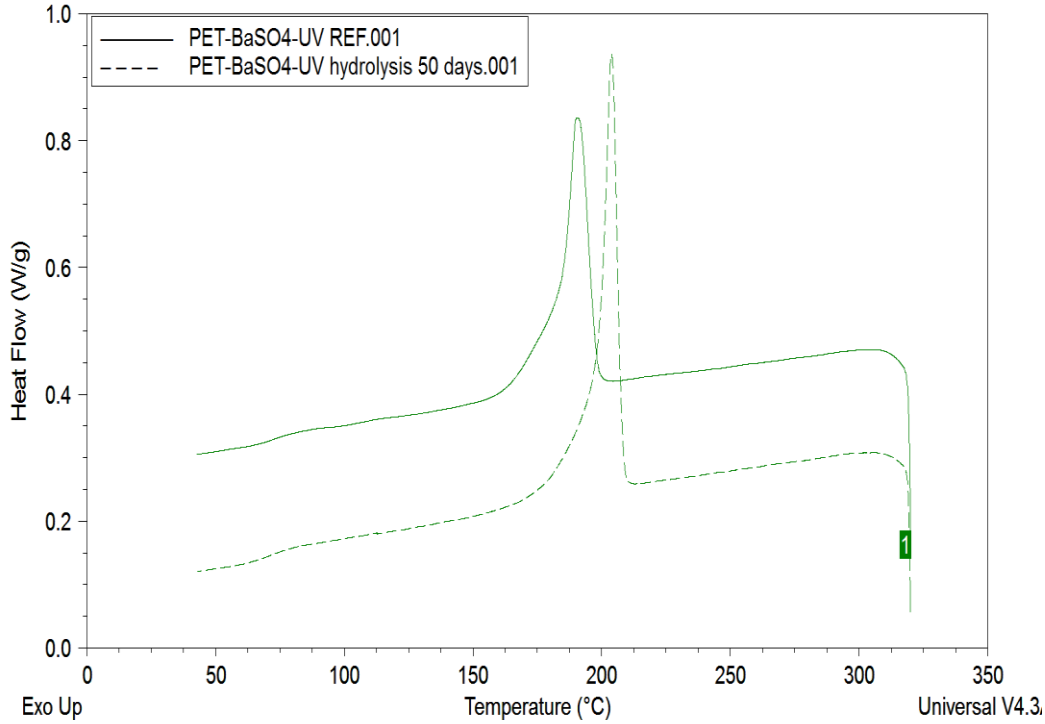

Figure A.12 DSC thermograms (cooling run) of untreated and 50-day hydrolysed PET-$BaSO_4$-UV